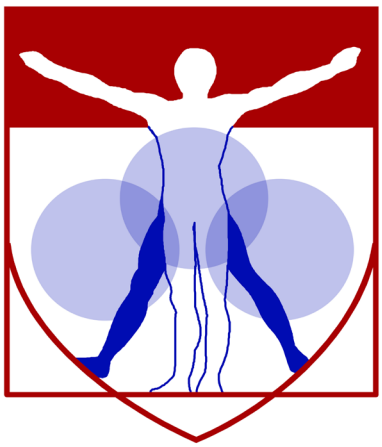

PENN
CENTER for
MUSCULOSKELETAL
DISORDERS

16th Annual Scientific Symposium/Retreat

Wednesday, November 13, 2019
Smilow Rubenstein Auditorium/Commons
8:00am-6:30pm
www.med.upenn.edu/pcmd/

Table of Contents

Page

Symposium Agenda……..... 1

Penn Center for Musculoskeletal Disorders Components…… 2-12

Center Overview……2-3

Core I-Biomechanics……... 4

Core II-Histology..……...…… 5

Core III-MicroCT…… 6

Pilot Grant Program.…… 7-11

Visiting Professorship Series……12-13

Symposium Participants…… 14-18

Speaker Abstracts……..……..……19-28

Other Abstracts…… P1-P83

Biomechanics……. P1-P20

Histology……..... P21-P48

MicroCT……... P49-P56

Miscellaneous……..…… P57-P83

Notes……..

We gratefully acknowledge the financial support provided by the National Institute of Arthritis, Musculoskeletal and Skin Diseases of the National Institutes of Health and the University of Pennsylvania, Perelman School of Medicine for our Center.

Penn Center for Musculoskeletal Disorders
Scientific Symposium Agenda

November 13, 2019

Smilow Rubenstein Auditorium ♦ University of Pennsylvania

08:00 – 09:00am	**Registration and Poster Set-up**
09:00 – 09:20am	**Welcome and Overview** *Louis J. Soslowsky, Ph.D.*
09:20 – 10:20am	**Session I: New Member Session** (Moderator: X. Sherry, Liu, PhD) ♦ *Véronique Lefebvre, Ph.D., "Dissecting Genetic Mechanisms Controlling Skeletal Cell Lineage Specification and Differentiation."* ♦ *Peter B. Noël, Ph.D., "Advancements in CT: More Information with Less Dose."* ♦ *Shuying Yang, M.D., M.S., Ph.D., "Regulation of RGS Protein in Inflammatory Arthritis."*
10:20 – 11:00am	**Break and Poster Session (Even Numbered)**
11:00 – 12:00pm	**Session II: Affiliate Member Session** (Moderator: Robert Mauck, PhD) ♦ *Fadia Kamal, PharmD, Msc, Ph.D., Penn State Hershey, "Regulation of GPCR in Cartilage Development and Disease."* ♦ *Nancy Pleshko, Ph.D., Temple University, "Non-Destructive Applications of Optical Spectroscopy for Assessment of Tissue Pathology and Regeneration."* ♦ *David Waning, Ph.D., Penn State Hershey, "Skeletal muscle weakness: What's bone got to do with it?"*
12:00 – 01:15pm	**Poster viewing and lunch (provided) in Smilow Commons**
01:15 – 02:15pm	**Session III: Pilot Grantee Session** (Moderator: Maurizio Pacifici, PhD) ♦ *Carla Scanzello, MD, PhD, "Time-Dependent Changes in Macrophage Profiles in a Murine Model of Osteoarthritis."* ♦ *Yanqing Anna Gong, PhD, "Plasminogen is Critical for Bone Fracture Repair by Promoting the Functions of Periosteal Mesenchymal Progenitors."* ♦ *Nathaniel Dyment, PhD, "Tendon-to-Bone Repair: How do we create the zones?"*
02:15 – 02:55pm	**Break and Poster Session (Odd Numbered)**
02:55 – 03:00pm	**Carl T. Brighton, MD, PhD August 20, 1931 – July 3, 2019**
03:00 – 3:45pm	**Academics to Industry Panel** (Moderator: Louis Soslowsky, PhD) *Jason Burdick, PhD, Bhavana Mohanraj, PhD, Michael Dishowitz, PhD*
03:45 – 04:45pm	**Keynote Speaker** (Moderator: Louis Soslowsky, PhD) *"Strategic Approaches for the Translation of Concept to Product in Regenerative Medicine"* *Anthony Ratcliffe, Ph.D., President and CEO of Synthasome, Inc.*
04:45 – 05:00pm	**Final Comments Preceding Poster Session and Reception**
05:00 – 06:30pm	**Poster Session, Presentation of Poster Awards and Reception in Smilow Commons**

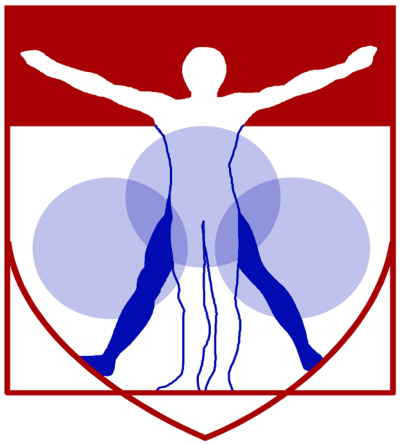

PENN

CENTER for

MUSCULOSKELETAL

DISORDERS

Center

Components

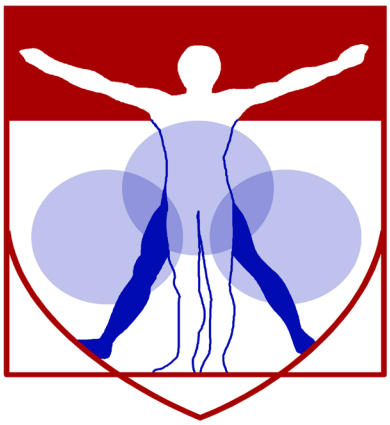

PENN

CENTER for

MUSCULOSKELETAL

DISORDERS

Center Overview

OVERVIEW OF THE PENN CENTER FOR MUSCULOSKELETAL DISORDERS

Director: Louis J. Soslowsky, PhD (soslowsk@upenn.edu)
Associate Director: Maurizio Pacifici, PhD (PacificiM@email.chop.edu)

Musculoskeletal-related conditions in the United States account for 132 million visits to physicians' offices, 29 million visits to emergency rooms, 15 million hospital outpatient visits, and cost over $850 billion each year. Further, musculoskeletal injuries in the United States cause workers to miss more than 440 million days of work annually. In fact, more than one in four Americans has a musculoskeletal impairment. With the widespread increase in athletic and recreational activities, and the increase of the elderly population at large, these numbers are expected to rise substantially. Musculoskeletal injuries represent a critical health concern which must be better understood and better treated. To do so, a dedicated and focused strategic effort is required that optimizes research translation from the bench to the bedside in an efficient and effective manner.

The Penn Center for Musculoskeletal Disorders (PCMD) will continue to enhance the research productivity of, and provide critical resources and programs to, investigators to address multidisciplinary research strategies for musculoskeletal problems. The overall goal of this Center is to promote cooperative interactions among investigators, accelerate and enrich the effectiveness and efficiency of ongoing research, foster new collaborations and new research, and ultimately, translate our research efforts into better and new therapies for musculoskeletal disorders. The central theme of the Center will continue to be "Musculoskeletal Tissue Injury and Repair". This theme is broad (as it includes all musculoskeletal tissue types, such as bone, cartilage, disc, ligament, meniscus, muscle, and tendon), focused (as takes advantage of commonalities in approaches across tissue types), and clinically significant (as it fosters development of assays, procedures and knowledge in preclinical animal and human models of translational relevance). It is important to note that our PCMD is not a "bone center" nor is it a "muscle center". Rather, it is truly a "musculoskeletal center" and has emerged as the recognized home for musculoskeletal research across the Penn campus and as a technical and intellectual resource for the broader Philadelphia musculoskeletal research community.

One focus of our Center is to translate research themes, approaches, and paradigms that are consistent across different tissues. Musculoskeletal tissues have much in common and their similarities are often overlooked when focus is restricted to a single tissue type. For example, the role of inflammatory cytokines is well studied in several tissue injury and repair scenarios; yet specific findings in one tissue-type are not always known and applied in other tissues. Similarly, the availability of technologies for imaging blood vessel formation in vivo to monitor healing in a given tissue is not always known and available to researchers focusing on other tissues. Given that approaches routinely used to evaluate mechanisms in one tissue could aid researchers in other areas, our Center will work to foster this critical cross-talk.

To provide a further focus for our Center, we will continue to develop programs with an emphasis on small animal models utilizing unique and sophisticated methods that can cross length scales to pre-clinical large animal models and human testing. Although large animal models for many human diseases exist and are essential for translational studies, small animals (e.g., mouse and rat) have become more commonly used for fundamental discovery of disease mechanism and initial therapeutic development due to availability of transgenic and knockout approaches and molecular tools, low cost, ease of handling and housing, and other practical issues. However, performing certain assays and experiments in mice and rats can be challenging and these difficulties often cannot be overcome in single investigator laboratories. The PCMD will provide unique expertise and sophisticated analytical tools to investigate musculoskeletal tissues across length scales.

Thus, the primary overall aims of this Center are to enhance and advance the research productivity of investigators in musculoskeletal tissue injury and repair by:

Aim 1: Providing innovation within critical resource core facilities in areas that cross disciplines, length scales, and hierarchies. These core facilities are μCT Imaging, Biomechanics, and Histology.

Aim 2: Developing a pilot and feasibility grant program for investigators, with direct mentorship, whereby new approaches, ideas, and collaborations can be developed prior to seeking extramural funding.

Aim 3: Developing educational and research enrichment programs spanning tissue types, research approaches, and paradigms, through which members can learn from national leaders and from each other.

High quality musculoskeletal research is currently being conducted by many groups at Penn. While many bring sophisticated approaches to bear on musculoskeletal problems, few groups have the required expertise and facilities to perform high quality and specialized assays in their own labs. Furthermore, most investigators are not aware of approaches utilized, and results obtained, in other tissues that may have direct relevance on their research questions. Ultimately, close cooperation, communication, and collaboration among researchers across musculoskeletal tissue types and from a wide variety of disciplines will significantly enhance the research of our members. The Center will provide opportunities to integrate multi-disciplinary techniques to determine mechanisms for tissue function, injury, degeneration, repair, and regeneration, with the ultimate goal of advancing the diagnosis, treatment, and prevention of diseases and injuries of the musculoskeletal system.

In addition to the specific features described in this proposal, there is an intangible feature of our Center that should not be overlooked. Although our musculoskeletal program is strong nationally, the Penn biomedical research community is large and diverse. As such, the Center serves as an essential mechanism to highlight our successes and the importance and excitement of musculoskeletal research across campus, as well as to institutional leadership. Having a strong voice for musculoskeletal researchers is critical to support our collective and individual research goals. In these ways, the Center - with essential support from the P30 - has become and remains an indispensable resource and advocate for our community.

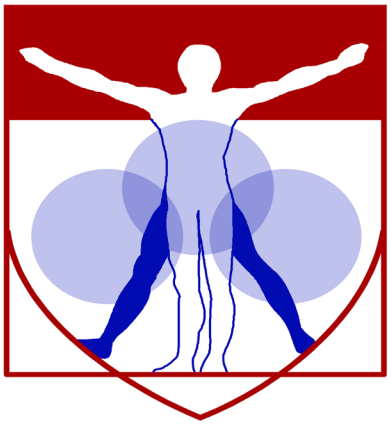

PENN

CENTER for

MUSCULOSKELETAL

DISORDERS

Core I

Biomechanics

Biomechanics Core

Core Director: Robert Mauck, Ph.D. (lemauck@pennmedicine.upenn.edu)
Technical Director: Snehal Shetye, Ph.D. (shetye@upenn.edu)

The overall objective of the Biomechanics Core is to develop and provide a wide range of innovative biomechanical approaches to evaluate musculoskeletal tissue function in the context of damage, repair, and regeneration, and to provide training and funding for new projects and collaborations utilizing these assays. Over the last decade, our Biomechanics Core at the Penn Center for Musculoskeletal Disorders (PCMD) has grown into a thriving resource for the University of Pennsylvania and Philadelphia area musculoskeletal research community. In this submission, we will further expand our services to meet the increased demand for specialized techniques and develop new and innovative methods that address the multi-scale mechanics of musculoskeletal tissues. These developments will provide customized services that enhance the research productivity of our members. The Specific Aims of the Biomechanics Core are:

- To provide guidance and training on the capabilities, advantages, and disadvantages of the various methodologies to assess musculoskeletal tissue biomechanical function through formal educational enrichment programs and one-on-one interactions

- To provide expertise and service for biomechanical assays of musculoskeletal tissues

- To develop innovative biomechanical testing techniques that will be applicable to Musculoskeletal research, and in particular those that provide information across tissue length scales

- To provide funding for the development of new projects and collaborations and to develop preliminary and/or feasibility data for investigators.

Successful completion of these aims will significantly enhance the environment and the capabilities of researchers at the University of Pennsylvania, leading to new approaches to address musculoskeletal disorders and new collaborations between Center faculties who may have not previously included biomechanical function approaches in their musculoskeletal research programs.

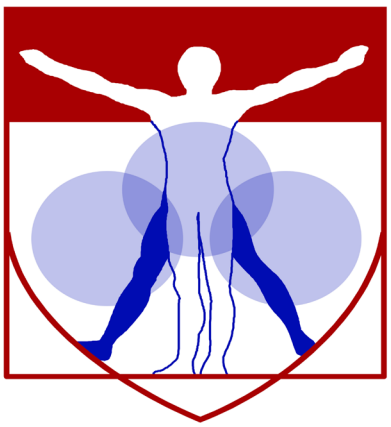

PENN

CENTER for MUSCULOSKELETAL DISORDERS

Core II

Histology

Histology Core

Overview and Mission

The mission of the Penn Center for Musculoskeletal Disorders (PCMD) Histology Core is to provide comprehensive, high quality histology services to musculoskeletal researchers at the University of Pennsylvania and the broader research community.

The Specific Aims of the core are:

- To provide guidance and training on the capabilities, advantages, and disadvantages of the various methodologies to assess musculoskeletal tissue structure and composition through formal educational enrichment programs and one-on-one interactions.
- To provide expertise and service for histological and histomorphometric assays of musculoskeletal tissues.
- To develop new histologically-based techniques that will be applicable to musculoskeletal research.
- To provide funding for development of new projects and collaborations and to develop preliminary and/or feasibility data for investigators.

Services Offered

The core offers a complete spectrum of services from sample preparation and processing, to sectioning, staining and analysis, with capabilities for paraffin, plastic and frozen histology. The core provides state of the art equipment in each of these areas, which can be accessed either on a self-service basis (upon completion of training) or a full-service basis through our full-time histology technician. Service fees are highly competitive, with significant subsidies offered for PCMD members.

- Consultation and protocol development (no charge for first 6 hours)
- Paraffin processing, embedding and sectioning
- Plastic processing and sectioning
- Frozen sectioning, including cryofilm method for undecalcified bone and teeth
- Routine histochemical staining
- Imaging and histoquantitation
- Training in histology techniques

If you are using the core for the first time, we highly recommend scheduling a meeting with one of the core co-directors and the core technician to discuss the scope of your project and specific needs.

We are very happy to provide letters of support for grant applications. To request a letter, please contact the core co-directors and provide the project title, a brief description of the project and core services you propose to use.

Please visit the core website for more information: www.med.upenn.edu/pcmd/histologymain.html

Co-Directors

Ling Qin, Ph.D. (Plastic and Frozen Histology)
Associate Professor of Orthopaedic Surgery
qinling@pennmedicine.upenn.edu
215 898 6697

Lachlan Smith, Ph.D. (Paraffin Histology)
Assistant Professor of Neurosurgery
lachlans@pennmedicine.upenn.edu
215 746 2169

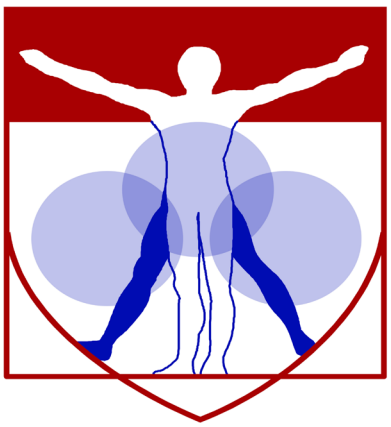

PENN

CENTER for MUSCULOSKELETAL DISORDERS

Core III

MicroCT

MicroCT Core

Director: X. Sherry Liu, Ph.D. (xiaoweil@pennmedicine.upenn.edu)

The development of high-resolution micro-CT (μCT) during the past two decades has revolutionized the quantitative assessment of calcified and X-ray dense tissue morphology. With the capability of non-destructive, three-dimensional (3D) visualization of tissue structure, μCT has largely supplanted traditional histomorphometry and become a gold standard for calcified tissue density and microstructure evaluation for many measures. Due to the low intrinsic X-ray contrast of non-mineralized tissues, traditional applications of μCT in musculoskeletal research have been limited to mineralized tissue. However, the development of contrast-enhanced imaging methods has greatly broadened applications of μCT to include musculoskeletal soft tissues as well. These cutting-edge image-based quantification methods not only enable characterization of soft-tissue morphology, but some also yield insight into tissue composition, such as glycosaminoglycan (GAG) density, which is associated with soft-tissue function and mechanics. Another important advance in the past decade is in vivo μCT imaging of living small animals. Research of musculoskeletal tissue injury and repair has been progressively utilizing animal models of human disease. Unlike many assays that require sacrificing the animal to extract tissues for analysis, in vivo μCT enables longitudinal evaluation of changes in a particular animal non-invasively over time. This new imaging strategy minimizes the number of animals required while enhancing statistical power. With these developments, μCT can now provide a deep and quantitative understanding of the genetic influences on the skeleton, as well as remodeling events in hard and soft tissues during repair, treatment, and with altered loading scenarios. Further, a μCT modality for clinical imaging of calcified tissue microstructure, called high-resolution peripheral quantitative CT (HR-pQCT), has recently been developed. This technology inaugurated a new era of non-invasive quantitative skeletal imaging, and has become a powerful tool for clinical research of musculoskeletal disorders. The overall objective of the μCTIC is to offer a wide range of μCT imaging approaches to evaluate musculoskeletal tissue injury and repair, and to provide training and consultation for new projects and collaborations utilizing these assays.

The Specific Aims for the μCTIC are:

- To provide guidance and expertise on the use of μCT imaging for musculoskeletal research through educational enrichment programs and one-on-one interactions
- To provide a range of μCT imaging resources, expertise, and services for the study of the structure, function and physiology of the musculoskeletal system in laboratory animals and humans
- To develop new μCT imaging-based techniques that will be applicable to musculoskeletal research
- To provide funding for the development of new projects and collaborations and to develop preliminary and/or feasibility data for investigators.

Successful completion of these Aims will significantly enhance the environment and capabilities of researchers at the University of Pennsylvania, leading to novel and innovative approaches to address musculoskeletal disorders and to new collaborations between Core faculty who may not have previously included human and/or animal imaging in their musculoskeletal research programs.

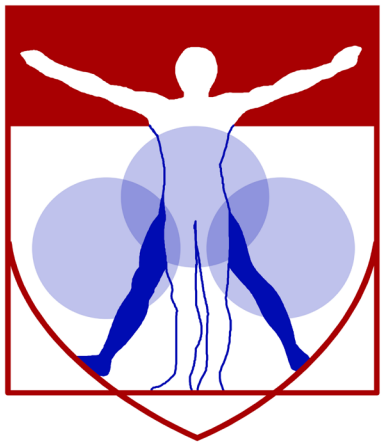

PENN

CENTER for

MUSCULOSKELETAL

DISORDERS

Pilot Grant Program

PENN CENTER FOR MUSCULOSKELETAL DISORDERS
PILOT AND FEASIBILITY GRANT PROGRAM

The Penn Center for Musculoskeletal Disorders has an ongoing Pilot and Feasibility Grant Program. Submissions should be related to musculoskeletal tissue injury and repair which is the broad focus of the Center and Grants are only eligible for Center members (if you are not a member but would like to become one, please contact pcmd@pennmedicine.upenn.edu). For more information on our Cores and Center in general, please see our web site at www.med.upenn.edu/pcmd . We are anticipating that the next Center grant submission deadline will be in Spring 2019.

Eligibility

- Only Full Center members are eligible. If you are not currently a member, please go to the link: http://www.med.upenn.edu/pcmd/memberinfo.shtml
- Categories of applicants include: 1) Established investigators with a proposal to test the feasibility of a new or innovative idea in musculoskeletal tissue injury and repair representing a clear and distinct departure from their ongoing research, 2) Established investigators with no previous work in musculoskeletal tissue injury and repair interested in testing the applicability of their expertise on a problem in this area, and 3) New investigators without significant extramural grant support as a Principal Investigator to develop a new project.
- Pilot and Feasibility Grants must use at least one of the Center's Research Cores.
- Pilot project awardees are eligible for one year, with a second year to be considered (budgets will be for $20-50,000 per year and timelines should be for one or two years). The second year of funding, the dollar amount of which would only be for up to half the year one budget, will be considered based on the progress report submitted after the first year of funding and funding availability in the Center. Please note that second year funding will often not be awarded, and when awarded, will be done so primarily to new investigators; second year funding to senior investigators will be quite rare.
- It is expected that these Pilot grants will lead to funding through other independent, extramural mechanisms. Therefore, the likelihood of future extramural funding will enter into the evaluation of these proposals.

Format

- Applications should be formatted loosely in the style of an NIH R03 grant (http://grants.nih.gov/grants/guide/pa-files/PA-18-488.html). The main body of the application (Specific Aims through Research Design and Methods-sections 4-7 below) is limited to five pages. The application should be in a single pdf file. The format should be:

1) Cover Page (not NIH face page) with grant title, PI name (and co-PI name if applicable), affiliation, contact information
2) Budget and brief justification (note that equipment is not allowed) (Please use form PHS398, Page 4)
3) NIH Biosketch of PI (and co-PI if applicable) (in the new NIH format)
4) Specific Aims
5) Significance
6) Innovation
7) Approach
8) Brief Statement of Category of Investigator per guidelines above
9) Brief Statement of How this Funding will lead to other Extramural Funding
10) Human Subjects and/or Vertebrate Animal Subjects (if applicable)
11) Consultants (if applicable)
12) Literature Cited
13) Certification of Patient Oriented Research (if applicable)

The completed proposal are submitted via the PCMD website by going to the uploaded as a single PDF file.

Please do not hesitate to email pcmd@pennmedicine.upenn.edu with any questions or comments.

Penn Center for Musculoskeletal Disorders Pilot & Feasibility Grants
(all grants awarded since inception of Center)

Awarded 2019-2020
Jaimo Ahn, M.D., Associate Professor of Orthopaedic Surgery, Perelman School of Medicine: "The Interplay of Notch Suppression and Hypoxia on Bone Regeneration"

Riccardo Gottardi, Ph.D., Assistant Professor of Pediatrics, CHOP Pulmonary Medicine: "Impact of scaffold microporosity in guiding local stem cell differentiation for osteochondral repair"

Lachlan Smith, Ph.D., Assistant Professor of Neurosurgery: "Emergent Nucleus Pulposus Cell Heterogeneity during Intervertebral Disc Development and Growth"

Awarded 2018-2019
Miltiadis Zgonis, M.D., Assistant Professor of Orthopaedic Surgery, Perelman School of Medicine: "Development, Maturation, and Function of Meniscal Radial Elements"

Joel Boerckel, Ph.D., Assistant Professor of Bioengineering and Orthopaedic Surgery, Perelman School of Medicine: "Role of YAP/TAZ in osteoprogenitor cell-induced angiogenesis for vascularized bone repair" *(awarded extramural funding from NIH/NIAMS R01AR074948 and R01AR073809)*

Awarded 2017-2018
Nathaniel Dyment, Ph.D., Assistant Professor of Orthopaedic Surgery, Perelman School of Medicine: "Murine anterior cruciate ligament reconstruction model to understand the cellular origins and mechanisms of repair"

Yangqing Gong, Ph.D., Research Assistant Professor of Medicine, Perelman School of Medicine: "Role of plasminogen in mesenchymal stem cell function and post-injury bone regeneration"

Carla Scanzello, M.D., Ph.D., Assistant Professor of Medicine, Perelman School of Medicine: "Importance of Macrophage Responses in Osteoarthritis"

Susan Volk, V.M.D., Ph.D., D.A.C.V.S., Assistant Professor of Small Animal Surgery, School of Veterinary Medicine: "The Regulatory Roles of Type III Collagen in the Cartilage Collagen Network: Implications for Osteoarthritis Prevention and Treatment"

Awarded 2016-2017
Joseph Baur, Ph.D., Assistant Professor of Physiology Institute for Diabetes, Obesity and Metabolism, Perelman School of Medicine: "Targeting NAD metabolism in muscular dystrophy" *(awarded extramural funding from Elysium Health)*

Yongwon Choi, Ph.D. Leonard Jarett Professor of Pathology and Lab Medicine, Perelman School of Medicine: "Cell adhesion regulation of multiple-myeloma induced bone destruction"

X. Sherry Liu, Ph.D., Assistant Professor of Orthopaedic Surgery and Bioengineering, Perelman School of Medicine: "Mechanical Consequences of Modeling- vs. Remodeling-Based Bone Formation" *(awarded extramural funding from the NSF Award #1661858)*

Hongtao Zhang, Ph.D., Research Assistant Professor, Department of Pathology and Lab Medicine, Perelman School of Medicine: "Novel cartilage-targeting Fc fusion proteins as novel and effective treatments for osteoarthritis"

Awarded 2015-2016

Yejia Zhang, MD, PhD, Department of Physical Medicine and Rehabilitation, "Inhibition of ADAM-8 to reduce intervertebral disc degeneration" *(Awarded extramural funding from the VA Pilot Grant; VA Competitive Pilot Fund)*

Oren Friedman, MD, Department of Otorhinolaryngology, Perelman School of Medicine: "Effect of injury to cartilage and recovery treatment with FGF-18"

Harvey Smith, MD, Department of Orthopaedic Surgery, "Impact of Pre-Culture and In Vivo Remobilization on Engineered Disc Replacement" *(Awarded extramural funding from the VA RX002274-01A1)*

Tejvir Khurana, MD, PhD, Department of Physiology, Perelman School of Medicine: "Role of the IL-15 / IL-15Rα axis in modulating muscle-tendon-bone adaptation and repair"

Awarded 2014-2015

Joshua F. Baker, MD, MSCE, Department of Rheumatology & Epidemiology/Perelman School of Medicine: *"Assessment of Intramyocellular Fat Accumulation in Rheumatoid Arthritis Using MR Spectroscopy*"

Russ P. Carstens, MD, Department of Renal-Electrolyte and Hypertension Division, Perelman School of Medicine: "Roles of Epithelial Splicing Regulatory Proteins in Craniofacial Development" *(awarded extramural funding NIH 1R56DE024749 and awarded R01 NIDCR)*

Foteini Mourkioti, PhD, Department of Orthopaedic Surgery/Perelman School of Medicine: "A Novel Molecular Mechanism in Chronic Skeletal Muscle Injury" *(supported in part from the IRM)*

Chamith Rajapakse, PhD, Department of Radiology/Perelman School of Medicine: "Biomechanics of Hip Fracture Assessed by MRI" *(Awarded extramural funding from the NIH R01 AR068382)*

Awarded 2013-2014

X. Sherry Liu, PhD, Department of Orthopaedic Surgery, Perelman School of Medicine: "Structure and Strength Recovery in Post-Lactation Bone" *(awarded extramural funding from the NIH R03 AR065145 and NSF Career Award #1653216)*

Ling Qin, Ph.D., Department of Orthopaedic Surgery, Perelman School of Medicine: "Novel Anabolic Treatment for Radiation-Induced Osteoporosis" *(awarded extramural funding from the NIH R01AR066098)*

Lachlan Smith, Ph.D. Department of Orthopaedic Surgery, Perelman School of Medicine: "Molecular Mechanisms of Failed Vertebral Bone Formation in Mucopolysaccharidosis VII" *(awarded extramural funding from the NIH R03 AR065142 and the MPS Society)*

Hansell H. Stedman, MD, Department of Surgery, Perelman School of Medicine: "Molecular Pattern Recognition in Acute and Chronic Injury to Muscle and Myotendinous Junction" *(awarded extramural funding from the NIH R01NS094705)*

Awarded 2012-2013

Jason Burdick, PhD, Department of Bioengineering, School of Engineering and Applied Science: "Acelluar Fibrous Scaffolds for Stem Cell Recruitment and Cartilage Repair" *(awarded extramural funding from the NIH R01 EB008722)*

James L. Carey, MD, MPH, Department of Orthopaedic Surgery, Perelman School of Medicine: "Development of a Large Animal Model of Osteochondritis Dissecans" *(awarded extramural funding from the NIH R01 EB008722)*

Andrew Kuntz, MD, Department of Orthopaedic Surgery, Perelman School of Medicine: "Effects of Intra-Articular Glenohumeral Injection of a Nonsteroidal Anti-Inflammatory Drug on Shoulder Joint Mechanics in a Rat Model"

Arjun Raj, PhD, Department of Bioengineering, School of Engineering and Applied Science: "Single Cell Analysis of Molecular and Micromechanical Heterogeneity in Mesenchymal Stem Cells and Engineered Tissues"

Awarded 2011-2012

Struan F.A. Grant, PhD, Department of Pediatrics, Children's Hospital of Philadelphia and Perelman School of Medicine: "Utilization of ChIP-seq to Identify Genes Regulated by Osterix"

Motomi Enomoto-Iwamoto, DDS, PhD, Department of Orthopaedic Surgery, Children's Hospital of Philadelphia and Perelman School of Medicine: "Tendon Repair by Retinoic Acid Receptor Agonists" *(awarded extramural funding from the NIH R21 AR062193)*

Ian N. Jacobs, MD, Department of Otorhinolaryngology: Head and Neck Surgery, Children's Hospital of Philadelphia and Perelman School of Medicine: "A Pilot Study for the Development of a Rabbit In-Vivo Tissue- Engineered Cartilage Graft for Pediatric Laryngotracheal Reconstruction" *(awarded extramural funding from The Triological Society)*

Awarded 2010-2011
Susan W. Volk, VMD, PhD, Dipl ACVC, Department of Small Animal Surgery, School of Veterinary Medicine: "The Role of Type III Collagen in Bone Repair and Regeneration"

Jaimo Ahn, MD, PhD, Department of Orthopaedic Surgery, Perelman School of Medicine: "Toward the Identification of Molecular Pathway Alterations in Aged Fracture Healing: A Pilot Study Utilizing a Genetic Model of Senescence" *(awarded extramural funding from the NIH R03 AG040670)*

Shannon Fisher, MD, PhD, Department of Cell and Developmental Biology, Perelman School of Medicine: "Requirement for Osterix in Skull Formation and Maintenance of Adult Bone in Zebrafish" *(awarded extramural funding from the NIH R21 DE021509)*

Awarded 2010-2011 (Jointly with IOA)
Olena Jacenko, PhD, Department of Animal Biology, School of Veterinary Medicine: "Aging of the hematopoietic niche" *(awarded extramural funding from the NIH R01 DK088334-01)*

Eileen M. Shore, PhD, Departments of Orthopaedic Surgery and Genetics, Perelman School of Medicine: "Modulation of Progenitor Cell Differentiation through BMP Signaling" *(awarded extramural funding from the NIH R01 AR041916-15)*

Kurt D. Hankenson, DVM, PhD, Department of Animal Biology, School of Veterinary Medicine: "Notch Signaling in Bone Regeneration" *(awarded extramural funding from the DOD CDMRP)*

Awarded 2009-2010
Ling Qin, PhD, Department of Orthopaedic Surgery, School of Medicine: "Mechanisms of EGFR Action on Bone" *(awarded extramural funding from the NIH R01 DK095803)*

Steven Scherer, MD, PhD, Department of Neurology, Perelman School of Medicine: "Are N-cadherin and L1 Adhesion Molecules Required for Recovery of Muscle Strength after Nerve Injury?"

Nader M. Hebela, MD, Department of Orthopaedic Surgery, Perelman School of Medicine: "A Pre-Clinical Rodent Model of Intervertebral Disc Autograft Transplant" *(awarded extramural funding from the DOD/CDMRP/PROP OR090090)*

Awarded 2008-2009
Sunday O. Akintoye, BDS, DDS, MS, Department of Oral Medicine, School of Dental Medicine: "Orofacial Bone Marrow Stromal Cells Promote Bisphosphonate-Associated Jaw Osteonecrosis" *(awarded extramural funding from the NIDCR R21 DE022826)*

Margaret M. Chou, PhD, Departments of Cell and Developmental Biology, Perelman School of Medicine: "Mechanisms of TRE17/USP6 Function in the Etiology of Aneurysmal Bone Cyst" *(awarded extramural funding from the NIH-NCI R01 CA168452 and R21-CA18601)*

Kenneth W. Leichty, MD, Department of Surgery, Perelman School of Medicine: "The Role of Inflammation in Regenerative Fetal Tendon Wound Healing" *(awarded extramural funding from the NIH DP2 DK083085)*

Kathleen M. Loomes, MD, Department of Pediatrics, Children's Hospital of Philadelphia: "The Role of Jag1 in Osteogenesis"

Eileen M. Shore, PhD, Departments of Orthopaedic Surgery and Genetics, Perelman School of Medicine: "Analysis of an ACVR1 Knock-in Mouse Model for FOP*" (awarded extramural funding from the NIH R01 AR041916-15S1)*

Awarded 2007-2008
Sherrill L. Adams, PhD, Department of Biochemistry, School of Dental Medicine: "Collagen III-deficient Mice as a Model for Musculoskeletal Wound Repair"

Kurt D. Hankenson, DVM, PhD, Department of Animal Biology, School of Veterinary Medicine: "Regulation of Bone Formation by Novel Activators of Canonical Wnt Signaling"

Awarded 2006-2007
Robert J. Pignolo, MD, PhD, Department of Medicine, Perelman School of Medicine: "Stem Cell Rescue of the Osteoporotic Phenotype in a Mouse Model of Accelerated Aging" *(awarded extramural funding from the NIH R01 AG028873)*

Robert L. Mauck, PhD, Department of Orthopaedic Surgery, Perelman School of Medicine "Meniscus Repair with a Novel Aligned Nanofiber Scaffold" *(awarded extramural funding from the NIH R01 AR056624 and the VA RR & D)*

Christopher S. Chen, MD PhD, Department of Bioengineering, School of Engineering and Applied Science: "Mechanotransduction in Mesenchymal Stem Cells" *(awarded partial funding as Co-Investigator on NIH P41 EB001046)*

Pedro K. Beredjiklian, MD, Department of Orthopaedic Surgery, Perelman School of Medicine: "Role of Hyaluronic Acid Receptors in Tendon Healing" (*awarded extramural funding from the NIH R21 AR052393*)

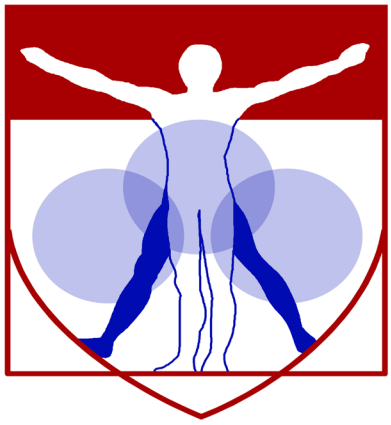

PENN

CENTER for

MUSCULOSKELETAL

DISORDERS

Visiting Professorship Series 2019-2020

Visiting Professorship Series-Academic Year 2019-2020

Tuesday, September 17, 2019, 1:30pm – 2:30pm, CRB Austrian Auditorium
Title: *"Towards a better understanding of Musculoskeletal development and arthritis pathogenesis: A Systems approach"*
Hiroshi Asahara, M.D., Ph.D.
Professor of MEM, Department of Molecular Medicine
Scripps Research, California Campus

Tuesday, October 15, 2019, 1:30pm – 2:30pm, CRB Austrian Auditorium
Title: *"Osteocytes and Connexin Channels in Mechanotransduction and Hormonal Response in Bone"*
Jean Jiang, Ph.D.
Professor and Zachry Distinguished University Chair
Department of Biochemistry and Structural Biology,
UT Health San Antonio

ANNUAL SCIENTIFIC SYMPOSIUM (all day event)
Wednesday, November 13, 2019, 8:00-6:30pm/Smilow Rubenstein Auditorium/
Title: *"Strategic approaches for the Translation of Concept to Product in Regenerative Medicine"*
Anthony Ratcliffe, Ph.D.
President and CEO of Synthasome, Inc.

Tuesday, December 10, 2019, 1:30-2:30pm, CRB Austrian Auditorium
Title: ***"****Osteoarthritis: Thinking Beyond the Cartilage"*
Kyle Allen, Ph.D.
Associate Professor, Associate Chair for UG Studies, ABET Coordinator
J. Crayton Pruitt Family Department of Biomedical Engineering
University of Florida

Tuesday, January 21, 2020, 1:30-2:30pm, CRB Austrian Auditorium
Title: *"Imaging across scales: visualizing tissue to subcellular mechanobiology in cartilage health and disease"*
Corey Neu, Ph.D.
Donnelly Family Endowed Associate Professor of Mechanical Engineering
University of Colorado, Boulder

Tuesday, February 25, 2020 1:30-2:30pm, CRB Austrian Auditorium
Title: ***"****Microtubules, Osteocyte Mechanotransduction, and the Surprising Regulation of Sclerostin"*
Joseph P. Stains, Ph.D.
Associate Professor of Mechanical Engineering
Iterim Director of Musculoskeletal Research
University of Maryland

Tuesday, March, 2020 1:30-2:30pm, CRB Austrian Auditorium
Title: TBD

Tuesday, April 14, 2020 1:30-2:30pm, CRB Austrian Auditorium
Title: *"TBD"*
Fabrisia Ambrosio, Ph.D., MPT
Associate Professor of Physical Medicine & Rehabilitation
Director Rehabilitation for UPMC International
University of Pittsburgh

Tuesday, May, 20201:30-2:30pm, CRB Austrian Auditorium
Title: TBD

Tuesday, June, 2020 1:30-2:30pm, CRB Austrian Auditorium
Title: TBD

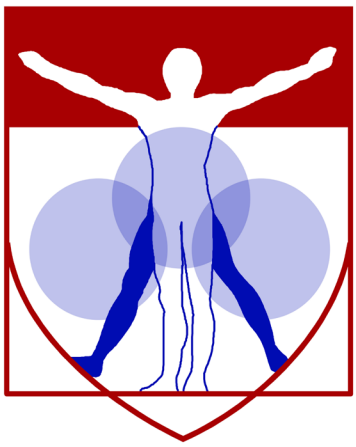

PENN
CENTER for
MUSCULOSKELETAL
DISORDERS

Symposium Participants

Last Name	First Name	Email	Affiliation
Abruzzo	Alexandra	tug37261@Temple Univ.edu	Temple Univ
Agnello	Kimberly	kagnello@vet.upenn.edu	UPenn
Alavi	Abass	Abass.alavi@uphs.upenn.edu	UPenn
Ali Akbari Ghavimi	Soheila	aliakbaris@email.chop.edu	CHOP
Allen	Robyn	roallen@vet.upenn.edu	UPenn
Angelozzi	Marco	angelozzim@email.chop.edu	CHOP
Anvari	Golnaz	tug10568@Temple Univ.edu	Temple Univ
Ashinsky	Beth	Beth.ashinsky@gmail.com	UPenn
Azar	Tala	talaazar@seas.upenn.edu	UPenn
Babak	Michael	papah@udel.edu	UPenn
Bansal	Sonia	soniab@seas.upenn.edu	UPenn
Barbe	Mary	mary.barbe@Temple Univ.edu	Temple Univ
Barnum	Carrie	cbarnum@pennmedicine.upenn.edu	UPenn
Baxter	Josh	josh.baxter@pennmedicine.upenn.edu	UPenn
Beach	Zakary	zakary.beach1@gmail.com	UPenn
Bellas	Evangelia	evangelia.bellas@Temple Univ.edu	Temple Univ
Berger	Anthony	Anthony.berger@Temple Univ.edu	Temple Univ
Billings	Paul	BillingsP@email.chop.edu	CHOP
Bizzaro	Candice	bizzaroc@email.chop.edu	CHOP
Blum	Samantha	sgb003@jefferson.edu	Thomas Jefferson Univ
Boerckel	Joel	boerckel@pennmedicine.upenn.edu	UPenn
Bonilla	Kelsey	kelsey.bonilla@uphs.upenn.edu	UPenn
Bonnevie	Eddie	edbon@pennmedicine.upenn.edu	UPenn
Bova	John	jbova21@gmail.com	UPenn
Brewer	Niambi	nbrewer@pennmedicine.upenn.edu	UPenn
Burdick	Jason	burdick2@seas.upenn.edu	UPenn
Caffeé	Laurel	lcaffee@nursing.upenn.edu	UPenn
Carlson	Jaclyn	jaclynca@upenn.edu	UPenn
Caron	Bob	rcaron@pennmedicine.upenn.edu	UPenn
Caston	Eleanor	tug47777@Temple Univ.edu	Temple Univ
Catheline	Sarah	cathelines@email.chop.edu	CHOP
Chakkalakal	Salin	salin@pennmedicine.upenn.edu	UPenn
Chen	Chider	chenc10@upenn.edu	UPenn
Chery	Daphney	daphney.chery@pennmedicine.upenn.edu	UPenn
Christiani	Thomas	christiani@rowan.edu	Rowan Univ
Chung	Rebecca	rebecca.chung@pennmedicine.upenn.edu	UPenn
Chung	Juliet	chungj7@email.chop.edu	CHOP
Collins	Joseph	jmcollin@seas.upenn.edu	UPenn
Cristino	Danielle	Danielle.Cristino@pennmedicine.upenn.edu	UPenn
Cruz	Geneva	tuh04212@Temple Univ.edu	Temple Univ
Cullen	D. Kacy	dkacy@pennmedicine.upenn.edu	UPenn
Dai	Eric	ericnan@seas.upenn.edu	UPenn
Daniels	Ryan	rydan@pennmedicine.upenn.edu	UPenn
Darrieutort-Laffite	Christelle	christelle.darrieutortlaffite@gmail.com	CHU de Nantes
Das	Suradipp	suradip@pennmedicine.upenn.edu	UPenn
Dear	Kayley	kdear@seas.upenn.edu	UPenn
Deepak	Vishwa	deepakv@upenn.edu	UPenn
DeSantis	Gabriel	gdes@seas.upenn.edu	UPenn
Di Caprio	Nikolas	tuf97303@Temple Univ.edu	Temple Univ
Dinella	Susan	sdinella@pennmedicine.upenn.edu	UPenn
Dishowitz	Michael	dishowit@upenn.edu	UPenn
Drazan	John	john.drazan@gmail.com	UPenn
Du	Jing	jingdu@psu.edu	Penn State Univ
Dyment	Nat	dyment@pennmedicine.upenn.edu	UPenn
Eastburn	Emily	eae@seas.upenn.edu	UPenn

Esterhai	John	John.Esterhai@uphs.upenn.edu	UPenn
Evans	Mary	mkevans@seas.upenn.edu	UPenn
Even	Kayla	tuf78888@Temple Univ.edu	UPenn
Falcon	Jessica	Falcon@Temple Univ.edu	Temple Univ
Farber	Daniel	Daniel.farber@pennmedicine.upenn.edu	UPenn
Fioravanti	Gabriella	gabriella.fioravanti@jefferson.edu	Thomas Jefferson Univ
Freeman	Theresa	theresa.freeman@jefferson.edu	Thomas Jefferson Univ
Fryhofer	George	George.Fryhofer@uphs.upenn.edu	UPenn
Fujino	Keitaro	Keitaro.Fujino@pennmedicine.upenn.edu	UPenn
Fung	Ashley	afung@seas.upenn.edu	UPenn
Galarraga	Jonathan	jgala@seas.upenn.edu	UPenn
Ganji	Elahe	elaganji@udel.edu	Univ of Delaware
Gaur	Amit	amit.gaur@jefferson.edu	Thomas Jefferson Univ
Gawri	Rahul	rahulgawri@hotmail.com	UPenn
Gehret	Paul	gehretp@seas.upenn.edu	UPenn
Gong	Yanqing	gongy@pennmedicine.upenn.edu	UPenn
Gordon	Kent	kent.gordon@bioventusglobal.com	Bioventus
Gottardi	Riccardo	gottardir@email.chop.edu	UPenn/CHOP
Granquist	Eric	eric.granquist@pennmedicine.upenn.edu	UPenn
Greer	Christopher	greerc@pennmedicine.upenn.edu	UPenn
Gui	Tao	Tao.Gui@pennmedicine.upenn.edu	UPenn
Gullbrand	Sarah	sgullb@pennmedicine.upenn.edu	UPenn
Hammel	Jennifer	tuf87662@Temple Univ.edu	Temple Univ
Hast	Michael	hast@pennmedicine.upenn.edu	UPenn
Haughan	Joanne	jhaughan@vet.upenn.edu	UPenn
Helbig	Kimberly	helbigkg@email.chop.edu	CHOP
Henning	Elizabeth	ehenning@pennmedicine.upenn.edu	UPenn
Heo	Su Chin	heosc@upenn.edu	UPenn
Hickok	Noreen J	Noreen.Hickok@jefferson.edu	Thomas Jefferson Univ
Hilliard	Brendan	hilliard@Temple Univ.edu	Temple Univ
Hong	Shijie	HONGS@email.chop.edu	CHOP
Hu	Baofeng	baofeng@upenn.edu	UPenn
Huang	Xiaobin	huangx1@email.chop.edu	CHOP
Huegel	Julianne	jhuegel08@gmail.com	UPenn
Hullfish	Todd	todd.hullfish@pennmedicine.upenn.edu	UPenn
Ita	Meagan	meita@seas.upenn.edu	UPenn
Jacenko	Olena	jacenko@vet.upenn.edu	UPenn
James	Aaron	awjames@jhmi.edu	Johns Hopkins Univ
Jamison	David	djamison@icloud.com	Drexel Univ
Jester	Cherie	cherieg@pennmedicine.upenn.edu	UPenn
Ji	Xing	jix@email.chop.edu	CHOP
Jiang	Zhirui	zhirui.jiang@pennmedicine.upenn.edu	UPenn
Jiang	Jie	jie.jiang@som.umaryland.edu	Univ of Maryland
Jo	Stephanie	stephanie.jo@pennmedicine.upenn.edu	UPenn
Joeng	Kyu Sang	joeng@pennmedicine.upenn.edu	UPenn
Kahle	Elizabeth	erk59@drexel.edu	Drexel Univ
Kamal	Fadia	fkamal@pennstatehealth.psu.edu	Penn State Univ
Kamalitdinov	Timur	timkam@seas.upenn.edu	UPenn
Kandel	Shital	tuf90290@temple.edu	Temple Univ
Karuppaiah	Kannan	kannank02@yahoo.com	UPenn
Kartha	Sonia	skartha@seas.upenn.edu	UPenn
Kc	Ranjan	kcr@email.chop.edu	CHOP
Kegelman	Chris	ckeg@seas.upenn.edu	UPenn
Kelly	John	john.kelly@uphs.upenn.edu	UPenn
Kim	Minwook	kimm12@email.chop.edu	CHOP
Kim	Dong hwa	kimd1@pennmedicine.upenn.edu	UPenn

Klyne	David	d.klyne@uq.edu.au	Temple Univ
Kolasinski	Sharon	sharon.kolasinski@uphs.upenn.edu	UPenn
Koyama	Eiki	koyamae@email.chop.edu	CHOP
Kwok	Bryan	bk589@drexel.edu	Drexel Univ
Lau	Yian Khai	adrianlau02@gmail.com	UPenn
Le Goff	Benoit	benlegoff@gmail.com	CHU de Nantes
Leahy	Thomas	tpleahy@seas.upenn.edu	UPenn
Lee	Yeonju	yeonju.lee@pennmedicine.upenn.edu	UPenn
Lee	Wen-Chih	LEEW2@email.chop.edu	CHOP
Lefebvre	Veronique	lefebvrev1@email.chop.edu	CHOP
Leiphart	Ryan	rleip@seas.upenn.edu	UPenn
Levin	Scott	scott.levin@pennmedicine.upenn.edu	UPenn
Li	Yihan	yihanl@seas.upenn.edu	UPenn
Li	Ke	LIK4@email.chop.edu	CHOP
liang	Dongming	dol@pennmedicine.upenn.edu	UPenn
Linardi	Renata	rlinardi@upenn.edu	UPenn
Liu	Sherry	xiaoweil@pennmedicine.upenn.edu	UPenn
Loebel	Claudia	loebelcl@seas.upenn.edu	UPenn
Long	Fanxin	longf1@email.chop.edu	CHOP
Lounev	Vitali	vlounev@pennmedicine.upenn.edu	UPenn
Lovering	Rich	rlovering@som.umaryland.edu	Univ of Maryland
Mai	David	damai@seas.upenn.edu	UPenn
Marcolongo	Michele	marcolms@drexel.edu	Drexel Univ
Martinez	Jerahme	jerahme.martinez@gmail.com	UPenn
Mason	Devon	dmason1@nd.edu	UPenn
Mauck	Robert	lemauck@pennmedicine.upenn.edu	UPenn
Mavridis	Anastasia	mavridis.a@husky.neu.edu	UPenn
McBeath	Rowena	rowena.mcbeath@gmail.com	Thomas Jefferson Univ
Mehta	Samir	samir.mehta@uphs.upenn.edu	UPenn
Mohanraj	Bhavana	mbhavana@upenn.edu	UPenn
Moharrer	Yasaman	yasamanm@seas.upenn.edu	UPenn
Morales	Leon	leonmorales89@gmail.com	UPenn
Muir	Victoria	vgmuir@seas.upenn.edu	UPenn
Mundy	Christina	matticolac@email.chop.edu	CHOP
Newton	Joseph	josephbnewt@gmail.com	UPenn
Nguyen	Jie	nguyenj6@email.chop.edu	CHOP
Nguyen	Michael	nguyenm6@email.chop.edu	CHOP
Nguyen	Vu	vunguyen@upenn.edu	UPenn
Nijsure	Madhura	mnijsure@seas.upenn.edu	UPenn
Noël	Peter	peter.noel@pennmedicine.upenn.edu	UPenn
Nuss	Courtney	cnuss37@gmail.com	UPenn
Ortved	Kyla	kortved@vet.upenn.edu	UPenn
Osuna	Carlos	cosuna@seas.upenn.edu	UPenn
Pacifici	Maurizio	PacificiM@email.chop.edu	CHOP
Pan	Wei	weipan@pennmedicine.upenn.edu	UPenn
Park	Na Rae	na.park@pennmedicine.upenn.edu	UPenn
Pasha	Saba	pashas@email.chop.edu	UPenn
Patel	Jay	jaymilanpatel@gmail.com	UPenn
Paul	Ryan	ryanpaul@Temple Univ.edu	Temple Univ
Peredo	Ana	anapperedo@gmail.com	UPenn
Pleshko	Nancy	npleshko@Temple Univ.edu	Temple Univ
Prendergast	Margaret	prendm@seas.upenn.edu	UPenn
Pyeritz	Reed	reed.pyeritz@uphs.upenn.edu	UPenn
Querido	William	williamquerido@gmail.com	Temple Univ
Quindlen-Hotek	Julia	juliaq@seas.upenn.edu	UPenn
Raja	Harina	harina@pennmedicine.upenn.edu	UPenn

Rajapakse	Chamith	chamith@pennmedicine.upenn.edu	UPenn
Rajpar	Sam	ibtesam.rajpar@jefferson.edu	Thomas Jefferson Univ
Ratcliffe	Anthony	anthonyratcliffe@synthasome.com	Synthasome
Richardson	Dr. Dean	dwr@vet.upenn.edu	UPenn
Roberts	Douglas	douglaswfroberts@gmail.com	UPenn
Rux	Danielle	ruxd@email.chop.edu	CHOP
Scanzello	Carla	crscanzello@gmail.com	UPenn & VA
Schaer	Thomas	tpschaer@vet.upenn.edu	UPenn
Schmidt	Elaine	schmidtelaine2@gmail.com	UPenn
Seeley	Rebecca	seeleyr@email.chop.edu	CHOP
Seravello	Donna	donnser@upenn.edu	UPenn
Shapses	Sue	shapses@rutgers.edu	Rutgers
Shetye	Snehal	snehalshetye@gmail.com	UPenn
Sinder	Benjamin	sinderb@email.chop.edu	CHOP
Singh	Sagar	sagars@seas.upenn.edu	UPenn
Smith	Gail	smithgk@upenn.edu	UPenn
Smith	Harvey	harveysmith27@gmail.com	UPenn
Smith	Lachlan	lachlans@pennmedicine.upenn.edu	UPenn
Song	Hee Kwon	heekwon.song@pennmedicine.upenn.edu	UPenn
Song	Fangfang	songf1@email.chop.edu	CHOP
Song	Chao	songc2@email.chop.edu	CHOP
Soslowsky	Lou	soslowsk@upenn.edu	UPenn
Spiro	Bob	bob.spiro@aesculapbiologics.com	Aesculap, Inc
Spitsin	Sergei	spitsins@email.chop.edu	CHOP
Stanley	Alexandra	lexystanley@gmail.com	UPenn
Steinberg	David	david.steinberg@pennmedicine.upenn.edu	UPenn
Stoeckl	Brendan	bdstoeckl@gmail.com	UPenn
Struss	Michael	tuf19432@Temple Univ.edu	Temple Univ
Sullivan	Anna Lia	annalia@udel.edu	Univ of Delaware
Syrcle	Jason	syrcle@upenn.edu	UPenn
Tang	Waixing	waixing@pennmedicine.upenn.edu	UPenn
Taylor	Brittany	brtay@pennmedicine.upenn.edu	UPenn
Thompson	Gary	thompsong@rowan.edu	Rowan Univ
Tichy	Elisia	etichy@pennmedicine.upenn.edu	UPenn
Towler	Will	owtowler@gmail.com	UPenn
Tseng	Wei-Ju	weits@pennmedicine.upenn.edu	UPenn
Volk	Susan	swvolk@vet.upenn.edu	UPenn
Wang	Bin	bin.wang@jefferson.edu	Thomas Jefferson Univ
Wang	Baomei	baomei.wang@pennmedicine.upenn.edu	UPenn
Wang	Wenzheng	wenzheng.wang@pennmedicine.upenn.edu	UPenn
Waning	David	dwaning@psu.edu	Penn State Univ
Wehrli	Felix	Felix.wehrli@pennmedicine.upenn.edu	UPenn
Wei	Yulong	yulongwei0121@gmail.com	UPenn
Weiss	Stephanie	weisssn@gmail.com	UPenn
Winkelstein	Beth	winkelst@seas.upenn.edu	UPenn
Wisdom	Katrina	kmwisdom@seas.upenn.edu	UPenn
Witherel	Claire	claire.witherel@gmail.com	UPenn
Xia	Boao	boao.xia@pennmedicine.upenn.edu	UPenn
Xu	Meiqi	mqx@upenn.edu	UPenn
Yang	Yanmei	yanmei.yang@jefferson.edu	Thomas Jefferson Univ
Yang	Feikun	feikun@vet.upenn.edu	UPenn
Yang	Shuying	shuyingy@upenn.edu	UPenn
Yao	Lutain	lutian@pennmedicine.upenn.edu	UPenn
Yu	Wei	Wei.Yu@pennmedicine.upenn.edu	UPenn
Yuan	Gongsheng	gsyuan@upenn.edu	UPenn
Zemel	Babette	Zemel@email.chop.edu	CHOP

Zhang	Deyu	deyuz@pennmedicine.upenn.edu	UPenn
Zhang	Yejia	yejiazhang07@gmail.com	UPenn
Zhang	Chenghao	chenghao.zhang@pennmedicine.upenn.edu	UPenn
Zhong	Leilei	leileiz@pennmedicine.upenn.edu	UPenn
Zhou	Yilu	yiluz@pennmedicine.upenn.edu	UPenn
Zintner	Shannon	smithsm@email.chop.edu	CHOP
Zlotnick	Hannah	zlotnick@seas.upenn.edu	UPenn

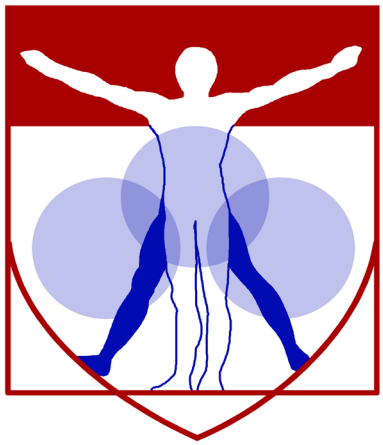

PENN

CENTER for

MUSCULOSKELETAL

DISORDERS

Speaker Abstracts

Dissecting Genetic Mechanisms Controlling Skeletal Cell Lineage Specification and Differentiation

Véronique Lefebvre, Ph.D.

Translational Research Program in Pediatric Orthopaedics, Department of Surgery/Division of Orthopaedic Surgery, Children's Hospital of Philadelphia, Philadelphia, USA

The development and adult homeostasis of our skeleton require proper specification and coordinated activities of several types of skeletal progenitor/stem cells and downstream differentiated cell types, including chondrocytes and osteoblasts. The cellular and molecular mechanisms governing these processes are complex and remain incompletely understood, limiting current understanding and treatment options for the many diseases that can affect our skeleton at any age. Research in my laboratory focuses on SOX genes, which encore transcription factors that rank highly in the regulatory hierarchy of cell lineage determination and differentiation in the skeletal system and many other systems. This talk will be a review of our recent milestones and current research directions. It will include an overview of the importance of maintaining SOX9 expression in chondrocytes to prevent premature growth plate cartilage closure postnatally and to ensure healthy articular cartilage homeostasis in adulthood. It will also include an overview of the importance of SOX4 and SOX11 expression in osteogenic progenitor cells and osteoblasts to ensure proper bone formation in development and proper bone remodeling in adulthood. Our findings will be discussed in the context of human diseases, including developmental disorders due to SOX gene mutations (SOXopathies), skeletal malformations (osteochondrodysplasias) and skeleton degenerative diseases (osteoarthritis and osteoporosis).

Getting more than requested from a CT scan

Peter B. Noël, PhD

Department of Radiology, Perelman School of Medicine, University of Pennsylvania, Philadelphia, USA.

Purpose: Scout scans are a mandatory part of CT examinations, but do not -yet- provide quantitative information. Purpose of this presentation was to develop and evaluate a method for areal bone mineral density (aBMD) measurement based on dual-layer spectral CT scout scans.

Methods: A post-processing algorithm using a pair of 2D virtual mono-energetic scout images (VMSIs) was established in order to semi-automatically compute aBMD at the spine. The method was assessed based on repetitive measurements of the standardized European spine phantom (ESP) at the standard scout scan tube current (30 mA), at other tube currents (10 to 200 mA), as well as with fat-equivalent extension rings simulating different patient habitus, and was compared to dual-energy X-ray absorptiometry (DXA), the gold standard technique. In two female patients, the feasibility of the method was assessed in-vivo for vertebrae L1 to L4 and the results were compared to age-matched reference values. Moreover, BMD was determined in a female patient population (n=91) with the proposed method, and T-scores were derived from these measurements, taking a young subset of the population as the reference. Finally, the BMD of a subset of the population presenting at least one osteoporotic fracture (n=10) was compared to the BMD of age-matched controls.

Results: Derived from standard scout scans, aBMD values measured with the proposed method highly correlated with DXA measurements (r=0.9925), and mean accuracy (DXA: 4.12%, Scout: 1.60%) and precision (DXA: 2.64%, Scout: 2.03%) were comparable. In particular, for phantom experiments the scout scan-based method seemed to perform better than DXA at low BMD values (accuracy DXA: 8.3%, Scout:4.79%). Moreover, when assessed at different tube currents, aBMD values did not differ significantly ($p \geq 0.20$ for all), suggesting that the presented method could be applied to scout scans with different settings. Besides, data derived from sample patients as well as first T-score representations agreed well with BMD values and T-score trend from a reference age-matched population. Finally, the mean BMD of patients presenting osteoporotic fractures was found significantly lower than that of the control group ($p<0.001$), suggesting that the developed method could be able to identify patients presenting higher fracture risk.

Conclusions: Based on dual-layer spectral scout scans, aBMD measurements were fast and reliable and highly correlated with DXA measurements. First measurements on patients were promising. Considering the number of CT acquisitions performed worldwide, this method could allow truly opportunistic osteoporosis screening at a larger scale. A possible implementation could consist in performing these measurements automatically and alerting the clinician only if a certain level of BMD, or a certain T-score, is not reached.

References: Laugerette, Alexis, et al. "DXA-equivalent quantification of bone mineral density using dual-layer spectral CT scout scans." European radiology (2019): 1-11.

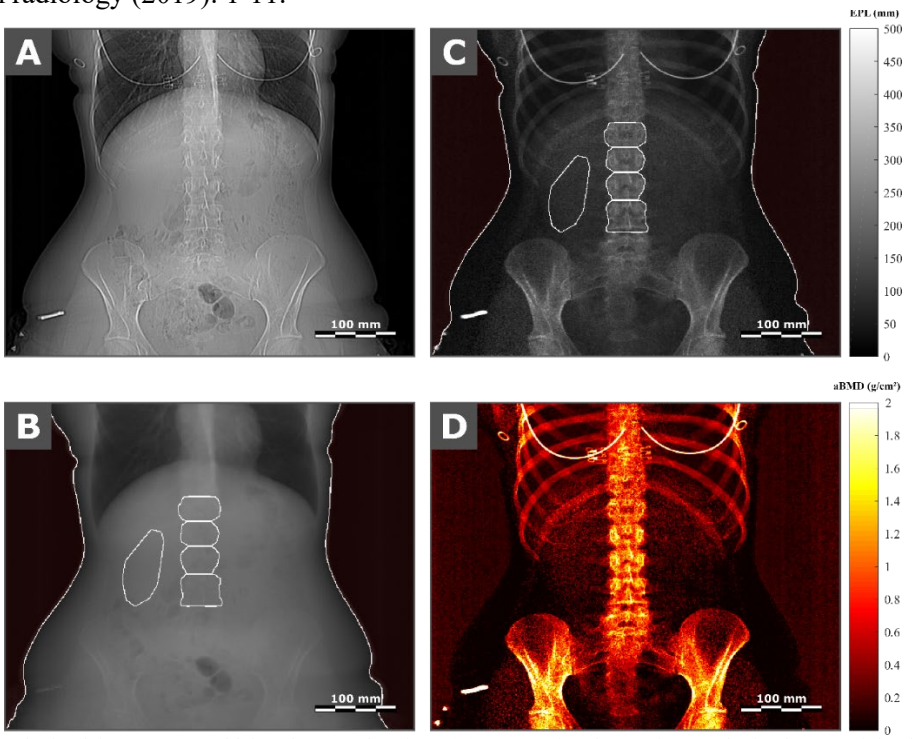

Figure 1: Typical scout images obtained for a 28-year-old female control patient. (A) Conventional scout image obtained as a weighted sum of the data from the two detector layers and equivalent to images generated by single-energy CT scanners. (B) A scatter image (Compton and coherent scattering) and (C) a photo-electric scout image generated from the pair of high- and low-energy raw data. The unit of (B) and (C) is mm and corresponds to equivalent path length (EPL) in a virtual object having scatter and photo-electric attenuation properties of water. Images (B) and (C) show segmented regions used for the analysis, corresponding to vertebrae, soft-tissue and background. (D) DXA-equivalent areal BMD map expressed in g/cm², generated from the pair of scatter/photo-electric images.

“Regulation of RGS protein in inflammatory arthritis”

Shuying (Sheri) Yang, MD, MS, PhD
Associate Professor, Department of Basic & Translational Sciences
School of Dental Medicine

Rheumatoid arthritis (RA) is the most common inflammatory disease, which currently lacks effective treatment. Targeting this unmet need, we discovered a new proinflammatory factor Regulator of G Protein Signaling 12 (RGS12), the largest RGS protein which contains functional PDZ and PTB domains. Transcriptomic analysis revealed that RGS12 critically regulates inflammatory process mainly in RA macrophages. Global and macrophage conditional RGS12 knockout mice were resistant to collagen-induced arthritis including joint swelling and bone destruction. Mechanistically, RGS12 directly binds NF-κB to activate its phosphorylation and nuclear translocation through PTB domain and NF-κB regulates RGS12 expression in a transcriptional manner. The nuclear translocation ability of NF-κB and RGS12 can both be enhanced by Cyclooxygenase-2 (COX2). Furthermore, ablation of RGS12 via RNA interference significantly blocks the inflammatory process *in vivo* and *in vitro*. These results demonstrate that RGS12 is a proinflammatory factor and plays a critical role in the pathogenesis of inflammatory arthritis through controlling RGS12/NF-κB axis.

GPCR Regulation in Osteoarthritis

Elijah L. Carlson[1], Vengadeshprabhu Karuppagounder[1], William J. Pinamont[1], Gregory M. Young[1], Natalie Yoshioka[1], Adeel Ahmed[1], Eric M. Schott[2], Heather K Le Bleu[2], Monaliza El-Quadi[2], Daniel Myers[2], Reyad Elbarbary[1], Michael J Zuscik[3], **Fadia Kamal[1*]**

[1] *Center for Orthopedic Research and Translational Sciences, Department of Orthopedics and Rehabilitation, Penn State College of Medicine, Hershey, Pennsylvania, USA.*

[2] *Center for Musculoskeletal Research, University of Rochester Medical Center, Rochester, New York, USA*

[3] *Department of Orthopedics, University of Colorado Denver, Denver, USA*

Osteoarthritis (OA) is a debilitating disease of the joints that involves progressive cartilage degeneration, with no available therapy. Chondrocytes acquire an aberrant hypertrophic phenotype in OA leading to cartilage degeneration. G protein-coupled receptors (GPCRs) are widely expressed on chondrocytes, and activation of the GPCR-Gα has been shown to maintain chondrocytes in a non-hypertrophic state. In pathological conditions, increased activation of GPCR-Gβγ and its increased interaction with GPCR kinases (GRK2 particularly) lead to GPCR desensitization and dampened Gα signaling. Importantly, we recently reported the therapeutic efficacy of inhibiting Gβγ-GRK2 in several diseases, but its role in OA is unknown. Our **preliminary data** show that GRK2 expression is elevated in chondrocytes of human OA cartilage and in a posttraumatic OA mouse cartilage. Thus, we **hypothesize** that Gβγ-GRK2 signaling drives chondrocyte hypertrophy (CH) and its inhibition attenuates OA progression.

Methods: We determined the role of articular chondrocyte GRK2 signaling in CH and cartilage degeneration in OA using a tamoxifen-inducible conditional chondrocyte GRK2 knockout (GRK2-KO) mouse. Then, using wild type mice, we determined the therapeutic efficacy of Gβγ-GRK2 inhibition in OA using novel and FDA approved pharmacological inhibitors of Gβγ-GRK2. OA was induced by surgical destabilization of the medial meniscus (DMM) in 3 months old mice. GRK2-KO or drug treatment was initiated 8 weeks post-DMM until 12 weeks when mice were sacrificed. Articular cartilage structural changes were evaluated via Saf-O-Fast green staining, histomorphometry, OARSI scoring and microCT. Molecular events were examined using immunofluorescent staining.

Results: We found that conditional GRK2-KO and pharmacological Gβγ-GRK2 inhibition recover Gαs signaling in OA cartilage, attenuate CH, thus exerting chondroprotective and anabolic effects. In corroborating experiments, we found that inhibition of Gβγ-GRK2 signaling in *ex vivo* cultures of human cartilage explants led to attenuated CH.

Conclusion: Our findings (i) suggest that Gβγ-GRK2 signaling is a driver of CH in OA, and (ii) identify novel and FDA approved agents with Gβγ-GRK2 inhibitory effect as a novel therapeutic strategy for OA.

Non-Destructive Applications of Optical Spectroscopy for Assessment of Tissue Pathology and Regeneration

Nancy Pleshko
Dept. of Bioengineering, Temple University, Philadelphia, PA 19122 USA
npleshko@temple.edu

Tissue engineering approaches are being developed to overcome the limitations of current repair methods, due in large part to the challenges of regenerating native diseased tissues. Current gold standard techniques to assess the composition and integrity of engineered and repairing tissues, including histology, biochemical evaluation, and mechanical testing, are destructive, which limits real time monitoring of tissue development. This is an important area to address, as engineered tissues developed in similar environments can exhibit very different matrix and biomechanical properties. Accordingly, non-destructive techniques to assess engineered tissues during development such that appropriate compositional endpoints can be defined are desirable. Fourier transform infrared (FTIR) spectroscopy in the mid and near-infrared range are intrinsically label free, can be non-destructive, and provide specific information on the chemical composition of tissues. Here, we describe the use of spectroscopic techniques for non-destructive assessment and imaging of tissue repair and regeneration, and discuss the potential for clinical translation.

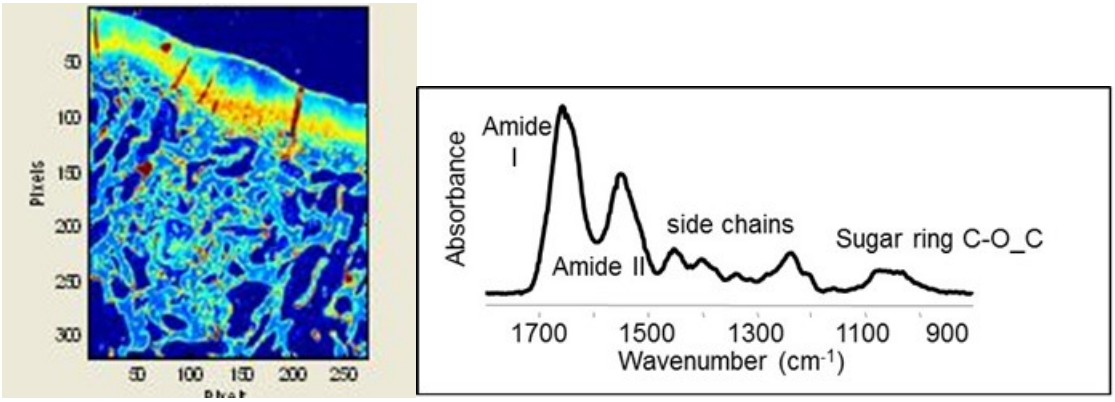

Figure 1. FTIR image of a histological section of repairing cartilage defect and subchondral bone (left). The contrast is based on inherent molecular vibrations of sugar rings in glycosylated proteins. Fundamental infrared absorbances in cartilage arise from collagen amide and side chain absorbances, and proteoglycans (right).

Skeletal muscle weakness: What's bone got to do with it?

David Waning, Ph.D.
Associate Professor
Penn State College of Medicine
Department of Cellular and Molecular Physiology

Skeletal muscle weakness is a major paraneoplastic syndrome in many advanced cancers that increases morbidity and mortality. Using models of solid tumor metastases to bone, we have shown that bone-derived TGFβ leads to skeletal muscle weakness. A proteomic analysis for oxidized proteins of muscle from mice with bone metastases revealed that the ryanodine receptor/calcium release channel (RyR1) on the sarcoplasmic reticulum (SR), a key protein involved in skeletal muscle E-C coupling, was oxidized. Oxidized RyR1 leads to SR Ca^{2+} channel leak and muscle weakness. Inhibiting RyR1 Ca^{2+} leak with a Rycal (S107), restored muscle specific force without affecting tumor burden. Blocking bone resorption using the bisphosphonate, zoledronic acid, reduced serum TGFβ, reduced RyR1 oxidation, and improved skeletal muscle function. Mice with bone metastases also develop severe cachexia. In addition to TGFβ, activin A is also stored in the mineralized bone matrix and zoledronic acid reduced serum activin. Blocking activin signaling in mice with bone metastases using the activin receptor 2B antagonist, ACVR2B/Fc, protects mice against cachexia and improves survival but does not improve skeletal muscle specific force. Collectively, our data indicate a critical role of the bone microenvironment to cause skeletal muscle atrophy and weakness. Clinically, preservation of musculoskeletal health and functional status is a fundamental goal in the treatment of cancer patients to improve quality of life and reduce mortality. Combination therapies aimed at modulating bone-muscle crosstalk and improving muscle mass *and* function could be beneficial to patients.

TIME-DEPENDENT CHANGES IN MACROPHAGE PROFILES IN A MURINE MODEL OF OSTEOARTHRITIS

Authors: Cheng Zhou, Vu Nguyen, George R. Dodge, Herbert R. De'Broski, Carla R. Scanzello

Purpose: Macrophage infiltration in the synovial membrane and intra-articular fat pads is observed in osteoarthritis (OA) patients, and these leukocytes can contribute to catabolic and anabolic cytokine and protease production. In addition, macrophage activation has been associated with human OA symptoms. However, whether suppressing macrophages is appropriate for therapy in OA is unclear, as macrophages can also promote tissue repair. The purpose of this study is to characterize the timeline and phenotype of macrophages in SM and FP in a translationally relevant murine model of post-traumatic OA. We hypothesize that by understanding macrophage phenotypic variation during OA development, potential therapeutics and timing for intervention could be better characterized.

Methods: All animal research was conducted with institutional IACUC approval. C57BL/6 male mice (10-12 weeks old) were subjected to destabilization of medial meniscus (DMM) on the right hind leg, and the left leg was un-operated. Mice were sacrificed at three time points: baseline (no surgery control), 4 weeks post-surgery and 8 weeks post-surgery. Anterior synovial membrane + fat pad (SM/FP) tissues were dissected together, and tissues from 3 - 5 knees pooled for each sample. Cells were isolated enzymatically, stained with the Live/Dead™ Fixable Violet Dead Cell Stain Kit (Invitrogen) and the following 2 antibody panels: Macrophage panel: CD45-PerCP Cy5.5, Ly6C-APC, CD64-PE, PD-L1-Super Bright 645, PD-L2-FITC. T cell panel: CD45-PerCP Cy5.5, CD3-FITC, CD4-PE, CD8-APC. Multicolor flow cytometry was performed and data analyzed with FlowJo software. For the macrophage panel, after gating on single live cells, Ly6C$^+$ (infiltrating macrophage marker) and CD64$^+$ (resident macrophage marker) cells were expressed as percent of the CD45$^+$ population. PD-L1 (expressed by M1-type inflammatory macrophages) and PD-L2 (expressed by M2 reparative macrophages) expression was then characterized on populations of Ly6C and CD64 expressing cells. For T cell analysis, CD3, CD4 and CD8 expressing cells were quantitated.

Results: CD45$^+$ cell numbers were significantly increased on the DMM-operated side at both 4 & 8 weeks compared to baseline (5289 (IQR: 8477) at baseline, 27808 (IQR: 40214) at 4 weeks, and 13312 (IQR: 7690) at 8 weeks). Gating on the CD45$^+$ population, Ly6C$^+$ monocytes were the predominant monocyte/macrophage cell population, accounting for 51.2% (IQR: 10.05%) at baseline, 47.1% (IQR: 6.15%) at 4 weeks, and 62.5% (IQR: 18.55%) at 8 weeks. Numbers of Ly6C$^+$ monocytes, CD64$^+$ macrophages and CD64$^+$ Ly6C$^+$ monocyte/macrophages in SM/FP were all elevated at 4 weeks with sustained elevations in CD64$^+$ cells at 8 weeks (Fig. 1B). Proportions of CD64$^+$ cells were also increased post-DMM out to 8 weeks. (Fig. 1C) PD-L1 and PD-L2 were primarily expressed on CD64$^+$ cells, and not on Ly6C$^+$ monocytes. PD-L1$^+$CD64$^+$ macrophages were reduced in proportion at 4 weeks post-DMM, while PD-L2$^+$CD64$^+$ cells increased (Fig. 2A&B). A large percentage of CD45$^+$ cells did not express monocyte/macrophage markers, so T-lymphocytes in SM/FP were examined. CD3$^+$ T lymphocytes accounted for 5.28% (IQR: 3.32%) of CD45$^+$ cells at baseline, and increased both in percentage (Fig 2C, 4 weeks) and number (Fig. 2D, 4 and 8 weeks) after DMM. In addition, most CD3$^+$ cells were CD4$^+$ (46.2%, IQR: 23.5%) and this proportion did not change post-DMM, while no CD8$^+$ cells were detected.

Conclusions: After DMM-injury, increases in CD45$^+$ cells in the SM/FP tissues can be detected out to 8 weeks. Increases in Ly6C$^+$ monocytes at 4 weeks, with increases at 4 and 8 weeks in CD64$^+$ macrophages suggest recruitment of monocytes from the periphery and in situ differentiation into macrophages, similar to changes in these cell populations observed in models of sterile wounds. Whether proliferation of these cell types is occurring requires further study. Reduction in PD-L1 and elevation in PD-L2 on CD64$^+$ expressing cells at 4 weeks suggests that synovial resident macrophages may be more reparative (i.e. M2) in nature in this model. However, our previous work demonstrated macrophage upregulation of iNOS (expressed by M1 cells) and downregulation of CD206 (expressed by M2 cells). Thus, macrophage phenotypes in vivo after joint injury are complex and share characteristics of both inflammatory and reparative-type cells. In addition, up to 9% of CD45$^+$ cells infiltrating the SM/FP are T lymphocytes, and the majority are CD4$^+$. As both modulation of macrophages and T lymphocytes has shown some efficacy in ameliorating disease in other models, these observations are fundamental to understand the progression of OA-related inflammation and will be critical to the optimal timing of potential therapeutic interventions.

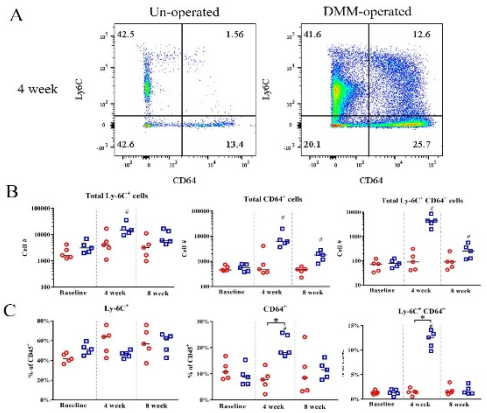

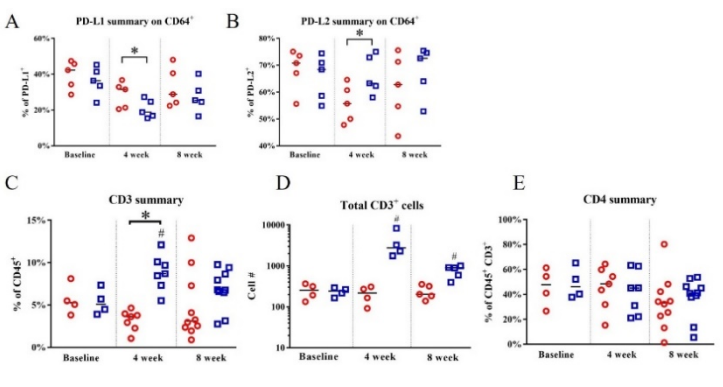

"Plasminogen is Critical for Bone Fracture Repair by Promoting the Functions of Periosteal Mesenchymal Progenitors."

Yanqing Anna Gong, PhD

Defect or insufficient bone repair and generation are common in patients with big trauma or diseases. How to improve bone repair remains a big challenge. Periosteal mesenchymal progenitors play a vital role in endogenous bone regeneration and repair. However, its function is limited in an ischemia hostile microenvironment after big fracture. Previous work shows that plasminogen (Plg) regulates wound healing and tissue repair. Here our studies aim to define the role of Plg in fracture healing. By using a mouse fracture model in wildtype and Plg deficient mice, we found that Plg deficiency impaired structural integrity of trabecular bone as well as development of cortical bone, leading to delayed and incomplete fracture healing in mice. Meanwhile, Plg deficiency significantly reduced thickness of expanded periosteum, an initial process for bone regeneration, indicating that Plg may promote bone repair through regulating function of periosteal mesenchymal progenitors. Interestingly, we found that Plg increased periosteal mesenchymal progenitor proliferation and migration in culture and protected them from cell death under ischemic conditions, suggesting a critical role of Plg in function of mesenchymal progenitors. Mechanistically, Plg activated cry61 by cleavage, a matrix-associated growth factor that is critical for bone regeneration. Plg failed to stimulate cell proliferation, migration with a cyr61 neutralizing antibody suggesting that Plg may regulate periosteal progenitor function through cyr61 activation. Our study suggests that Plg promotes periosteal progenitors proliferation, survival and migration and improves bone repair after fracture. Thus, targeting Plg may offer exciting therapeutic opportunities for improving fracture healing.

Tendon-to-Bone Repair: How do we create the zones?

Nathaniel A. Dyment

INTRODUCTION: Pivotal growth and development studies have elucidated key mechanisms required for the formation of the zonal tendon-to-bone insertion site (i.e., enthesis), including the hedgehog signaling pathway which is critical for fibrocartilage formation [1-2]. Unfortunately, studying these mechanisms during repair in the adult has been difficult, one reason being that traditional tendon-to-bone repair surgeries do not recreate a zonal insertion. However, ligament reconstructions with a tendon graft passing through a bone tunnel often result in zonal insertions [3-4]. Therefore, our lab uses novel transgenic mouse lines to trace the origin of cells that give rise to these zonal insertions and to determine signaling pathways that regulate their formation.

METHODS: All animals and procedures were approved by UPenn's IACUC. Multiple mouse lines were used in this study: 1) αSMACreERT2 inducible Cre mice were crossed with R26R-tdTomato Cre reporter mice trace the fate of SMA-expressing progenitor cells within the bone marrow adjacent to the tendon graft and 2) αSMACreERT2 mice were crossed with Smoothened (Smo) floxed mice to knockdown hedgehog signaling in the cells contributing to the tunnel integration process. ACL reconstructions (ACLR) were performed on αSMACreERT2;R26R-tdTomato (SMACre;tdTom) and αSMACreERT2;$Smo^{f/f}$ (SmoKO) mice. SMACre;tdTom mice were injected with tamoxifen 14 days before surgery, day of surgery, or 7 days postsurgery (T_{-14}, T_0, and T_7 groups, respectively). The percentage of tdTom+ cells within the insertions and adjacent bone were quantified on day 28 to determine the relative contribution of these cells to tunnel integration. To determine the role of hedgehog signaling, we either injected tamoxifen in SmoKO mice to inhibit the pathway or injected a hedgehog agonist (Hh-Ag1.5) 5X per week in SMACre;tdTom mice starting on the day of surgery to activate the pathway. We injected these mice with calcein 7 days before and demeclocycline 1 day before sacrifice and assessed the tunnel integration at day 14 postsurgery.

RESULTS: <u>αSMA-expressing bone marrow progenitor cells contribute to the tunnel integration.</u> Expression of αSMA was increased during early stages of the repair process such that the contribution of SMA-labeled cells to the tunnel integration was highest when tamoxifen was delivered in the first week post-surgery (T_0 group). The zonal attachments shared features with normal entheses, including tidemarks oriented perpendicularly to collagen fibers, Col1a1-expressing cells, alkaline phosphatase activity, and proteoglycan-rich matrix. <u>Hedgehog signaling regulates the tunnel integration process</u>. The area of mineralized fibrocartilage (MFC) in the insertions and the area of bone adjacent to the tunnel were not different in the SmoKO mice. However, the mineral deposition on day 14 (demeclocycline labeling) was significantly reduced in the SmoKO mice ($p < 0.05$). The animals receiving the Hh agonist over the course of two weeks had increased MFC at the tunnel interface and bone adjacent to the tunnel. A similar finding was seen in calcein deposition but the demeclocycline deposition lagged behind the control group. In addition, the agonist stimulated trabecular bone formation in regions beyond the tunnel interface, extending deep into the metaphysis in some samples.

DISCUSSION: Following ACL reconstruction, key events need to occur to integrate the tendon graft with adjacent bone in the tunnels. First, bone marrow progenitors must expand and infiltrate the periphery of the tendon graft. These cells then assemble collagen and proteoglycan-rich fibrocartilage that anchor to the adjacent bone, which is also produced by mesenchymal progenitors from the bone marrow. Finally, the fibrocartilage is mineralized to create a zonal insertion. Using insights from growth and development studies, we found that Hh signaling may be a critical regulator of tunnel integration after ACLR. We aim to further define the functional role and therapeutic potential of this pathway in tendon-to-bone repair in this model system that can then be translated to new therapies in more challenging scenarios such as rotator cuff repair.

REFERENCES: 1. Schwartz et al., *Development*, 2014; 2. Dyment et al., *Dev Biol*, 2015; 3. Kamalitdinov et al., *J Orthop Res*, 2019; 4. Hagiwara et al., *Ann NY Acad Sci*, 2019.

ACKNOWLEDGEMENTS: Work supported by NIH grants R00 AR067283 and P30 AR069619, the Thomas B. McCabe and Jeannette E. Laws McCabe Fund at Penn, and startup funds from the Department of Orthopaedic Surgery at UPenn.

"Strategic Approaches for the Translation of Concept to Product in Regenerative Medicine"

Anthony Ratcliffe, Ph.D., President and CEO of Synthasome, Inc.
2658 Del Mar Heights Road, #370
Del Mar, CA 92014

Recent advances in biology and bioengineering has lead to substantial opportunity for translation of technology to new products that can address previously unmet clinical needs, however that conversion of concept to product has been slow. While this progress demonstrates in part remaining major limitations in our understanding of diseases and pathways to therapy, a critical requirement for translation of knowledge to product, in addition to overcoming the technical hurdles, is the anticipation of successful commercialization. The cost of product development, meeting the requirements of the regulatory pathways, as well as the size of the anticipated market and time for adoption, must be considered. Modeling this at the beginning of a project can be used to indicate the technologies that may, and may not be appropriate. Meeting both therapeutic and commercial requirements are pre-requisites for long term success of a product in regenerative medicine.

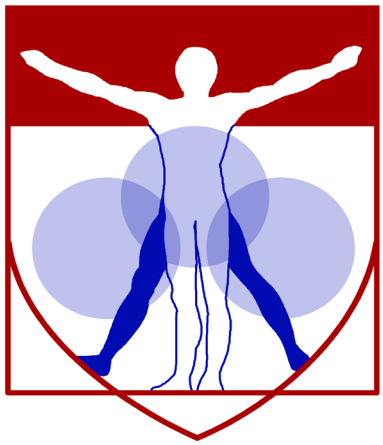

PENN

CENTER for

MUSCULOSKELETAL

DISORDERS

Biomechanics Abstracts

Gender Dependent Alterations in the Mechanical Response of Injured Collagen V Haploinsufficient Murine Tendons

Carlson JA[1], Johnston JM[1], Bonilla KA[1], Shetye SS[1], Nuss CA[1], Weiss SN[1], Rodriguez AB[1], Birk DE[2], Soslowsky LJ[1]
[1]McKay Orthopaedic Research Laboratory, University of Pennsylvania, Philadelphia, PA, [2] University of South Florida, Tampa, FL
Disclosures: Carlson JA(N), Johnston JM(N), Bonilla KA(N), Shetye SS(N), Nuss CA(N), Weiss SN(N), Rodriguez AB(N), Birk DE(N), Soslowsky LJ(N)

INTRODUCTION: Classic Ehlers-Danlos syndrome (*c*EDS) is most commonly characterized by haploinsufficiency in *COL5α1* with patients suffering from hyperextensible skin, joint instability and laxity. Collagen V is significantly upregulated following injury [1,2] and abnormal wound healing is associated with a diminished expression of collagen V [1,3]. Furthermore, estrogen in females is suggested to be associated with decreased collagen synthesis [4,5] and altered gene expression during repair [6]. However, the way gender-specific differences influence the healing response after injury and in the presence of collagen V deficiency has not yet been investigated. Therefore, the objectives of this study were to evaluate the mechanical response of injured patellar tendons over time in normal and *c*EDS mice, as well as differences between genders. We hypothesized that gender related differences in collagen V expression would result in an abnormal wound matrix in the injury response, contributing to the abnormal wound phenotype resulting in reduced mechanical properties of injured EDS tendons compared to normal tendons. In addition, the injury response in the female *c*EDS tendons will be inferior to that of male tendons due to these gender influences, resulting in greater mechanical properties of male tendons when compared to females.
METHODS: Adult male and female wild-type (WT) C57/BL6 and heterozygous (HET) ***Col5a1***$^{+/-}$ *c*EDS mice (n=120) at 120 days of age were used (IACUC approved). All mice underwent bilateral patellar tendon injury surgery as described [7] and were sacrificed 3 weeks or 6 weeks post-injury. *Mechanics.* The patella-patellar tendon-tibia complexes of all mice were dissected and prepared for mechanical testing [8]. Cross-sectional area was measured using a custom laser device [9]. Tendons were subjected to a viscoelastic testing protocol [8,10] consisting of: 1) preconditioning, 2) stress relaxation at strain levels of 2%, 3% and 4%, 3) a sinusoidal frequency sweep (10 cycles at 0.1, 1, 5, and 10 Hz) at each strain level, 4) return to gauge length, and 5) ramp to failure. Tendon length was measured at nominal load prior to test initiation. *Statistics.* Two-way ANOVAs with post-hoc Tukey tests were used to assess the effects of genotype (collagen V expression), gender, and their interaction on elastic and viscoelastic mechanical properties. Significance was set at $p \leq 0.05$ and trends at $p \leq 0.1$.
RESULTS: *Quasi-static:* WT male tendons had higher failure stress at 3w and 6w post-injury (PI), tissue modulus at 6w, and a trending increase in tissue modulus at 3w when compared to WT female tendons (Fig. 1A,B). WT male tendons also had higher failure loads and failure stiffness at 3w and 6w PI (Fig. 1C,D). HET males had higher failure stress and failure loads at 3w and 6w PI, and higher stiffness at 3w PI when compared to HET females (Fig. 1B,C,D). *Viscoelastic:* WT male tendons, when compared to WT female tendons 3w PI, had reduced dynamic moduli at 2% strain (.1 Hz and 1 Hz), with a trend towards a decrease at 2% strain, 10 Hz and 3% strain, 0.1 Hz, however no differences in HET mice between genders were seen at 3w PI (Fig. 2A,B). No WT differences in dynamic modulus were seen between genders at 6w PI (Fig. 2C,D). Additionally, WT males had a higher tan(δ) at 2% strain, .1 Hz at 3w and 6w PI when compared to WT females (data not shown). HET male and female tendons showed trending differences in dynamic modulus at 6w PI at lower frequencies at 3% and 4% strain (Fig. 2D, only 3% shown). The viscoelastic response of HET male tendons showed an increase in tan(δ) across all strains and frequencies (excluding 4%, 1 Hz and 4%, 10 Hz) 6w PI when compared to HET females (Fig. 3B, only 3% shown). Additionally, no differences were seen between genders or genotypes in cross sectional area (data not shown).
DISCUSSION: WT and HET male injured patellar tendons demonstrated higher material and structural properties compared to WT and HET female injured tendons, respectively, at both time points following injury. Reduction in collagen V had a greater effect on male tendon material response than female tendon response, which is consistent with previous findings in uninjured tendons [11]. When examining the viscoelastic response, although dynamic modulus was decreased in WT male tendons compared to WT female tendons 3w PI, these differences did not persist to 6w PI. Additionally, there were no gender differences in viscoelastic properties of HET tendons 3w PI, however, gender differences in these properties were seen in HET tendons 6w PI. This could be explained by a diminished late healing response in HET females compared to males, obscuring the increased effect of reduced collagen V on male tendons versus female tendons at the 6w time point. Male patellar tendon properties are more dependent on collagen V than female tendon properties and the reduction of collagen V affects the healing response of male and female tendons in differing capacities. Future work may include further characterizing the healing response through histological analysis to understand cellular differences that could explain these mechanical differences.
SIGNIFICANCE: This study demonstrates that gender-specific effects play an explicit role in tendon injury and healing and can influence the degree to which tendon properties of *c*EDS mice are affected.
REFERENCES: [1] Wenstrup RJ, et al. *J Biol Chem.* 2006. [2] Ainsworth SR, et al. *Clin Orthop Relat Res.* 1993. [3] Steinmann B, et al. *Connective Tissue and Its Heritable Disorders.* New York: Wiley-Liss; 2002. [4] Yu WD, et al. *Clin Orthop Relat Res.* 2001. [5] Kjaer M, et al. *J Anat.* 2006. [6] Hart DA, et al. *Clin Orthop Relat Res.* 1998. [7] Beason DP, et al. *J Biomech*, 2012. [8] Dunkman AA, et al. *Matrix Biol.* 2013. [9] Favata M, Bioengineering PhD Thesis Philadelphia: University of Pennsylvania. 2006. [10] Miller KS, et al. *J Biomech Eng.* 2012. [11] Carlson JA, et al. [Abstract] ORS 2018.
ACKNOWLEDGEMENTS: *This study was supported by NIH/NIAMS AR065995, AR044745 and the Penn Center for Musculoskeletal Disorders (AR069619).*

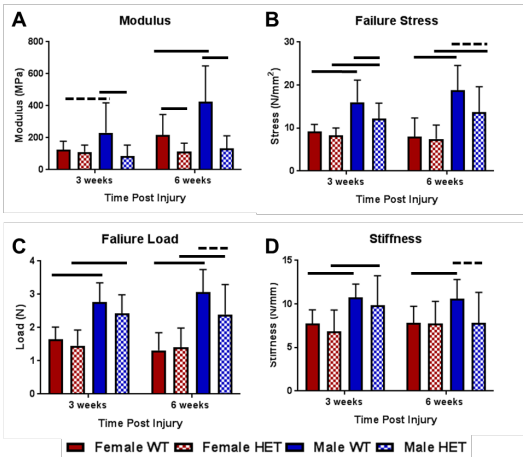

Figure 1. Material and structural and properties of female and male WT and HET patellar tendons. WT and HET male patellar tendons had increased moduli (A), failure stress (B), failure loads (C) and had increased stiffness (D) compared to female tendons.

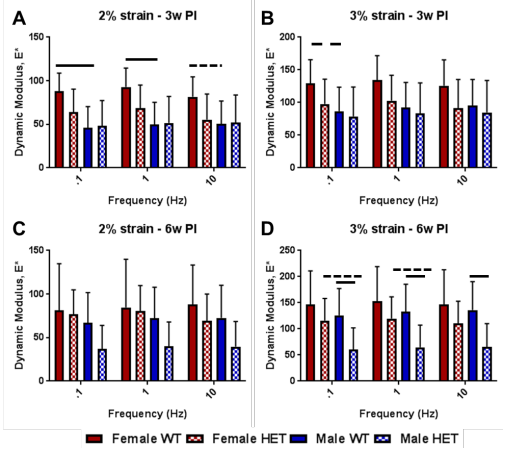

Figure 2. Dynamic moduli of female and male WT and HET patellar tendons. WT female patellar tendon dynamic moduli are increased across all frequencies at 2% strain, 3w PI (A), with no differences seen at 6w PI (C). Trending differences between genders were seen at lower frequencies at 3% strain, 6w PI (D).

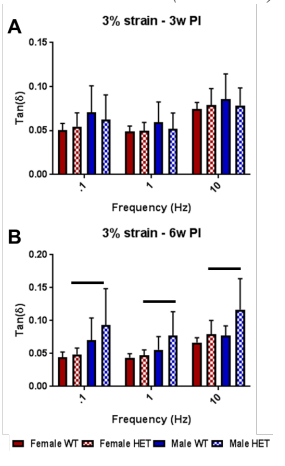

Figure 3. Tan(δ) of female and male WT and HET patellar tendons. HET male mice showed no differences in tan(δ) from HET female mice at 3w PI (A) but had increased tan(δ) measurements across all frequencies at 3% strain, 6w PI (B).

Crossed Screw Fixation is Stiffer than Novel Plate with Integrated Lag Screw: A Cadaveric Comparison of Two Methods for Talonavicular Arthrodesis

Danielle M. Cristino[1], Elaine C. Schmidt[1], Sreenivasulu Metikala, MD[2], Karim Mahmoud, MD[2], Michael W. Hast, PhD[1], and Daniel C. Farber, MD[2]
[1]Biedermann Lab for Orthopaedic Research, University of Pennsylvania, Philadelphia, Pennsylvania, [2]Department of Orthopaedic Surgery, University of Pennsylvania, Philadelphia, Pennsylvania
Danielle.Cristino@pennmedicine.upenn.edu

Relevant Disclosures: Danielle Cristino (N); Elaine Schmidt (N); Sreenivasulu Metikala (N), Karim Mahmoud (N); Michael Hast (5) DePuy Synthes, Stryker Orthopaedics, Zimmer Biomet, Integra; Daniel Farber (5) Stryker Orthopaedics, DJ Orthopaedics

INTRODUCTION: Talonavicular arthrodesis (TNA) has widespread indications in various foot and ankle pathologies, including arthritis, flatfoot deformity, and post-traumatic injury. Although successful fusion is achievable, reported nonunion rates still remain relatively high, ranging from 3-37%. The incidence of nonunion is linked to the inherent mobility of the ball and socket configuration of the talonavicular joint, which experiences high loads – even during partial weight-bearing. Traditionally, the goal of TNA surgery has been to maximize mechanical stability to achieve union. The purpose of the current study was to characterize the stiffness of a novel compression plate with an integrated lag screw (Figure 1A) to a traditional two compression screw technique (Figure 1B). It was hypothesized that the novel plate construct would exhibit greater stiffness than the traditional crossed screw technique.

METHODS: Seven matched pairs of fresh-frozen cadaveric specimens were utilized in the study (3F, 4M, 55-78 y.o.). Half of the specimens received two 5.0 mm partially threaded cannulated cancellous screws (SCR) inserted in a retrograde fashion (Stryker Orthopaedics). The contralateral limbs received a dorsomedial 3.5 mm compression plating system (PLT) with a combination of four 3.5 mm cortical screws and a retrograde 4.1 mm partially threaded cancellous screw integrated into the plate (Anchorage Plating System, Stryker Orthopaedics). To isolate the talonavicular joint for mechanical testing, the talus and navicular were excised from the foot and cast in urethane. Construct stiffness was evaluated in axial torsion (Fig. 2A), and cantilever bending applied in medial to lateral (M-L) (Fig. 2B) and plantar to dorsal (P-D) (Fig. 2C) directions on a test frame. Specimens were cyclically loaded to failure in the P-D configuration with an increasing sinusoidal waveform under displacement control at a frequency of 1 Hz. The applied displacements increased from 0.2 mm to 11 mm over 5,000 cycles. Gross failure was defined as 2 mm of permanent displacement, as determined with 3-D motion tracking data. Shapiro-Wilk tests were performed to test for normality. For non-Gaussian data, a Mann-Whitney-Wilcoxon Test was performed to identify potential differences between groups. Otherwise, two-tailed, equal variance t-tests were used to assess unknown responses across groups. The significance level was set at $p < 0.05$ for all tests.

RESULTS: SCR specimens were significantly stiffer in P-D bending ($p = 0.025$) and demonstrated a trend towards a higher number of cycles before failure ($p = 0.087$). Specifically, the SCR group had an average P-D bending stiffness of 130± 66.3 N/mm, while the PLT group had an average bending stiffness of 63.2±19.9 N/mm (Figure 3A). The number of cycles at failure was 2,981±724 and 2,349± 532 cycles for the SCR and PLT groups, respectively (Figure 3B). No significant differences in the torsional stiffness (Figure 3C) or M-L bending stiffness (Figure 3D) were observed between groups. The average torsional stiffness was 0.735±0.364 and 0.910± 0.424 Nm/deg for the SCR and PLT groups, respectively ($p= 0.620$). The average ML bending stiffness was 265±131 N/mm and 236±138 N/mm for the SCR and PLT groups, respectively ($p = 0.686$).

DISCUSSION: This benchtop study demonstrates that a novel compression plate with an integrated lag screw for talonavicular arthrodesis introduces more compliance than a traditional two screw construct. This result is most clearly demonstrated by the significantly lower stiffness in P-D bending, as well as the trend towards decreased resistance to deformation under cyclic loading, observed in the PLT group. Gapping of the lateral portion of the talonavicular joint during cyclic loading was observed in these assays, however it should be noted that this joint was mechanically tested in isolation. In a clinical setting in which the rest of the foot is intact, lateral gapping likely does not propagate to such an extent. If this motion is observed intraoperatively, a second independent lag screw may be used to provide lateral compression of the TN joint. This was not modeled in the current study. Furthermore, TNA frequently occurs in the setting of a triple arthrodesis, which includes fusion of the calcaneus to the cuboid and provides additional rigidity to the Chopart's joint. Despite these limitations, this study provides a valuable characterization of the two constructs in isolation and emphasizes the importance of achieving compression across the entire joint surface. Future work will involve mechanical testing of intact feet and a group in which the medial plate is combined with a lateral percutaneous screw.

SIGNIFICANCE/CLINICAL RELEVANCE: This study provided the first biomechanical evaluation of a novel compression plate with an integrated lag screw for talonavicular arthrodesis in cadaveric specimens. The results of this study emphasize the importance of and difficulties associated with providing compression and stability across the entire TN joint surface.

ACKNOWLEDGMENT: This study was funded in part by Stryker Orthopaedics

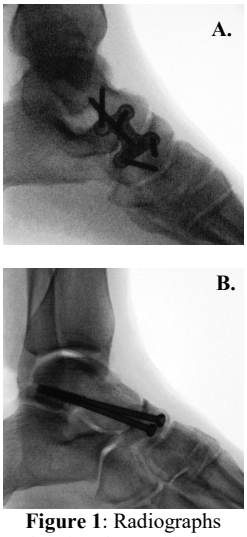

Figure 1: Radiographs showing the novel plate (A.) and the traditional two screw construct (B.).

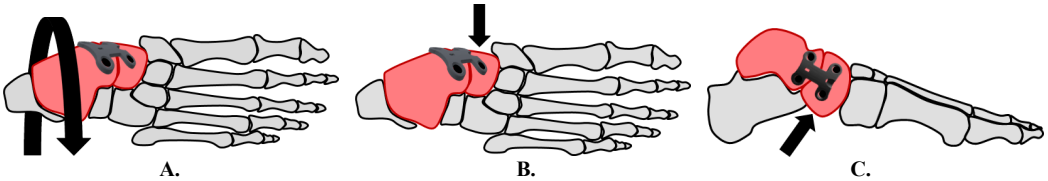

Figure 2: Loading configurations for mechanical testing. The talus and navicular (red) were tested in isolation.

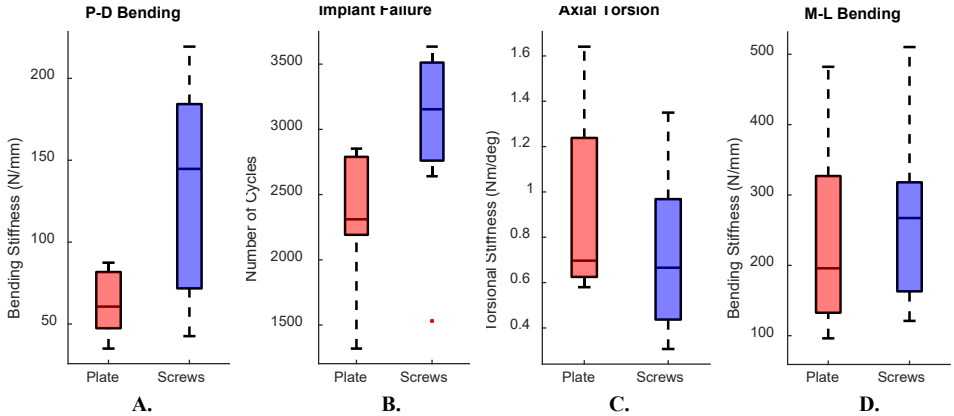

Figure 3: Mechanical testing results.

Improving the Neer and AO Classifications of Greater Tuberosity Fractures: A Computational Framework

[1]Kayley Dear, BS, [1]Josh Baxter, PhD, [2]Surena Namdari, MD, [1]Michael W. Hast, PhD
[1]Biedermann Lab for Orthopaedic Research, Department of Orthopaedic Surgery, University of Pennsylvania, Philadelphia, Pennsylvania
[2]Rothman Institute, Thomas Jefferson University, Philadelphia, Pennsylvania
hast@pennmedicine.upenn.edu

Relevant Disclosures: Michael W. Hast (N), Kayley Dear (N), Josh R. Baxter (N), Surena Namdari (N),

INTRODUCTION: Proximal humerus fractures are painful and debilitating injuries with an incidence rate that is expected to triple over the next thirty years [1]. Greater tuberosity (GT) fractures account for roughly 20% of proximal humerus fractures, and the vast majority of these injuries involve relatively small displacements of the GT bone fragment [2]. Traditionally, Charles Neer and the AO have classified the GT fragment as displaced (i.e. requires surgery) if it translates more than 5 mm from its anatomic position [3]. However, the Neer and AO classification systems do not take into account patient-specific anatomy, nor do they consider fragment orientation within the joint. The purpose of this study was to create a computational model that was capable of predicting subacromial impingement in patient-specific models. We hypothesized that the Neer and AO classification systems would not be able to accurately predict impingement in controlled simulations of GT fractures.

METHODS: Eight intact fresh-frozen upper extremity cadaveric specimens were utilized in this preliminary study (3F, 1M; 60-70 y.o). Specimens were scanned in the anatomic pose with a clinical CT scanner using 0.5 mm axial slice thickness. Humeral and scapular geometries were segmented into 3-D renderings. Using a custom Matlab script, virtual bones were aligned to the International Society of Biomechanics shoulder coordinate system [4]. 3-D geometries were then inserted into a validated OpenSim shoulder model, which includes scapular rhythm during dynamic activities [5]. Virtual joints were adjusted to ensure they recapitulated patient-specific anatomy captured with CT scans. Specifically, we ensured that the humeral head was centered in the nadir of concavity of the glenoid and appropriate space was afforded between the proximal-most point of the humerus and the inferior surface of the glenoid. Displaced GT fragments were created by slicing the humeri in the sagittal plane, 8mm medial to the lateral-most point of the GT. The GT fragments were systematically moved relative to the humerus with 4 different displacements (2.5, 5.0, 7.5, 10.0 mm) at 8 angles (0°, 45°, 90°, 135°, 180°, 225°, 270°, 315°) (**Fig 1A**). Once models were assembled, passive ROM tests were performed. Specifically, the models sequentially performed abduction from 0°-180° at 22 different elevation planes (-90° - 120°) (**Fig 1B**). For each motion, a binary determination of contact between the GT fragment and the acromion was determined with the onboard elastic foundation subroutine within OpenSim [6]. The probability of impingement for each ROM test was calculated by dividing the number of positive impingement motions by the total number of motions in a ROM test (22).

RESULTS: When averaging results from all 8 specimens, the average probability of impingement was 0.9%, 4.2%, 11.6%, and 21.1% for GT fragment displacements of 2.5, 5.0, 7.5 and 10.0 mm, respectively (**Fig 1C**). The majority of subacromial contact events occurred when arms were abducting in the 20°- 50° elevation planes. 7 out of 8 specimens did not experience impingement when the GT fragment was displaced 2.5 mm (**Fig 1D, *top***). 2 out of 8 avoided impingement with 5.0 mm of GT fragment displacement. One specimen experienced impingement at all GT fragment displacement levels, but no impingements were detected when the fragment moved anteriorly, or antero-inferiorly (**Fig 1D, *bottom***).

DISCUSSION: The low values of 0.9% and 4.2% for average probability of impingement for the 2.5 and 5.0 mm displacements suggest that the Neer and AO classification systems may provide reasonable clinical guidelines for assessing displaced GT fractures. This finding somewhat nullifies our initial hypothesis, but it should be noted that several specimens in this small cohort of specimens clearly violated these guidelines. In this preliminary study there were large variabilities associated with measurements between specimens, which is to be expected with a human population. Further work is being done to incorporate a larger sample size. This model does not account for internal/external rotation of the humerus, muscle forces, or translation of the glenohumeral joint. All of these issues will be addressed in future iterations of the study.

SIGNIFICANCE/CLINICAL RELEVANCE: Subacromial impingent is difficult to predict with current standards of care, which include planar radiographs and rules-of-thumb that utilize gross displacement of the GT fragment. Precision medicine approaches, which may include 3-D imaging and computational modeling within the clinic, may allow for the accurate prediction of shoulder function following GT avulsions.

REFERENCES: [1] Kannus+ Acta Orthop Scand, 2000. [2] Platzer+ Injury 2005. [3] Neer JBJS, 1970. [4] Wu+ J Biomech, 2005. [5] Saul+ CMBBE, 2015 [6] Bachner+ JSES 2019

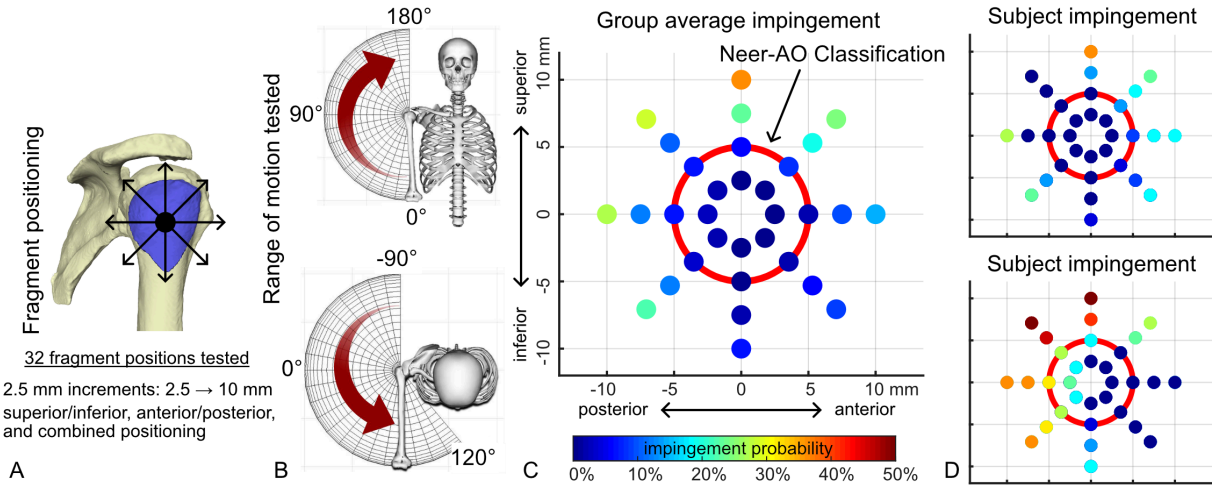

Fig 1. (A) The greater tuberosity fragment was iteratively positioned in 2.5 mm increments (B) and contact was simulated by creating abduction motions (*top*) in 22 different planes (-90° - 120°, *bottom*). (C) On average, fragment positioning of 5 mm or less from the anatomical position did not increase impingement probability. (D) While some individual specimens (*top*) had similar impingement profiles as the group average, other specimens *bottom*) experienced impingement with changes in fragment position as small as 2.5 mm.

Collagen Architecture Regulates Metabolic and Fibrotic Gene Expression in Engineered Adipose Tissue

Nikolas Di Caprio[1], Evangelia Bellas, Ph.D. [1]

[1]Department of Bioengineering, Temple University, Philadelphia, PA

Introduction: Obesity is a prevalent disease that affects more than 1 in 3 U.S. adults and increases the risk of significant comorbidities, such as type II diabetes, cardiovascular disease, stroke, some cancers and various musculoskeletal disorders. During obesity, adipocytes grow in size without a concomitant increase in angiogenesis, resulting in hypoxia and subsequent fibrosis. Fibrosis, or excess matrix deposition, crosslinking, and remodeling, ultimately leads to changes in ECM mechanics, such as ECM stiffness and architecture that drive cellular behavior. **As adipocytes are observed to dysfunction in fibrotic obese AT, it becomes essential to study how ECM mechanics influence adipocyte function.** Here, 3D collagen type I hydrogels were crosslinked with ethylene glycol-bis-succinic acid N-hydroxysuccinimide ester (PEGDS) to tune ECM mechanics, such as ECM stiffness and architecture, to investigate their direct effects on adipocyte function.

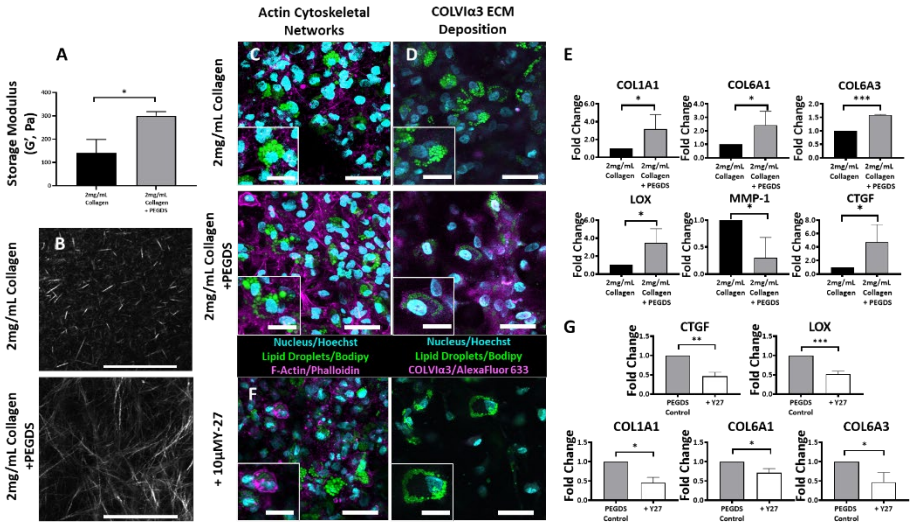

Figure 1. (A) Average equilibrated G' in control and 0.33% PEGDS:Collagen hydrogels. **(B)** SHG microscopy of control and 0.33% PEGDS:collagen hydrogels (Scale Bar: 50μm). Fluorescent confocal images of **(C)** stress fibers and **(D)** COL6α3 deposition of adipocytes encapsulated within control and 0.33% PEGDS:collagen constructs. **(E)** QPCR adipocyte gene expression fold change after 5 days 3D culture in either collagen control or 0.33% PEGDS:collagen constructs (n=3-4). **(F)** Confocal Images and **(G)** qPCR gene expression of adipocytes encapsulated within 0.33% PEGDS:collagen hydrogels with the addition of Y-27.

Methods: Collagen type I hydrogel architecture and stiffness were tuned by varying the mass ratios (0 & 0.33) of PEGDS to collagen. To form the 3D constructs, collagen type I hydrogels (2mg/mL) containing human adipocytes (8mil/mL) were incubated at 37°C for 30 minutes. To measure the mechanical properties, rheological time and strain sweeps (0.1-10% strain/1Hz) were performed. Second-harmonic generation (SHG) microscopy was used to visualize collagen architecture. Constructs were sacrificed after 5 days in 3D culture for imaging and gene expression. Constructs were fixed and stained for the presence of lipid accumulation (Bodipy), nuclei (Hoechst), and either F-actin (Phalloidin) or COLVIα3 (AlexaFluor 633). QPCR gene expression analysis was performed, looking at changes in metabolic and ECM-related gene activity. Cytoskeletal contractility was inhibited with the addition of 10μM Y-27632 (Y-27) with each media change every 48 hours.

Results and Discussion: Time sweep rheological testing resulted in increased storage modulus (2-fold) in 0.33% PEGDS:collagen hydrogels compared to the control **(Fig. 1A).** Further, SHG images of PEGDS:collagen revealed an altered ECM architecture **(Fig. 1B)**. Adipocytes encapsulated within PEGDS:collagen hydrogels expressed more cytoskeletal tension (via actin stress fibers) compared to the control **(Fig. 1C)**. Additionally, immunofluorescent staining of COLVIα3 showed increased deposition around adipocytes encapsulated within PEGDS:collagen hydrogels (**Fig. 1D).** Upon qPCR analysis, fibrotic-related gene expression was observed to be upregulated in adipocytes encapsulated in PEGDS:collagen hydrogels **(Fig 1E)** while adipogenic and metabolic gene expression remained unaffected **(Data Not Shown)**. However, the addition of Y-27632 (Y27) to PEGDS:collagen constructs allowed adipocytes to revert cytoskeletal tension, COLVIα3 deposition, and qPCR gene expression back to a healthy state **(Fig. 1F-G)**.

Conclusion: In summary, our results demonstrate that adipocytes are heavily influenced by their surrounding ECM mechanics, including stiffness and architecture. We have demonstrated that adipocytes respond to a stiff, altered ECM architecture by inducing fibrotic gene expression and increasing ECM deposition, which ultimately led to a dysfunctional fibrotic state. Our results also suggest that these mechanical cues sensed by adipocytes are regulated through actin cytoskeletal networks. Our future work consists of understanding the role of collagen VI on adipocyte function.

Acknowledgments: We would like to acknowledge funding support from Dr. Bellas's startup funds from Temple University and the NIH NIDDK Diabetic Complications Consortium DK07616 and DK115255 grants (to EB) for their financial support towards this project. We would also like to thank Jon Galarraga (Burdick Lab, UPenn) for his assistance in rheometry.

Validating a Novel Device to Assess Joint Level Function Outside of Biomechanics Laboratories

John F. Drazan[1], Todd J. Hullfish[1], Josh R. Baxter[1]
[1]University of Pennsylvania, Philadelphia, PA
john.drazan@pennmedicine.upenn.edu

Disclosures: John F Drazan (N), Todd J. Hullfish (N), Josh R. Baxter (N)

INTRODUCTION: Quantifying joint-level function is a critical step to establish the effectiveness of clinical treatments and therapeutics. The current gold standard for assessing joint-level function is isokinetic dynamometry. Unfortunately, the large size and high price point (>$40,000) of commercial isokinetic dynameters prevents its widespread use in the clinical space. To address this clinical of measuring joint-level function in the clinic, we have developed a novel, mobile isokinetic dynamometer. We established several design criteria including subject safety, adjustable isokinetic speed settings, and compatibility with commercially available attachments to test different joints. In this study, we developed the mechanical design of the system, validated the mechanical accuracy of the device, and demonstrated the functionality of device to measure muscle function in human subjects using plantar flexion as a test case. We hypothesized that our "clinical" device would demonstrate very strong agreement with a commercial dynamometer as demonstrated by an Inter-class Correlation Coefficient (ICC) value over 0.9 for peak torque, angular velocity, and peak power calculations.

METHODS: To ensure subject safety, we designed our dynamometer to act as passive energy sink. To meet this criteria, we incorporated a chain drive, a rack and pinion system, and a linear damper in series with a load cell rigidly attached to the frame (Figure 1). To increase clinical relevance, commercially available dynamometer attachments can be secured to the rotational shaft, which transmits joint torque to the linear damper through the chain drive and rack and pinion. The linear damper constrains velocity by forcing incompressible oil through an orifice with an adjustable diameter (Easylift, Bansbach, Germany). The linear damper is mounted to the rack and the load cell using clevis pins, allowing any number of testing rotational velocities to be quickly changed by "hot-swapping" dampers of different settings. Angular position and velocity are measured using a rotary potentiometer 100 kOhm, Sparkfun, Niwott, CO) affixed the shaft shared by the superior sprocket in the chain drive. We decided to measure linear force applied to the linear damper using an in series load cell (200 kg, S-Type load cell, Sparkfun, Niwott, CO) and calculate joint torque about generated about the rotational shaft. Data from both sensors are acquired using a commercially available microcontroller (Arduino Mega, Sparkfun, Niwott, CO) interfaced with MATLAB (Mathworks, Nantick, MA).

As a test case to demonstrate the clinical usability of our device, we first calibrated our device by applying known torques and then had healthy adults perform isokinetic plantar flexion contractions on it as well as a commercially available dynamometer. First, we applied known loads about the rotational shaft and measured the position and torques using motion capture (Raptor Series, Motion Analysis Corporation), a potentiometer, and in series load cell. To confirm the mechanical validity of our device, we correlated the applied torques with the experimentally derived loads. Next, we compared the performance of the novel device with a commercial device. Three healthy-young adults (3 Male; Age: 30 ± 3.7 y/o) performed plantar flexor contractions while prone on both our clinical device and a commercial dynamometer (Biodex 4, Shirley, NY) after providing written informed consent in this IRB approved study. Each subject's foot was secured to the clinical device using the same footplate as the commercial device. Each subject performed three plantar flexion contractions on our clinical device at three different damper settings that enabled slow (30°/s), medium (120°/s), and fast (210°/s) angular rotations. We calculated the average angular velocity during active plantar flexion on the clinical device and used these angular velocity values to set the angular velocity limit on the commercial dynamometer to provide "gold standard" data for each subject. We then calculated peak torque, average angular velocity during active plantar flexion, and peak power across all trials for both devices. We tested absolute agreement between to the clinical and commercial device using the "A-1" formulation of ICC.

RESULTS: The mechanical validation showed very strong agreement (r=0.999, maximum of 4% full scale error) for both torque and angular position with the reference values. The three subjects generated similar torque values (errors < 10%) at the three speeds between the clinical and commercial device (Figure 2). The peak torque, angular velocity, and peak power measurements of clinical device were in "very strong" agreement (ICC > 0.9) with the commercial device (Table 1).

DISCUSSION: There is a clear clinical need for quantifying joint-level function to assess patient outcomes following surgery or injury. However, the large size and high cost of commercial isokinetic dynamometers preclude their use in many clinical settings. In this study, we developed a novel "clinical" dynamometer that has a significantly smaller footprint (8 ft^2) than the commercial dynamometer (64 ft^2) while still demonstrating very strong agreement with both kinematic and kinetic measurements of maximal effort plantar flexion exercises. In contrast to the commercial device which uses an electrical motor, the angular velocity of the clinical device is restricted by a linear damper. This significantly reduces device complexity and size. Although we tested the ankle joint as a proof of concept, our device is compatible with other commercial attachments to allow testing about the elbow, knee, hip, and shoulder. Our device is also low-cost (< $1,100) and leverages simple electronics and dampers that can be quickly swapped out to tune the dynamometer performance.

SIGNIFICANCE/CLINICAL RELEVANCE: Isokinetic testing provides patient-specific information to clinicians regarding musculoskeletal treatment efficacy, however the size and cost of commercial dynamometers preclude their use as standard of care. Our device has potential to provide clinicians and researchers with a mobile yet accurate isokinetic dynamometer to assess joint-level function in humans.

ACKNOWLEDGEMENTS: This work was supported by the Thomas B. and Jeannette E. Laws McCabe Fund and NIH grant K12GM081259.

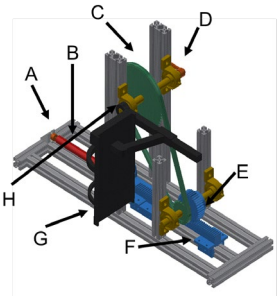

Figure 1: Diagram of Novel Isokinetic Dynamometer. A) load cell B) Linear Damper C) Chain drive D) Potentiometer E) Rack and pinion F) Low-friction trolley G) Footplate H) Commercial attachment point

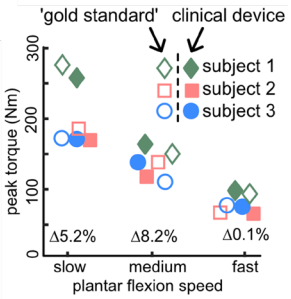

Figure 2: The clinical device exhibited small errors relative to the commercial device.

	ICC	95% Confidence Interval		*p* value
		Lower Limit	Upper Limit	
Torque	0.9672	0.9295	0.9849	<0.001
Velocity	0.9896	0.9664	0.996	<0.001
Power	0.9179	0.8462	0.9724	<0.001

Table 1: ICC Values testing absolute agreement between clinical device and commercial dynamometer.

Female Rat Supraspinatus Tendon Mechanical Properties Exhibit a Differential Response to Estrogen-Deficiency Depending on Reproductive History

Ashley K. Fung, Snehal S. Shetye, Chantal M. de Bakker, Yihan Li, X. Sherry Liu, Louis J. Soslowsky
McKay Orthopaedic Research Laboratory, University of Pennsylvania, Philadelphia, PA
afung@seas.upenn.edu

Disclosures: Ashley K. Fung (N), Snehal S. Shetye (N), Chantal M. de Bakker (N), Yihan Li (N), X. Sherry Liu (N), Louis J. Soslowsky (N)

INTRODUCTION: The prevalence of rotator cuff tears increases with age and postmenopausal women are at an even greater risk of developing full-thickness supraspinatus tendon tears [1]. Previous animal studies have supported these findings, demonstrating that an ovariectomy model of menopause led to reduced bone mineral density of the humeral head and decreased rotator cuff tendon strength [2,3]. Interestingly, recent preliminary data showed that prior to ovariectomy, reproductive female rats have inferior supraspinatus tendon and proximal humerus trabecular bone properties compared to virgin females; however, when subjected to ovariectomy, they experience a reduced rate of bone loss in the tibia compared to virgin females [4]. While these findings suggest a differential response in bone to estrogen-deficiency depending on reproductive history, how supraspinatus tendons are affected is unknown. Therefore, the objective of this study was to investigate the effect of reproductive history on female rat supraspinatus tendon mechanical properties following ovariectomy. We hypothesized that due to a dramatic decrease in estrogen levels and a high rate of early bone loss, ovariectomy will lead to a reduction in supraspinatus tendon mechanical properties.

METHODS: 58 female Sprague-Dawley rats (IACUC approved) were divided into virgin and reproductive groups. At age 4 months, reproductive rats underwent three cycles of reproduction, each consisting of a 3-week pregnancy, 3 weeks of lactation, and 3-6 weeks of post-weaning recovery. Virgin and reproductive rats underwent ovariectomy (OVX) surgery at 12 months of age and were sacrificed at 1 month (n=8/group), 3 months (n=8/group) or 6 months (n=5-7/group) post-OVX. Non-OVX, intact 13.5-month old virgin and reproductive female rats (n=7/group) were used as controls. Mechanics: Supraspinatus tendons were fine dissected and marked with stain lines for optical strain tracking. Cross-sectional area was measured using a custom laser device and humeri were secured in polymethyl methacrylate. Right supraspinatus tendons underwent quasi-static tensile testing, consisting of pre-conditioning (10 cycles from 0.5-1% strain), stress relaxation at 5% strain for 600s, dynamic frequency sweep at 5% strain (0.1-10Hz), and ramp to failure at rate of 0.3%/s. Statistics: Two-way ANOVAs were used to compare the effects of reproductive history and time after OVX with post-hoc Bonferroni corrections. Significance was set at $p \leq 0.05$ and trends at $p \leq 0.1$.

RESULTS: Cross-sectional area increased significantly in the reproductive group and trended towards increasing in the virgin group 1 month post-OVX (Fig 1A). By 6 months post-OVX, however, cross-sectional area was not different from control in either group. While stiffness trended towards increasing in the 3 month OVX reproductive group (Fig 1B), there were no changes in modulus in the reproductive groups. In contrast, modulus was significantly higher in the virgin non-OVX, control group compared to reproductive and significantly decreased in the virgin group at 1 and 3 months post-OVX (Fig 3C). At 6 months post-OVX, modulus in the virgin group increased compared to 1 month post-OVX and was significantly higher than the reproductive group. A similar trend was observed in the virgin group for dynamic modulus across all frequencies, where dynamic modulus was significantly lower at 1 month post-OVX and trended towards decreasing in the 3 month and 6 month groups, compared to control (Fig 1E). In the reproductive group, however, significant viscoelastic differences were observed at 1 month post-OVX. There was a significant increase in percent relaxation at 1 month post-OVX compared to control (Fig 1D), while dynamic modulus across all frequencies was decreased at 1 month compared to control, 3 month, and 6 month post-OVX groups (Fig 1E). Tan(δ) increased at 1 month post-OVX and was significantly higher than the virgin group at this time point (Fig 1F) with no differences at 3 months and 6 months.

DISCUSSION: This study investigated the effect of reproductive history on tendon properties following ovariectomy. Higher modulus in the virgin control group compared to the reproductive group was consistent with recent preliminary data for rats that had undergone 2 cycles of reproduction. Modulus had a significant interaction effect, where the virgin group experienced a reduction but the reproductive group exhibited no differences in response to OVX. Previous studies showed that rotator cuff tendon strength decreases with ovariectomy [2,3] and attributed these results to reduced structural integrity of the mineralized fibrocartilaginous insertion site. Other *in vitro* studies also found that estrogen plays a role in collagen synthesis and maintaining tissue elasticity [5,6]. Our findings suggest that, similar to bone, supraspinatus tendons of virgin and reproductive rats respond differently to estrogen deficiency. Interestingly, recent studies in bone uncovered several adaptation mechanisms, including redistribution of bone mass toward load-bearing compartments and increased bone mechano-sensitivity in reproductive rats, which may account for the protective effect of reproductive history on bone when subjected to estrogen deficiency [7]. Decreased viscoelastic parameters at 1 month post-OVX but recovery by 6 months in reproductive tendons suggest that additional tendon adaptation mechanisms developed during the course of reproduction may have altered the tendon response to estrogen deficiency later in life. Further studies are necessary to explore the mechanisms behind tendon adaptations in these models.

SIGNIFICANCE: This study highlights the importance of considering reproductive history during the diagnosis and treatment of rotator cuff injuries in post-menopausal women, particularly in the early stages of menopause where tendon properties were observed to change substantially.

REFERENCES: [1] Abate et al, 2014, *Menopause*. [2] Cadet et al, 2010, *J Orthop Res.* [3] Chen et al, 2015, *PLoS One*. [4] de Bakker et al, 2018, *J Bone Miner Res.* [5] Torricelli et al, 2013, *Age*. [6] Maman et al, 2016, *Connect Tissue Res*. [7] Li et al, 2018, *ORS Meeting*, 0695.

ACKNOWLEDGEMENTS: We thank H Zhao, WJ Tseng, and T Leahy for their assistance. This study was supported by NIH/NIAMS R03 AR065145, R01 AR071718, and the Penn Center for Musculoskeletal Disorders (P30 AR069619).

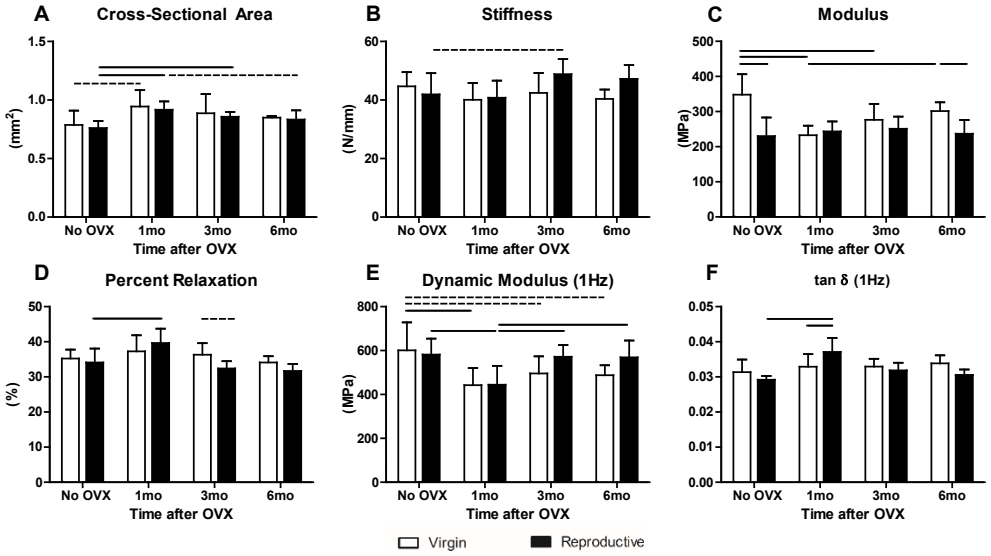

Figure 1: (A) Cross sectional area increased in the reproductive group at 1 month post-OVX but was not different from control by 6 months post-OVX. (B) Stiffness in the reproductive group trended towards increasing 3 months post-OVX, (C) but there were no differences in modulus in the reproductive rats. However, modulus significantly decreased in the virgin group at 1 and 3 months post-OVX. At 1 month post-OVX, the reproductive group exhibited (D) increased stress relaxation (E) decreased dynamic modulus and (F) increased tan(δ). Solid lines denote significance for $p \leq 0.05$ and dashed lines for trends $p \leq 0.1$.

Hydrogels reinforced with melt electrowriting for cartilage tissue engineering

Jonathan H. Galarraga,[1] Riccardo Levato,[2] Quentin Peiffer[2], Miguel Castilho[2], Jos Malda,[2] Jason A. Burdick[1]
[1]Department of Bioengineering, University of Pennsylvania, Philadelphia, United States
[2]Department of Orthopaedics, University Medical Center – Utrecht, Utrecht, Netherlands

Introduction: Hydrogels are commonly used to support the chondrogenesis of encapsulated mesenchymal stromal cells (MSCs) and the formation of neocartilage;[1,2] however, their low initial mechanics restrict their translation as implants *in vivo*. Although more loosely crosslinked (i.e., softer) hydrogels are more conducive to cartilage formation and maturation due to improved extracellular matrix (ECM) distribution,[1] the loading environments of articulating joints require that implants exhibit higher initial mechanics. To address this, we reinforced hyaluronic acid (HA) hydrogels with poly(caprolactone) (PCL) via melt electrowriting (MEW)[3,4] and investigated composite mechanical properties and cartilage formation.

Experimental Methods: *Material Synthesis and Composite Fabrication:* HA (75 kDa) was modified with norbornenes (NorHA, 20% mod.) and crosslinked in the presence of dithiothreitol, 0.05 wt% LAP photoinitiator, and visible light (400-500 nm) to yield NorHA hydrogels (2 wt%, ~ 2 kPa). MEW meshes comprised of PCL (200-800 µm filament spacing, 1mm thick) were fabricated using a custom-built MEW device as previously described.[2] To form composites, MEW meshes were filled with hydrogel precursor, which was subsequently photocrosslinked. *Material Characterization:* Compressive moduli of constructs were quantified via dynamic mechanical analysis (Q800, TA Instruments). *Cellular Outcomes:* Live/Dead assays were performed on encapsulated juvenile bovine MSCs (P1, 20x10^6 cells/mL) using calcein AM and ethidium homodimer stains. Initially and after 28 days, MSC-laden constructs were stained with alcian blue (sulfated glycosaminoglycan, sGAG) or anti-collagen type II (COL II) antibodies and analyzed with dimethylmethylene blue (DMMB) and hydroxyproline assays to quantify sGAG and collagen (COL) contents as previously reported.[2]

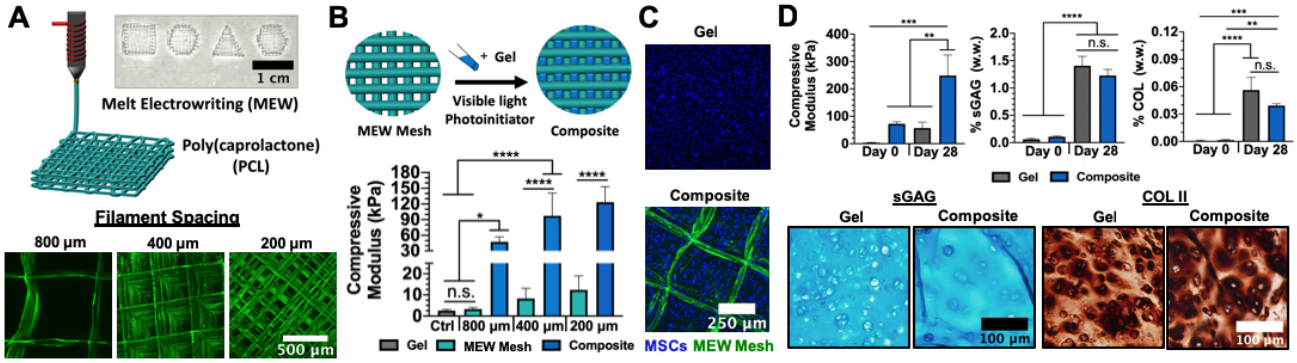

Results and Discussion: MEW meshes were formed into user-defined geometries and with variable filament spacings (Fig. 1A). Composites were fabricated by filling MEW meshes with hydrogel precursor and photocrosslinking, such that combinations of hydrogels with MEW meshes led to synergistic increases in compressive moduli, including an ~50-fold increase from the initial hydrogel modulus (Fig. 1B). The enhancement in mechanics observed is attributed to the ability of the hydrogel to mitigate MEW fiber buckling, which effectively increases the load-carrying capacity of MEW meshes.[3] Importantly, MSCs could be readily encapsulated in both NorHA hydrogels and composites without the need for molds (400 µm filament spacing, Fig. 1C). High cell viability (92.0 ± 2.7%) was observed after one week of culture, and homogenous filling of hydrogel within composites was achieved, as indicated by similar cell densities near the top (716±130 cells/mm^2) and bottom (638±77 cells/mm^2) of composites. Composites cultured in chondrogenic media for 28 days exhibited an ~2.5-fold increase in modulus; further, composites contained a significant amount of sGAG and COL after culture, with no significant differences in biochemical content or ECM (e.g., sGAG, COLII) staining when compared to hydrogels alone (Fig. 1D).

Conclusions: Composites comprised of NorHA hydrogels and MEW meshes were fabricated with high mechanical properties while conserving the chondrogenic potential of loosely crosslinked hydrogels. The levels of ECM formation and the mechanical properties achieved within these composites would not be attainable in NorHA hydrogels or MEW meshes alone. This approach has great potential towards the design of cell-laden implants for cartilage tissue engineering.

References: [1] Erickson et al. Osteoarthr. Cartil. **17**, 2009, 1639e1648. [2] Kwon et al. Adv. Healthcare Mater. **7**, 2018, 1701199. [3] Castilho et al. Scientific Reports. **8**, 2018, 1245. [4] Bas et al. European Polymer Journal **72**, 2015, 451–463.

Quantitative Comparison of Three Rat Models of Achilles Tendon Injury: A Multidisciplinary Approach

Huegel J[1], Boorman-Padgett JF[1], Nuss CA[1], Minnig MCC[1], Kuntz AF[1], Waldorff EI[2], Zhang N[2], Ryaby JT[2], Soslowsky LJ[1]
[1]McKay Orthopaedic Research Laboratory, University of Pennsylvania, Philadelphia, PA [2]Orthofix Inc., Lewisville, TX

INTRODUCTION: The Achilles tendon, while the strongest and largest tendon in the body, is frequently injured. Even after surgical repair, patients risk re-rupture and can have long-term deficits in function, with the rate of return to pre-injury level of activity reported to be as low as 16% [1]. Animal models of tendon injury are essential for understanding physiological processes of tendon repair and for testing the effects of potential therapeutics [2]. We have adapted and utilized three rat models of Achilles tendon injury (complete, full-thickness tear with post-operative immobilization, partial tear with post-operative immobilization, and a partial tear without post-operative immobilization). However, comparisons of the effects of these injuries on tendon mechanics and ankle joint function have not previously been made. Therefore, the objective of this study was to quantitatively define and compare the effects and relative impact on tendon properties and ankle function of the three Achilles tendon injury models. We hypothesized that animals receiving a complete tear would have inferior mechanical properties and ankle function compared to those receiving a partial tear, and that immediate loading after a partial tear would improve post-operative mechanical properties and ankle function compared to immobilized tendons.

METHODS: 144 adult male Sprague-Dawley rats (400-450 g) were used (IACUC approved). Animals underwent either full-thickness, blunt complete transection and repair of the right Achilles tendon [3] (with one week of post-operative plantarflexion immobilization (CT+IM, n=48) or full-thickness, partial-width transection (1.5 mm biopsy punch in center of tendon) without repair [4] (with one week of post-operative plantarflexion, PT+IM, n=48, or without IM, PT-IM, n=48). Animals were sacrificed at 1, 3, or 6 weeks (n=16/group/time point). Animals in 6 week groups underwent longitudinal in vivo ambulatory and passive ankle joint mechanics assessments [3]. At sacrifice, the Achilles-calcaneus complex was dissected out (n=6/group/time point) and processed for histological analysis. All other animals (n=10/group/time point) were frozen at -20°C and thawed for dissection prior to cross-sectional area measurement using a custom laser device and mechanical testing using a load controlled fatigue testing protocol (including frequency sweeps at 0.1Hz, 1Hz, 5Hz, and 10Hz, and fatigue cycling from 5 to 35N cycles at2 Hz until failure) [3]. Post-test, tendons were scanned using μCT at a 21μm resolution to assess for presence of heterotopic ossification (HO) within the healing tendon. Statistical comparisons were made between the CT+IM and PT+IM group and between the PT+IM and PT-IM group at each time point. Comparisons for mechanics, functional assessments, collagen fiber organization, and μCT metrics were made using one way ANOVAs with Bonferroni post-hoc tests. Histological comparisons were made using Kruskal-Wallis tests.

RESULTS: *Mechanical properties*: At 3 and 6 weeks post-injury, cross-sectional area was larger for CT+IM tendons compared to PT+IM (Fig 1A). PT+IM modulus was significantly greater than CT+IM at 1 and 6 weeks, but was significantly lower than PT-IM at 3 weeks (Fig 1B). Similar differences were also seen in stiffness (Fig 1C). Dynamic frequency sweeps at 0.125% strain also determined similar differences in dynamic modulus at all tested frequencies (data not shown). PT-IM tendons withstood significantly more fatigue cycles before failing than PT+IM tendons at 3 and 6 weeks, and only PT-IM tendons were able to produce a reliable fatigue response at 3 weeks (Fig 1D,E). Tissue modulus (Fig 1E) and both secant and tangent stiffness (data not shown) measured during fatigue testing were greater in PT+IM tendons than in CT+IM at 6 weeks, but there was no difference between PT groups in these metrics at this time (Fig 1E). *Histological observations*: No differences were determined in cell number (cellularity), nuclear shape, or collagen organization. *μCT*: The presence of heterotopic ossification was observed in almost all samples in all groups at all time points (no differences between models, data not shown). Bone volume was significantly higher in CT+IM tendons than PT+IM tendons at six weeks (Fig 2A); however, this mineralized tissue had decreased tissue mineral density (Fig 2B). *Functional assessments*: Ankle joint stiffness and range of motion (ROM) through dorsiflexion were significantly altered in CT+IM and PT+IM groups (Fig 3A,B). Ankles from complete tendon tears were stiffer than both partial tear groups at 14 days post-injury, but by 6 weeks, were only stiffer than the PT-IM group (Fig 3A). In contrast, CT+IM and PT+IM groups had similarly diminished dorsiflexion ROM (~60% decrease) at 14 days (Fig 3B). PT+IM joints regained significantly more ROM by 6 weeks, while CT+IM joints did not recover (Fig 3B). Few differences existed in plantarflexion parameters (data not shown). CT+IM animals also had significantly slower rate of loading (Fig 3C) and longer stance time (data not shown) during ambulation than PT+IM, even though overall speed was increased at 6 weeks (data not shown).

DISCUSSION: This study investigated differences in ankle function, tendon mechanics, and HO in three different models of Achilles injury. All models were reproducible and had distinct effects on measured parameters. Injury severity (CT vs PT) had a drastic influence on tendon healing, with complete tear causing diminished ankle mobility and decreased tendon mechanics throughout post-injury time points compared to partial tears. Changes in loading rate and stance time of the injured limb indicate that CT animals are altering ambulation patterns more severely, which may be due to loss of function or increased pain [5]. CT tendons also contained significantly more HO than PT tendons. However, differences in bone density between groups suggest that the mechanisms of HO development or maturation may vary between models. One week of plantarflexion IM had a strong effect on animals receiving a partial-width injury. Most notably, tendons in the PT+IM group failed extremely early during fatigue cycling 3 weeks post-injury (113±85 cycles), prohibiting fatigue analysis. Surprisingly, a partial tear injury without immobilization had no effect on ankle range of motion through dorsiflexion at any time point, while PT+IM animals demonstrated diminished function at all post-injury time points. Together, these results indicate that even short-term immobilization may impair healing and increase ankle stiffness in partial Achilles tears in rats. Future studies will investigate long-term effects of these models.

SIGNIFICANCE: All three models of Achilles injury could be useful for tendon healing investigations, chosen based on the prospective applications of a potential therapeutic. This work also sheds light on the universal occurrence of heterotopic ossification after surgically-induced injury in a rat Achilles tendon, as well as the potentially detrimental effects of complete immobilization/unloading on partial Achilles tears.

REFERENCES: [1] Barfod KW et al. J Bone Joint Surg, 2014. [2] Hast MW et al. Bone Joint Res, 2014. [3] Freedman BR et al. J Orthop Res, 2016. [4] Boorman-Padgett J et al. Trans ORS, 2018; 1454. [5] Caro AC et al. J Am Assoc Lab Anim Sci, 2014.

ACKNOWLEDGEMENTS: Funding was provided by Orthofix, Inc and the Penn Center for Musculoskeletal Disorders (P30 AR069619). We thank Stephanie Weiss, Daniel Gittings, Adnan Cheema, and Mengcun Chen for help with surgeries, and Peter Chan for help with μCT analysis.

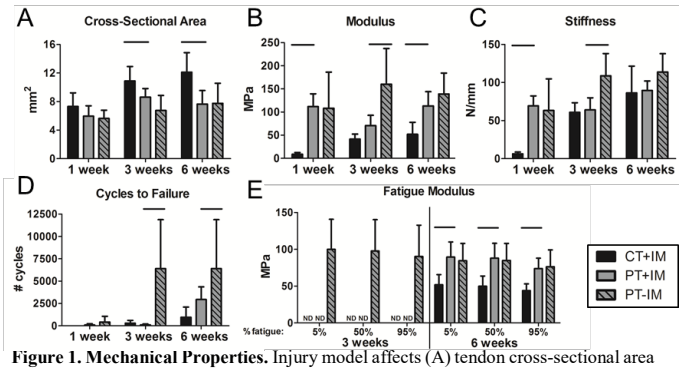

Figure 1. Mechanical Properties. Injury model affects (A) tendon cross-sectional area at 3 and 6 weeks; both injury mode and IM alter (B) tissue modulus and (C) tendon stiffness; immediate load bearing improves (D) cycles to failure at 3 and 6 weeks; and CT decreases (E) fatigue modulus at 6 weeks. ND: data was not able to be collected. Bars: p<0.025.

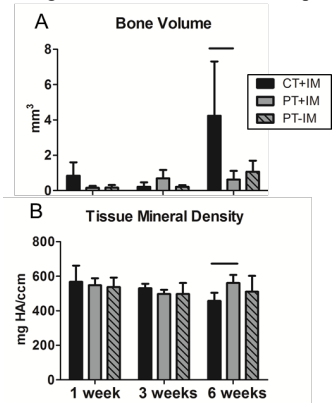

Figure 2. μCT Properties. (A) CT+IM showed (A) increased heterotopic bone volume but (B) decreased tissue mineral density at 6 weeks post-injury. Bars: p<0.025.

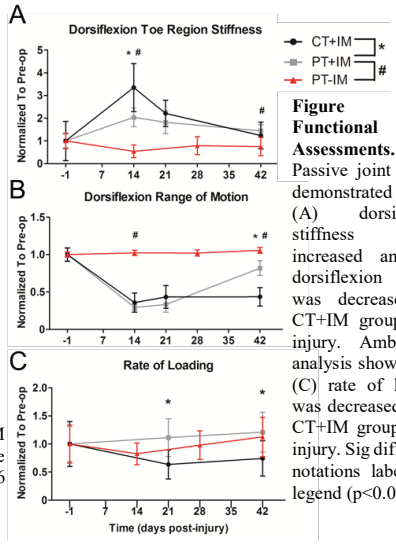

Figure 3. Functional Assessments. Passive joint testing demonstrated that (A) dorsiflexion stiffness was increased and (B) dorsiflexion ROM was decreased for CT+IM group post-injury. Ambulatory analysis showed that (C) rate of loading was decreased in the CT+IM group. post-injury. Sig difference notations labeled in legend (p<0.025).

Surgically repairing acute Achilles tendon rupture partially restores resting gastrocnemius tension

Todd J. Hullfish, Kathryn M. O'Connor, Josh R. Baxter
University of Pennsylvania, Philadelphia, PA
hullfish@pennmedicine.upenn.edu

Disclosures: Todd J. Hullfish (N), Kathryn M. O'Connor (N), Josh R. Baxter (N)

INTRODUCTION: Achilles tendon ruptures have increased by a factor of 10 in the past three decades, mostly affecting physically-active males [1]. Traditionally, these injuries have been treated as isolated tendon injuries by re-opposing the 'mop-like' ends of the tendon through either surgical intervention, where the ruptured tissue is sutured back together, or non-surgical intervention, where the ankle is immobilized in full plantarflexion and allowed to heal naturally. While re-rupture rates are below 5%, regardless of surgical or non-surgical treatment [2], functional deficits persist in two out of three patients [3]. These functional deficits have been linked to changes in medial gastrocnemius structure in patients treated non-surgically [4, 5] but it is unclear if surgically repairing the ruptured tendon restores muscle structure immediately following treatment. Therefore, the purpose of this study was to compare the muscle structure of Achilles tendon rupture patients treated surgically and non-surgically. To do this, we measured the resting muscle structure of the medial gastrocnemius of the injured limb before and after intervention. We hypothesized that patients who were surgically repaired would have longer and more pennate fascicles 2 weeks after intervention than non-surgical patients.

METHODS: Seventeen adults (13M/4F; Age: 43 ± 12; BMI: 27 ± 7) who suffered acute Achilles tendon ruptures and were treated by a single fellowship trained foot and ankle surgeon gave written informed consent before participating in this IRB approved study. Using ultrasound imaging, we measured the medial gastrocnemius at the first clinical visit when subjects opted for either non-surgical (N=9) or surgical (N=8) treatment and again at the second clinical visit 2 weeks after intervention. Surgical patients were placed in a splint before surgery and in a fully plantarflexed plater cast after. Non-surgical patients were placed in the cast during the first clinical visit. Images of the mid-muscle belly were acquired with an 8 MHz ultrasound transducer (LV7.5/60/128Z-2, SmartUs, TELEMED) while subjects lay prone on a treatment table with ankles supported by the edge of the table in the same position. We characterized the length and pennation of a constituent fascicle in the middle of the ultrasound image using custom written software (**Fig. 1A**). Fascicle length was quantified as the distance between a single fascicle's insertions into the deep and superficial aponeuroses. Fascicle pennation was calculated as the angle between the fascicle and the deep aponeurosis. To test our hypothesis that surgical patients would have longer and more pennate fascicles we calculated the change in muscle structure between the first and second scans compared them using one-way unpaired t-tests.

RESULTS SECTION: Surgically repairing the ruptured Achilles tendon decreased the pennation of the muscle but had a less consistent effect on the length of the fascicle (**Fig 1B,C**). Following surgical repair, half of the patients (4/8) demonstrated longer fascicles compared to the pre-surgical scans (average increased length 5.8 mm). However, the other half of patients demonstrated very little change or a slight decrease in fascicle length (average decreased length 3.2 mm). Conversely, surgically repairing the tendon decreased the resting pennation angle of the muscle compared to the patients who were treated non-surgically ($P = 0.008$). In the majority of these patients treated surgically, the muscle appeared to be overcorrected and displayed a less pennate configuration compared to the measurements made prior to treatment. Prior to treatment, the magnitudes of shorter and more pennate fascicles did not differ between treatment group.

DISCUSSION: Recent reports have challenged the conventional wisdom that Achilles tendon ruptures are isolated tendon injuries, and have shifted the clinical paradigm to restoring triceps surae muscle structure. While non-surgical treatment is an excellent option for many patient populations with an elevated risk of complications, surgical intervention appears to have a positive effect on muscle structure for many patients. The larger impact to pennation angle compared to fascicle length seems to suggest that some intramuscular tension is achieved by re-opposing the ruptured tissue but that tension is not great enough to fully stretch the fascicles and restore normal resting tone. Additionally, the increased variability in the surgical group suggests that some patients under go rapid muscle remodeling despite having good resting tone immediately following surgical repair in the operating room. Our future work is focused on determining the post-surgical loads that mitigate muscle remodeling while protecting the healing tendon from elongation.

SIGNIFICANCE/CLINICAL RELEVANCE: Surgically repairing Achilles tendon ruptures may improve muscle structure and increase resting tension in the muscle-tendon unit, which is beneficial for both tendon healing and muscle quality. However, post-operative care is likely a major driver of structural outcomes and should be a primary factor when treating patients with Achilles tendon ruptures.

REFERENCES: [1] Lantto+, *Scand JMed Sci Sports*, 2015; [2] Ochen+, *BMJ,* 2019; [3] Brorsson+, *Am J Sports Med,* 2017; [4] Peng+, *Foot Ankle Int*, 2019; [5] Hullfish+, *J Appl Physiol*, 2019;

ACKNOWLEDGEMENTS: This work was supported by the Thomas B. McCabe and Jeannette E. Laws McCabe Fund.

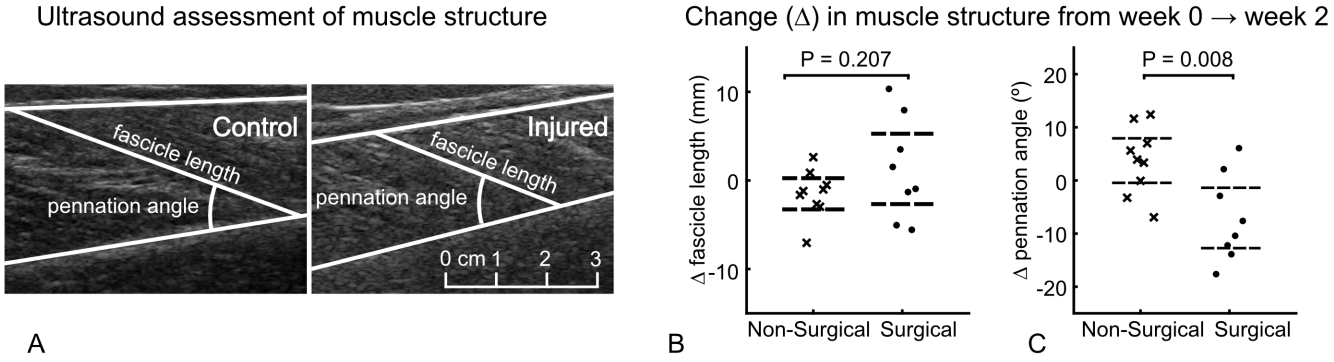

Fig 1. Fascicle length and pennation angle of the medial gastrocnemius muscle (A) were assessed using ultrasound imaging at the initial presentation (week 0, before surgery) and at the week 2 follow-up visit. Patients treated non-surgically did not demonstrate any changes in fascicle length (B) or pennation angle (C) between the week 0 and week 2 follow-up visit. However, patients who underwent surgical repair did show decreased pennation angle at week 2 compared to week 0.

Achilles tendon loading in an immobilizing boot is dependent on ankle angle and walking speed

Todd J. Hullfish, Kathryn M. O'Connor, Josh R. Baxter
University of Pennsylvania, Philadelphia, PA
hullfish@pennmedicine.upenn.edu

Disclosures: Todd J. Hullfish (N), Kathryn M. O'Connor (N), Josh R. Baxter (6-OPED, VACOped – provided immobilizing boots at no cost)

INTRODUCTION: Achilles tendon ruptures have increased 10-fold in the past three decades [1], leading to long-term functional deficits in nearly two-thirds of patients [2]. These functional deficits have been attributed to the elongation of the tendon [3] as well as the remodeling of plantarflexor muscles [4] which have both been shown to occur immediately following injury and worsen throughout the healing process. To counter this, rehabilitation protocols have been developed to strike a balance between protecting the healing tendon from re-rupture while allowing patients to return to activities of daily living as early as possible. Immobilizing boots are often used in place of plaster casts 2 weeks, which promote wound care and ambulation. Typically, a patient starts with this boot locked in a maximally plantarflexed position for 4 weeks, at which point the range of motion is slowly increased for another 4 weeks before removing the boot completely. At the same time, the patient is progressing from partial to full weight bearing to begin loading the healing tendon. Recent evidence suggests that small changes to this loading of the healing tendon in an immobilizing boot may have positive impacts on outcomes [5]. However, Achilles tendon loading is neither proscribed nor quantified during immobilization. Therefore, the purpose of this study was to quantify the amount of tendon loading experienced while walking in an immobilizing boot with respect to prescribed ankle angle and walking speed. We hypothesized that tendon loading would increase with increased walking speed and decrease with increased plantarflexion angle.

METHODS: Three healthy-young adults (2M/1F; Age: 28.6 ± 4.6 y/o; BMI: 30 ± 7) walked over flat ground while wearing an immobilizing boot after providing written informed consent in this IRB approved study. We collected lower extremity kinematics and kinetics using a 12-camera motion capture system (Raptor Series, Motion Analysis Corporation) and 3 embedded force plates (BP600900, AMTI). Subjects were asked to walk in normal shoes as well as in an instrumented immobilizing boot (VACOped, OPED) at 4 prescribed ankle angles: 0, 10, 20, and 30 degrees plantarflexion, which we set using an adjustable posterior strut that we instrumented with an inline load cell (LCM200, Futek) to quantify boot loading during gait. This boot was also fitted with a wirelessly triggered microcontroller (Feather 32u4, Adafruit) that collected and wrote load cell data in real time to an SD card. An instrumented insole (Loadsol, Novel) was placed in both the immobilizing boot and the lab shoe to quantify load experienced by the tendon. These data were streamed wirelessly to a handheld device (iPod Touch, Apple) running a manufacturer provided app (Loadsol App, Novel). Subjects completed five gait cycles in each ankle condition at self-selected slow, medium, and fast walking speeds. We simultaneously collected motion capture, insole, and immobilizing boot data and synchronized and averaged these data across 3-5 gait cycles per walking condition. Tendon load was calculated as the moment about the ankle divided by the Achilles tendon moment arm (5.5 cm) and normalized to subject body weight (**Figure 1**). To test our hypothesis that tendon loading increases with walking speed and decreases with ankle angle we first calculated mean tendon loading for each condition and then determined the magnitude of differences between them.

RESULTS SECTION: As expected, tendon loading was highest in the shod condition with no ankle bracing and lowest in the fully plantarflexed immobilizing boot (**Table 1**). On average, tendon loading decreased by 24.6 ± 1.2% between each ankle condition across all walking speeds. Walking faster increased tendon loading for each condition but the differences were not as large and more variable, increasing by 7.7 ± 3.2% on average (**Figure 2**).

DISCUSSION: Rehabilitation following Achilles tendon rupture is focused on modifying the loading biomechanics of the tendon to stimulate tendon healing and good patient outcomes. In this study, we developed an instrumented immobilizing boot that quantifies boot loading and Achilles tendon loading using self-contained sensors. Our initial findings show that tendon loading is dependent on both walking speed and ankle angle. Using this approach, our future work is focused on identifying tendon loading profiles that are associated with superior patient outcomes. Once we establish these loading profiles, we will have the quantitative data needed to improve rehabilitation protocols with patient-specific loading prescriptions. Understanding how patients respond to different levels of loading intensity and frequency would allow clinicians to modify patient specific rehabilitation procedures to mitigate the loss of long term function. Additionally, monitoring tendon loading throughout healing could help identify the development of complications such as re-rupture earlier in the rehabilitation process making interventions more effective.

SIGNIFICANCE/CLINICAL RELEVANCE: Quantifying tendon loading throughout healing may provide clinicians with critical new insights regarding patient progression throughout rehabilitation and improve long term outcomes.

REFERENCES: [1] Lantto+, *Scand JMed Sci Sports*, 2015; [2] Brorsson+, *Am J Sports Med,* 2017; [3] Silbernagel+, *Am J Sports Med,* 2012; [4] Hullfish+, *J Appl Physiol,* 2019; [5] Aufwerber+, *Am J Sports Med*, 2019

ACKNOWLEDGEMENTS: This work was supported by the Thomas B. McCabe and Jeannette E. Laws McCabe Fund

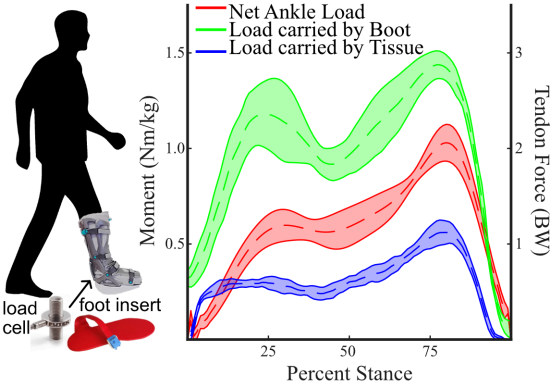

Figure 1

Tendon Load (%BW)			
	Slow	**Medium**	**Fast**
Shod	227 ± 10	236 ± 14	246 ± 13
Boot 00	178 ± 14	197 ± 19	199 ± 30
Boot 10	143 ± 7	160 ± 15	176 ± 16
Boot 20	111 ± 14	131 ± 26	139 ± 26
Boot 30	94 ± 18	105 ± 25	113 ± 31

Table 1

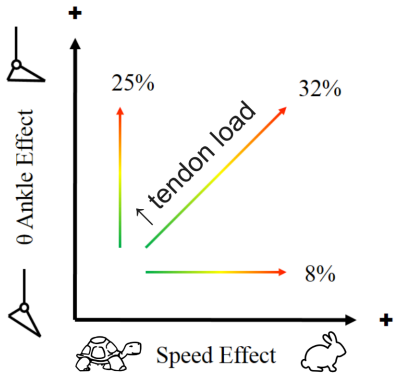

Figure 2

Figure 1. To quantify the load carried by the boot (green) and Achilles tendon (blue), we instrumented an immobilizing boot with a load cell and load-sensitive foot insert. **Table 1.** Achilles tendon loading (normalized by bodyweight) differed based on both walking speed and ankle position. **Figure 2.** The effects of ankle angle had a 3-times greater effect on Achilles tendon loading than increases in walking speed.

Biomimetic Proteoglycans Modulate the Biomechanics of Cartilage Pericellular Matrix

Elizabeth R. Kahle[1], Biao Han[1], Prashant Chandrasekaran[1], Chao Wang[1], Evan Phillips[1], Katsiaryna Prudnikova[1], Michele Marcolongo[1], Lin Han[1]
[1]Drexel University, Philadelphia, PA.

Introduction: In articular cartilage, chondrocytes are surrounded by a 3-5 μm thick pericellular matrix (PCM) that translates the biophysical changes occurring in the extracellular matrix (ECM) to biological signals directing cellular metabolism. The PCM is a highly sensitive entity with changes in cell metabolism and its degeneration is an early indicator of the initiation of injury-induced OA. In fact, changes of the PCM precede any detectable histological or tissue-level biomechanical changes. As degeneration progresses, the mechanotransducing abilities of the PCM are greatly impaired in part due to the pronounced catabolism of matrix molecules. In turn, the disrupted PCM leads to perturbed cell mechanotransduction, contributing to the vicious cycle of aggravated chondrocyte catabolism and irreversible cartilage breakdown. Currently OA intervention strategies do not have the sensitivity of targeting these early OA events associated with the PCM, and most therapies are palliative and cannot attenuate OA or restore joint function. Recently, our group has synthesized a suite of biomimetic proteoglycans (BPGs), composed of natural chondroitin sulfate bristles (CS) and a polymer backbone, that mimic the architecture and water uptake capabilities of native proteoglycans. We have demonstrated the ability of BPG10, a ~180 kDa mimic with ~7-8 CS bristles, to passively diffuse through all zones of cartilage with preferential localization to the PCM [2-4]. With their enzymatically resistant synthetic cores, BPGs are attractive alternative therapies to molecularly engineer degenerative cartilage. The goal of this study is to investigate the impact of BPG10 in the microscale biomechanical properties of cartilage PCM, and to determine the interactions of BPG10 with PCM biomolecules.

Methods: *Immunofluorescence-guided Atomic Force Microscopy (IF-AFM).* BPG10 was synthesized [2] and fluorescently labeled with DCCH. 10 mm lateral femoral osteo-chondral plugs were harvested from adult bovine knees and diffused with 10 mg/mL BPG10 or 1× PBS control for 24 hrs. Following diffusion, plugs were embedded in OCT and unfixed 8 μm sagittal sections were obtained using Kawamoto's film-assisted cryo-sectioning [5]. Using collagen VI IF AFM nanomechanical mapping, we quantified the effective indentation modulus, E_{ind}, of the PCM and ECM via a microspherical tip ($R \approx 2.5$μm, $k \approx 0.6$ N/m, 10μm/s rate, μMasch) and an MFP-3D AFM [6]. *Molecular Force Spectroscopy (MFS).* Colloidal tips ($R \approx 2.25$μm, $k \approx 0.03$ N/m, 10μm/s rate, μMasch) or nano-sized tips (pyramidal shape, $R \approx 50$ nm, $k \approx 0.12$ N/m, 10μm/s rate, Bruker) were incubated with either thiolated BPG10 or thiolated aggrecan for 48 hrs to achieve functionalized probes [7]. Freshly cleaned gold substrates were incubated with thiol-BPG10, thiol-aggrecan, or 11-mercaptoundecanol (as control) for 48 hrs. Adhesion forces between opposing aggrecan molecules were measured in 1× PBS and then in the presence of 20 nM BPG10 (added *in situ*, Fig. 2). All other MFS experiments were performed in 1× PBS. Colloidal MFS experiments were performed at $n \geq 6$ positions, with ≥15 indents per position, for all conditions and dwell times. Single MFS experiments were performed at $n \geq 7$ positions, with ≥ 35 indents per position obtained. Only ~6 indents per position displayed adhesion and were used for analysis. For each recorded force curve, the maximum adhesion force, F_{ad}, was extracted from the retrace curve and the adhesion energy, E_{ad}, from the integral of the approach-retrace curves. Statistical tests were performed at $\alpha = 0.05$.

Results: *IF-AFM.* Using IF-AFM, we quantified a 55% increase in elastic modulus, E_{ind}, of the PCM of BPG10 diffused tissue compared to controls ($p = 0.0378$). The modulus of the ECM exhibited a moderate trend of increase with the presence of BPG10, which is not significant ($p = 0.130$). However, a wider distribution of modulus values were observed at this concentration of BPG10 for the ECM (as seen in the literature, [8]) (Fig. 1b). The data corroborate with our previous observation that BPG10 is primarily localized in the PCM, with a lesser amount dispersed throughout the ECM (Fig 1a) [4]. *MFS.* The presence of BPG10 significantly increased the aggrecan-aggrecan adhesion (Fig. 2a), as signified by the higher maximum adhesion force and total adhesion energy (Fig 2b). Lastly, single molecular interactions between BPG10 and matrix molecule functionalized substrates were investigated (Fig. 3a). A hydroxyl self-assembled monolayer (OH-SAM) was included as a negative control demonstrating minimal adhesion forces and energy with BPG10 (0.076 ± 0.002 nN and 0.195 ± 0.02 fJ, respectively). Interactions between single BPG10 molecules showed increased adhesion force (n.s) and energy ($p = 0.007$) over BPG10-aggrecan contact (Fig. 3b).

Discussion: Our data clearly illustrated the capability of BPG10 in molecularly engineering the micromechanics of the PCM by its localization, and thus modulation of the osmotic environment through its fixed charges. The association of BPG10 to the PCM is surprising in that BPGs are made with a synthetic polymer core; there are no protein motifs to interact with native matrix molecules. We attribute this localization to the preferential molecular interactions between BPG10 and PCM molecules. Indeed, aggrecan, the major proteoglycan of cartilage matrix, is more concentrated [9], and undergoes much faster turnover [10] in the PCM. Free BPG10 can provide physical bridging to significantly increase aggrecan-aggrecan adhesion, as shown in the colloidal and experimental mechanical analysis. With the single molecular force experiment, we showed that the interaction energy per pair of BPG10-aggrecan is 0.497 ± 0.073 fJ, and BPG10-BPG10 is 0.629 ± 0.056 fJ, demonstrating a greater affinity of BPG10 for itself with moderate interactions to aggrecan. This experiment has established baseline interactions for intact aggrecan to non-degraded BPG10 with future work examining molecular interactions with other key matrix molecules. Our ongoing studies will look into the impact of BPG10 in modulating chondrocyte mechanotransduction in both healthy and OA cartilage.

Significance: This study demonstrates the ability of biomimetic proteoglycans to molecularly engineer cartilage PCM micromechanical properties, and demonstrated that BPG10 enhances the adhesion and integration of aggrecan, the major cartilage proteoglycan, at the molecular level. This work has the potential in the treatment of early cartilage degeneration by restoration of cell micromechanical niche and consequently mechanobiology.

References: [1] Chery, DR. et al, 2018. [2] Prudnikova, K et al., 2017. [3] Phillips, ER et al., 2019. [4] Phillips, ER et al., 2019 [7] Kawamoto, T et al., , 2014 [6] Wilusz, RE. et al., 2012 [7] Han, L., et al., 2008 [8] Wilusz, RE., et al.,2013 [9] Poole, C.A., et al, 1991 [10] Quinn, T.M., et al., 1999.

Acknowledgements: Supported by NSF CMMI-1826202 and CURE (state of Pennsylvania).

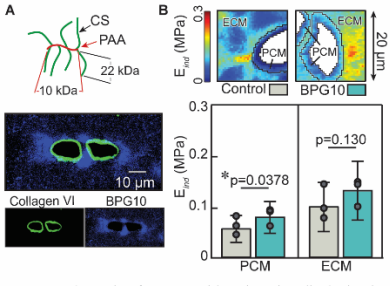

Fig. 1a) Schematic of BPG10 with IF imaging displaying its preferential localization to the PCM. **Fig. 1b)** Representative indentation modulus maps of control and BPG10 diffused cartilage with an increased E_{ind} in the PCM of BPG10 samples (dots represent each of n=3 animals, mean ± std. dev., *: p< 0.05).

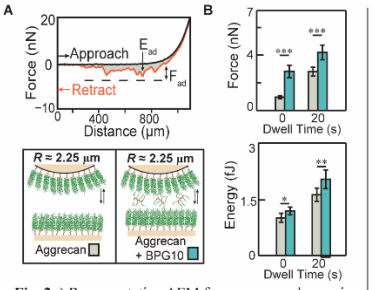

Fig. 2a) Representative AFM force curve and experimental set-up of molecular adhesion with BPG10 *in situ*. **Fig. 2b)** Presence of free BPG10 increases adhesion between aggrecan molecules (mean ± 95% CI, *: p< 0.05, **: p< 0.01, ***: p< 0.001).

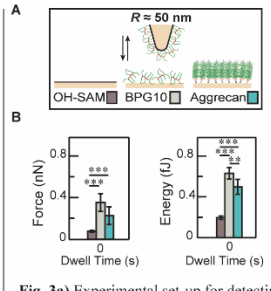

Fig. 3a) Experimental set-up for detecting single molecular interactions with OH-SAM serving as control. **Fig. 3b)** BPG10 adheres strongest to itself vs. aggrecan (mean ± 95% CI, **: p< 0.01, ***: p< 0.001).

Alpha Smooth Muscle Actin-expressing Bone Marrow Progenitor Cells Contribute to Tunnel Integration Following ACL Reconstruction

Timur B. Kamalitdinov[1], Keitaro Fujino[1,2], Yaping Ye[1], Xi Jiang[1], Snehal S. Shetye[1], Ashley B. Rodriguez[1], Andrew F. Kuntz[1], Miltiadis H. Zgonis[1], Nathaniel A. Dyment[1]

[1]University of Pennsylvania, Philadelphia, PA, [2]Osaka Medical College, Osaka, Japan.

timkam@seas.upenn.edu

Disclosures: None

INTRODUCTION: The coordinated events that give rise to zonal tendon/ligament insertions into bone (i.e., enthesis) during development are well established. These mechanisms are less known in the adult because traditional reattachment surgeries of avulsed tendon to bone result in disorganized scar and do no re-establish a zonal enthesis. Ligament injuries, such as the anterior cruciate ligament (ACL), are often reconstructed by passing a tendon graft through a bone tunnel, which does yield zonal attachments. Therefore, ligament reconstructions can serve as a test platform to better understand the mechanisms that drive adult zonal tendon-to-bone repair. Tunnel integration following ACL reconstruction is driven by cells outside the graft [1], presumably from the bone marrow stroma. However, markers that define this progenitor population and the signaling pathways that regulate the repair response are not established. Quiescent resident mesenchymal progenitor cells expressing α-smooth muscle actin (αSMA) have been shown to contribute to new bone formation and fracture repair [2]. Moreover, αSMA expression is increased in the amplifying progenitor population following injury. The objective of this study was to label αSMA amplifying progenitor cells to determine their relative contribution to tendon-to-bone attachments and surrounding bone during tunnel integration following ACL reconstruction.

METHODS: All animals and procedures were approved by UPenn's IACUC. Experimental Design. Inducible Cre mice driven by αSMA (SMACre^{ERT2}) were crossed with Ai9-tdTomato Cre reporter mice resulting in double positive mice (SMACre;tdTom). These mice were then crossed with transgenic Col1a1(3.6kb)-CFP mice. The triple positive mice were used to trace the contribution of αSMA-expressing cells in the bone marrow to Col1a1-expressing cells within attachments formed during the tunnel integration process. ACL reconstruction surgery was performed in 3-4 month old mice (20 total). Anterior drawer tests were performed on a subset of mice just after surgery (N=5-6/group) while remaining mice were assessed histologically at 1, 2, and 4 weeks post-surgery (N=3-5/group). Tamoxifen was injected on either post-surgery days 0, 3, and 6 (Early Injection Group) to target the original amplifying progenitor pool or days 7, 10, and 13 (Late Injection Group) to target αSMA-expressing cells after the initial expansion. Mineralization labels were given 7 days (Calcein) and 1 day (Demeclocycline) before sacrifice in all mice assigned to histology. ACL Reconstruction. The ACL was excised near the femoral insertion. The tibial and femoral tunnels were drilled with 27G needles. A tail tendon autograft was passed through the tunnels and anchored to outer cortices with stainless steel washers. Biomechanical Testing. Following sacrifice, left limbs were cleaned of extraneous soft tissue and the distal half of each tibia was potted in a custom fixture that allowed for adjustment of tibial plateau angle. The distal end of the femur was lowered into a custom fixture that could control knee flexion. The knee joint was tested for anterior and posterior stability by cyclic loading between ±0.4N for 10 cycles and the 10th cycle was used to quantify stability. Samples are defined as: Intact – intact left knee, ACLT – ACL transected left knee (transected on testing machine after testing intact), ACLR – ACL reconstruct right knee, ACLRT – ACLR graft transected right knee (transected on testing machine after testing ACLR). Multiplexed Mineralized Cryohistology. Knees were fixed in formalin, embedded, and sectioned undecalcified with cryofilm and each section was subjected to four rounds of imaging including 1) fluorescent GFP reporters and mineralization label, 2) tartrate-resistant acid phosphatase (TRAP) fluorescent staining, 3) alkaline phosphatase (AP) fluorescent staining, and 4) toluidine blue (TB) staining. Layered composite images of these rounds were made in image editing software. Histological Analysis. Labeling efficiency (% tdTom+ cells) of mineralized fibrocartilage of attachments and osteocytes in newly formed bone was quantified using Fiji. Statistical Analysis. One-way ANOVA with state of ACL ($\alpha = 0.05$, Bonferroni post-hoc) was used to compare biomechanical parameters. Mann-Whitney U test ($p < 0.05$) was used to compare differences in tdTom+ labeling efficiencies.

RESULTS: Biomechanical Analysis. Anterior drawer test showed that reconstruction restored 47% of anterior stability compared to ACL transected limbs (Fig 1D). ACL Reconstruction. By 2 weeks post-surgery, SMACre;tdTom+ cells infiltrated the graft (Fig. 2B), anchored collagen fibers to underlying bone (Fig. 2C), and expressed AP (Fig. 2D) near the tidemark (Fig. 2 dotted line) as they mineralized the fibrocartilage to create a zonal attachment. Fate Mapping of SMACre;tdTom+ Bone Marrow Progenitor Cells. SMACre;tdTom+ cells contributed to 30-50% of all cells within the mineralized fibrocartilage of the attachments with no statistical difference between groups ($p > 0.05$, Fig. 3A). Mineralized fibrocartilage was not present at 1 week post-surgery. SMACre;tdTom+ cells expressed high levels of Col1a1(3.6-kb)-CFP within the remodeling tendon graft. CFP intensity decreased with time with lowest intensities at 4 weeks. One week post-surgery, SMACre;tdTom+ cells formed woven bone adjacent to the tunnel interface. After 1 week, most of the stromal expansion was over and the SMACre;tdTom+ cells began forming new bone or attachments. Two weeks post-surgery, bone surrounding the tunnels was more organized (B in Fig. 2A) which continued to 4 weeks post-surgery. Labeling the original amplifying progenitor pool during the first week of repair resulted in significantly higher labeling efficiency of osteocytes in newly formed bone at D28 ($p < 0.05$, Fig. 3B). Interestingly, there was a significant drop in labeling efficiency with time in the late injection group (D14 vs D28) but not the early injection group (D7 vs D28) (Fig. 3B).

DISCUSSION: Recreating the spatiotemporal events needed to create a functional zonal tendon-to-bone attachment are critical to producing a functional repair. The murine ACL reconstruction model in this study can serve as a test platform to specifically target cells, genes, and pathways that regulate zonal tendon-to-bone repair. Overall, the SMACre;tdTom mouse model is efficient at targeting cells that contribute to tunnel integration and the targeting can be tuned temporally. While αSMA-expressing bone marrow progenitor cells have been shown to produce new bone during repair [2], this study demonstrates that they also have the potential to produce fibrocartilage within bone tunnel attachments. A limitation of this study was that not all cells within newly formed bone at 1 week post-surgery can be confirmed to be osteocytes. Future studies will use the SMACre^{ERT2} mice to target specific genes and pathways involved in enthesis development to determine their functional role in adult tendon-to-bone repair.

REFERENCES: 1. Kobayashi et al., Am J Sports Med, 2005. 2. Grcevic et al., Stem Cells, 2012.

ACKNOWLEDGEMENTS: Work supported by NIH grants R00 AR067283, P30 AR069619, the Thomas B. McCabe and Jeannette E. Laws McCabe Fund at Penn, and startup funds from the Department of Orthopaedic Surgery at UPenn.

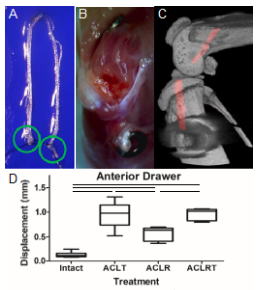

Fig. 1: ACL reconstruction procedure and anterior drawer test. Bars denote $p < 0.05$.

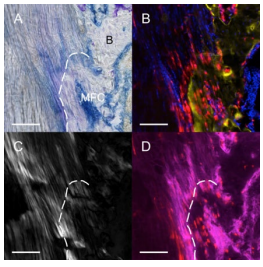

Fig. 2: MFC tendon-to-bone attachments form in tunnels 2 weeks post-surgery. Scale = 100μm. MFC – mineralized fibrocartilage, B – bone.

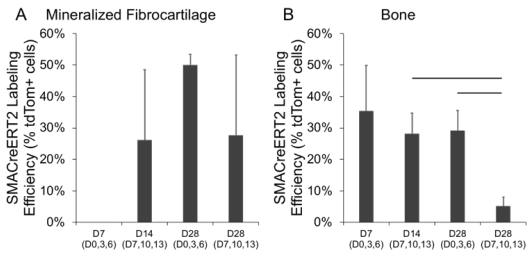

Fig. 3: Fate mapping of SMACre;tdTom+ bone marrow progenitor cells reveals spatiotemporal contributions to tunnel integration. Error bars: SD. Lines denote $p < 0.05$.

Nanomechanical Signatures of Nascent Matrix in Embryonic Cartilage and Meniscus

Bryan Kwok[1], Prashant Chandrasekaran[1], Chao Wang[1], Eiki Koyama[2], Nathaniel A. Dyment[3], Robert L. Mauck[3], Lin Han[1]
[1]Drexel University, Philadelphia, PA; [2]Children's Hospital of Philadelphia, Philadelphia, PA; [3]University of Pennsylvania, Philadelphia, PA.

Disclosures: RL Mauck (8, *JOR Spine*), no other disclosures.

Introduction: One challenge in cartilage and meniscus repair is the limited success in rebuilding regenerated matrix to recapitulate the composition, structure, and mechanical function of native, healthy tissues [1, 2]. To this day, most regeneration strategies have focused on increasing the anabolism of cells, while there are fewer attempts aimed at harnessing matrix assembly and function [3]. Understanding the initial development of native matrix will thus establish a crucial benchmark to guide the design of effective cartilage and meniscus regeneration. The objective of this study was to determine the nanomechanical properties of the developing nascent matrix in embryonic cartilage and meniscus. We tested embryonic tissues in mice, which enables the studies of in vivo embryonic development at well-defined stages. Further, given that embryonic tissues are highly cellularized, we separated the local mechanical properties of the newly forming (nascent) matrix from that of the cells via our recently established IF-guided AFM nanomechanical mapping [4].

Methods: Embryos from wild-type C57BL/6J mice were harvested from pregnant female mice at 17.5 days after fertilization (E17.5). For histological staining, freshly dissected knee joints were fixed in 4% PFA, embedded into paraffin, and microtomed into 5-µm thick sagittal sections. We then applied Hematoxylin and Eosin (H&E) and Safranin-O/Fast Green histological staining to assess cellularity and sGAG distribution. To assess the distribution of pericellular matrix (PCM)-specific matrix molecules, we performed immunofluorescence (IF) staining of collagen VI (X18082113, Fitzgerald) and perlecan (UH2820793, Invitrogen). For atomic force microscopy (AFM) mechanical testing, freshly dissected knee joints were embedded in OCT and cryotomed into 12-µm thick sagittal sections ($n \geq 3$ for both tissues). To quantify the nanomechanical properties of nascent matrix, we applied the IF-guided AFM to cryo-sections in 1× PBS, using a microspherical tip ($R \approx 2.25$ µm, $k \approx 0.6$ N/m, Bruker Nano) and a Total Internal Reflection Fluorescence (TIRF)-MFP-3D (Asylum Research). AFM probing was guided by the perlecan IF image as a biomarker of the nascent PCM. For cartilage, the test was performed in regions within the few cell layers of the joint surface, which develops into permanent articular cartilage, rather than into the secondary ossification center, in post-natal tissues [5]. For each region of interest, we obtained a map of 40 × 40 indentations in a 20 × 20 µm^2 area, and calculated the effective indentation modulus, E_{ind}, using finite thickness-corrected Hertz model [6]. To determine the microscale matrix heterogeneity, we evaluated the correlation between E_{ind} and distance between each location to its closest cell surface, $d_{matrix\text{-}to\text{-}cell}$, via linear regression. In all statistical tests, significance level was set at $\alpha = 0.05$.

Results: In the embryonic knee joint, at E17.5, both articular cartilage and meniscus showed high cellular density, as expected (Fig. 1a). Sulfated GAGs were present in both cartilage and meniscus, and was much more concentrated in cartilage (Fig. 1a). The two PCM biomarkers, collagen VI and perlecan, showed different patterns of distribution. Collagen VI was more intensely expressed within the few cell layers of joint surfaces, where the indentation was performed, and within the meniscus (Fig. 1b). Perlecan was more homogeneously distributed throughout the joint. Notably, both molecules were present throughout the matrix located between the densely packed cells (Fig. 1b). Guided by the perlecan IF, we quantified the micro-scale modulus of cartilage and meniscus nascent matrices (Fig. 2a). At this age, the meniscus showed a higher modulus (10.7 ± 4.7 kPa, mean ± std) than cartilage (9.1 ± 2.9 kPa) ($p < 0.001$, Fig. 2b). In both tissues, we found a positive correlation between local E_{ind} and distance-to-cell surface, $d_{cell\text{-}to\text{-}matrix}$. This correlation was stronger in cartilage matrix than in the meniscus, as indicated by the higher slope ([0.38 0.52] for cartilage and [0.11 0.29] for meniscus, 95% CI). Further, this correlation was able to interpret $R^2 = 5.1\%$ of the total variation for the cartilage modulus, but only 0.5% for meniscus matrix (Fig. 2c).

Discussion: This study is the first to define the local nanomechanical features of nascent matrix in embryonic cartilage and meniscus. First, the ubiquitous presence of perlecan and collagen VI suggests that, at E17.5, nascent matrix resembles the composition of the PCM in post-natal tissues. The territorial/interterritorial extracellular matrix (T/IT-ECM), which is devoid of these two molecules, has not yet been developed. This suggests that, in both tissues, the PCM is the first structural unit built up by cells during embryonic development. This also corroborates with literature showing that the PCM is where the earliest matrix molecular assembly, such as collagen fibrillogenesis, takes place [7]. Further, the differentiated distribution of collagen VI and perlecan indicates that, as early as E17.5, the regions that would later develop into cartilage and subchondral bone have already differentiated in terms of PCM composition, which could contribute to their differences in mechanoregulation and cell fate in post-natal joint growth.

In embryonic cartilage, despite the absence of T/IT-ECM, the nascent PCM of cartilage already exhibited marked heterogeneity, as signified by the increasing gradient of local modulus with respect to cell-to-matrix distance (Fig. 2). In contrast, the meniscus matrix showed a much weaker correlation despite having a higher modulus, suggesting a more delayed development of meniscus matrix. Collectively, these findings suggest that the PCM is the first to be assembled in native tissue and starts to exhibit tissue-specific composition and mechanical features early in development. Therefore, modulating the neo-PCM in engineered tissue could provide crucial cues for harnessing cell phenotype and matrix formation in vitro. Building on these findings, our ongoing studies are further examining the composition, structure, and nanomechanics of nascent embryonic tissues at various ages (e.g., E15.5 and P0).

Significance: This study defines and delineates the local nanomechanical properties of nascent matrix in embryonic cartilage and meniscus at E17.5, and shows that the PCM is the first structural unit established in vivo. This work opens the door for understanding the development of nascent embryonic matrix in vivo, providing a crucial benchmark for guiding cartilage and meniscus regeneration.

References: [1] Mauck+ 2003. [2] Sweigart+ 2001. [3] Mauck+ 2000. [4] Chery+ 2017. [5] Acuna+ 2018. [6] Dimitriadis+ 2002. [7] Wenstrup+ 2004.

Acknowledgements: This work is supported by NSF CMMI-1751898 and NIH AR075418. We thank the UPenn Singh Center for Nanotechnology for the use of TIRF MFP-3D.

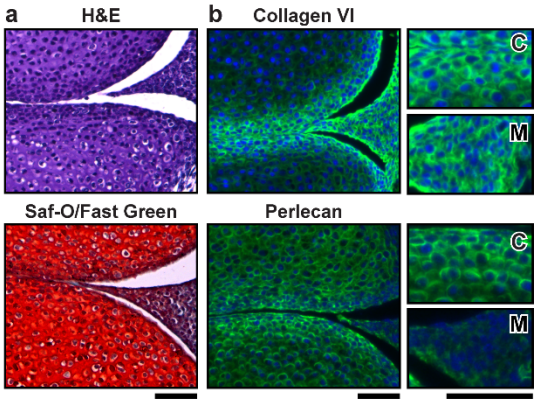

Fig. 1 a) H&E and Safranin-O/Fast Green histology of E17.5 WT murine knee joint. **b)** Immunofluorescence (IF) shows ubiquitous distribution of collagen VI and perlecan in nascent matrix of cartilage (C) and meniscus (M). Scale bar: 50 µm.

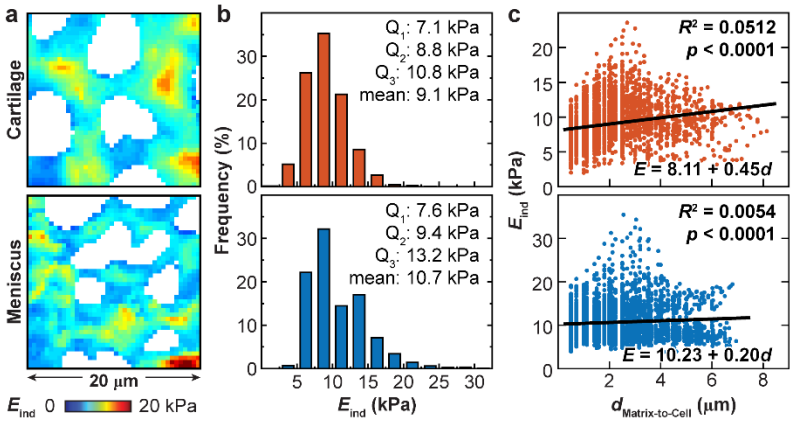

Fig. 2 Micromodulus of E17.5 cartilage and meniscus nascent matrix via IF-AFM. **a)** Representative modulus maps. **b)** Histogram of nascent matrix modulus distribution (≥ 3,000 indents from $n \geq 3$ animals). **c)** Correlation between local matrix micromodulus and matrix-to-cell surface distance.

Collagen VI Plays an Important Role in FDL Tendon Mechanics that is Distinct from the Role of Biglycan

Ryan J Leiphart[1], Snehal S Shetye[1], Hai Pham[2], Stephanie N Weiss[1], Marian F Young[2], Louis J Soslowsky[1]
[1]McKay Orthopedic Research Laboratory, University of Pennsylvania, Philadelphia, PA
[2]National Institute of Dental and Craniofacial Research, National Institutes of Health, Bethesda, MD

Disclosures: RJ Leiphart (N), SS Shetye (N), H Pham (N), SN Weiss (N), MF Young (N), LJ Soslowsky (N)

INTRODUCTION: While tendons are largely composed of tension-bearing collagen I fibers, other lower abundance matrix proteins with lesser known functions are also present. For example, collagen VI is a nonfibrillar collagen that enriches the pericellular matrix (PCM), and biglycan is a small, leucine-rich proteoglycan that regulates fibrillogenesis [1,2]. Deficiency in either collagen VI or biglycan is known to impact tendon mechanics [3,4]. While collagen VI and biglycan are known to interact, their interactions in native tendon, and the impact on tendon mechanics, remain unknown [5]. Therefore, the objective of this study was to determine how the roles of collagen VI, biglycan, or interactions involving both molecules affect FDL tendon mechanics. We hypothesized that knockout of collagen VI would reduce FDL tendon mechanical properties more than knockout of biglycan, while blocking interactions by knocking out both molecules would lead to a larger reduction in these properties than the reduction seen in either knockout alone.

METHODS: *Animals and Dissection*: 2 month old male wild-type (WT) (n=16), *Col6a2*$^{-/-}$ (n=11), *Bgn*$^{-/0}$ (n=12), and *Col6a2*$^{-/-}$/*Bgn*$^{-/0}$ (n=13) mice were used in this study (IACUC approved). FDL tendons were dissected from the left hind limb. The tendon sheath was fine dissected off the tendon. Tendon cross-sectional area (CSA) was measured with a custom laser device, and stain lines were applied for optical tracking [6]. *Mechanical Testing*: The FDL tendon was gripped with sandpaper, leaving a 5mm gauge length. The testing protocol consisted of 10 cycles of preconditioning between 0.01-0.02N at 1Hz, a 5 minute hold, a 5% stress relaxation for 10 minutes, a 1 minute hold, and a ramp to failure at 0.5% strain/s. Stress relaxation, stiffness, max load, modulus, and max stress were computed. Dynamic collagen fiber realignment was measured throughout the ramp-to-failure test using a crossed polarizer setup [7]. *Statistics*: For mechanical properties, a one-way ANOVA with Bonferroni post-hoc tests was used to compare across genotypes. For fiber alignment data, a two-way ANOVA with Tukey correction for multiple comparisons was used to compare across genotype and strain. Significance was set at $p<0.05$, and trends were set at $p<0.10$.

RESULTS: WT tendons had larger CSA than tendons from all knockout genotypes (Fig 1A). *Bgn*$^{-/0}$ tendons had larger CSA than *Col6a2*$^{-/-}$ and *Col6a2*$^{-/-}$/*Bgn*$^{-/0}$ tendons. WT tendons were stiffer and had higher max loads than tendons from all knockout genotypes (Fig 1B,C). *Bgn*$^{-/0}$ tendons were stiffer than *Col6a2*$^{-/-}$ and *Col6a2*$^{-/-}$/*Bgn*$^{-/0}$ tendons. *Bgn*$^{-/0}$ and *Col6a2*$^{-/-}$ tendons had higher max loads than *Col6a2*$^{-/-}$/*Bgn*$^{-/0}$ tendons. WT and *Bgn*$^{-/0}$ tendons exhibited a larger percent relaxation than *Col6a2*$^{-/-}$ and *Col6a2*$^{-/-}$/*Bgn*$^{-/0}$ tendons (Fig 2A). No differences in moduli were observed between groups (Fig 2B). *Col6a2*$^{-/-}$ and *Col6a2*$^{-/-}$/*Bgn*$^{-/0}$ tendons had higher max stresses than WT and *Bgn*$^{-/0}$ tendons (Fig 2C). During the ramp to failure, WT tendons realigned between 3% and 5% strain (Fig 3). Bgn$^{-/0}$ tendons realigned between 5% and 7% strain. *Col6a2*$^{-/-}$ and *Col6a2*$^{-/-}$/*Bgn*$^{-/0}$ tendons realigned between 1% and 3% strain. At 3% and 5% strain, *Col6a2*$^{-/-}$ and *Col6a2*$^{-/-}$/*Bgn*$^{-/0}$ tendons were more aligned, and WT tendons trended towards more alignment, compared to *Bgn*$^{-/0}$ tendons.

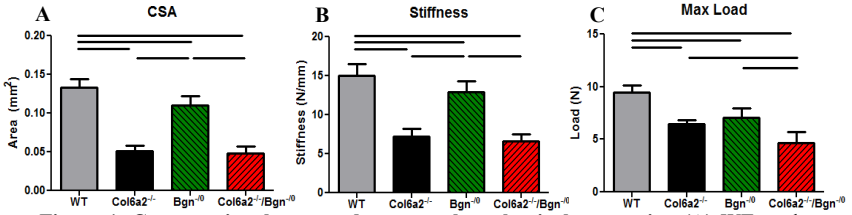

Figure 1. Cross-sectional area and structural-mechanical properties. (A) WT tendons had a larger CSA than all knockout genotypes. (B) WT tendons were stiffer than all knockout genotypes. (C) WT tendons had a higher max load than all knockout genotypes. Bars indicate $p<0.05$.

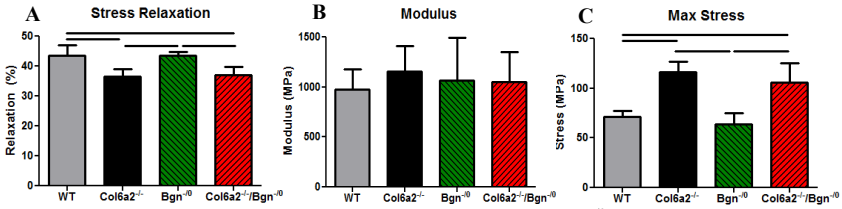

Figure 2. Viscoelastic and material properties. (A) WT and *Bgn*$^{-/0}$ tendons exhibited more stress relaxation than either collagen VI knockout models. (B) No differences in moduli were observed between genotypes. (C) Both collagen VI knockout tendons had higher max stresses than WT and *Bgn*$^{-/0}$ tendons. Bars indicate $p<0.05$.

DISCUSSION: While biglycan deficiency led to some decreases in FDL structural-mechanical properties (stiffness, max load), collagen VI deficiency led to larger reductions in structural-mechanical and viscoelastic properties. Knockout of biglycan or collagen VI led to smaller, less stiff, and weaker tendons than WT, but *Bgn*$^{-/0}$ tendons were larger and stiffer than *Col6a2*$^{-/-}$ tendons. Biglycan deficiency led to delayed fiber realignment compared to WT tendons, while collagen VI deficiency led to earlier realignment. *Col6a2*$^{-/-}$ tendons were less viscoelastic than *Bgn*$^{-/0}$ and WT tendons. These results agree with our hypothesis that collagen VI deficiency would reduce tendon mechanical properties more than biglycan deficiency. These mechanical and viscoelastic changes did not correspond to similar differences in material properties (modulus, max stress). There were no differences in moduli between WT, *Bgn*$^{-/0}$, and *Col6a2*$^{-/-}$ tendons, and *Col6a2*$^{-/-}$ tendons had higher max stresses than WT and *Bgn*$^{-/0}$ tendons. Our hypothesis that either knockout would reduce material properties was rejected. The different responses between the structural-mechanical and material properties could be due to smaller CSA in knockout tendons. Contrary to our hypothesis, knocking out both molecules did not amplify the differences seen in the *Col6a2*$^{-/-}$ mice. *Col6a2*$^{-/-}$ and *Col6a2*$^{-/-}$/*Bgn*$^{-/0}$ tendons had similar CSA, stiffness, moduli, max stress, stress relaxation, and fiber realignment. Due to its proximity to tendon cells within the tendon PCM, collagen VI is likely an important regulator of tendon cell behavior. The results of this study suggest that collagen VI regulation is so robust that it dominates any biglycan regulatory effects. This study is limited in that the knockouts are global. Changes in neighboring tissues, such as muscle and bone, may confound the effects of these knockout models on tendon properties specifically. Future studies will aim to elucidate the mechanisms by which collagen VI and biglycan regulate tendon properties. Another surprising finding in this study is that the biglycan knockout results differ from those of a previous study, which may be due to differences in CSA measurement [4]. The laser device used in the present study is more precise than the previous approach [6]. Overall, this study demonstrates that collagen VI and biglycan play distinct roles in regulating tendon mechanics and that collagen VI has a larger impact on mechanical properties.

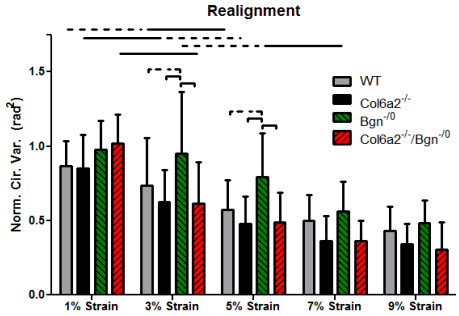

Figure 3. Fiber realignment during ramp to failure. Compared to WT tendons, *Bgn*$^{-/0}$ tendons realigned later. *Col6a2*$^{-/-}$ and *Col6a2*$^{-/-}$/ *Bgn*$^{-/0}$ tendons realigned earlier. A lower circular variance value indicates more alignment. Smooth bars compare adjacent strain values. Notched bars compare between genotypes. Solid bars indicate $p<0.05$, and dashed bars indicate $p<0.10$.

SIGNIFICANCE: This study reveals unique roles of collagen VI and biglycan in tendon mechanics and demonstrates that collagen VI has a larger impact on mechanical properties. These results provide further understanding of the role of lower abundance matrix proteins in tendon function.

REFERENCES: [1] Ritty TM et al. *Structure*. 2003. [2] Ameye L et al. *FASEB J*. 2002. [3] Izu Y et al. *Matrix Biol*. 2011. [4] Robinson PS et al. *J Biomech Eng*. 2005. [5] Wiberg C et al. *J Biol Chem*. 2002. [6] Favata, M *University of Pennsylvania*. 2006. [7] Lake SP et al. *J Orthop Res*. 2009.

ACKNOWLEDGEMENTS: This work was supported by the NIH (P30AR069619, T32AR007132), the Intramural Research Program of the NIH, NIDCR (Z01DE000379), and the NSF GRFP.

Combining Shear-thinning and Temporal Covalent Crosslinking in a Hyaluronic Acid Hydrogel for Degenerated Spinal Disc Repair

Victoria G. Muir, Sarah Gullbrand, Beth Ashinsky, Robert L. Mauck and Jason A. Burdick
Departments of Bioengineering and Orthopaedic Surgery, University of Pennsylvania, 210 South 33rd Street, Philadelphia, PA 19104, USA

Introduction: Hydrogels are water-swollen networks that are used to deliver therapeutics (e.g., growth factors, cells) or mechanical signals to musculoskeletal tissues for repair and regeneration. Injectable hydrogels represent a class of materials that allows simple introduction into tissues through their design (e.g., shear-thinning, gelation during injection). While shear-thinning properties permit easy injection, these hydrogels often exhibit low mechanical properties. In contrast, *in situ*-forming hydrogels can reach high moduli, but injection can be challenging (e.g., timing, extrusion from injection site during gelation). To combine injectability and strong mechanics in the same formulation, we created an interpenetrating network (IPN) hyaluronic acid (HA) hydrogel consisting of a shear-thinning guest-host network (GH) and a redox-catalyzed *in situ*-forming covalent network. IPN HA hydrogels were evaluated for their gelation and properties towards biomaterials for degenerated spinal disc repair.

Materials and Methods: The guest-host network consisted of adamantane-modified HA (AdHA, guest) and cyclodextrin-modified HA (CDHA, host). The covalent network was formed *in situ* using methacrylated HA (MeHA) with redox catalysts ammonium persulfate (APS) and tetramethyl-ethylenediamine (TEMED). 5wt% IPN hydrogels were created by one-pot mixing of 2wt% MeHA, 3wt% GH, 5mM APS, and 2.5mM TEMED (unless otherwise specified) in PBS (Fig. 1a). Shear oscillatory rheometry was used to assess mechanics. 5wt% IPN HA hydrogels were injected into harvested rabbit lumbar discs *ex vivo* and then *in vivo* into a degenerated spinal disc rabbit model.

Results and Discussion: IPN HA hydrogels exhibited interesting properties, such as early shear-thinning and temporal covalent crosslinking. At t = 0, 3wt% GH and 5wt% IPN were crosslinked via the GH network, whereas the 2wt% MeHA network flowed easily (Fig. 1b and c). Onset of gelation in the IPN was tuned by altering concentrations of redox initiator (Fig. 1d). Furthermore, the IPN shows improved recovery of mechanical strength after high strain compared to the MeHA network alone (Fig. 1e,f). IPN hydrogels were injected into harvested rabbit lumbar discs (Fig. 1g and h). After injection, IPN hydrogels remain localized in the cavity of the spinal disc due to early GH crosslinking (Fig. 1h). Mechanical and histological analysis of IPN hydrogel injections into an *in vivo* degenerated disc rabbit model is ongoing.

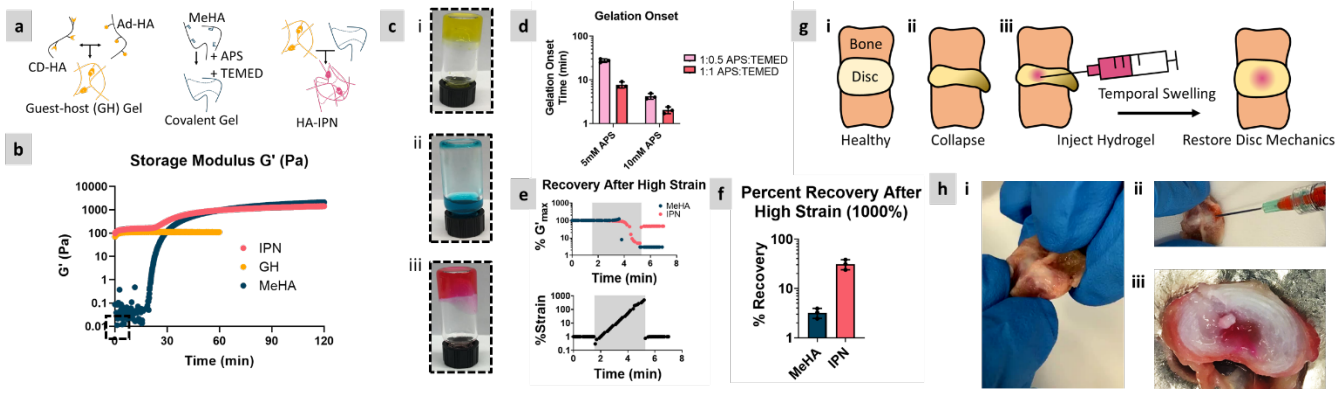

Figure 1. (a) Schematic of interpenetrating network chemistry. (b) Rheological analysis of hydrogel gelation kinetics. (c) Macroscopic gel behavior at t = 0 for (i) 3wt.% GH, (ii) 2wt.% MeHA, and (iii) 5wt.% IPN. (d) Time of gelation onset for 5wt.% IPN at varying APS and TEMED concentrations. Molar ratios of APS:TEMED indicated. (e) Rheological analysis of storage modulus (G') as a function of strain (1 – 1000%) for 2wt.% MeHA (pink) and 5wt.% IPN (blue). (f) Percent recovery of G' after 1000% strain. (g) Schematic of (i) healthy spinal disc, (ii) degenerated, collapsed spinal disc, and (iii) injectable hydrogels for spinal disc repair. (h) Depiction of *ex vivo* disc rabbit model (i) harvested rabbit lumbar disc, (ii) injection of hydrogel into disc, and (iii) disc cross section after hydrogel injection (blue). Error bars show ± standard deviation.

Conclusions: HA IPN hydrogels were prepared in a one-pot mixing approach. Early mechanical properties can be tuned to achieve clinically-relevant injectability. Furthermore, HA IPNs show promising potential as an injectable repair strategy for degenerated spinal discs.

Changes in Clinical Measures and Tissue Adaptations in Collegiate Swimmers Across a Competitive Season

Ryan W Paul[1], Angela Tate[2], Joseph Sarver[3], Laura DiPaola[2], Jeffery Yim[2], Stephen Thomas[1].
[1]Temple University, Kinesiology, [2]Arcadia University, Physical Therapy, [3]Drexel University, Bioengineering

Purpose/Hypothesis: In the 2016-2017 NCAA season, 22,375 collegiate swimmers competed competitively and many of them often experience shoulder pain (Sein et al., 2010), causing the athlete to either refrain from swimming or continue swimming with pain, ultimately leading to rotator cuff pathology. Overuse (increased training volume) has been associated with rotator cuff pathology in overhead athletes resulting in adaptive changes. Decreased endurance and ROM have been found in competitive swimmers along with being related to pain (Beach et al., 1992). It has also been found that swimmers with pain/disability have an altered supraspinatus tendon structure as measured with ultrasound (Tate et al., 2017). This study serves to investigate the relationship between pain and disability, training volume, range of motion, endurance, and tissue adaptations in the shoulders of collegiate swimmers throughout a competitive season.
Methods: 30 collegiate swimmers were assessed three times (T1, T2, T3) throughout the season for pain, disability, ROM, endurance and tendon organization. Ultrasound images of the supraspinatus tendon were collected from both arms. The ultrasound images were analyzed using custom MATlab software.
Results: Disability decreased and endurance increased throughout the season with no observed changes in pain. Bilateral internal rotation (IR) and horizontal adduction decreased significantly between all timepoints, except horizontal adduction between T2 and T3, which stayed constant. No significant changes were observed in tendon organization.
Clinical Relevance: Large amounts of IR have been associated with a high risk of impingement (Yanai and Hay, 2000). The relationship between pain, disability, endurance and ROM may suggest that a reduction of IR could protect the swimmers' shoulder by limiting impingement through the pull and recovery phases.

Sein ML, et al. *British Journal of Sports Medicine*, 44(2), 105-113, 2010.
Beach M, et al. *The Journal of Orthopaedic and Sports Physical Therapy*, 16(6), 262-268, 1992.
Tate A, et al. *APTA Combined Sections Meeting*, 2017.
Yanai I, Hay J. *Medicine and Science in Sports and Exercise*, 32(1), 30-40, 2000.

Nitinol Staple Fixation of Clavicle Fractures Results in a More Flexible Construct than Plating

Elaine C. Schmidt[1], Chelsea Hendow[1], Liane Miller[1], Kayley Dear[1], Samir Mehta[1], Michael W. Hast[1]
[1]University of Pennsylvania, Philadelphia, PA
hast@pennmedicine.upenn.edu

Relevant Disclosures: E.C. Schmidt: None, Kayley Dear: None, Chelsea Hendow: None, Liane Miller: None, S. Mehta: 2; AO North America, Smith and Nephew, Zimmer. 3B; Smith and Nephew, Synthes. 5; Amgen Co., Medtronic, Smith and Nephew, Zimmer. 8; Current Opinion in Orthopaedics, Wolters Kluwer Health. 9; Pennsylvania Orthopaedic Society, M.W Hast: None

INTRODUCTION: Midshaft clavicle fractures are often reconstructed with plates and screws, but these implants cause poor cosmesis and irritation, which may result in a second surgery for hardware removal [1]. This has driven the need for innovation in clavicle fixation, including the use of smaller 2.7 mm plates [2, 3]. However, these techniques have not definitively shown improvements in hardware-related complication rates [4]. Thus, areas of possible improvement remain in the operative management of these fractures. Continuous compression implants (CCIs) fabricated with shape-memory alloys, such as Nitinol, provide an attractive alternative to plate and screw fixation, due to their low profile and ability to provide compression at the fracture site. The use of CCIs gained traction in foot and ankle reconstructions [5], but the technology has not yet been tested in the milieu of clavicular fixation. We hypothesized that CCI-based reconstructions would decrease resistance to external loads compared to plate and screw fixation.

METHODS: This study was performed with 36 synthetic and 12 matched pairs of fresh-frozen, osteopenia-confirmed cadaveric clavicles (8F, 4M, 80 ± 8 years old). The synthetic study consisted of four reconstruction techniques: a single superiorly-placed staple (SS; n=6), a single anteroinferiorly-placed staple (AS; n=6), a 3.5 mm reconstruction plate (PLT; n=12), and two Nitinol staples placed orthogonally to each other (2S; n=12) (Fig 1). The cadaveric study examined three reconstruction techniques: PLT (n=8), 2S (n=8), and a new group with a 2.7 mm reconstruction plate placed combined with a Nitinol staple (PLT+SS; n=8) (Fig 1). All specimens underwent non-destructive 4-point bending (loading in superior-inferior direction, 2 mm deflections) and axial torsion tests (+/- 10°) for 10 cycles each. Half of each group was then subjected to either a 3-point cantilever bend to failure (0.5mm/s), or cyclic failure under increasing torsion (+0.1 Nm/cycle) until implant breakage or bending exceeding 30 mm. Groups were evaluated for normality and equal variance and compared using one-way ANOVAs ($p<0.05$).

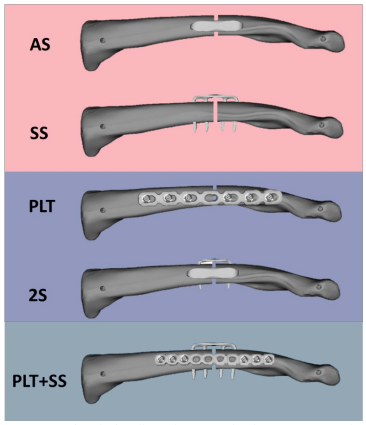

Fig 1: Clavicle fixation techniques examined in this study. Groups highlighted in pink were tested with synthetic bones, groups highlighted in blue were tested in cadaveric specimens. Purple represents overlap of synthetic and cadaveric test groups.

RESULTS: In comparison to plated groups, the single-staple and double-staple groups demonstrated significantly decreased resistance to bending and torsion. For example, the synthetic and cadaveric PLT group exhibited significantly higher bending rigidity than all other groups in superior-inferior 4-pt bending ($p<0.001$), except for the cadaveric PLT+SS group (Fig 2). In cantilever failure tests, the failure mode for PLT and AS groups was bending >30mm, while all other groups exhibited catastrophic bone fractures primarily at the medial-most components of the implants. In destructive torsional testing, failure modes for cadaveric specimens were primarily due to implant tear-out (75%). (Fig 3A,C). Synthetic bone specimens primarily failed via implant breakage (67%) (Fig 3B, D).

DISCUSSION: In accordance with our hypothesis, the use of Nitinol staples resulted in reconstructions that were significantly less stiff than those created with plates and screws. Single staples provided inadequate construct stiffness in non-destructive and destructive tests and are not currently indicated for stand-alone use in the clavicle or in osteoporotic bone. However, the lack of permanent deformation of constructs during non-destructive cadaveric testing suggests that CCI fixation – particularly for configurations reinforced by an additional staple or plate – may provide adequate relative stability while the patients is in rehabilitation and protected from large ranges of motion and high external loads. Strikingly, the synthetic models produced failure mechanisms that were completely different from the cadaveric specimens, suggesting that plastic models are poor surrogates in these mechanical tests.

SIGNIFICANCE/CLINICAL RELEVANCE: Clavicle fracture fixation continues to be a challenging clinical problem, and improving fixation while minimizing cosmesis and irritation is a worthwhile clinical endeavor. This study also highlights the need for better synthetic bone analogs, especially for osteoporotic bone.

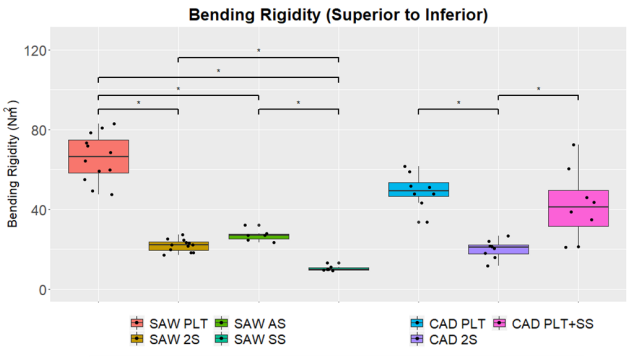

p-values

PLT vs 2S	<0.001	PLT vs 2S	<0.001
PLT vs AS	<0.001	PLT vs PLT+SS	0.241
PLT vs SS	<0.001	2S vs PLT+SS	0.002
2S vs AS	0.181		
2S vs SS	0.008		
AS vs SS	0.002		

Fig 2: Results from non-destructive 4pt bend tests on Sawbones (SAW) and cadaveric (CAD) specimens.

REFERENCES: [1] Wijdicks., et al, Arch Orthop Trauma Surg. 2012. [2] Galdi, B., et al. J Orthop Trauma. 2013. [3] Pulos, N., et al. Injury. 2016. [4] Alzahrani, M. M., et al. J Orthop Trauma. 2018. [5] Schipper, O. N., et al. Orthop Clin N Am. 2019.

ACKNOWLEDGMENT: This study was funded in part by DePuy Synthes.

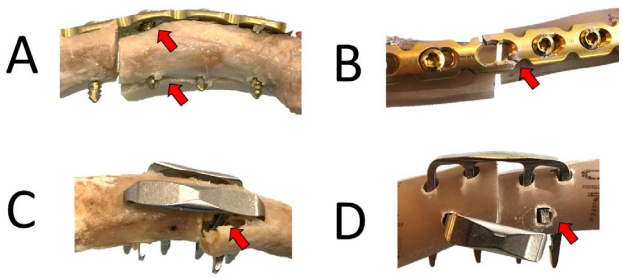

Fig 3: Differences in failure modes for cadaveric and synthetic specimens for the PLT and 2S groups.

An Engineered Porcine Accessory Carpal Osteochondral Unit as a Model for Treatment of Thumb OA

Brendan D. Stoeckl[1,2], Hannah M. Zlotnick[1,2,4], Megan J. Farrell[1], Liane M. Miller[1], Josh R. Baxter[1], Thomas P. Schaer[3], Michael W. Hast[1], David R. Steinberg[1,2], Robert L. Mauck[1,2,4]

[1] Department of Orthopaedic Surgery, University of Pennsylvania, Philadelphia, PA, USA. [2] Translational Musculoskeletal Research Center, Philadelphia VA Medical Center, Philadelphia, PA, USA.[3] Comparative Orthopaedic Research Lab, School of Veterinary Medicine, University of Pennsylvania, Kennett Square, PA, USA. [4] Department of Bioengineering, University of Pennsylvania, Philadelphia, PA, USA

Introduction: Given that the opposable thumb is central to all activities of daily living, trapezio-metacarpal (TMC) osteoarthritis (OA) has a significant impact on quality of life. In order for technologies that seek to replace articular cartilage (and bone) with a living, functional tissue to progress towards translation, appropriate large animal models are required. In this study, we explored the porcine accessory carpal (AC) bone as a model for TMC OA, and evaluated a method for fabricating an engineered AC replacement.

Materials and Methods: Eight AC bones were isolated from adult Yucatan minipigs. Cartilage mechanics were evaluated along the midline of the AC articular surface via stress relaxation indentation tests. μCT was performed before and after cartilage contrast enhancement with Lugol's solution. 3D models of bone and cartilage were generated and used to visualize geometry and map the cartilage thickness. Using data from CT, a musculoskeletal model was generated in OpenSim, and the relative motion of the AC and its contact forces was evaluated through a passive range of motion. In 3 forelimbs, a TekScan pressure sensor was inserted into the joint. The carpus was moved through a range of angles, while contact forces were measured. In Solidworks, an implant of the articulating cartilage surface and first third of the AC bone was designed based on the μCT data. A 2mm x 5mm "keel" was added for fixation. Positive molds were 3D printed out of an ABS-like photopolymer. To fabricate elastomeric negative molds, Sylgard 184 (polydimethylsiloxane, PDMS) was poured over the 3D printed designs. To fabricate porous anatomical implants, poly(ε-caprolactone) (PCL) was dissolved in chloroform at 20% wt/vol and mixed with NaCl crystals. Zirconium nanoparticles were included for radio-opacity. The slurry was poured into the mold and the solvent was evaporated. Implants were demolded and the salt was leached. Next, a pilot implantation was performed in an adult minipig. A reciprocating saw was used to remove the surface of the AC and a 2mm burr was used to create a slot for the keel. The construct was fixed in place with two 1mm Ø bicortical screws. After 1 week, the animal was sacrificed and the implant was retrieved and evaluated.

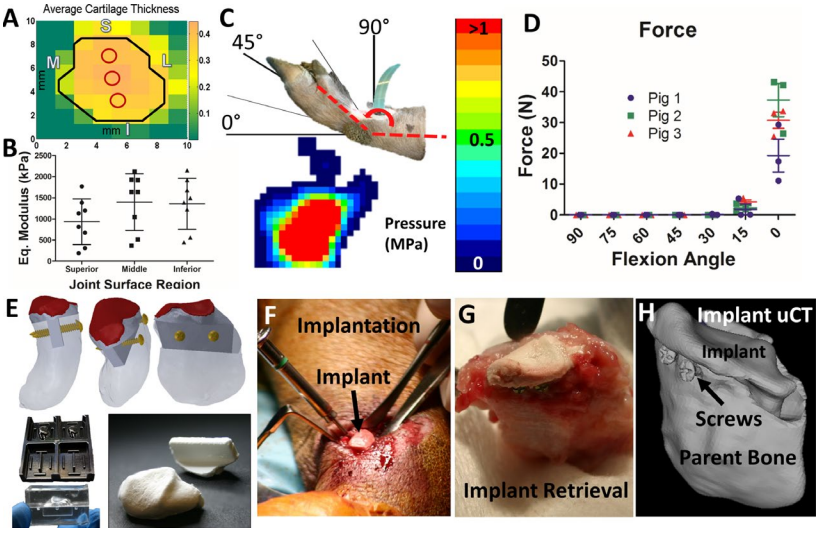

[A] Cartilage thickness. Red circles = location of indentation tests, results of which are in [B]. [C] Schematic and [D] results of TekScan experiment. [E] Implant design, mold, and construct. [F] Surgical Implantation. [G] Implant retrieval and [H] μCT.

Results and Discussion: The cartilage surface of the pig AC consists of a main saddle-shape that articulates with the ulnar carpal bone and a facet that interacts with the ulna. Average cartilage thickness was 350-500 μm. The equilibrium modulus in the superior, middle, and inferior regions was 0.93 +/- 0.54, 1.40 +/- 0.67, and 1.36 +/- 0.60 MPa, respectively. In the OpenSim model, contact force remained ~0N as the carpus was extended, until ~20° flexion. After this point, force increased and reached a peak of 67N at full extension (not shown). In the *ex vivo* experiment, force across the joint remained close to 0N until 15° of flexion, and then rose rapidly, reaching its maximum of 29.1±10.5N at 0°. These results suggest that the AC is essentially unloaded unless the carpus is fully extended (e.g., during standing). Using anatomic renderings generated from μCT, an implant was designed to replace the articular surface of the porcine AC. After 3D printing a positive mold, a PDMS negative mold was produced which was used to create a porous PCL implant. This was implanted into a living pig, which began weight bearing soon after surgery. The implant remained intact and in place at 1 week.

Conclusions: By using the porcine AC as a model for the human trapezium, evaluating its mechanics, and function, designing and fabricating an anatomic construct, and implanting it in a living animal, this study advances our work towards total biologic resurfacing for the treatment of TMC OA in humans.

Localized Delivery of Ibuprofen via a Bilayer Delivery System (BiLDS) for Supraspinatus Tendon Healing in a Rat Model

Brittany L. Taylor[1,2], Dong Hwa Kim[1,2], Julianne Huegel[1,2], Sophie J. Burkholder[1], Stephanie N. Weiss[1,2], Courtney A. Nuss[1,2], Harina A. Raja[1,2], Louis J. Soslowsky[1,2], Robert L. Mauck[1,2], Andrew F. Kuntz[1,2], Joseph Bernstein[1,2]
[1]Philadelphia VA Medical Center, Philadelphia, PA, [2]McKay Orthopaedic Research Laboratory, University of Pennsylvania, Philadelphia, PA,
brtay@pennmedicine.upenn.edu

Disclosures: B. L. Taylor (N), D.H. Kim (N), J. Huegel (N), S. Burkholder (N), S. N. Weiss (N), C. A. Nuss (N), H. A. Raja (N), L. J. Soslowsky (5; Orthofix), R. L. Mauck (8; JOR Spine), A. F. Kuntz (N), J. Bernstein (7B; CORR)

INTRODUCTION: The high prevalence of tendon re-tear following rotator cuff repair motivates the development of new therapeutics to promote improved tendon healing. Controlled delivery of non-steroidal anti-inflammatory drugs (NSAIDs) to the repair site via an implanted scaffold is a promising option for modulating inflammation in the healing environment. Previous work confirmed the *in vitro* sustained release of ibuprofen (IBP) from Labrafil-modified poly(lactic-co-glycolic) acid (PLGA) microspheres within sintered poly(ε-caprolactone) (PCL) electrospun scaffolds [1]. Biocompatibility of this bilayer delivery system (BiLDS) was also demonstrated with primary rat bicep and Achilles tenocytes *in vitro* [1, 2]. However, the effect of these IBP-releasing BiLDS on tendon healing *in vivo* is unknown. Therefore, the objective of this study was to investigate the effects of sustained release of IBP from BiLDS implanted at the repair site in a rat supraspinatus injury and repair model. We hypothesized that the controlled release of IBP from BiLDS would improve tendon healing by decreasing the expression of pro-inflammatory cytokines, thus improving tendon remodeling and mechanics.

METHODS: *BiLDS Fabrication*: PLGA microspheres with 300μL of Labrafil® M1944CS oil and with or without 30mg/mL of IBP were created as described [1]. 170μg of the microspheres, with or without IBP, were entrapped between two sintered 3x5mm scaffolds to generate BiLDS_IBP or BiLDS implants, respectively. Based on *in vitro* release studies, we predicted that the100μm thick BiLDS would deliver approximately 270μg of IBP to the injury site over 8 weeks. *BiLDS In Vivo Implantation*: 90 adult male Sprague-Dawley rats (400-450g) underwent bilateral supraspinatus detachment and repair (IACUC approved) [3]. Animals were randomly divided into groups receiving no scaffold (No_BiLDS), BiLDS with empty microspheres (BiLDS), and BiLDS with IBP-loaded microspheres (BiLDS_IBP) (n=30/group). BiLDS were secured proximally to the tendon via sutures and distally to the bone tunnel drilled through the greater tuberosity. Animals were sacrificed at 1, 4, and 8 weeks post-surgery. The right supraspinatus tendons and blood serum were collected at the time of sacrifice for biological assessment. *Biological Assessment:* Sagittal sections were stained with H&E, imaged at 20X and graded for cell shape and cellularity (n=6/group/timepoint). RNA was extracted from tendons harvested one week post-surgery (n=6/group) and qRT-PCR was run in quadruplicate using TaqMan assays on a QuantStudio 12K Flex Real-Time PCR System [4]. Genes of interest included markers of inflammation (TNF-α, IL-1b, IL- 6, and IL-10, Prostaglandin E2, CD68 and CD163), tendon repair (TGF-β1, TGF-β3, bFGF1 and VEGFb) and tendon remodeling (COL I, III, and IV, MMPs -2,-3,-9 and -13, tenascin, tenomodulin, and aggrecan). Expression was normalized to the internal control (GAPDH) and fold change was calculated by normalizing treatment groups to the untreated control, No_BiLDS. ELISA for TNF-α and IL-6 was performed on protein isolates from the excised tendons and for IBP in serum samples collected at 4 and 8 weeks (n=6/group/timepoint). *Tensile Mechanical Testing*: The cross-sectional area of the left intact supraspinatus tendons from animals sacrificed at 4 and 8 weeks (n=12/group/timepoint) was measured using a custom laser device. Ex vivo tensile testing was performed as follows: preload, preconditioning, stress relaxation, and ramp to failure. Modulus, stiffness, maximum load, and maximum stress were computed. *Statistics:* Two-way ANOVA and normality tests were performed on all datasets. To compare between groups at each timepoint, one-way ANOVA or Kruskall-Wallis tests were performed, depending on normality. To compare over time within each treatment group, Welch's t-tests or Mann-Whitney U tests were performed. Significance was set at $p<0.05$ (*); ** denotes $p<0.01$ and ***denotes $p<0.001$.

RESULTS: There were no statistically significant differences in cell shape, cellularity, and expression of tendon healing genes or IL-6 cytokine expression between the treatment groups at each timepoint (data not shown). IBP was undetectable in the serum of all animals at 4 and 8 weeks (data not shown). Tendons treated with BiLDS_IBP expressed significantly less TNF-α compared to untreated tendons, No_BiLDS, at 8 weeks and both BiLDS groups decreased in TNF- α at the protein level over time (Fig. 1A). Stiffness, modulus, maximum stress, and maximum load of the untreated tendons (No_BiLDS) were significantly greater than in either of the treated groups, BiLDS and BiLDS_IBP, at 4 weeks (Fig. 1B-D). Stiffness, maximum stress, and maximum load increased for all groups over time (Fig. 1B & 2D). Modulus and maximum stress of the treated tendons in the BiLDS group were lower in comparison to the No_BiLDS group at 8 weeks, but there were no differences in these parameters between the No_BiLDS and BiLDS_IBP groups at 8 weeks (Fig. 1C & 1D). There were no significant differences in stiffness (Fig. 1B) and maximum load at 8 weeks or in tendon cross-sectional area at either 4 or 8 weeks (data not shown).

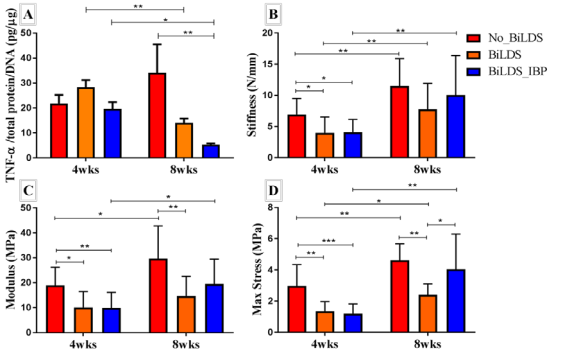

Figure 1. (A) Treated tendons, BiLDS and BiLDS_IBP, significantly decreased in cytokine expression of TNF-α over time and IBP-treated tendons expressed significantly less TNF-α than the untreated tendons, No_BiLDS, at 8 weeks. The untreated tendons, No_BiLDS, exhibited significantly greater (B) stiffness, (C) modulus, and (D) maximum stress at 4 weeks in comparison to the treated tendons, BiLDS and BiLDS_IBP. Data presented as mean ± SD. (*p<0.05, **p<0.01, ***p<0.001)

DISCUSSION: Although the use of BiLDS and BiLDS_IBP was not therapeutically beneficial for rat rotator cuff healing in terms of mechanics, the release of IBP from BiLDS significantly decreased pro-inflammatory signaling in the late healing phase. There were no substantial changes in gene expression 1 week post-repair with either treatment (BiLDS or BiLDS_IBP) compared to standard surgical repair (No_BiLDS). Therefore, we are unable to conclude the biological effect of the BiLDS with and without IBP on tendon repair at this time. Further investigation is ongoing to evaluate additional tendon healing markers at the protein level up to 8 weeks post-repair. Mechanical testing results indicated both BiLDS and BiLDS_IBP were detrimental to tendon mechanics compared to surgical repair alone, especially at early timepoints. Previous work revealed no significant differences in structural properties after surgical repair with and without the implantation of a single layered PCL scaffold in a rat rotator cuff injury and repair model [5]. Therefore, the decreased mechanics seen with the use of BiLDS in this study may be due to the increased size of the BiLDS compared to a single-layer PCL scaffold. Implanting a substantially thicker scaffold into the tight subacromial space in the rat shoulder may have caused supraspinatus impingement and negatively affected early tendon healing. Despite this, the BiLDS and BiLDS_IBP constructs remained intact, led to decreased pro-inflammatory expression over time, and recovered the tendon structural properties by 8 weeks. Future studies are required to elucidate the effect of the BiLDS and BiLDS_IBP on tendon mechanics at later timepoints and in larger defects in which supplementation with a scaffold may be necessary to stabilize repair.

SIGNIFICANCE: This study investigates a biocompatible nanofibrous bilayer delivery system (BiLDS) for localized delivery of ibuprofen to mitigate inflammation in a rat rotator cuff repair model. Further evaluation is necessary to elucidate the beneficial effects of the system in a larger animal model.

REFERENCES: [1] Taylor et al., ORS 2018 (Poster No. 0356), [2] Kim et al., ORS 2018 (Poster No. 1462), [3] Huegel et al., J Orthop Res., 35:1250-1257, 2017, [4] Reno et al., Biotechniques, 22:1082-1086, 1997, [5] Beason et al., JSES, 21:245-250, 2012.

ACKNOWLEDGEMENTS: This project was funded by a VA Merit Grant (O0979-R), the Penn Center for Musculoskeletal Disorders (NIH/NIAMS P30 AR069619), and a Vice Provost for Research fellowship to B. Taylor. We thank Adnan Cheema, Corinne Riggin, and Hetty Rodriquez for their assistance.

Magneto-patterned mesenchymal stem cell laden hydrogels recapitulate cartilaginous matrix gradients

Zlotnick HM[1,2,3], Clark AT[4], Gullbrand SE[1,3], Carey JL[1,3], Cheng XM[4], Mauck RL[1,2,3]
[1]Dept. of Orthopaedic Surgery, University of Pennsylvania, Philadelphia, PA, [2]Dept. of Bioengineering, University of Pennsylvania, Philadelphia, PA, [3]Translational Musculoskeletal Research Center, Philadelphia VA Medical Center, Philadelphia, PA, [4]Dept. of Physics, Bryn Mawr College, Bryn Mawr, PA
zlotnick@seas.upenn.edu

Disclosures: JLC (3C-Vericel, 5-Vericel, 8-AJSM), RLM (8-JOR Spine).

Introduction: The developing osteochondral interface is typified by a low chondrocyte density and marked interdigitation of cartilaginous and mineralized matrix to strongly adhere the two layers. In repair scenarios, mimicry of this cell distribution may improve the integration of engineered tissues with the underlying subchondral bone. However there are few, if any, cytocompatible 3D cell positioning methods to achieve this patterning[1,2]. Here, we developed a novel magneto-patterning method to generate cell gradients in 3D hydrogels. To do so, a paramagnetic MRI contrast agent, gadodiamide (Gd), was mixed into a crosslinkable hydrogel precursor, creating a magneto-responsive solution. We hypothesized that mesenchymal stem cells (MSCs) in solution would move away from a nearby permanent magnet, generating depth-dependent gradients in cellularity (and eventual matrix deposition) after crosslinking to lock the cells in place.

Methods: Construct fabrication. Bovine MSCs (P2) were suspended ($20x10^{-6}$/mL) in 1% methacrylated hyaluronic acid (MeHA)[3] with 0.05% LAP crosslinker and 200mM Gd, and injected into a mold (4:1.3mm diameter:height), above a permanent magnet (15/16" diameter x ½" thick, B_{rmax}=1.32T). Following magnetic field exposure (0, 2, 5, or 10 min) (**Fig. 1A**), the solution was UV-crosslinked (**Fig. 1B**), generating a cell-laden hydrogel. Samples were serially washed to promote Gd release, and cultured in chemically defined media with 10 ng/mL TGF-β3. Gd washout. MRI (4.7T) was used to image hydrogels +/- Gd (n=4) over 24 hours in media. T1 relaxation times were computed[4]. Cell position analysis. Constructs (n=2-4) were diametrically halved, labeled with Hoechst stain, and imaged after 2 days of culture. Max projection images were divided in 5 regions from the top (1) to the bottom (5) of the constructs, and cell number was quantified in each region using FIJI. Matrix staining. After 3 weeks of culture, constructs (n=4) were paraffin sectioned, and stained with Alcian blue (proteoglycans), and Picrosirius red (collagen). Regional strain transfer. After 3 weeks of culture, the local mechanical properties of constructs (n=5-6) were measured using a custom-built compression device[5]. Vic-2D image correlation software was used to calculate Lagrangian strains from the images. Data shown was taken from the 12% strain step. Statistics. Data = mean + SD. Significance: $p<0.05$. Fig. 1 and 2: Kruskal-Wallis test followed by Dunn's post-hoc test. Fig. 3: unpaired two-tailed t-test.

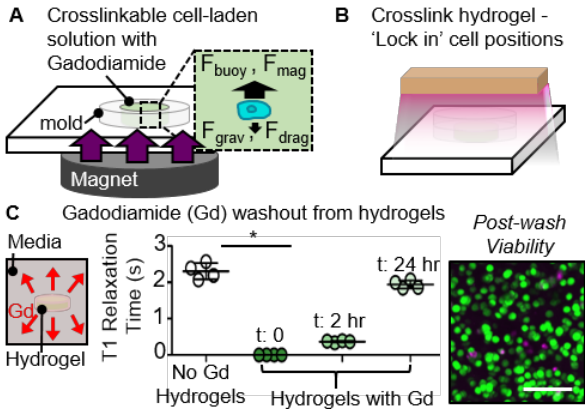

Figure 1. *Fabrication of magneto-patterned cell-laden hydrogels.* (A) Magnetic field is applied. (B) Cell positions are 'locked in' via UV-crosslinking. (C) Gd diffused out of the gels, as measured by MRI. * $p<0.05$. Calcein-AM (green; live cells), Ethidium homodimer-1 (magenta; dead cells). Scale bar = 100 µm.

Results: Because Gd decreases the MRI T1 relaxation time, as Gd (<600 Da) diffuses out of the crosslinked hydrogels, the T1 relaxation time of the hydrogels increases (**Fig. 1C**). The encapsulated MSCs were therefore only transiently exposed to Gd, and remained viable post-washout. The developed magneto-patterning method effectively decreased the percentage of cells in the bottom region of the constructs with increasing exposure to the magnetic field (**Fig. 2**). These cell distributions were consistent with previous computational simulations[6], which optimized the parameter space for this work. As hypothesized, the local strain in the bottom region of the magneto-patterned constructs, where there were less cells and matrix deposition, trended higher (**Fig. 3**).

Discussion: This study demonstrates that viable cells can be positioned within transiently paramagnetic hydrogels to recapitulate cartilaginous matrix gradients (**Fig. 1, 2, 3**). While long-term exposure to Gd can decrease cell viability[7], our data show that it quickly washes out of the constructs (**Fig.1**). The paramagnetic fluid is present for long enough to facilitate cell positioning (**Fig. 2**), without requiring intracellular magnetic labels, which can inhibit chondrogenesis[1]. Using this system, we successfully generated constructs with distinct cell/matrix-sparse and cell/matrix-rich regions (**Fig. 3**). In the future, we will investigate the mechanical competence of the cell/matrix-rich region and the osseointegration of the cell/matrix sparse region in a relevant large animal cartilage defect model. We expect enhanced endogenous cell infiltration in cell/matrix-sparse region. Lastly, we will exploit this highly tunable system to pattern a bone-promoting agent opposite the cell gradient to further enhance the osseointegration of an engineered construct.

Significance: This magneto-patterning strategy may be useful to recreate not only the osteochondral interface, but also other soft tissue-to-bone musculoskeletal junctions, defined by cellular gradients, to ultimately improve the mechanical function and integration of engineered tissues.

References: [1] Kostura+ 2004. [2] Grogan+ 2012. [3] Burdick+ 2005. [4] Pickup+ 2004. [5] Kim+ 2017. [6] Zlotnick+ SB3C 2019. [7] Anil-Inevi+ 2018.

Acknowledgements: This worked was supported by the Department of Veterans' Affairs, the NSF (CMMI: 15-48571), and the NIH/NIAMS (R01 EB008722, T32-AR007132, and P30AR069619).

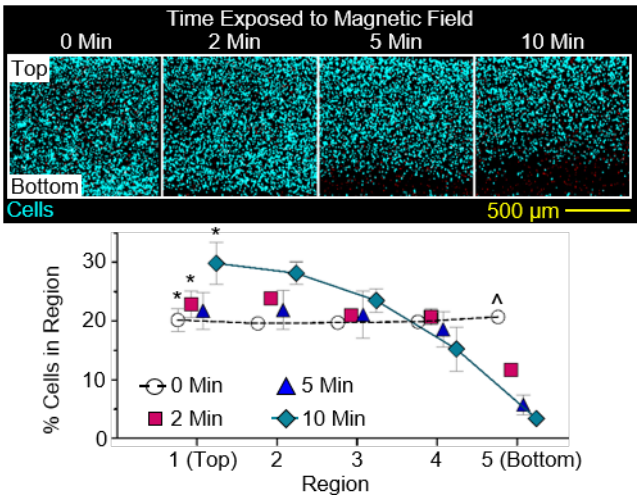

Figure 2. *Cell distribution in hydrogels after magnetic field exposure.* *, ^ denotes significance ($p<0.05$) compared to region 5, and compared to the 10 minute exposure, respectively.

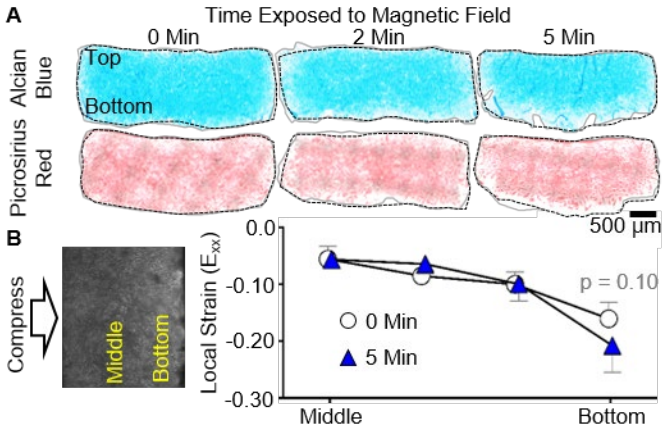

Figure 3. *Depth-dependent matrix deposition in constructs leads to differential strain transfer in the bottom of the constructs after 3 weeks of culture.*

Anterior Drawer Tests to Quantify the Stability of the Murine Knee

Snehal S. Shetye[1], Yusuke Hagiwara[2], Ashley B. Rodriguez[1], Miltiadis H. Zgonis[1], Andrew F. Kuntz[1], Nathaniel A. Dyment[1]
[1]University of Pennsylvania, Philadelphia, PA, [2]Nippon Medical School Hospital, Tokyo, Japan
shetye@pennmedicine.upenn.edu

Disclosures: SS Shetye (N), Y Hagiwara (N), AB Rodriguez (N), MH Zgonis (N), AF Kuntz (N), NA Dyment (N).

INTRODUCTION: Murine models of altered knee loading are routinely used to study the pathogenesis of post-traumatic osteoarthritis (PTOA). Such models include anterior cruciate ligament (ACL) transection, ACL rupture, or destabilization of the medial meniscus (DMM) [1]. These surgeries are typically applied to transgenic mice (i.e., knockout models) to better understand the role of certain genes and pathways in the pathogenesis. However, many of these studies have not investigated the stability of the knee following these surgical interventions and genetic treatments. We aimed to address this gap in knowledge by developing two methods to test the anterior-posterior stability of the knee following ACL injury and/or reconstruction.

METHODS: Experimental Design. All animals and procedures were approved by UPenn's IACUC. Adult mice were assigned to two methods of measuring knee stability through load-control anterior-posterior drawer tests. *Faxitron group*: Mice were assigned to intact (n=9), ACL transection (ACLT, n=9), and ACL reconstruction (ACLR, n=8) groups. The ACLT and ACLR mice were assessed at 4 weeks post-surgery. *Instron group*: Anterior-posterior drawer were applied to intact limbs, then the ACL was transected using a 25G needle and the test was conducted again on the same specimen (n=3). ACL transection and reconstruction procedure. All surgical procedures were performed under a microscope. One knee joint of each mouse was subjected to ACLT and/or ACLR. The contralateral knee joint served as an intact control. Following general anesthesia and aseptic preparation of the surgical site, tail tendon fascicles (3-4 cm long) were harvested from the proximal tail. The tendon bundles were maintained in PBS and sutured at both ends with 7-0 nylon. Surgical transection of the ACL was achieved via mid-vastus incision and subsequently transecting the ACL with a 27G needle [2]. After confirmation of significant anterior drawer and intact PCL, 27G needles were used to drill tunnels originating at the ACL femoral and tibial footprints through the femur and tibia. The tail tendon bundle was folded over and passed through the tunnels and secured to the upper lateral femoral epicondyle with a stainless-steel washer endobutton. External tibial fixation was achieved by tensioning the graft with the knee in extension and tying the tail tendon bundle to an additional endobutton. *Faxitron drawer test*: Following sacrifice and isolation of hindlimbs, the tibia was fixed to a styrofoam block with 27G needle and then anchored to imaging platform of Faxitron LX-60. A needle was passed through the femur and suture was anchored to the needle then passed over a pulley at the edge of the platform and attached to a 10g weight. The weight was applied in the anterior direction, an x-ray was acquired, then the weight was applied in the posterior direction followed by another x-ray acquisition. X-rays were overlaid and the displacement of the anterior surface of the femur between anterior and posterior images was measured and then normalized to the anterior-posterior width of the tibial plateau. *Instron drawer test*: Following sacrifice, left hindlimbs were isolated and all extraneous soft tissue removed under a dissection microscope. All capsule ligaments, including the cruciates and collaterals, along with the menisci were left intact. The distal half of each tibia was potted in an acrylic tube using PMMA. This construct was then loaded onto a material testing machine. The potted tibial end was fixed in a custom fixture that allowed for adjustment of tibial plateau angle. The distal end of the femur was lowered into another acrylic tube affixed to a custom fixture that could control knee flexion by rotating the femur around the joint center of rotation (Fig. 2). The knee joint was tested for anterior and posterior stability by cyclic loading between ±0.4N for 10 cycles and the 10th cycle was used to quantify stability. *Stats*. Mann-Whitney U tests were conducted ($p<0.017$ for Faxitron test to account for multiple comparison and $p<0.05$ for Instron test)

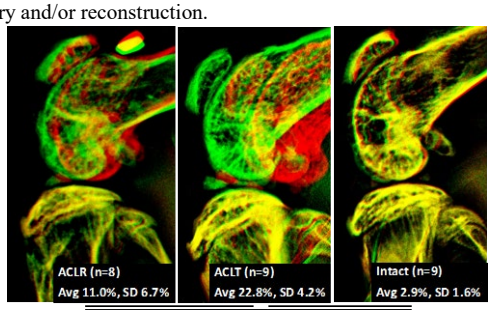

Figure 1: ACLT displays significantly greater anterior-posterior translation compared to ACLR or intact controls via Faxitron method. Bars at bottom indicate $p < 0.017$.

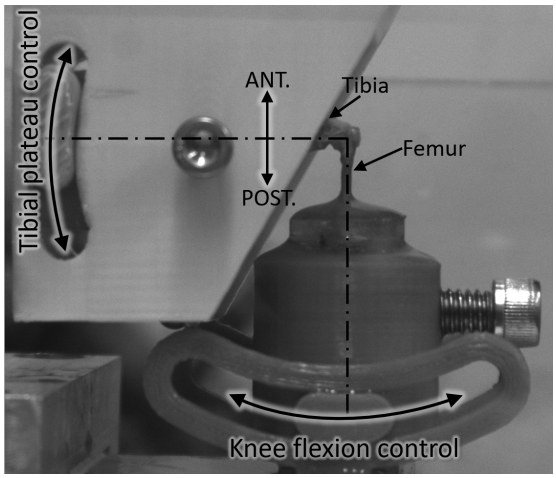

Figure 2: Instron setup to quantify the stability of murine knee. The custom fixtures allow for fine adjustment of knee flexion and orientation of the tibial plateau.

RESULTS: *Faxitron test*: Femurs from the ACLT samples translated a distance that equated to 22.8±6.7% of the tibial plateau width, which was 8X greater than intact controls (2.9±1.6%) (Fig. 1). The ACL reconstruction procedure restored over 50% of the stability lost by ACLT (11.0±6.7%) ($p < 0.05$). *Instron test:* ACLT samples experienced 104.1±63.5% more anterior translation when compared with intact controls ($p<0.05$, Fig. 3).

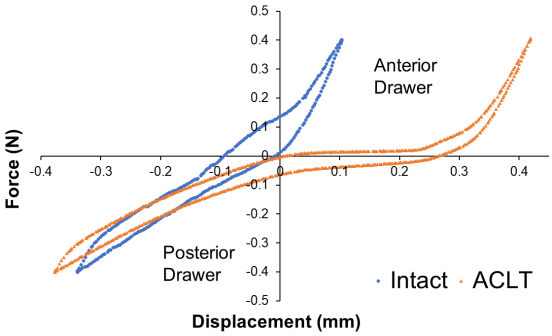

Figure 3: Representative graph depicting the loss of anterior stability after transection of the ACL. Lower left quadrant demonstrates that knee posterior stability remains intact.

DISCUSSION: In order to better understand the genetic/biologic mechanisms that regulate PTOA pathogenesis in these murine models, we need a better understanding of the mechanical stability of the knee joint following these treatments. These two test methods presented here offer researchers practical options to measure the anterior-posterior stability of the murine knee joint within PTOA models. Both methods are sufficient to detect statistical differences in displacement following an applied load. The Instron method requires specialized grips to adjust the tibia and femur correctly, making it more complex. However, viscoelastic properties can be measured with the Instron method unlike the Faxitron method. The observed percent change in displacement fell well within previous reports for anterior drawer tests in ACL-deficient human knees [3, 4].

SIGNIFICANCE/CLINICAL RELEVANCE: As murine PTOA models become more prevalent, it is imperative that the mechanical stability of the joint be assessed in these models, especially surgical models that lead to mechanical instability of the knee. These two test methods provide researchers with new protocols to assess anterior-posterior stability of the knee joint and show that ACLT results in murine knees correlate with previous studies in human knees.

REFERENCES: [1] Blaker CL et al., *J Orthop Res,* 2017 *(*35)424–439 [2] Dyment et al., *Osteoarthritis Cartilage*, 2015 (23)1-11 [3] Furman W. et al., *JBJS* 1976 (58)179-185 [4] Hsieh HH et al., *JBJS* 1976 (58)87-93

ACKNOWLEDGEMENTS: Study supported in part by the Penn Center for Musculoskeletal Disorders (P30 AR069619) and NIH (R00 AR067283).

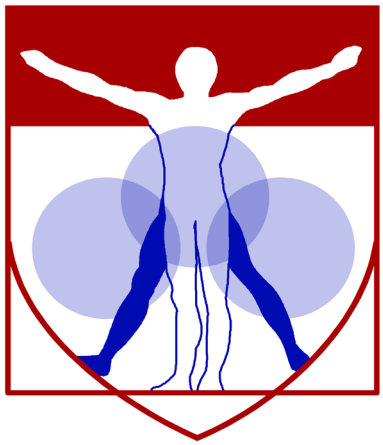

PENN

CENTER for

MUSCULOSKELETAL

DISORDERS

Histology Abstracts

Dynamic Changes in the Porcine Meniscus and Articular Cartilage After Meniscal Injury

Sonia Bansal[1,2], Liane M. Miller[1,2], Jay M. Patel[1,2], Kamiel S. Saleh[1], Brendan D. Stoeckl[1,2], Dawn M. Elliott[3], Michael W. Hast[4], Miltiadis H. Zgonis[1,2], and Robert L. Mauck[1,2]

[1]McKay Orthopedic Research Laboratory, University of Pennsylvania, Philadelphia, PA [2]Translational Musculoskeletal Research Center, CMC VA Medical Center, Philadelphia, PA [3]Multi-Scale Fiber-Reinforced Tissue Biomechanics Laboratory, University of Delaware, Newark, DE [4]Biedermann Laboratory for Orthopaedic Research, University of Pennsylvania, Philadelphia, PA

soniab@seas.upenn.edu

Disclosures: JM Patel (3, *NovoPedics)* RL Mauck (8, *JOR Spine*).

INTRODUCTION: The meniscus is an integral load-bearing tissue in the knee [1] that is commonly injured [2]. The functional role of the meniscus has been widely studied in small animal models in service of understanding controlled joint degradation after meniscus destabilization [3]. These studies focus primarily on the cartilage and joint rather than on the impact of injury on the meniscus itself given the small size of the rodent meniscus. A number of studies suggest, however, that even smaller injuries may have long term deleterious effects on the joint as evidenced by the early onset of OA in humans with small excisions of meniscus tissue to treat tears in the inner zone [4,5]. While post-injury joint degeneration is an established clinical problem, progression of disease in the meniscus itself is not well known. In a previous study, we evaluated the short-term (one month) effects of arthroscopic meniscus injury in a Yucatan minipig model on whole joint, meniscus, and cartilage mechanics, and on meniscus and cartilage histopathology [6]. That study indicated that destabilization of the medial meniscus (DMM) via detachment of the anterior horn led to altered transfer of load across the tibial plateau, decreases in cartilage mechanics, and loss of proteoglycans in both the cartilage and the meniscus. Conversely, a longitudinal vertical defect, which maintains meniscus-mediated load transfer in the knee, resulted in few changes in any of these quantitative outcomes. Here we evaluated the longer term (three month) outcomes of these meniscus injuries in order to determine the progression of macro- and meso-scale changes of the meniscus and joint.

METHODS: Juvenile (6 month old) Yucatan minipigs underwent bilateral arthroscopic surgery and each limb received one of the following injuries to the medial meniscus: sham, DMM, or a vertical longitudinal tear (1/5 arc length, red-white zone) (n=6/group/time point). Animals were euthanized at one or three months, and joints were harvested for a series of macro- and meso-scale analyses. In macro-scale tests, intact joints were compressed to 1x body weight (400 N) at a flexion angle of 45° using a custom rig and universal test frame. Thin film pressure sensors (TekScan #6900-110) were inserted into the joint to measure load transfer through the medial compartment [7]. Next, joints were assessed for macroscopic changes to the meniscus and for cartilage wear (using India ink) [8]. Subsequently, medial menisci were harvested and sectioned (16 micron thickness, vertical plane, anterior and posterior horns) for histological analysis of proteoglycan (PG) content (Safranin O/Fast Green). Osteochondral segments from the medial tibial plateau were isolated and indented using a spherical indenter (2 mm diameter) to determine cartilage mechanical properties in the regions covered by the meniscus and cartilage [9]. Next, microCT analysis of the subchondral bone was performed. These samples were then decalcified, embedded, sectioned, and stained for proteoglycans (Safranin O/Fast Green) [10]. Sections were graded using the OARSI scoring method [8] by five blinded observers (scale: 0-25, best to worst).

RESULTS: Joints with sham-operated menisci showed no macroscopic indications of degeneration at any time point. Conversely, DMM-treated joints showed signs of wear at both one and three months. Vertical tears were visible in the meniscus at both one and three months but did not result in marked degeneration of cartilage surfaces (not shown). When joint-level mechanics were assessed, DMM-treated joints had an increase in peak contact pressure and decreased contact area on the tibial plateau at one month. This effect did not persist to three months **(Fig. 1A,B)**. While there were minimal changes to subchondral bone (not shown), cartilage indentation modulus in the cartilage-meniscus contact region decreased in DMM operated joints at one month and continued through three months. Interestingly, joints in which menisci were subjected to a vertical tear had no change in cartilage mechanics at 1 month, but a decrease in indentation modulus at 3 months **(Fig. 2A)**. OARSI scoring significantly increased, indicating osteoarthritic changes, in DMM joints at one month. This effect was somewhat attenuated, but remained significantly elevated, at three months **(Fig. 2B)**. Vertical tears did not result in a change in OARSI scoring at either time point. Finally, DMM-treated menisci had less intense staining for PGs compared to shams at one month, and this was sustained through three months. Menisci subjected to a vertical tear had a trending decreases compared to sham at three months **(Fig. 3A,B)**.

DISCUSSION: This study investigated meniscal and joint remodeling in a minimally invasive (arthroscopic) large animal surgical model of meniscus injury. Interestingly, we found that load transfer through the meniscus was significantly altered at 1 month post-DMM, but that this had returned to sham levels by 3 months. This was potentially due to a wide, fibrovascular scar tissue noted at the site of detachment, which had developed at 1 month and matured by 3 months to restore load transmission. Despite this normalization of load transfer, the effects of DMM-injury and early unloading caused a sustained decrease in cartilage mechanics in the tibial cartilage. The persistent reduction in cartilage modulus is consistent with previous reports using both small [3] and large animal [12,13] models of meniscal release. While some measures were persistently altered after DMM, other measures appeared to return towards sham levels. For example, PG content in the anterior horn of the meniscus and OARSI scores were less distinct from sham at the 3 month time point compared to the 1 month time point. This may indicate a dynamic remodeling process, wherein the healing of the severed meniscal attachment in the DMM group restored load transfer and slowed the rate of joint degeneration. Future work will extend the study duration to detail the temporal progression of post-injury joint and tissue remodeling in these animals, as well as explore the age dependence of this process.

SIGNIFICANCE/CLINICAL RELEVANCE: Understanding the progression of joint disease after meniscal injury will improve repair strategies and inform surgical decision making.

REFERENCES:

[1] Makris+ 2011 [2] Mordecai+ 2014 [3] Glasson+ 2007 [4] Roos+ 1995 [5] Lohmander+ 2007 [6] Bansal+ 2019 [7] Bedi+ 2010 [8] Little+ 2010 [9] Meloni+ 2017 [10] Sennett+ 2018 [11] Doyran+ 2017 [12] Waller+ 2017 [13] Kuroki+ 2011

ACKNOWLEDGEMENTS: This work was supported by the NIH and the Department of Veterans Affairs.

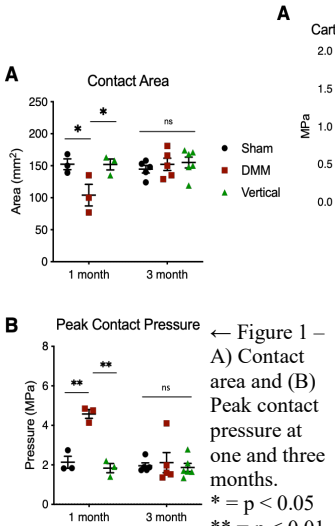

← Figure 1 – A) Contact area and (B) Peak contact pressure at one and three months. * = p < 0.05

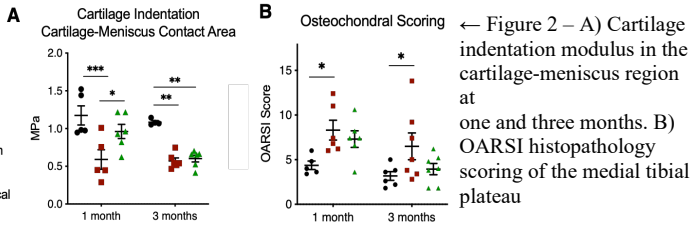

← Figure 2 – A) Cartilage indentation modulus in the cartilage-meniscus region at one and three months. B) OARSI histopathology scoring of the medial tibial plateau

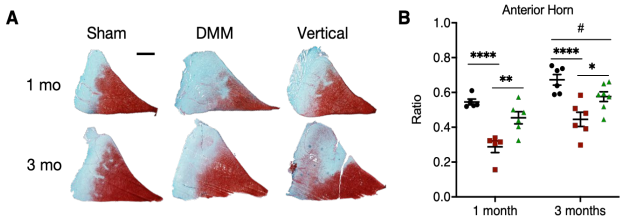

↑ Figure 3 – A) Representative Safranin-O/Fast Green histology of the anterior horn of the medial meniscus. Scale bar = 2 mm. B) Proteoglycan staining area in the anterior horn # = p < 0.1, * = p < 0.05, ** = p < 0.01,

F4/80 Tendon Resident Macrophages and Potential Cross-Talk with Tendon Fibroblasts During Growth

Catherine A. Bautista[1], Xi Jiang[1], Kyu Sang Joeng[1], Nathaniel A. Dyment[1]

[1]University of Pennsylvania, Philadelphia, PA

cbaut@seas.upenn.edu

Disclosures: Catherine A. Bautista (N), Xi Jiang (N), Kyu Sang Joeng (N), Nathaniel A. Dyment (N)

INTRODUCTION: Tendon cells oriented in linear arrays within tendon fascicles are known as tenocytes (i.e., internal tendon fibroblasts). Tenocytes are thought to be a relatively homogenous population and the majority of these cells express collagen via measurements in our Col1a1(3.6kb)CFP (Col1CFP) reporter mice. However, there is a Col1CFP(-) cell population that we previously demonstrated to have intracellular signal of the MMP-cleavable probe MMPSense [1], suggesting that this cell population could be a subset within the tenogenic lineage or could be outside the tenogenic lineage (i.e., myeloid). Therefore, the objective of this study was to determine the origin, distribution, and expression profile of these cells within tendons during postnatal growth.

METHODS: All procedures were approved by UPenn's IACUC. Transgenic mice. Two transgenic mouse lines were used in this study: i) Col1a1(3.6kb)CFP mice containing 3.6kb of the Col1a1 promoter driving CFP expression [2] and ii) ScxCre and Ai9 R26R-tdTomato (ScxCre;Ai9) double transgenic mice [3]. Experimental design. Tail tendons (TTs) were isolated from ScxCre;Ai9 and Col1CFP mice for explant culture. Knees from Col1CFP mice at P4, P28, and P56 mice were used for patellar tendon (PT) immunofluorescence (n=3/time point). TTs and femurs from P28 mice were used for cell sorting and gene expression analysis (2 mice per biological sample; n=3). TT explant culture and F4/80 immunolabeling. TTs were cultured in individual channels of 6-channel slides (Ibidi µ-Slide VI) with 200 nM MMPSense 645 FAST MMP-activated fluorescent dye for 2 days (n=5 TTs). On Day 2, TTs were stained with rat anti-F4/80 primary and Alexa Fluor 555 secondary antibodies. Immunofluorescence. Knees were fixed, embedded, sectioned, stained with rat anti-F4/80 primary and AF647 secondary antibodies, stained with Hoechst, and imaged. Image quantification. CFP intensities were recorded for each cell in the tendon and the percentage of positive cells were computed. F4/80-labeled cells were counted manually in Fiji. Cell isolation and gene expression analysis. TTs were serially digested to discard surface cells and obtain internal cells. Bone marrow cells were obtained from each femur. Isolated cells were labeled with anti-F4/80 microbeads and magnetically sorted to obtain F4/80-enriched and F4/80-depleted populations. RNA was isolated from the sorted populations using TRIzol and converted to cDNA. cDNA was analyzed using qPCR with TaqMan Gene Expression Assays for *18S*, *Col1a1, Mmp2, Mmp13, Mmp14, Adgre1, Csf1,* and *Csf1r.* Statistics. Cell number quantification and qPCR results were compared via Kruskal-Wallis followed by Mann Whitney U tests adjusted for multiple comparisons ($p < 0.017$).

RESULTS: MMPSense(+) cells within tendons were not derived from a tenogenic lineage. Since we previously found that a subpopulation of cells within tendon fascicles displayed intracellular MMPSense signal but did not express Col1CFP, we aimed to determine whether these cells were derived from a tenogenic lineage. We delivered MMPSense to ScxCre;Ai9 TTs and found that none of the MMPSense(+) cells (Fig. 1A; yellow arrowheads) were tdTomato(+). MMPSense(+) cells were F4/80(+) resident macrophages. Since MMPSense(+) cells were not within the tenogenic lineage, we next asked whether they were macrophages. In fact, F4/80 immunolabeling (Fig. 1B; magenta) showed positive staining for MMPSense(+) cells (yellow arrowheads). Percentage of F4/80(+) cells increased with age. We next measured the distribution of resident tendon macrophages during postnatal growth. F4/80 immunofluorescence revealed a significant increase in F4/80(+) cells (Fig. 2) in PTs from P4 to P28 and P56 (3.6±0.6, 7.5±1.0, and 8.7±2.4%). Conversely, there was a decrease in the percentage of Col1CFP cells in the same mice (92.0±2.9, 82.1±8.8, and 76.9±7.7%). F4/80-depleted tendon cell population expressed elevated levels of *Mmp2* and *Mmp14.* Since the macrophages were MMPSense(+), we next measured expression of a number of MMPs expressed within tendon. F4/80-depleted tendon cells ("TT F4/80-") expressed 4.7-fold and 7.1-fold higher levels of *Mmp2* and *Mmp14,* respectively, compared to F4/80-enriched tendon cells ("TT F4/80+") (Fig. 3). Conversely, F4/80-enriched tendon cells expressed 3.3-fold higher levels of *Mmp13* compared to F4/80-depleted tendon cells. F4/80-depleted cell population expressed elevated levels of *Csf1* whereas F4/80-enriched population expressed higher levels of *Csf1r.* There is known Csf1-mediated crosstalk between fibroblasts and macrophages. Therefore, we measured the levels of *Csf1* and *Csf1r* expression in these tendon cell populations. There was 6.0x greater *Csf1* expression in F4/80-depleted tendon cells compared to F4/80-enriched tendon cells. *Csf1r* expression was 66.6x greater in the F4/80-enriched tendon cell population compared to the depleted population.

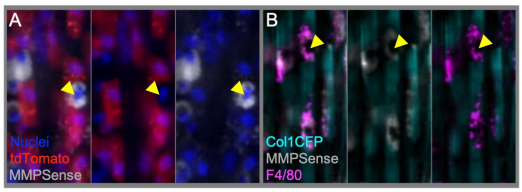

Fig 1. MMPSense-treated ScxCre;Ai9 (A) and Col1CFP (B) tendons.

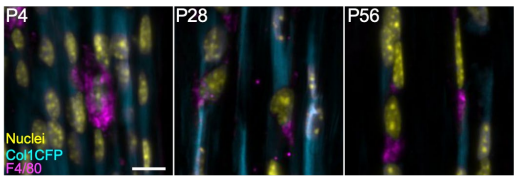

Fig 2. F4/80 immunofluorescence in Col1CFP tendons (scale=10µm).

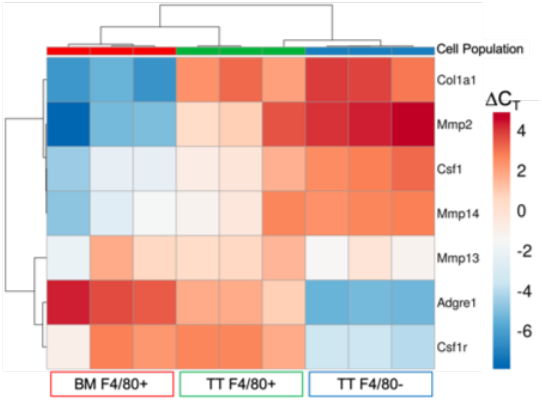

Fig 3. Gene expression of sorted cells.

DISCUSSION: To better understand tendon pathologies and to develop therapeutics, we must improve our understanding of the cell populations within tendon, the markers that define stages of the lineage, and the pathways that regulate differentiation and subsequent function. We demonstrated in this study that there is a population of F4/80(+) resident macrophages juxtaposed with Col1CFP(+) fibroblasts in linear arrays in the tendon fascicle. This macrophage population is also MMPSense(+) unlike the Col1CFP(+) fibroblasts, suggesting differential roles during postnatal growth. The role of these cells in postnatal growth is still unknown but could be related to immunomodulation, tissue homeostasis, - and/or extracellular matrix assembly – all of which we will study in the future. The fact that these macrophages are juxtaposed with Col1CFP(+) cells suggests that there is crosstalk between these cell populations. Fibroblasts in other tissues are known to express CSF1 that acts on macrophages through the CSF1 receptor [4]. Our results suggest that this crosstalk may be true in tendon as well. How this crosstalk affects the overall function of these cells during tendon growth is the aim of our future studies.

SIGNIFICANCE/CLINICAL RELEVANCE: An improved understanding of the cellular markers and signaling pathways that define and regulate the tendon lineage will be crucial to developing new therapies to attenuate the progression of pathologies and improve repair outcomes following injury. This study gives new insight into potential roles of tendon resident macrophages during tendon growth and their interaction with Col1-expressing tendon fibroblasts.

REFERENCES: 1) Bautista C, et al., ORS, 2019; 2) Kalajzic I, et al., JBMR, 2001; 3) Blitz E, et al., Dev Cell, 2009; 4) Ireland L, Front Cell Dev Biol, 2018.

ACKNOWLEDGEMENTS: Work supported by NIH grants R00 AR067283, P30 AR069619, UPenn URF Research Grant, and UPenn startup funds.

Gnas inactivation alters adipose tissue properties during progression to heterotopic ossification

Niambi Brewer, John T Fong, Deyu Zhang, Frederick S Kaplan, Robert J Pignolo, Eileen M Shore

Heterotopic ossification (HO) is a common physiological response to severe tissue trauma such as combat blast injuries, high impact trauma, and hip replacements. The investigation of rare genetic disorders provides insight into the aberrant mechanisms that cause HO formation and leads to identification of targets for pharmacological intervention in both genetic and non-genetic forms of HO. HO in the rare genetic disorder, Progressive Osseous Heteroplasia (POH), initiates in subcutaneous soft tissues then progresses into deeper connective tissues. POH is caused by inactivation of *GNAS*, a gene that encodes the alpha stimulatory subunit of G proteins (Gsα). Our previous work demonstrated that adipose derived stromal cells (ASCs) from *Gnas*$^{p\text{-}KO}$ mice exhibit enhanced osteogenic and impaired adipogenic potential *in vitro*, supporting that osteogenesis and heterotopic bone in POH occurs at the expense of adipogenesis, however, the pathophysiology of POH remains poorly understood. To examine the mechanisms and signals that lead to initiation of heterotopic bone caused by *GNAS* inactivation in osteogenic progenitor cells, we developed an *in vivo* HO model using *Gnas*-null mice (*Gnas*$^{fl/fl}$*;Cre-ER*^{T2} or *Gnas*$^{fl/fl}$*;Ai9*$^{fl/fl}$*;Cre-ER*^{T2}) that consistently and reliably induces spontaneous HO. Through microCT, histologic, and immunohistochemistry analyses in cross-sectional and longitudinal studies, this model initiates HO within subcutaneous adipose tissues with progressive expansion over time. Using the same model and methods, we investigated the tissue changes that precede HO formation and identified increased extracellular matrix content, as well as a shift from white to beige adipose tissue, including UCP1 expression and decreased adipocyte size and lipid content. Cell implant studies showed that fluorescent-labeled Gnas-null ASCs implanted into a Gnas-null host form significantly more HO than Gnas-null hosts without implant. However, wildtype (WT) ASCs also induce HO in a Gnas-null background, although less robustly than mutant ASCs, suggesting that the tissue microenvironment strongly influences cell fate. Further, neither WT nor Gnas-null ASCs implanted into a control background formed HO, supporting that the mutant osteogenic progenitor cells are insufficient to induce HO. These data highlight the importance of the microenvironment within the adipose tissue in supporting ectopic bone formation by Gnas inactivation and provide insights into the pathophysiology of POH and other *GNAS*-related disorders.

Investigating the effects of Hedgehog antagonist, LDE225, on osteochondroma formation and growth plate function

Juliet Chung, Eiki Koyama, Maurizio Pacifici and Christina Mundy
Translational Research Program in Pediatric Orthopaedics, Division of Orthopaedic Surgery, The Children's Hospital of Philadelphia, Philadelphia, Pennsylvania

Hereditary Multiple Exostoses (HME) is a pediatric skeletal disorder characterized by benign cartilaginous tumors called exostoses or osteochondromas (OC). They form along the perichondrial border of growth plates in several skeletal elements. The majority of cases are caused by loss of function mutations in the heparan sulfate (HS)-synthesizing enzymes EXT1 or EXT2, resulting in systemic HS deficiency. The HS chains are components of cell surface and extracellular matrix-associated proteoglycans (HSPGs). HSPGs interact with numerous HS-binding proteins, such as hedgehog (Hh) proteins and regulate protein distribution, bioavailability and target of action. Our lab and others have shown that Hh signaling plays a prominent role in early skeletal development and maintains growth plate function. In the case of HME, a deficiency in HS in growth plates allows for broader distribution and distribution of Indian hedgehog that could diffuse into the perichondrium, activate signaling in chondroprogenitor cells, and result in OC formation. Given the findings from these studies, we asked whether the clinically relevant Hh antagonist, LDE225, could 1) reduce OC formation in vivo and/or 2) interfere with normal growth plate maintenance. LDE225 (40 mg/kg) effectively reduced OC formation in long bones, rib cartilage, and cranial base in our conditional *Ext1*-mutant mice compared to control littermates. A major concern with using a Hedgehog antagonist in the pediatric population is growth plate closure. Thus, we sectioned and carried out histological staining on vehicle and LDE225-treated long bones. After histological examination, it was observed that LDE225 did indeed close the growth plate of the long bones. We then tested a range of doses (0, 2 and 10 mg/kg) on wildtype mice. Long bones and ribs were processed for histology to examine the effects of LDE225 on the growth plate. The growth pates were closed in mice treated with 10 mg/kg LDE225, but the growth plates remained open in mice treated with 2 mg/kg. Ongoing studies include testing LDE225 at 2mg/kg on our HME mouse model to determine whether this dose is sufficient to reduce or prevent OC formation.

YAP and TAZ coordinate endochondral bone development

Joseph M Collins[1], Nathaniel A. Dyment[1], and Joel D. Boerckel[1]
[1]Departments of Orthopaedic Surgery and Bioengineering, University of Pennsylvania, Philadelphia, PA.

Disclosures: Joseph M Collins (N), Nathaniel A. Dyment (N), Joel D. Boerckel (N)

Introduction: In development, bone formation occurs through two distinct modes: intramembranous and endochondral ossification. Intramembranous ossification involves the direct osteogenic differentiation of local progenitors. In contrast, endochondral ossification initiates from a cartilage anlage, which is replaced by bone through chondrocyte hypertrophy, co-mobilization of osteoprogenitors and blood vessels, and matrix remodeling, culminating in bone formation. The molecular mechanisms which differentially contribute to intramembranous vs. endochondral ossification during embryonic development are poorly understood. We recently reported that YAP and TAZ combinatorially promote skeletal development in vivo[1] with homozygous deletion of both genes causing perinatal lethality. At the 2019 ORS meeting, we reported that YAP and TAZ play key roles in limb development *in utero*. Deletion of YAP and TAZ from Osterix1-expressing cells delayed and impaired development of the primary ossification center (POC), where bone formation occurs through endochondral ossification, but only moderately affected the bone collar, where bone formation occurs through intramembranous ossification[2]. Here, we sought to determine the underlying cellular mechanisms.

Materials and Methods: We conditionally deleted YAP and TAZ from Osx1-expressing cells ($YAP^{fl/fl}$;$TAZ^{fl/fl}$;Osx1-GFP::Cre, hereafter KO^{osx}) and evaluated embryonic humeral bone development in comparison to littermate wild type ($YAP^{fl/fl}$;$TAZ^{fl/fl}$, hereafter WT) and Osx1-GFP::Cre wild type ($YAP^{WT/WT}$; $TAZ^{WT/WT}$;Osx1-GFP::Cre, hereafter WT^{osx}) controls.[1,2,3] Embryos were harvested at 15.5 days (E15.5) and 17.5 days (E17.5) post-conception. Embryonic forelimbs were processed by cryohistology. Protein and GFP fluorophore localization were performed by immunofluorescent staining and quantified in ImageJ using defined regions of interest. Comparisons were made using Student's t-test. A p-value less than 0.05 was considered significant. Each embryo was considered an independent sample. All procedures were performed with IACUC approval.

Results: Previously, we found that Osx-conditional YAP/TAZ deletion significantly reduced the cell density of the POC, but only modestly reduced cell density in the bone collar. To determine whether YAP/TAZ deletion specifically altered the mobilization of the targeted osteoprogenitors, we evaluated Osx1-GFP-labeled cells in both WT^{osx} and KO^{osx} mice. YAP/TAZ deletion reduced GFP^+ osteoprogenitors in the POC but only moderately reduced the GFP^+ cell density in the bone collar (Fig. 1, green). Next, to determine the effects of YAP/TAZ deletion on osteogenesis in these regions of interest, we evaluated alkaline phosphatase (ALP) activity and mineralized matrix deposition. YAP/TAZ deletion significantly reduced ALP activity in the POC, but did not alter ALP activity or mineralization in the bone collar (Fig. 2).

In addition to osteoblast-lineage cells, Osx1-GFP::Cre is also expressed in hypertrophic chondrocytes. Therefore, we next evaluated chondrocyte hypertrophy and cartilage matrix remodeling in WT and cKO mice at E17.5 (Fig. 3A,B). Using WT mice, we identified three distinct subzones of the hypertrophic cartilage, based on morphology and Collagen-10 immunolocalization, which we term the hypertrophic initiation, maturation, and remodeling zones. YAP/TAZ deletion had no effect on hypertrophic initiation, but significantly lengthened the hypertrophic maturation zone. Most notably, YAP/TAZ deletion caused hypertophic chondrocyte persistence and failure to resorb, leading to an extended, cone-shaped hypertrophic remodeling zone, characterized by Collagen 10-rich extracellular matrix and high intracellular immunolocalization of the vascular permeability factor, VEGF-A.

It was recently reported that invading neovascular capillaries are primarily responsible for hypertrophic matrix resorption.[4] Therefore, we next immunostained for the endothelial cell marker, endomucin, and found that YAP/TAZ deletion from $Osx1^+$ cells disorganized and reduced the number of cartilage-resorbing capillaries, which localized only near the outer base of the cone-shaped hypertrophic remodeling zone (Fig. 3C,D). Consistent with excess VEGF-A expression by the hypertrophic chondrocytes, the vasculature within the POC was also disorganized and leaky, as evidenced by extravascular red blood cell accumulation. Finally, vessels that did successfully migrate into the POC of the KO^{osx} limbs were substantially less associated with GFP^+ osteoprogenitors (Fig. 1B).

Discussion:
Together, these data suggest that YAP and TAZ in Osx1-expressing cells are critical for endochondral primary bone formation, but are dispensable for intramembranous ossification in the bone collar, raising questions about the physiological roles of YAP and TAZ in osteogenic differentiation, per se. These data further identify crucial roles of YAP and TAZ in cartilage maturation, hypertrophic matrix remodeling by cartilage-resorbing capillaries, neovascular integrity, and osteoprogenitor mobilization. YAP/TAZ-dependent osteoprogenitor mobilization may occur by cell non-autonomous recruitment and/or cell-autonomous migration and/or proliferation. Collectively, these data underscore the importance of endothelial-chondrocyte and endothelial-osteoprogenitor cell crosstalk during limb morphogenesis.

References
1. Kegelman+ FASEB J 2018. Collins+ ORS 2019. 3. Rodda+ Development 2006. 4. Romeo+ Nature Cell Biology 2019.

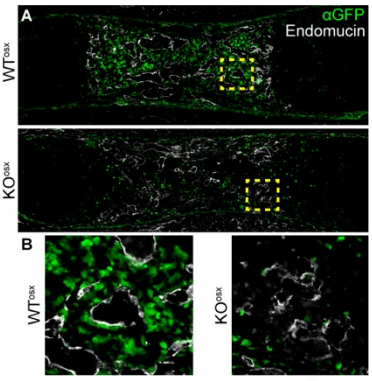

Figure 1. E17.5 Humeri immunostained for Endomucin and GFP

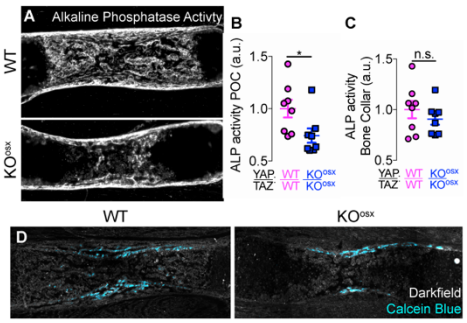

Figure 2. **(A)** Representative E17.5 WT and KOosx humeri stained for Alkaline Phosphatase Activity (ALP). **(B,C)** Region of interest quantification of E17.5 ALP activity. **(D)** Representative E17.5 WT and KOosx humeri stained for Calcein blue.

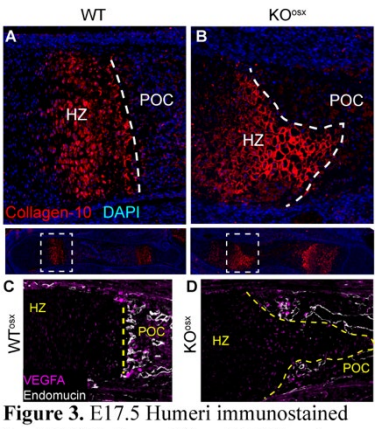

Figure 3. E17.5 Humeri immunostained for **(A,B)** Collagen-10 and DAPI and **(C,D)** VEGFA and Endomucin.

Primary Cilia Drive Postnatal Articular Cartilage Morphogenesis Through Proteoglycan Production and Chondrocyte Organization in Mouse Limbs

Kimberly Helbig[1], Danielle Rux[1], Biao Han[2], Minwook Kim[1], Lin Han[2], Eiki Koyama[1], Maurizio Pacifici[1]
[1]Children's Hospital of Philadelphia, Philadelphia, PA [2]Drexel University, Philadelphia, PA

Disclosures: None

INTRODUCTION: Synovial joints are essential for skeletal function and body movement. Unfortunately, articular cartilage (AC) is highly susceptible to degeneration due to disease/injury and exhibits poor repair capacity that current clinical strategies fall short of amending. To improve these strategies, more information is needed on mechanisms of AC development and, specifically, how it acquires its functional, zonal organization during postnatal development to include: lubricant-producing surface zone cells; round, column-aligned, and load-resistant intermediate zone cells; and mineralized, deep zone cells that attach to subchondral bone. Recent work from our lab tackled this central issue using mouse models. Histologic analyses revealed distinct phases of development and growth. At birth, AC consists of randomly distributed cells in a thin and matrix-poor tissue that rapidly thickens by 3 weeks of age. However, AC doesn't acquire its multi-zonal and columnar organization until 8 weeks of age. Genetic lineage tracing showed that while cell proliferation plays a minimal role, cell translocation represents a major driver of tissue morphogenesis [1]. In this study, we asked whether and how primary cilia regulate AC morphogenesis. These mechanical- and morphogen-transducing cell surface organelles are crucial to mammalian development and, importantly, previous studies show their involvement in growth plate chondrocytes and also in osteoarthritis [2-4]. However, their specific roles in postnatal AC morphogenesis have remained unclear, mainly due to the fact that conditional loss-of-function approaches also led to growth plate defects. To circumvent this issue, we employed a joint-specific approach using *Gdf5Cre*.

The objectives of this work were: 1) to establish that primary cilia function specifically in synovial joint development and clarify mechanism(s) by which they function in the joint, and 2) to provide detailed insight into the morphogenesis of articular cartilage during postnatal stages of growth.

METHODS: Conditional loss of primary cilia function in joint cells was accomplished by crossing *IFT88-flox* mice to *Gdf5Cre*. Animals were collected for histology throughout postnatal development (birth, 3wks, 8wks, 6mo: N>5/group) and sectioned in a sagittal orientation to visualize AC zone formation. AFM-based nano-indentation was performed on freshly dissected cartilage in 1XPBS using a spherical AFM probe (R ~ 12.5um, nominal k = 5.4 N/m) [5]. Data was collected from tibial plateau and femoral condyle at 8 weeks; a student's T-test was used with significance of $p<0.05$. To address potential mechanisms, control and mutant animals were crossed to a *Gli1-LacZ/+* reporter line, a live readout of hedgehog signaling. LacZ reporter expression was revealed by whole mount β-galactosidase staining of disarticulated mouse knees. All animal procedures were approved by the CHOP institutional animal care and use committee.

RESULTS: Our approach for primary cilia ablation was specific and efficient. Staining for acetylated tubulin to visualize primary cilia confirmed their presence in control AC, but not in mutant AC (**Fig 1A**). Importantly, primary cilia formation (and function) was unaffected in mutant growth plates (**Fig 1B**). Overall, we found that up to 3 weeks, mutant AC was largely comparable to controls with minor histologic changes (**Fig 2A**). However, mature mutant tissue (> 6 weeks of age) exhibited a drastic drop in proteoglycan content, and lacked columnar organization (**Fig 2B**). This was accompanied by a severe disruption in aggrecan deposition and organization (**Fig 2C**). Consequently, mechanical testing revealed a significant reduction in indentation modulus of AC in mutant animals (**Fig 3A**). Lastly, whole mount imaging of a *Gli1-LacZ/+* reporter revealed drastic and regional changes in mutant animals (**Fig 3B**) consistent with disruption of hedgehog signaling.

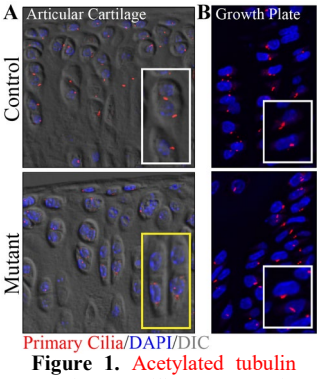

Figure 1. Acetylated tubulin staining. **A)** Cilia are present in control AC, but not mutant. **B)** Cilia are present in growth plates of controls and mutants.

DISCUSSION: Taken together, our data affirm that primary cilia function is required for synovial joint morphogenesis. Current data specifically suggest that these organelles are critical for proteoglycan production and chondrocyte organization during the late juvenile-adult stages of AC morphogenesis and require the function of hedgehog signaling. Two of our especially intriguing results will require further exploration: 1) the mutant phenotype progresses rapidly following normal ambulation during mouse development around 3 weeks of age suggesting that this mouse model may prove useful for understanding the function of mechanical loading for chondrocyte organization, and 2) whole mount imaging of *Gli1-LacZ/+* reporter expression suggests divergent functions of articular chondrocytes based on location in the tibial plateau and that primary cilia modulate these functions.

SIGNIFICANCE/CLINICAL RELEVANCE: Articular cartilage owes its biomechanical strength and resilience to its structure developed during postnatal skeletal growth, but little is known about this critical morphogenetic process. Work described here reveals novel information that will prove useful to design more effective medical intervention strategies for congenital and acquired joint disease/injury.

REFERENCES: [1] Decker, et al. 2017. [2] Song, et al. 2007. [3] Yuan, et al. 2016. [4] Chang, et al. 2012. [5] Doyran, et al. 2017.

ACKNOWLEDGEMENTS: We acknowledge support and advice from Drs. Rosa Serra (UAB) and Robert Mauck (UPenn). Research is supported by NIH R01-AR062908 (Maurizio Pacifici), F32-AR074227 (Danielle Rux) and P30-AR069619 (UPenn Center for Musculoskeletal Disorders core labs).

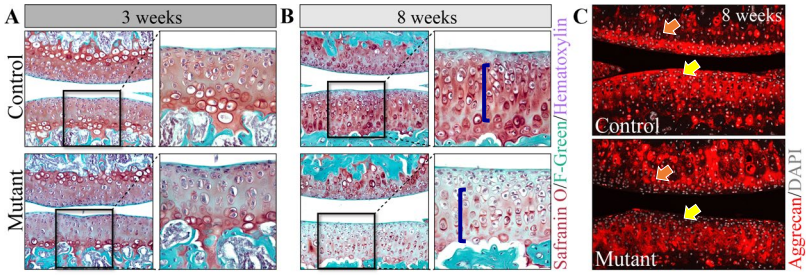

Figure 2. (A-B) Safranin O-stained sections show proteoglycan and chondrocyte organization. Mutants display slight reduction of proteoglycan at 3 weeks but organization consistent with controls **(A)**. At 8 weeks, mutants exhibit a drastic reduction of proteoglycan accompanied by disorganization of chondrocytes in the deepest layers ( ) **(B)**. **(C)** Mutants also display reduced ( ) and disorganized ( ) Aggrecan at 8 weeks.

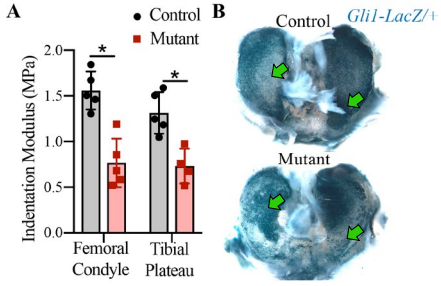

Figure 3. (A) AFM-based testing reveals reduced mechanical properties of mutant AC at 8 weeks. **(B)** Wholemount *Gli1-LacZ* in tibial plateau AC shows regional misregulation ( ) in mutants at 8 weeks.

Collagen and Prg4 Fluorescent Reporter Mice Establish Unique Subsets of Tendon Fibroblasts

Xi Jiang[1], Catherine Bautista[1], Anjana Srikumar[1], Andrew Hendrix[2], Courtney Thompson[3], Alexander Kuang[1], Andrew Kim[1], Nathaniel A Dyment[1]
[1]University of Pennsylvania, Philadelphia, PA; [2]University of Toledo, Toledo, OH; [3]Univeristy of Notre Dame, South Bend, IN
Email of Presenting Author: dyment@pennmedicine.upenn.edu

Disclosures: None.

INTRODUCTION: Markers that define stages of the tendon cell lineage are needed to better understand tenogenic differentiation and devise improved therapies to treat injury/disease. We previously reported heterogeneity within the internal tendon fibroblast population residing within tendon fascicles using Col1a1(3.6kb), Col1a1(2.3kb), and Col6a1 reporter mice [1-2]. Therefore, the objectives of the current study are to quantify the number and measure endogenous gene expression profiles of reporter-positive cells within multiple tendons and ligaments during early postnatal growth to define this heterogeneity.

METHODS: Transgenic Mice. All animal procedures were approved by UPenn's IACUC. Five transgenic mouse lines were used in this study: 1) **ScxGFP** – promoter of the tendon marker scleraxis driving GFP, 2) **Col3.6CFP** - Col1a1(3.6kb)-CFP mice contain 3.6kb of the Col1a1 promoter driving CFP [3], 3) **Col2.3GFP** - Col1a1(2.3kb)-GFP mice contain 2.3kb of the Col1a1 promoter driving GFP expression [3], 4) **Col6GFP** – BAC containing Col6a1 promoter driving GFP expression, and 5) **Prg4Cre;tdTom** – Prg4CreERT2 inducible Cre and R26R-tdTomato double transgenic mice. Experimental Design. Limbs were isolated from P4, P14, and P28 mice (tamoxifen given to Prg4Cre;tdTom mice 3 days before) for cryohistological analysis in all lines (70 mice) and for laser capture microdissection (LCM) and qPCR in just the Col2.3GFP line (12 mice). The patellar tendon (**PT**), cruciate ligaments (**ACL-PCL**), Achilles tendon (**AT**), and supraspinatus tendon (**ST**) were analyzed for histology (n=4-6/group). For LCM, **Col2.3+** cells were isolated from the tendons/ligaments and compared with the midsubstance region from the same tissues (n=4/group). Cryohistology. Limbs were fixed, embedded, stained with DAPI, and imaged. Laser capture microscopy (LCM). Limbs were fixed, embedded, and sectioned. Slides were dehydrated and GFP+ cells or midsubstances of tissues were isolated using the ArcturusXT. Microfluidic qPCR Array. RNA was extracted from LCM samples and preamplified for 93 targets and 3 housekeeping genes. qPCR reactions for 96 samples and 96 genes were run on Fluidigm's 96.96 Dynamic Array IFC yielding 9,216 individual Ct reactions. Image Quantification. The GFP intensity was recorded for each cell within the tendon/ligament midsubstance. An equivalent minimum threshold was applied and the percentage of positive cells was computed. Statistics. One-way ANOVAs with either tissue type or age as fixed factors were used to analyze the number of reporter cells in the histological sections and LCM qPCR results. Principal component analysis and hierarchical clustering were used to summarize the qPCR data.

RESULTS: Age and tissue dependence of fluorescent reporters. Both age and type of tendon/ligament had an effect on reporter expression in all 5 lines (Fig. 1; $p < 0.05$). Col3.6CFP correlated strongly with ScxGFP and therefore only Col3.6CFP is reported in this abstract. The Achilles tendon demonstrated regional variation (example image from Col2.3GFP mice shown in Fig. 2) where the calcaneal region of the midsubstance (AT-Cal) was different than the rest of the midsubstance (AT-Mid). Therefore, these regions were analyzed separately. The AT-Cal correlated with the ACL-PCL while the AT-Mid correlated with the PT. The ST correlated more with the AT-Cal and ACL-PCL than AT-Mid and PT. Col3.6CFP mice were expressed by the highest number of cells overall with Col6GFP being highly expressed in the ACL-PCL, AT-Cal, and ST. The collagen reporters mostly decreased or maintained expression with age, with the AT-Cal and ACL-PCL displaying dramatic decreases from P14 to P28 in the ScxGFP, Col3.6CFP, and Col2.3GFP lines (Fig. 1). Conversely, the Prg4Cre;tdTom line increased expression with age and displayed stronger expression in the ACL-PCL, ST, and AT-Cal. Col2.3GFP+ cells display unique expression profile compared with tendon midsubstance. Principal component analysis of Col2.3GFP+ cells vs. tendon/ligament midsubstance in the ACL-PCL, AT-Cal, AT-Mid, PT, and ST at P4, P14, and P28 revealed that age had the greatest effect on overall variance followed by GFP vs. midsubstance then structure (i.e., type of tendon/ligament). Hierarchical clustering (correlation distance and average linkage) revealed that P4 samples were within their own cluster while P14 and P28 were intermixed (Fig. 3). Within the P14 and P28 ages, a cluster of Col2.3GFP+ cells emerged (highlighted in Fig. 3). Col2.3GFP+ cells expressed higher levels of GFP, Gmnn, Mmp13, and Tgfb1 at multiple ages ($p < 0.05$). Col2.3GFP+ cells also expressed higher levels of all measured MMPs (Mmp2, 13, 14, 16) at P28 ($p < 0.05$). In terms of age, several genes increased tremendously (> 4 fold, $p < 0.05$) with age: Dcn, Fn1, Gja1, and Prg4. Endogenous Prg4 expression correlated with the number of Prg4Cre;tdTom+ cells. Finally, Postn and Mmp14 significantly decreased with age ($p < 0.05$).

DISCUSSION: In order to better understand tendon pathologies and to develop improved repair strategies, we must first improve our understanding of the tendon lineage, including markers that define cells at multiple stages of tenogenic differentiation. Using fluorescent reporter mice, we demonstrated significant age- and tissue-dependent changes in the different fluorescent markers. Of particular interest are the Col2.3GFP and Prg4Cre;tdTom lines. Col2.3GFP was more concentrated (expressed by smaller subset of cells) than Col3.6CFP but also displayed severe reductions in expression within the ACL-PCL and AT-Cal with age while expression remained fairly consistent in other tendons. Additionally, Col2.3GFP+ cells were enriched for cell cycle (Gmnn) and matrix remodeling genes (Mmp's and Tgfb1), which may provide insight into their function during tendon growth. On the other hand, Prg4 expression, both endogenous and fluorescent reporter, increased with age. Our understanding of the functional role of Prg4 in tendon is limited, but the increased expression with age suggests that it may be expressed by cells in the later stages of the tenogenic lineage.

SIGNIFICANCE: An improved understanding of the cellular markers and signaling pathways that define and regulate the tendon lineage will be crucial to developing new therapies to attenuate the progression of pathologies and improve repair outcomes following injury. The anatomical and temporal differences in reporter and endogenous expression found in this study indicate that these reporter mice identify unique subsets of cells within the tenogenic lineage.

REFERENCES: 1. Dyment N, et al., PLOS One, 2014; 2. Jiang X, et al., ORS, 2018; 3. Kalajzic I, et al., JBMR, 2001.

ACKNOWLEDGEMENTS: Work supported by NIH grants R00 AR067283, P30 AR069619, and startup funds from Dept. Orthopaedic Surgery at UPenn.

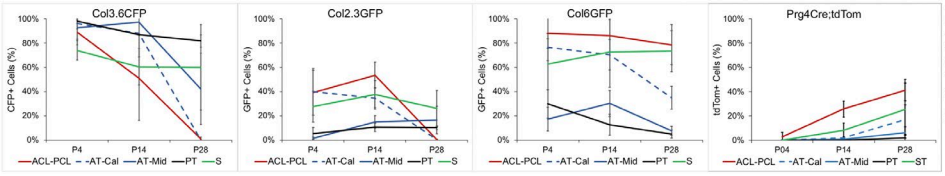

Fig. 1: Age (P4, P14, and P28) and tissue-dependent (type of tendon/ligament) changes in the number of fluorescent reporter cells.

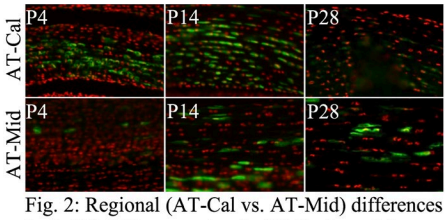

Fig. 2: Regional (AT-Cal vs. AT-Mid) differences in Col2.3GFP expression in AT. Red: nuclei.

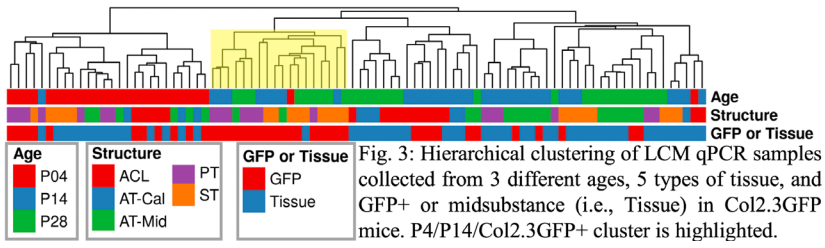

Fig. 3: Hierarchical clustering of LCM qPCR samples collected from 3 different ages, 5 types of tissue, and GFP+ or midsubstance (i.e., Tissue) in Col2.3GFP mice. P4/P14/Col2.3GFP+ cluster is highlighted.

Abnormal Vascularity and Extracellular Matrix Remodeling are Associated with Impaired Secondary Ossification in Mucopolysaccharidosis VII

Zhirui Jiang[1], Casey P. Johnson[2], Olli Nykänen[3], Mikko Nissi[3,4], Yian Khai Lau[1], Meilun Wu[1], Kai D. Ludwig[2], Jutta Ellerman[2], Margret L. Casal[5], Lachlan J. Smith[1]
[1]University of Pennsylvania, Philadelphia, PA; [2]University of Minnesota, Minneapolis, MN; [3]University of Eastern Finland, Kuopio, Finland; [4]University of Oulu, Oulu, Finland
zhirui.jiang@pennmedicine.upenn.edu

Disclosures: Zhirui Jiang (N), Casey Johnson (N), Olli Nykänen(N), Mikko Nissi (N), Yian Khai Lau (N), Meilun Wu (N), Kai Ludwig (N), Jutta Ellerman (N), Margret Casal (N), Lachlan Smith (5-Ultragenyx; 9-ORS Spine Section)

INTRODUCTION: Mucopolysaccharidosis VII is a genetic, lysosomal storage disease characterized by deficient beta-glucuronidase activity, which results in accumulation of poorly degraded glycosaminoglycans (GAGs) in cells and tissues [1]. MPS VII patients exhibit severe skeletal abnormalities, including dysplasia of the vertebrae and long bones. Resulting impaired mobility, pain and paralysis negatively impact quality of life [2]. Previous studies in our lab using the naturally occurring canine MPS VII model showed that formation of secondary ossification centers (SOCs) is markedly delayed in both vertebrae and long bones [3]. Conversion of cartilage to bone in SOCs is a multi-stage process that requires step-wise differentiation of chondrocytes, vascularization, cartilage matrix resorption and formation of mineralized bone matrix [3]. We showed previously that MPS VII chondrocytes in SOC epiphyseal cartilage exhibit impaired hypertrophic differentiation capacity [4]. Our objectives in the current study were to establish whether abnormal cartilage vascularity and impaired matrix resorption and mineralization also contribute to delayed SOC formation in MPS VII dogs, using novel, contrast-free MRI-based susceptibility-weight imaging (SWI) [5,6] and histological assays.

METHODS: With IACUC approval, thoracic vertebrae were obtained postmortem from control (heterozygous) and MPS VII-affected dogs at 9 days-of-age. This is the age immediately preceding commencement of secondary ossification in controls [4]. *Cartilage Vascularity:* Vertebrae (n=3) were imaged on a 9.4T MRI scanner using a high-spatial-resolution (91 µm isotropic) 3D gradient echo sequence with magnetic susceptibility weighted to provide detailed visualization of epiphyseal cartilage vascularity [5,6]. Images were post-processed using a quantitative susceptibility mapping (QSM) pipeline to better visualize and quantify cartilage vessels [5,6]. Vessel density, thickness, branching and connectivity were then quantified using uCT Ray v4.0 software. *Cartilage Matrix Remodeling:* For assessment of enzyme activity in epiphyseal cartilage, coronal, calcified cryosections of vertebrae (n=5) were stained for either alkaline phosphatase (ALP, a marker of matrix mineralization) or tartrate-resistant acid phosphatase (TRAP, a marker of matrix resorption). The number of TRAP-positive chondroclasts per cartilage canal was quantified. Additional vertebrae (n=5) were processed for paraffin immunohistochemistry, with sections stained for matrix metalloproteinase-9 (MMP-9, required for neovascularization). The number of MMP-9-positive epiphyseal chondrocytes was quantified. *Statistical Analysis:* Differences in quantitative metrics between control and MPS VII were established using Mann-Whitney tests ($p<0.05$).

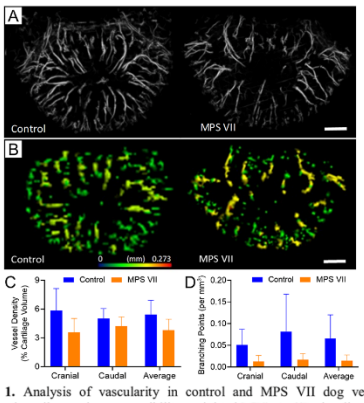

Figure 1. Analysis of vascularity in control and MPS VII dog vertebral epiphyseal cartilage using susceptibility-weighted MRI. **A.** 3D visualization of cartilage vessels (axial view). **B.** Heat map of vessel thickness. **C.** Quantification of vessel density and **D.** Number of branching points. Bar=1mm.

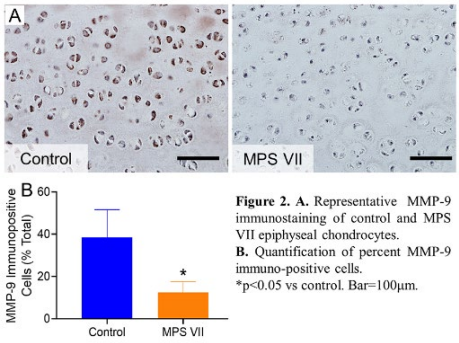

Figure 2. A. Representative MMP-9 immunostaining of control and MPS VII epiphyseal chondrocytes. **B.** Quantification of percent MMP-9 immuno-positive cells. *p<0.05 vs control. Bar=100µm.

RESULTS: *Cartilage Vascularity:* SWI and QSM were successfully applied to reveal detailed 3D renderings of vertebral epiphyseal cartilage vascularity (Figs 1A and B). While vessel thickness was similar in MPS VII compared to controls (Fig 1B), quantitative assessments revealed lower vessel density and connectivity (branching) in MPS VII vertebrae (~70% and 22% of control, respectively; Figs 1C and D), although the differences did not reach statistical significance. *Cartilage Matrix Remodeling:* The number of MMP-9-positive chondrocytes was significantly lower for MPS VII (~33% of control, Fig 2). There was punctate ALP staining surrounding chondrocytes in control epiphyses; however, staining was completely absent in MPS VII (Fig 3A). Finally, the number of TRAP-positive chondroclasts per cartilage canal was a significantly lower in MPS VII (~13% of control, Figs 3B and C).

DISCUSSION: Vascularization and matrix remodeling are critical for effective cartilage-bone conversion during the process of endochondral ossification. We successfully applied novel, contrast-free SWI and QSM MRI-based techniques for detailed visualization of vascularity in canine vertebral epiphyseal cartilage. Preliminary findings suggest that vessel density and architecture may be abnormal in MPS VII, but this should be confirmed through analysis of additional samples and at additional skeletal sites. The lower number of MMP-9-positive chondrocytes in MPS VII supports our previous mRNA results [8], and suggests impaired cartilage neovascularization, while altered TRAP and ALP expression likely reflect the diminished matrix resorption and mineralization capacity, respectively, of MPS VII cartilage cells. Ongoing studies seek to establish the molecular mechanisms linking lysosomal storage and GAG accumulation to altered cartilage vascularization and matrix remodeling, with the long term goal of developing improved therapies to normalize bone formation in MPS VII patients.

SIGNIFICANCE/CLINICAL RELEVANCE: MPS VII patients exhibit crippling skeletal deformities for which there are no effective treatments. In this study we provide novel insights into the mechanisms underlying impaired bone formation in MPS VII using a clinically-relevant large animal model.

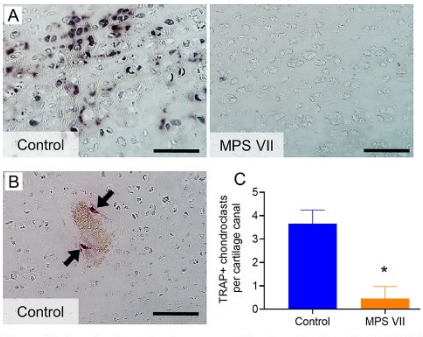

Figure 3. Impaired matrix turnover and mineralization in MPS VII epiphyseal cartilage. **A.** ALP staining is present in controls but absent in MPS VII cartilage. **B.** TRAP-positive chondroclasts (arrows) in a cartilage canal of a control. **C.** Number of TRAP-positive chondroclasts per cartilage canal (*p<0.05 vs control). Bar=100µm.

REFERENCES: [1] Sly+ J Biol Chem; [2] Montano+ J Med Genet 2016; [3] Karsenty+ Annu Rev Cell Dev Bi 2009; [4] Peck+ Mol Genet Metab 2015; [5] Nissi+ Magn Reson Med 2014; [6] Reichenbach+ Radiology 1997; [7] Schweser+ Z Med Phys 2016; [8] Peck+ Bone 2019.

ACKNOWLEDGEMENTS: Funding from the NIH, National MPS Society and WM Keck Foundation. Animal care provided by staff at the Penn Resource Center for Animal Models is gratefully acknowledged.

Ultrastructural Analysis of Different Skeletal Cell Types in Mucopolysaccharidosis Dogs at the Onset of Postnatal Growth

Zhirui Jiang[1], Yian Khai Lau[1], Margret L. Casal[1], Lachlan J. Smith[1]
[1]University of Pennsylvania, Philadelphia PA

Disclosures: Zhirui Jiang (N), Yian Khai Lau (N), Margret Casal (N), Lachlan Smith (5-Ultragenyx; 9-ORS Spine Section)

INTRODUCTION: The mucopolysaccharidoses are a family of inherited lysosomal storage disorders caused by deficiencies of enzymes that degrade glycosaminoglycans (GAGs) [1]. GAGs accumulate in cells and tissues resulting in multi-organ manifestations. Progressive skeletal abnormalities, including kyphoscoliosis and joint dysplasia, are hallmarks of most subtypes including MPS I (alpha-L-iduronidase deficiency) and VII (beta-glucuronidase deficiency). In previous work using naturally-occurring canine models of these diseases, we showed that both MPS I and VII dogs exhibit failures of endochondral ossification during postnatal growth, including delayed cartilage-bone conversion in secondary ossification centers [2-4], and low bone volume and mineral density in primary ossification centers [4]. The underlying cellular basis of these abnormalities remains poorly understood. The objective of this study was to conduct an ultrastructural examination of lysosomal storage and quantify pathological changes to other organelles across different skeletal cell types in MPS I and VII dogs at the onset of postnatal growth.

METHODS: With IACUC approval, vertebral bodies were obtained postmortem from 9-day-old normal (control), MPS I and MPS VII-affected dogs (each n=5), fixed in glutaraldehyde/ paraformaldehyde overnight and decalcified. Samples were post-fixed in 2% osmium tetroxide prior to *en bloc* staining with 2% uranyl acetate. Thin (80nm) sections were stained with uranyl acetate and lead citrate and imaged using transmission electron microscopy (TEM; JEOL JEM-1010). Ultrastructural analyses were performed for resting, proliferating and hypertrophic growth plate chondrocytes (RC, PC and HC, respectively), and osteoblasts (OB) and osteocytes (OCY) in primary ossification centers. The following parameters were measured using ImageJ software: cell area occupied by vacuoles (lysosomal storage, %), rough endoplasmic reticulum (ER) lumen diameter, and number of mitochondria and Golgi. For each sample, measurements were performed for 3 cells of each type, with results averaged prior to statistics. Detection of apoptotic cells was carried out on paraffin sections from thoracic vertebrae using in situ cell death (TUNEL assay) detection kit (Sigma, USA) following manufacture's instruction. Statistical differences were established via ANOVA with pairwise post-hoc Tukey's tests ($p<0.05$).

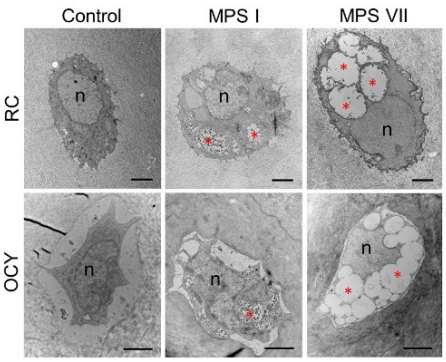

Figure 1. TEM of resting chondrocytes (RC) and osteocytes (OCY) in the vertebrae of 9-day-old control, and MPS I and VII-affected dogs. Bar=2µm. Asterisks = vacuoles (lysosomal storage); n=nucleus.

RESULTS: All skeletal cell types examined from MPS VII vertebrae exhibited significantly elevated lysosomal storage (vacuoles as a percent of cell area) compared to control cells (Figs. 1 and 2). Storage was greatest and most striking for MPS VII osteocytes, occupying ~50% of the total cell area. Storage was also elevated in MPS I compared to control, but did not reach significance for any cell type. Rough ER lumen were significantly dilated for MPS I resting chondrocytes compared to both control and MPS VII (Figs. 3A and B). Rough ER lumen were also dilated in MPS VII resting chondrocytes, but not significantly compared to control. There were no significant differences in ER lumen diameter between groups for other cell types. There was elevated TUNEL staining in MPS VII epiphyseal cartilage compared to controls, indicating increased apoptosis of resting chondrocytes secondary to storage (Fig. 3C). There were no significant differences in the number of mitochondria or Golgi between groups for any cell type.

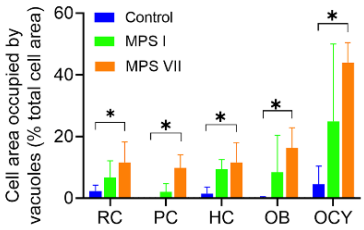

Figure 2. Relative lysosomal storage (cell area occupied by vacuoles) in resting (RC), proliferating (PC) and hypertrophic (HC) chondrocytes, osteoblasts (OB) and osteocytes (OCY) of 9-day-old control, and MPS I and VII affected dogs. *p<0.05 vs control.

DISCUSSION: Abnormal development of the vertebrae and long bones is a hallmark of skeletal disease in MPS patients; however, the underlying cellular mechanisms remain poorly understood. In general, skeletal manifestations are more severe in MPS VII compared to MPS I. In the current study we showed that both bone and cartilage cells from MPS VII dog vertebrae exhibit significantly elevated lysosomal storage from early in postnatal life. Storage in chondrocytes may impair proliferation and differentiation ability, contributing to delayed epiphyseal cartilage-bone conversion and longitudinal bone growth. Storage in osteoblasts and osteocytes likely negatively impacts bone formation and turnover. Interestingly, storage was greatest in MPS VII osteocytes, potential reflecting the relative age of these cells. Once entombed within the bone matrix, osteocytes are relatively inaccessible to exogenous drugs, which may in part explain why bone disease is recalcitrant to treatments such as enzyme replacement therapy. Rough ER dilation (highest for MPS I resting chondrocytes) is a marker of ER stress and may negatively impact protein synthesis and cell health. In conclusion, these results highlight the importance of very early diagnosis and intervention for preventing the progression of skeletal manifestations of MPS, and the need for new therapies that effectively target skeletal cells that reside in dense, avascular microenvironments.

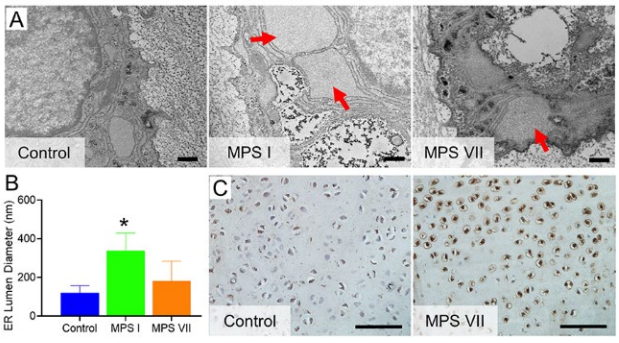

Figure 3. A. Representative images showing dilated rough ER lumen (arrows) in resting chondrocytes of 9-day-old MPS I and VII dog vertebrae. Bars=500nm. **B.** Quantification of rough ER lumen diameter; *p<0.05 vs control and MPS VII. **C.** TUNEL staining showing elevated numbers of apoptotic resting chondrocytes in MPS VII vertebral epiphyseal cartilage. Bars=100µm.

SIGNIFICANCE/CLINICAL RELEVANCE: MPS patients exhibit severe skeletal disease for which there are currently no effective treatments. The results of this study provide insights into how storage differentially effects major skeletal cell types, and highlights the need for early and target delivery of therapeutic agents to these cells to prevent progression of crippling skeletal deformities.

REFERENCES: [1] Neufeld+ The Metabolic and Molecular Bases of Inherited Disease, 2001; [2] Smith + J Orthop Res 2010; [3] Peck+ Mol Genet Metab 2015; [4] Chiaro+ Bone 2013.

ACKNOWLEDGEMENTS: Funding received from the NIH and National MPS Society. Animal care provided by staff at the Penn Resource Center for Animal Models is gratefully acknowledged.

Cellular and Molecular Mechanisms Regulating Synovial Joint Cavitation

Minwook Kim[1], Heejong Kim[2], Kimberly G. Helbig[1], Danielle R. Rux[1], Nancy Pleshko[3], Benjamin A. Garcia[2], Eiki Koyama[1], Maurizio Pacifici[1]
[1]Children's Hospital of Philadelphia, [2]University of Pennsylvania, Temple University, Philadelphia, PA
Kimm12@email.chop.edu

Disclosures: No disclosures.

INTRODUCTION: Joint cavitation is an essential process and one of the most dramatic events during embryonic joint development and morphogenesis. It involves a stepwise separation of opposed cartilaginous elements along a prospective boundary, eventually creating a fluid-filled synovial space and lubricated articular surfaces, permitting unhindered joint motion, and sustaining skeletal function and quality of life [1]. However, quite little is known about its underlying mechanisms and coordination with other joint traits. In the early embryonic limb, the skeletal primordia are initially composed of uninterrupted cartilaginous elements. The first morphological sign of joint initiation is the emergence of the interzone, a mesenchymal condensation of compacted round cells expressing growth and differentiation factor 5 (GDF5) [2]. We previously showed that interzone GDF5+ progeny cells produce most joint tissues over time [3]. Over developmental time, GDF5+ cells spatially located in the medial interzone region become flat and gradually separate from each other along the prospective joint cavitation line [4]. The cells flanking this line will differentiate in articular chondrocytes, with concurrent accumulation of synovial fluid and completion of joint cavitation [5]. However, the exact mechanisms by which the GDF5+ cells become separated from each other, how this process relates to synovial fluid production, and how the cavitation process is brought to completion remain all unanswered questions. We directed our study to address these critical questions.

METHODS: All animal procedures were approved by Children's Hospital of Philadelphia IACUC. To control timed-pregnancy, wild type mice were mated overnight and separated in the morning, and noon on the day of separation was considered E0.5. To assess skeletal growth and joint cavitation process, whole mount embryo staining with Alcian blue (pH 1.0) was carried out from E11.5 to E18.5 at 24 hr interval (n=5/group). For histological evaluation, time-matched hindlimbs were embedded in paraffin and sectioned at 5 µm (n=4/group). To capture critical moments during the cavitation process, embryos were harvested at short intervals between E14.5 and E15.5 and at 1 hr intervals between E15 (12 am) to E15.13 (3 am). Alcian blue (pH1.0 and 2.5), H&E and Saf-O staining was performed using paraffin embedded sections. Hylauronic acid (HA), versican and versican fragment were evaluated by immunohistochemistry. Infrared spectroscopy (FT-IRIS) was carried to quantify spatiotemporal changes of extracellular proteins. To discover possible new regulators, mass spectrometry was performed using embryonic tissues from distinct locations: (a) proliferating cartilage = future 'bone'; (b) interzone = future 'articular cartilage'; (c) intra joint ligaments = future 'ACL'; and (d) skin. Stages were E14.5 and E18.5 (before and after cavitation, respectively). Significance was determined by 2-way ANOVA with Tukey's post hoc ($p<0.05$).

RESULTS: A prospective joint capsule initially appeared at E12.5, and knee flexion angle was about ~30° at that stage and reached a maximum (110°) at E15.5 **(Fig 1A)**. Cavitation started within a remarkably short 3 hour window (between E15 and E15+3hr) and continued through distinct steps: (i) Small distinct bubble-like pockets first appeared at incipient interface between femoral condyle apex and opposing meniscus **(Fig 1B)**; (ii) The pockets started to merge generating a growing and extending cavity, with cells becoming separated from the intervening matrix **(Fig 1C)**; (iii) Cells on either side of skeletal elements became fully separated and retained a round cell morphology at this stage; and (iv) Cells on the articular surface began to reorient and became polarized **(Fig 1D)**. FT-IRIS showed that collagen and sugar content were high at E15+3hr in prospective articular cartilage, meniscus and ligaments during cavitation compared to adjacent shaft (proliferating) cartilage **(Fig 2A and B)**. Sugar content within the developing joint tissues markedly increased compared to shaft (proliferating) cartilage by E18.5 **(Fig 2C)**. Mass spectrometry showed that articular (interzone; red arrow) and proliferating (future 'bone'; green arrow) cartilage shifted to primary and secondary direction. In particular, levels of RHAMM (receptor for HA mediated motility), TMEM2 (cell surface hyaluronidase) and IFITM2 (interferon induced transmembrane protein 2) were significantly higher ($p<0.001$) before (E14.5) than after (E18.5) cavitation. Interestingly, TMEM2 was exclusively expressed in interzone cartilaginous tissue before (E14.5) cavitation **(Fig 3)**.

DISCUSSION: Our data reveal that the knee joint cavitation process involves a rapid and previously unsuspected series of steps occurring within a short time window (E15-E15.25). Morphologically, the process starts with emergence of distinct small bubble-like pockets forming at the interface between femoral condyle apex and opposing meniscus. With time, similar pockets form on the tibial side. We do not know what regulates the topography of these steps, but remarkably, they temporally overlap attainment of maximal knee flexion, arguing that there is strict regulatory coordination between pocket formation location and flexion. The marked increase of sugar content before cavitation detected by FT-IRIS suggests robust accumulation of glycosaminoglycans (i.e., HA), consistent with previous findings and in relation to high expression of RHAMM, TMEM2 and IFITM2 at E14.5 (before cavitation). TMEM2 (cell surface hyaluronidase) expression in developing articular cartilage but not shaft cartilage is of particular interest because it could cleave HA into intermediate size fragments and facilitate cavitation. It suggests a mechanism by which the cleaved HA fragments bound to RHAMM could recruit fluids leading to joint cavitation. Ongoing studies are examining more closely the expression and topographical distribution of RHAMM, HASE, HA synthase 2 (HAS2) during cavitation. We are also investigating the joint phenotypes after conditional deletion of HAS2 in developing joints.

SIGNIFICANCE/CLINICAL RELEVANCE: This study provides novel insights into mechanisms underlying joint development and cavitation. Understanding the basic biology and mechanisms of action of synovial progenitor cells could be translated into future joint disease therapies, including using synovial progenitor cells for musculoskeletal tissue repair and regeneration.

ACKNOWLEDGEMENTS: This work was supported by the NIH (R01 AR062908). **REFERENCES:** [1] Buckwalter+ 1997, [2]. Mitrovic+ 1978, [3] Koyama+ 2008, [4] Archer+ 2003, [5] Pacifici+ 2006

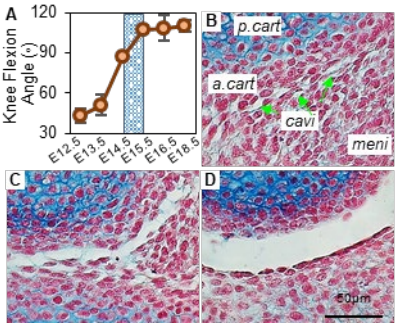

Fig. 1. Joint development and cavitation. (A) Flexion angle determined by whole mount embryo staining with Alcian blue (n=5/group), **(B-D) Stepwise cavitation mechanisms: (B)** Bubble-like pockets (green arrows) appear along prospective cavitation line, merge and generate a continuous space. **(C)** Initial cavitation begins to occur at the apex of femoral condyle and extends along the line. **(D)** Cell/matrix on the opposite skeletal sites become fully separated, and cells on either surface begin to reorient followed by cell polarization and matrix reorganization. (Alcian blue; scale bar = 50µm)

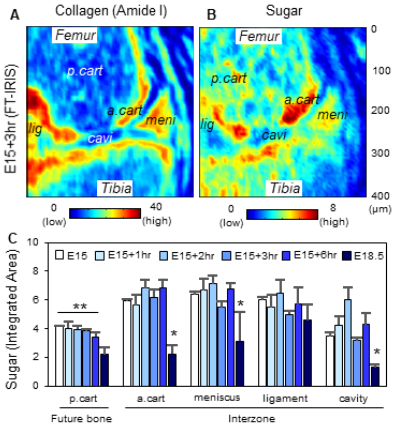

Fig. 2. Spatiotemporal distribution of extracellular matrix components by FT-IRIS. (A) Amide I, **(B)** Sugar **(C)** Sugar content (integrated area). (*p.cart* = proliferating cartilage (future 'bone'), *a.cart* = articular cartilage, meni = meniscus, lig = ligament, cavi = joint cavity (interzone); Wild type mouse at E15-E18.5; n=6/group; $p<0.05$; * E18.5 vs. other groups on tissue type; ** p.cart vs. a.cart, meniscus and ligament)

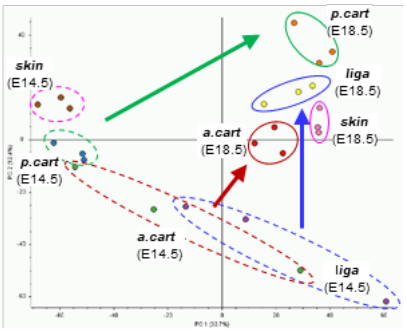

Fig. 3. PCA analysis of synovial progenitors isolated at E14.5 (before) and E18.5 (after cavitation) by Mass Spectrometry. (n=3/group)

mTORC1 Signaling Inhibits Early Tenocyte Differentiation and Enhances Tenocyte Maturation In Tendon

Yeonju Lee[1], Nathaniel A. Dyment[1], Kyu Sang Joeng[1]
[1]University of Pennsylvania, Philadelphia, PA

INTRODUCTION: Tendon plays an important role in human motion by transmitting forces from muscle to bone. Tendon fibroblasts (tenocytes) drive postnatal tendon growth by regulating extracellular matrix expansion which mainly result from collagen fibril maturation (fibrillogenesis). Tenocytes originate from tendon stem/progenitor cells and undergo unique postmitotic morphological maturation to be fully functional. This morphological maturation results in a long and thin shape with a large number of cytoplasmic extensions that create cell to cell and cell to extracellular matrix interaction. However, the underlying biological mechanisms regulating tenocyte differentiation and morphological maturation are not clear. The goal of this study is to identify biological mechanisms regulating tenocyte differentiation and maturation by elucidating multifaceted function of mTORC1 signaling.

METHODS: To understand the function of mTORC1 in early differentiation, we quantified *Col1(2.3)-GFP* positive tenocyte population in a tendon-specific mTORC1 loss-of-function mouse model (*Scx-Cre;Raptor*$^{fl/fl}$) and gain-of-function mouse model (*Scx-Cre;Tsc1*$^{fl/fl}$) . Achilles and patellar tendons were analyzed at various age points: 7, 14, 21 and 30 days after birth. Rapamycin was injected into the gain-of-function mouse model (from day 22 to 29 after birth) to perform pharmacological rescue experiments. To understand the function of mTORC1 in morphological maturation of tenocyte, we developed immunofluorescence imaging technique using Zo-1 and Phalloidin antibody. Patellar tendon from loss-of-function mouse model (*Scx-Cre;Raptor*$^{fl/fl}$) were analyzed at multiple time points (day 7, 14, 21 and 30 after birth). All quantitative data were analyzed using students t-test.

RESULTS: The number of *Col1(2.3)-GFP* positive tenocytes was increased in both Achilles and patellar tendon of *Scx-Cre;Raptor*$^{fl/fl}$ loss of function mice compared to wild type (WT) mice. In contrast, the number of *Col1(2.3)-GFP* positive tenocytes significantly decreased in both Achilles and patellar tendon of *Scx-Cre;Tsc1*$^{fl/fl}$ gain of function mice. Rapamycin (mTORC1 inhibitor) treatment in both WT and *Scx-Cre;Tsc1*$^{fl/fl}$ mice increased *Col1(2.3)-GFP* positive tenocytes. These results indicate that mTORC1 signaling inhibits early differentiation of tendon cells into *Col1(2.3)-GFP* positive tenocytes. To understand the function of mTOR1 in tenocyte morphogenesis, we analyzed the changes of nuclear shape, cell body area, and protrusion number between wild-type and *Scx-Cre;Raptor*$^{fl/fl}$ loss of function mice. In wild-type, we found that tenocytes became larger and rounder at early stages and then subsequently became flat and narrow at later stages. *Scx-Cre;Raptor*$^{fl/fl}$ mice showed more flat and narrow tenocytes, even at early stages. These data suggest that reduced mTORC1 signaling is required for tenocyte morphogenesis.

DISCUSSION: Our results indicate that mTORC1 signaling is an important regulator of early tendon differentiation and tenocyte morphogenesis. Our gain-and loss-of-function studies with *Col1(2.3)-GFP* transgenic mouse support the inhibitory function of mTORC1 in early tenocyte differentiation. The analysis of tenocyte morphology using *Scx-Cre;Raptor*$^{fl/fl}$ loss of function mice suggests that mTORC1 signaling is required for proper tenocyte morphogenesis. Further study will be needed to investigate the contribution of mTORC1 to gene expression pattern during tendon differentiation.

SIGNIFICANCE/CLINICAL RELEVANCE: This study will contribute to understanding with tendon and mTORc1 signaling for tendon development.

ACKNOWLEDGEMENTS: This work is partly supported by the National Institutes of Health under award numbers K01AR069002 (KSJ). We thank Dr. Ronen Schweitzer for providing *Scx-Cre* mouse line.

Global Knockout of *Fgf9* Results in Enlarged Bone Ridges and Differential Gene Expression in Muscle but Not Bone

Connor Leek[1], Ryan C. Locke[1], Iman Bhattacharya[1], David M. Ornitz[2], and Megan L. Killian[1]
[1]University of Delaware, Newark, DE, [2]Washington University School of Medicine St. Louis Missouri

Disclosures: None

INTRODUCTION: Tendons transmit mechanical forces from muscle to bone at tendon attachment sites.[1–3] Tendon attachments are typically found along bone ridges and these ridges aid in the distribution of mechanical force and resist bone bending.[4,5] During vertebrate development, as the initiation of bone ridges are regulated by *Scx* and *Bmp4*, and knockout of *Scx* leads to decreased size of bone ridges, such as the deltoid tuberosity (DT).[4] Conversely, the DT becomes enlarged in $Fgf9^{null}$ mice compared to wild-type (WT) mice.[6] In this study, we quantified the size of the DT in $Fgf9^{null}$ mice and measured cellular proliferation and phenotypes of the developing DT in WT and $Fgf9^{null}$ mice.

METHODS: All experiments were approved by University of Delaware Institutional Animal Care and Use Committee. $Fgf9^{null}$ embryos and WT littermates were generated as described in previous literature.[7] $Fgf9^{WT/Ex}$; Cre positive females were bred with $Fgf9^{flx/flx}$; Cre negative males to generate $Fgf9^{null}$ mutant mice and wildtype $Fgf9^{WT/Ex}$ mice (WT) and genotyped using a commercial vendor (Transnetyx). Limbs from embryonic (E16.5) and neonatal mice (P0) were collected following euthanasia and fixed in 4% paraformaldehyde (PFA) for 24 hours. For histology, forelimbs from all time points (n=3/genotype; timepoint) were decalcified, paraffin sectioned (7 µm), stained with Hematoxylin and Eosin Y (H&E), and imaged on an inverted microscope (Imager A2, Zeiss). For WT and $Fgf9^{null}$ embryos at E16.5, area and number of DT hypertrophic chondrocytes were manually measured. Whole-mount staining was performed using Alcian Blue/Alizarin staining (n=7/genotype at P0).[8] To measure proliferation, a pregnant dam was injected with EdU (Click-iT™ EdU Alexa Fluor™ 647 Imaging Kit, Invitrogen) at E16.5 of pregnancy and euthanized two hours later. Proliferating cells (n=3/genotype) were labeled with Hoechst as a nuclear counterstain. EdU+ cells and nuclei were imaged using fluorescence microscopy and counted. Quantitative assessment of DT size (using whole-mount staining), proliferation (EdU+ cells), and cell size (H&E) were analyzed using ImageJ (NIH).[9] Fluorescent *in situ* hybridization (FISH) was performed for *Scx, Pthlh, Gli1,* and *Fgf9* probes on E16.5 samples using RNAscope Multiplex Fluorescent Reagent Kit v2 (Advanced Cell Diagnostics) (n=2/genotype). RNA extraction was performed on E18.5 embryos (n=3/genotype) and followed RNeasy kit protocol (Qiagen). Bulk total RNA were sequenced in Illumina HiSeq 2000 (Paired-end 2*50bp; threshold length=30bp; Phred score=28) following library preparation (NEBNext® Ultra™ RNA Library Prep kit for Illumina). RNA quality was assessed before and after sequencing (fragment analyzer and FastQC, respectively) and mapped to the mouse reference genome Grcm38 (mm10), and quantified (HT-Seq). Statistical analyses to compare cell and tissue morphometry between genotypes (e.g., DT size and chondrocyte area) were performed using Prism (GraphPad) with Student's t-test and two-way ANOVA (repeated measure by region) to compare percent proliferation at E16.5.

RESULTS: $Fgf9^{null}$ mice had larger DTs than WT mice at P0 (Figure1A, B). There was a clear Alcian blue staining on the DT of $Fgf9^{null}$ mice that was absent in WT mice (Figure 1A). The difference in size became apparent after E16.5 as the DT of $Fgf9^{null}$ mice had more enlarged chondrocytes and the DT of WT mice began to mineralize (Figure 2A, D). We observed hypertrophic chondrocytes in the DT of E18.5 and P0 $Fgf9^{null}$ mice (Figure 2E) that were absent from the DT of WT mice (Figure 2B). $Fgf9^{null}$ mice had larger area of hypertrophic chondrocytes compared to WT mice at E16.5 (Figure 2G). Attachments of $Fgf9^{null}$ mice had a lower percentage of proliferating cells compared to WT attachments (Figure 2H). Fewer proliferating cells did not affect the overall cell density (Data not shown). From our RNA-Seq findings, we discovered 805 differentially expressed genes expression between $Fgf9^{null}$ and WT muscle and only 1 differentially expressed gene (which was sex-dependent) in bone. In the normally developing attachment, *Fgf9* was primarily expressed in connective tissue surrounding the DT (Figure 3A, B). Additionally, $Fgf9^{null}$ mice have increased *Gli1* expression (Figure 3D) and similar *Pthlh* (Figure 3F) expression at the DT attachment compared to WT mice (Figure 3C and E) at E16.5.

DISCUSSION: We confirmed previous work that $Fgf9^{null}$ mice have enlarged DTs compared to WT mice. This phenotype may not be due to differences in cell proliferation but rather through regulation of hypertrophic chondrocyte size which may persist longer during DT growth in $Fgf9^{null}$ mice compared to WT mice. From RNA-Seq findings, we showed that deletion of *Fgf9* resulted in differential gene expression in muscle, but not bone. These findings elucidate the potential role that *Fgf9* may play in muscle-bone crosstalk during development.

SIGNIFICANCE: Skeletal muscle is necessary for the growth and maintenance of bone ridges via both the physical application of mechanical forces during contraction but also via paracrine/endocrine signaling from muscle to bone. Findings from this work elucidate the potential new role that Fgf9 plays in regulating bone shape which could have implications in attachment development and growth.

REFERENCES: [1] Biewener, et al. Bone, 1996. [2] Benjamin, et al. Comp. Biochem. Physiol. Part A Mol. Integr. Physiol., 2002. [3] Zelzer, et al. Birth Defects Res. C. Embryo Today, 2014. [4] Blitz, et al. Dev. Cell, 2009. [5] Rot-Nikcevic, et al. Dev. Genes Evol, 2006. [6] Hung, et al. Dev. Biol, 2007. [7] Lin, et al. Genesis, 2006. [8] Schneider, et al. Humana Press 2012. [9] Rigueur, et al. Nat. Methods, 2014.

ACKNOWLEDGMENTS: Institutional Development Award (IDeA) from the National Institute of General Medical Sciences of the National Institutes of Health under grant number P30GM103333 (PI: Buchanan).

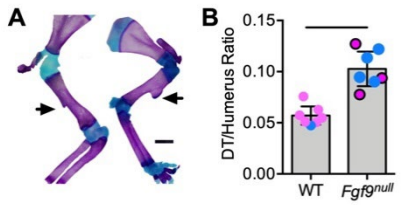

Figure 1: *Fgf9null* mice have an enlarged DT when compared to WT mice. **(A)** Cartilage (Alcian blue) and bone (Alizarin red) were visualized using whole mount staining of *Fgf9null* and WT mice at P0 (scale bar=1mm), black arrows = DT. **(B)** Normalized area of DT was larger in *Fgf9null* mice compared to WT mice at P0 (Pink; female and blue; male). Data are biological replicates and mean ± 95% CI; bar = $p < 0.05$.

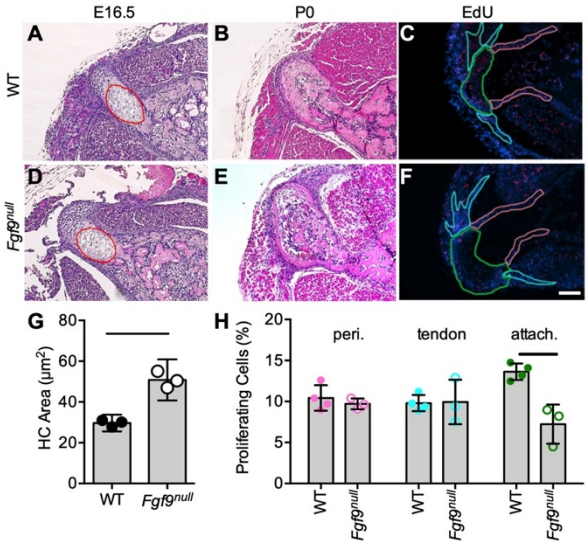

Figure 2: *Fgf9null* mice have larger hypertrophic chondrocytes and fewer proliferating cells at attachment compared to WT mice. DTs were qualitatively larger in (D&E) *Fgf9null* embryos compared to (A&B) WT embryos at both E16.5 and P0. Red circle = region of hypertrophic chondrocytes (HC), and area of HCs was quantified at E16.5, shown in (G). Cell proliferation was measured in regions of the DT for both (C) WT and (F) *Fgf9null* embryos at E16.5 (scale bar = 50µm). Outlined regions in C&F: perichondrium (peri.; pink), tendon (tendon; teal), and attachment (attach.; green). (H) *Fgf9null* embryos had lower percentage of proliferation in DT attachments compared to WT embryos. Data presented are biological replicates with mean ± 95% CI; bar indicates significant difference ($p < 0.05$).

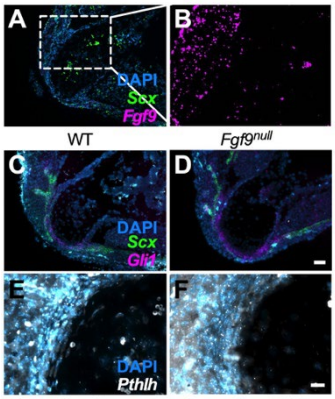

Figure 3: Gene expression using FISH at E16.5. **(A,B)** *Fgf9* mRNA is predominantly expressed in the surrounding muscle with limited expressed within bone. **(C-D)** Increased *Gli1* mRNA expression in the DT attachment of $Fgf9^{nuill}$ embryos was visualized using FISH compared to WT embryos (scale bar = 50µm). **(E-F)** DT attachments of $Fgf9^{null}$ embryos had similar expression of *Pthlh* compared to attachments of WT embryos (scale bar = 20µm).

Interactive Effects of Lactation History and Estrogen Status on Cellular Activities of Rat Maternal Bone

Yihan Li[1], Yilu Zhou[1], Chantal de Bakker[1], Hongbo Zhao[1], Luqiang Wang[1], Leilei Zhong[1], Lutian Yao[1], Ling Qin[1], X. Sherry Liu[1]

[1] McKay Orthopaedic Research Laboratory, University of Pennsylvania, Philadelphia, PA.

Pregnancy and lactation dramatically alter the female skeleton but exert protective effects on postmenopausal fracture risk. We found that Lactation rats with 2-3 cycles of reproduction and lactation had attenuated bone loss in response to ovariectomy (OVX) *vs.* Virgin rats. We hypothesized that lactation history and estrogen status may have interactive effects on bone cell activities.

Histology indicated greater osteoblast and osteoclast numbers in the 4wk post-OVX *vs.* intact group in both Virgin and Lactation rats (age 13 mo, n=7-10/group), but were unaffected by lactation history (FigAB). Intriguingly, adipocyte number (N.Adi) in the intact group was 8.3-fold greater in Lactation *vs.* Virgin rats. Moreover, OVX induced a 2.6-fold elevation in N.Adi in Virgins ($p=0.2$) but reduced N.Adi by 62% in Lactation rats (FigCD). Regardless of lactation history, BMMSCs (n=3-4/group) formed more colonies in OVX *vs.* intact rats; however, colony formation was not affected by lactation history (FigE). Moreover, the rate of BMMSC proliferation was not affected by either lactation history or estrogen status. After 7 days of adipogenic induction, % area of lipid droplets in Virgins was 3.6-fold greater in the OVX *vs.* intact group, while no difference was found in Lactation rats. Interestingly, in the OVX group, lipid area was 92% lower in Lactation *vs.* Virgin rats (FigFG). We postulate that cycles of reproduction and lactation lead to an accumulation of adipocytes in the bone marrow; however, combined effects of lactation history and estrogen deficiency may alter the bone marrow environment against adipogenesis, which may partially account for the protective effect of lactation history against estrogen deficiency-induced bone loss.

Under OVX conditions, 51% greater MMP13+ and 39% greater CtsK+ osteocytes (FigH-J), 33% greater canalicular area, and a trend toward 11% greater lacunar area ($p=0.07$, FigI-M) were found in Lactation *vs.* Virgin rats, while no difference was found in the intact group (n=3-4/group). Increased peri-cellular fluid space may increase fluid shear stress on osteocytes and cell processes, which may explain our previous findings that lactation history enhanced bone's mechano-responsiveness only when subjected to estrogen deficiency.

In summary, the interactive effects of lactation history and estrogen status alter the adipogenic capacity of BMMSCs and osteocyte activities, which may protect the maternal skeleton from estrogen deficiency later in life.

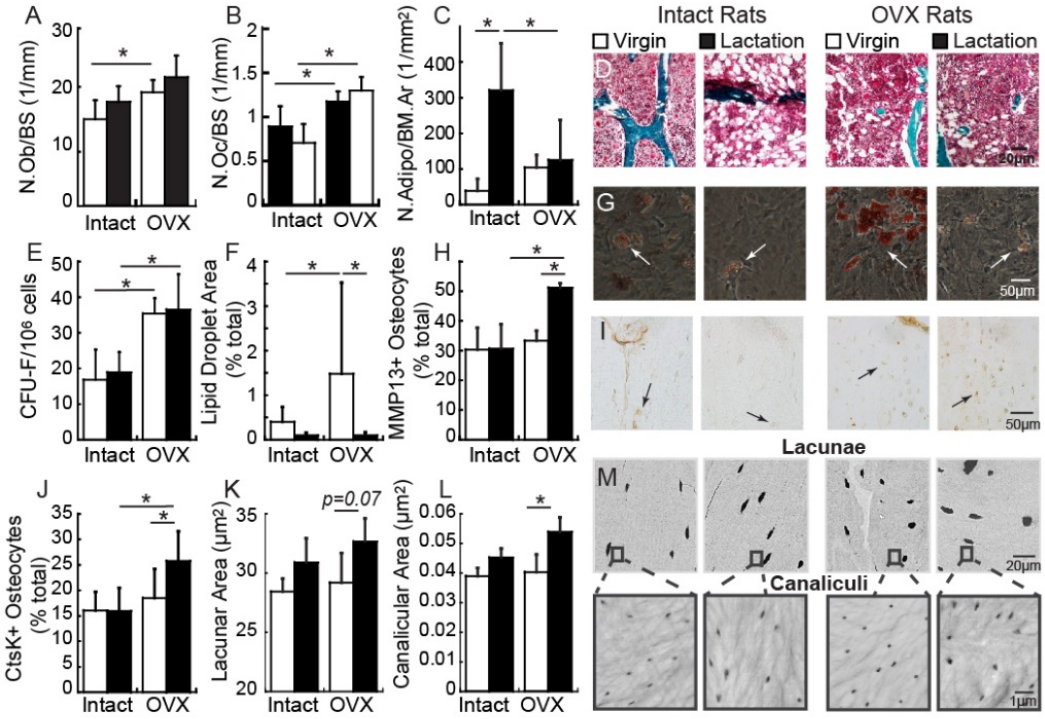

Comparisons between virgin and reproductive rats in intact and OVX conditions in (A) osteoblast, (B) osteoclast, and (C-D) bone marrow adipocyte number, (E) BMMSC CFU-F, (F) percent lipid droplet area, (G) BMMSC adipogenic oild red O staining, (H) percent MMP13 positive osteocytes, (I) MMP13 immunostaining, (J) percent CtsK-postive osteocytes, (K) lacunar area, (L) canalicular area, (M) bSEM images of LCS structure. Arrows indicate positively stained cells. *: $p<0.05$.

YAP/TAZ-dependent transcription regulates cytoskeletal response to hydrogel stiffness

Devon E. Mason [1,2,3*], Sebastián L. Vega [4], Su-Jin Heo [1], Ryan Daniels [1,5],

Jason A. Burdick [2], Robert L. Mauck [1,2], Joel D. Boerckel [1,2,3]

[1] McKay Orthopaedic Research Laboratory, University of Pennsylvania, Philadelphia, PA. [2] Department of Bioengineering, University of Pennsylvania, Philadelphia, PA. [3] Department of Aerospace and Mechanical Engineering, University of Notre Dame, Notre Dame, IN. [4] Department of Biomedical Engineering, Rowan University, Glassboro, NJ. [5] Department of Cellular and Molecular Biology, University of Pennsylvania, Philadelphia, PA.

Actomyosin contractility and focal adhesion remodeling enable cell attachment to extracellular matrix (ECM) in minutes and initial cell spreading completes in 30-45 minutes. We have previously shown that transcription inhibition increases actin polymerization more than 3-fold in 24 hours and that the mechanotransductive transcriptional co-activators yes-associated protein (YAP) and transcriptional co-activator with PDZ-binding domain (TAZ) indirectly regulate this response by modulating transcription. Therefore, cytoskeletal activation of YAP/TAZ-dependent transcription feeds back to the cytoskeleton. However, how transcription during cell attachment influences cytoskeletal response to ECM stiffness is unknown.

To address this question, endothelial colony forming cells (ECFCs) were seeded on soft (1 kPa) or stiff (18 kPa) RGD functionalized methacrylated hyaluronic acid (MeHA) hydrogels which were then collected for immunofluorescence ($n = 21$ cells) or qPCR ($n = 3$ samples). Average focal adhesion length (from .92 μm to 1.49 μm; $p < .0001$) and number of focal adhesions per cell (22.18 to 167.3; $p < .0001$) were greater on stiff hydrogels 4 hours after seeding. Focal adhesion maturation on stiff hydrogels coincided with a more than 2-fold increase in expression of the YAP/TAZ-dependent target gene Cyr61, as compared to soft hydrogels ($p < .0002$). To determine the role of *de novo* gene expression in the rapid response to the ECM stiffness we impaired transcription with the global transcription inhibitor actinomycin D. ECFCs plated on soft hydrogels in the presence of the actinomycin D increased the number of both small (<1 μm; from 15.5 to 36.8; $p < .0001$) and large (>1 μm; from 6.7 to 14.3; $p < .002$) focal adhesions per cell. In contrast, transcription inhibition on stiff hydrogels had little effect on the number of small (<1 μm; from 79.7 to 64.4; $p > .88$) or large (>1 μm; from 87.6 to 79.4; $p > .99$) focal adhesions. These results suggest that transcription during attachment is dispensable on stiff hydrogels, but are required for reducing cytoskeletal tension on soft substrates.

Next, we pretreated ECFCs with actinomycin D for 36 hours and either fixed immediately or replated on glass. ECFCs treated with actinomycin D and then fixed were composed exclusively of large stress fibers and focal adhesions, more so than DMSO treated controls. However, ECFCs replated under continuous transcription inhibition failed to form any stress fibers and only contained small peripheral focal adhesions. This suggests that continuous transcription limits cytoskeletal maturation, but a mature cytoskeleton fails to form without an existing template, under conditions of prolonged transcription inhibition.

Non-immunogenic utrophin gene therapy is effective in animal models for muscular dystrophy

Morales L, Song Y, Malik AS, Greer CD, Petrov MT, Zhou S, Kozyak BW, Nghiem PP, Khurana TS, Kornegay JN, Stedman HH

The essential product of the Duchenne muscular dystrophy (DMD) gene is dystrophin[1], a rod-like protein[2] that protects striated myocytes from contraction-induced injury[3]-[4]. Dystrophin-related protein or utrophin retains most of the structural and protein binding elements of dystrophin[6]. Importantly, normal thymic expression in DMD patients[5] should protect utrophin by central immunologic tolerance. We designed a codon-optimized, synthetic transgene encoding a miniaturized utrophin (μUtro), deliverable by AAV vectors. Here we show that μUtro is a highly functional, non-immunogenic substitute for dystrophin, preventing the most deleterious histological and physiological aspects of muscular dystrophy in small and large animal models. Following systemic administration of an AAV-μUtro to neonatal dystrophin-deficient mdx mice, histological and biochemical markers of myonecrosis and regeneration are completely suppressed throughout growth to adult weight. In the dystrophin-deficient Golden Retriever model, μUtro non-toxically prevented myonecrosis even in the most powerful muscles. In a stringent test of immunogenicity, focal expression of μUtro in the deletional-*null* German Shorthaired Pointer model produced no evidence of cell-mediated immunity, in contrast to the robust T cell response against similarly constructed μDystrophin (μDystro). These findings support a model in which utrophin-derived therapies might be used to treat clinical dystrophin deficiency, with a favorable immunologic profile and preserved function in the face of extreme miniaturization.

Rcn3 Is Involved In Postnatal Tendon Maturation By Regulating Collagen Fibrillogenesis.

Na Rae Park[1], Snehal Shetye[1], Douglas R. Keene[2], Sara Tufa[2], David M. Hudson[3], Marilyn Archer[3], and Kyu Sang Joeng[1]
[1]University of Pennsylvania, Philadelphia, PA, [2]Shriners Hospital for Children, Portland, OR, [3]University of Washington, Seattle, WA
Email of Presenting Author: Na.Park@pennmedicine.upenn.edu

Disclosures: Na Rae Park (N), Snehal Shetye (N), Douglas R. Keene (N), Sara Tufa (N), David M. Hudson (N), Marilyn Archer (N), Kyu Sang Joeng (N)

INTRODUCTION: Tendon plays a critical role in joint motion by transmitting force from muscle to bone. This transmission of force is facilitated by its structure, which consists of an aligned and organized type I collagen. Tendon injuries are a significant orthopaedic problem because the healing process is very slow and surgical intervention cannot restore normal mechanical strength and structural integrity, which often causes long-term disability and pain. Despite this significant clinical relevance, the cellular and molecular mechanisms regulating tendon maturation, homeostasis, and injury repair are poorly understood. Rcn3 is an ER protein localized to the secretory pathway ([1], [2]) but its specific function in tendon and other tissues has not been established yet. Rcn3 is predicted to be a chaperone protein and a calcium signaling mediator with a calcium binding motif. The objective of this study is to determine the function of Rcn3 in postnatal tendon maturation and collagen fibrillogenesis.

METHODS: To test our hypothesis, we generated a tendon-specific Rcn3 loss-of-function mouse model (*Scx-Cre;Rcn3$^{fl/fl}$*). Histological analysis were conducted on patellar and Achilles tendons at multiple time points (day 5, 10, 21, and 30 after birth). Biomechanical uniaxial tests were performed on 2-month old mouse Achilles tendons (n=3) to measure their mechanical properties. Transmission electron microscopy (TEM) was performed to measure the distribution of collagen fibril diameter of Achilles tendon in 2-month old mice (n=3). Collagen cross-link and mass spectral analysis were performed to examine the changes in post-translational modification of type I collagen in 1-month old mice. All quantitative data were analyzed using student's t-test.

RESULTS: Histological analysis showed that *Scx-Cre;Rcn3$^{fl/fl}$* (tendon-specific Rcn3 loss-of-function model) mice exhibited significantly decreased tendon thickness in both patellar (Fig. 1A) and Achilles tendon (Fig. 1B). The quantification result showed that the thickness is 40% decreased in patellar tendon (Fig. 1C) and 24% decreased in Achilles tendon (Fig 1D). The *Scx-Cre;Rcn3$^{fl/fl}$* mice also showed significantly increased cell density compared with those of control. These results indicate that loss of Rcn3 causes impaired tendon development and maturation. The decreased tendon thickness with increased tenocyte density prompted us to examine the diameter of collagen fibril which is critical for tendon thickness. Interestingly, the transmission electron microscopy (TEM) analysis showed that *Scx-Cre;Rcn3$^{fl/fl}$* mice has a relatively smaller distribution of tendon fibril diameter on 2-month mice (Fig. 2). These results suggest that smaller diameter of collagen fibril caused decreased tendon thickness in mutant mice. We performed collagen cross-link and mass spectral analyses to determine if Rcn3 played a role in regulating post-translational modifications of type I collagen. The C-telopeptide cross-linking lysine was over-hydroxylated in mutant mice, which resulted in increased levels of the collagen cross-link hydroxylysylpyridinoline (HP). To examine the changes in mechanical properties of mutant tendon, uniaxial biomechanical test was performed on Achilles tendons. Consistent with histological analysis, the cross-sectional area was significantly decreased in Achilles tendon (Fig 3A). Failure load (Fig. 3B) was significantly reduced in *Scx-Cre;Rcn3$^{fl/fl}$* mice when compared with control mice, and stiffness (Fig. 3C) was tending to decrease without statistical significance. Further analysis with increased animal number will be performed to confirm current biomechanical analysis.

DISCUSSION: Our study suggests that Rcn3 is an important regulator of postnatal tendon maturation. Transmission electron microscopy (TEM) analysis and the expression of Rcn3 in ER suggest that Rcn3 could be a regulator of collagen fibrillogenesis by regulating collagen synthesis, secretion, and modification. Further cellular, molecular, and biochemical analyses will be required to confirm the precise function of Rcn3 in regulating collagen biosynthesis. Future studies will also investigate a function for Rnc3 as a calcium signaling mediator in tendon.

SIGNIFICANCE/CLINICAL RELEVANCE: This study will contribute to understanding of regulatory mechanism for postnatal tendon development and homeostasis, which may provide the basis for understanding the biological mechanism of tendon injury repair.

REFERENCES: [1] Tsuji+, 2006 [2] Jin+, 2016

ACKNOWLEDGEMENTS: This work is partly supported by the National Institutes of Health under award numbers K01AR069002 (KSJ). We thank to Dr. Ronen Schweitzer for providing *Scx-Cre* mouse line.

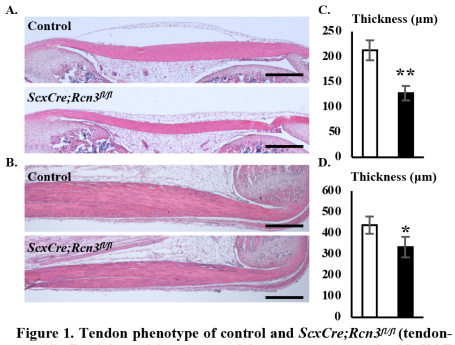

Figure 1. Tendon phenotype of control and *ScxCre;Rcn3$^{fl/fl}$* (tendon-specific Rcn3 loss-of-function model) mouse at 1 month old. H&E stained patella tendon section (A) and Achilles tendon section (B). Thickness of patellar tendon (C) and Achilles tendon (D). (White bar indicates control mice, Black bar indicates *ScxCre;Rcn3$^{fl/fl}$* mice, * indicates P<0.05 and ** indicates P<0.01 between genotypes, n=3)

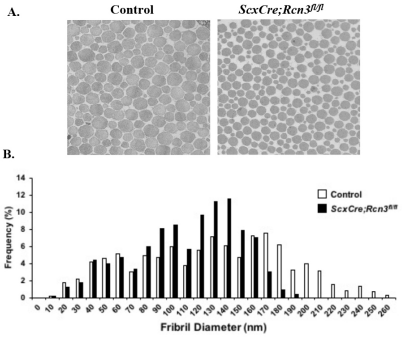

Figure 2. Transmission electron microscopy (TEM) of Achilles tendons from control and *ScxCre;Rcn3$^{fl/fl}$* (tendon-specific Rcn3 loss-of-function model) mouse at 2-month old. TEM image (A) and frequency graph (B). (White bar indicates control mice, Black bar indicates *ScxCre;Rcn3$^{fl/fl}$* mice, n=3)

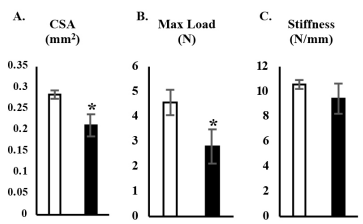

Figure 3. Mechanical property of control and *ScxCre;Rcn3$^{fl/fl}$* (tendon-specific Rcn3 loss-of-function model) mouse at 2-month old. Cross-sectional Area (A), max load (B) and stiffness (C) of Achilles tendon. (White bar indicates control mice, Black bar indicates *ScxCre;Rcn3$^{fl/fl}$* mice, * indicates P<0.05 between genotypes, n=3)

Controlled Release from Mechanically-Activated Microcapsules in Developing Tissue Microenvironments

Ana P. Peredo[1,2,3], Yun Kee Jo[4], Daeyeon Lee[4], George R. Dodge[2,3], Robert L. Mauck[1,2,3]
[1]Department of Bioengineering, University of Pennsylvania, Philadelphia, PA, [2]McKay Orthopaedic Research Lab, Department of Orthopaedic Surgery, University of Pennsylvania, Philadelphia, PA, [3]Translational Musculoskeletal Research Center, Corporal Michael J. Crescenz Veterans Affairs Medical Center, Philadelphia, PA,
[4]Department of Chemical and Biomolecular Engineering, University of Pennsylvania, Philadelphia, PA
anapperedo@gmail.com

INTRODUCTION

Tissues in the musculoskeletal system are continuously subjected to mechanical forces that regulate homeostasis during normal tissue function [1-3] and in degeneration and regeneration after injury [4-5]. We recently posited that this same mechanical environment could be used to control drug release and enable the therapeutic delivery of molecules when needed, leading to improved outcomes and faster healing. To that end, we developed mechanically-activated microcapsules (MAMCs) for on-demand drug delivery using a custom micro-fabrication system [6]. Here, we extended the application of this new technology by developing a suite of MAMCs with different mechano-activation and degradation profiles, and probed the stability of their mechano-activation after culture in physiologic environments, including residence *in vivo* (subcutaneous implantation) and in the context of maturing tissue engineered constructs.

METHODS

Spherical MAMCs were fabricated using a glass capillary microfluidic device [5]. An inner solution of bovine serum albumin (BSA) (with Alexafluor488-BSA for visualization) was used as a model drug while the middle phase contained 85:15 poly (lactic co-glycolic) acid (PLGA) (with Nile Red for visualization). MAMCs were collected in various molar solutions of NaCl. This was done to increase collecting solution osmolarity and cause capsule shrinkage during hardening (osmotic annealing). After hardening, MAMC diameter and shell thickness were measured using confocal microscopy. To probe MAMC mechano-activation in a 3D 'repair'/tissue maturation model, small (D: 30.7μm, t: 2.8μm) and large (D: 54.5μm, t: 1.6μm) MAMCs (at $1.2x10^5$ MAMCs/mL per type) were embedded into a 2% agarose hydrogel along with bovine MSCs ($60x10^6$ cells/mL). Cylindrical constructs (⌀=4mm, t=2.25mm) were cultured for 5 weeks in chondrogenic media (+TGF-β3) (**Fig. 1A**). At 1 and 5 weeks, constructs were subjected to Live/Dead staining, sectioned and stained for glycosaminoglycan (GAGs, Alcian Blue) and collagen (Picrosirius Red) content, and tested for mechanical properties [6]. Additional samples were dynamically compressed between parallel plates (from 2-20% strain at 5Hz) for 1 or 5 hrs. and subsequently imaged to determine mechanically-induced release of MAMC contents (**Fig. 1B-F**).

In another study, MAMC stability was analyzed in basal media (with 10% FBS) and bovine synovial fluid *in vitro* for up to 28 days at 37ºC (**Fig. 2A-B**). To investigate MAMC stability in a physiological environment, small or large MAMCs were embedded in 500kPa PEGDA hydrogels at 0.2% v/v and implanted subcutaneously in athymic rats for up to 28 days (**Fig. 2C**). At day 7 and 28, rats were sacrificed and hydrogels were extracted and imaged, after which they underwent dynamic compression as previously described (**Fig. 2, C-D**) to probe their retention of mechano-activation. Normally distributed data was analyzed by one-way or two-way ANOVA followed by Tukey's post-hoc; non-normally distributed data was analyzed via Kruskal-Wallis test with Dunn's Multiple Comparison or Bonferroni post-hoc.

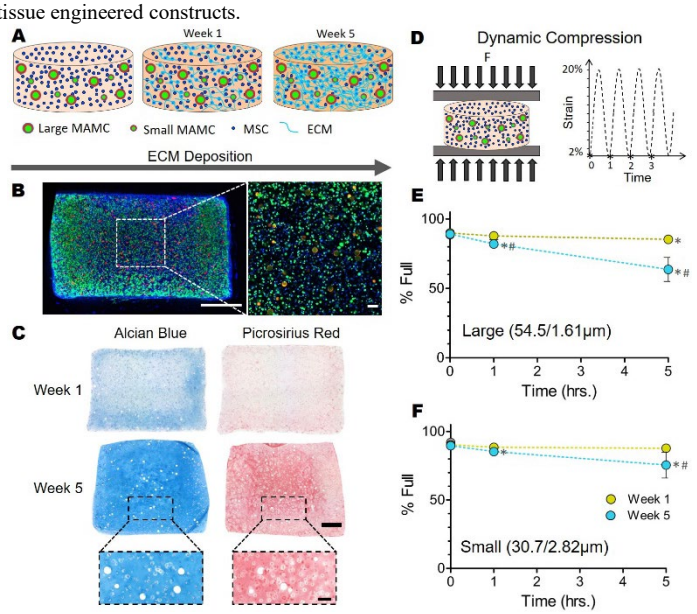

Figure 1: Large and small MAMCs were embedded in MSC-seeded hydrogels and cultured for 5 weeks (A). Cells remained viable at 5 weeks (live cells = green, nuclei=blue, MAMC shells = red) (B). Constructs matured with time, as evidenced by increased GAG and collagen staining (C). With dynamic compression (D), large MAMCs (E) were more susceptible to rupture than small MAMCs (F) in mature constructs. (Scale bar of full gel =1mm, zoom in =100um: * p<0.05 vs. 0 hrs, # vs. Week 1)

RESULTS

MAMCs of different thickness and diameter were prepared through controlled osmotic annealing. Those with thicker shells and smaller diameters (i.e. higher t/D ratio) had an increased resistance to rupture. MSC-laden constructs matured over time, as illustrated by an increase in GAG and collagen staining around encapsulated MAMCs (**Fig. 1C**). The construct equilibrium modulus increased from 17.8 ± 4.7kPa at week 1 to 149.2 ± 20.5kPa at week 5. This increased matrix stiffness resulted in greater activation of MAMCs within constructs when subjected to 5 hrs. of dynamic loading on day 28, with larger MAMCs remaining more sensitive to load (**Fig. 1E**) compared to smaller MAMCs (**Fig. 1F**). Large MAMCs were less stable over time *in vitro* in synovial fluid, while small MAMCs remained patent (and retained their inner contents) over a 28-day period in all solutions (**Fig. 2A-B**). A similar trend was observed with MAMCs implanted subcutaneously, yet by 28 days, a greater percentage of MAMCs of both sizes had lost patency compared to *in vitro* incubation (**Fig. 2C**). However, large MAMCs continued to rupture more than small ones after 5 hrs. of dynamic compression (**Fig. 2E**).

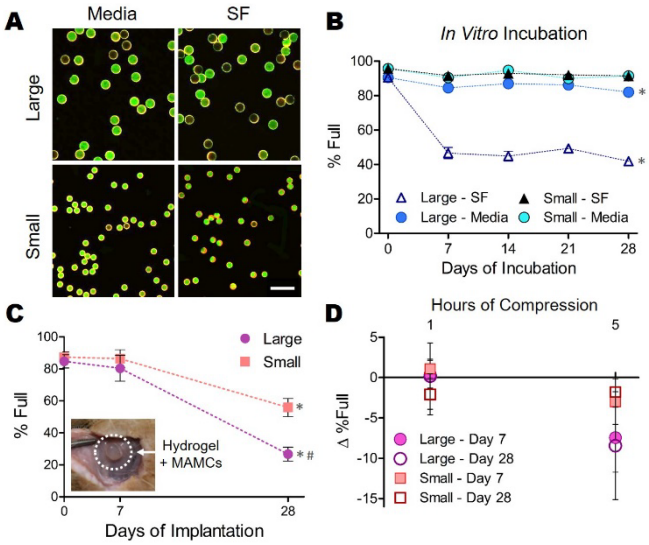

Figure 2: Small MAMCs remained stable over time while large MAMCs were less stable in synovial fluid (SF) incubation by day 28 (A-B). In the same manner, after subcutaneous implantation for up to 28 days (C, inset), small MAMCs were more stable over time *in vivo* than larger MAMCs (C). Large MAMCs ruptured more with increased dynamic loading than small MAMCs (D). (* p≤0.05 vs. Day 0 or 0 hrs, # vs. Media, 30.7/2.8μm)

DISCUSSION

In this study, we expanded the range of microcapsule dimensions that could be produced, creating a suite of MAMCs with a wide range of mechano-sensitivity and stability profiles. Furthermore, we demonstrated the utility of MAMCs in a healing, matrix growth and maturation setting by showing higher activation of MAMCs upon sufficient matrix deposition (compared to little activation before matrix production). MAMCs in cell-laden constructs did not alter cell viability or hinder matrix production, and these co-encapsulated MAMCs retained their contents throughout culture. We also evaluated, for the first time, MAMC stability in an *in vivo* setting. Varying MAMC size and shell thickness resulted in different MAMC stability profiles with *in vivo* incubation, with higher t/D MAMCs demonstrating higher stability both *in vitro* and *in vivo*. Taken together, these data demonstrate the potential of this MAMC technology for on-demand mechanically-mediated drug delivery. Utilizing MAMCs with different rupture profiles could enable the sequential delivery of different therapeutic molecules necessary at different stages of healing and regeneration, providing improved tissue repair and more rapid return to function.

ACKNOWLEDGEMENTS

This work was supported by the National Institutes of Health (R01 AR071340) and the Penn Center for Musculoskeletal Disorders.

The surface zone of articular cartilage is maintained as a unique tissue in synovial joints

Danielle Rux[1], Kimberly Helbig[1], Maurizio Pacifici[1]

[1]*Translational Research Program in Pediatric Orthopaedics, Children's Hospital of Philadelphia*

Synovial joints are essential for skeletal function and body movement. Unfortunately, articular cartilage (AC) is highly susceptible to congenital- and age-related diseases and exhibits poor repair capacity that current clinical strategies fall short of amending. To improve these strategies, more information is needed on mechanisms of AC development during postnatal stages, and maintenance and response to injury during adulthood. Mature AC consists of: flat, lubricant-producing surface zone cells; round, column-aligned, and load-resistant intermediate zone cells; and mineralized, deep zone cells that attach to bone. A long-held hypothesis proposes that the surface zone acts as the first point of protection against osteoarthritis and that damage to the surface zone leads to progressive destruction of the underlying articular cartilage, making surface zone cells an ideal target for therapeutic intervention. These cells secrete lubricants into the joint capsule (including *Prg4*/lubricin) and have also been suggested to include stem cells for articular cartilage maintenance and injury response. Overall, it is clear that the surface zone is crucial to articular cartilage function, but mechanisms by which this layer of cells accomplishes these tasks and is maintained remain ambiguous. The goal of our ongoing study was to assess surface zone dynamics/turnover during adult life.

Recently, we generated a *Prg4CreERt2* transgenic mouse allele that enables examination of *Prg4*-expressing cells (namely, the surface zone of articular cartilage) throughout growth, aging and injury. In this study, we combined this allele with fluorescent reporters knocked into the Rosa26 locus (Rosa-GFP, Rosa-tdTomato, and Rosa-Mosaic) and made use of wholemount confocal and 2-photon imaging of the tibial plateau. We induced with low-dose tamoxifen at two stages during early adulthood (8 or 18 weeks) in order to label a limited number of cells and monitored animals up to 1 year of age. We observed two key findings: 1- surface zone cells contribute primarily to turnover of the surface zone rather than contributing to underlying layers of chondrocytes, and 2-turnover is dependent on spatial location (lateral vs. medial condyle and anterior vs. posterior) suggesting differential maintenance mechanisms. Given these preliminary studies, we propose that the surface zone is a unique tissue in articular cartilage maintained distinctly from the underlying deep zone articular chondrocytes and that it responds in a region-dependent manner to meet loading demands of the joint. Ongoing work is focused on understanding the dynamics and mechanical responses of surface zone cells and identifying morphogenetic mechanisms required to their characteristics. These mechanisms could represent targets of therapeutic intervention against joint deterioration/osteoarthritis in the future.

Aberrant muscle tissue repair by mutant ACVR1 FOP muscle stem cells

Alexandra Stanley, Elisia Tichy, Jacob Kocan, Foteini Mourkioti, and Eileen M. Shore

Perelman School of Medicine, University of Pennsylvania, Department of Orthopaedic Surgery, Cell and Developmental Biology, 3450 Hamilton Walk, Philadelphia, PA 19104, USA.

In the rare genetic disease fibrodysplasia ossificans progressiva (FOP), progenitor cells are mis-regulated to differentiate to heterotopic extra-skeletal bone in connective tissues. Mutations in the BMP type I receptor ACVR1/ALK2 cause FOP, with the R206H mutation as the most prevalent. This increases BMP signaling to promote increased downstream chondro-/osteogenic gene expression and heterotopic ossification (HO) formation in FOP patients. HO formation is often initiated by injury to skeletal muscle. In the conditional knock-in mouse model for $ACVR1^{R206H}$, HO develops within skeletal muscle cardiotoxin (CTX) injury. Additionally, injured $Acvr1^{R206H/+}$ muscle tissue appears more fibrotic and does not repair as efficiently as $Acvr1^{+/+}$ muscle tissue, indicating that skeletal muscle repair is impeded by the $ACVR1^{R206H}$ mutation. The regenerative potential of skeletal muscle is dependent on the function of muscle stem cells (MuSCs). Additionally, non-myogenic mesenchymal progenitor cells (or fibro/adipogenic progenitors, FAPs) are in close association with regenerating muscle fibers and support myogenesis; these cells, considered mesenchymal progenitors based on their ability to differentiate to adipocytes and osteoblasts, are a source of pro-myogenic signals that support muscle regeneration. We examined the effect of the $ACVR1^{R206H}$ mutation on MuSCs and FAPs alone by isolating the two populations using fluorescent activated cell sorting (FACS) and analyzed proliferation. $Acvr1^{+/+}$ and $Acvr1^{R206H/+}$ MuSCs and FAPs proliferated similarly after CTX injury. We investigated the ability of $Acvr1^{+/+}$ and $Acvr1^{R206H/+}$ MuSCs to differentiate *in vitro*. $Acvr1^{+/+}$ MuSCs cultured in myogenic media differentiate normally and form branching myofibers (high fusion index) by day 7 of culture, but $Acvr1^{R206H/+}$ MuSCs form underdeveloped fibers that fail to fuse (low fusion index). $Acvr1^{+/+}$ FAPs cultured with $Acvr1^{R206H/+}$ MuSCs leads to proper myofibers formation and fusion, while $Acvr1^{R206H/+}$ FAPs cultured with $Acvr1^{+/+}$ MuSCs form undeveloped fibers with a low fusion index. This suggests that the FAP population under the influence of the $ACVR1^{R206H}$ mutation contributes largely to the poor muscle regeneration seen in FOP lesions. We also demonstrate the effect of environment on MuSC repair capacity, with decreased engraftment of $Acvr1^{+/+}$ MuSCs transplanted into injured $Acvr1^{R206H/+}$ skeletal muscle tissue. Taken together, our data support the impact of the $ACVR1^{R206H}$ FOP mutation on the differentiation capacity of MuSCs to regenerate skeletal muscle and the impact of FAPs on the function of MuSCs.

Differential Mechanics and Healing Outcomes of Small and Large Partial-Width Defects in the Tendon Attachment of the Rat Rotator Cuff

Anna Lia Sullivan, Rachel Klink, Ryan C. Locke, Megan L. Killian
University of Delaware, Newark, DE

Disclosures: None

INTRODUCTION: Partial-width rotator cuff tears are common musculoskeletal injuries that can propagate into large tears that require surgical intervention [1]. Healing and mechanical outcomes following surgical intervention remain highly variable [2]. Pre-clinical studies have primarily focused on understanding the healing and/or degenerative processes of full-width rotator cuff tears [3,4], however how rotator cuff tear progression occurs in vivo remains elusive. Our lab recently developed an in vivo rat model of small-width rotator cuff defects [5, 6]. These injuries increase strain concentrations at the remaining intact attachment [6] and heal via fibrosis [5], but do not propagate into full width tears in vivo [5]. In this study, we aimed to compare healing and mechanical outcomes of a large-width tear to a small-width tear. We hypothesized that small and large defects heal via fibrosis but that defect size matters, and that large defects would propagate into a full-width tears after 3-weeks and have poorer healing outcomes (e.g., increased fibrosis/cellularity), and that larger defect widths would result in worsened mechanical outcomes with critical defect size at which mechanical properties are reduced drastically.

METHODS: Mature Long Evans rats (n=4 previous dams, 321 ± 9g) were used under the accordance of the University of Delaware IACUC. Under anesthesia (isoflurane carried by oxygen), rats underwent a surgical procedure to model small- and large-width full-thickness tears of the infraspinatus (IS) tendon attachment using 0.3mm (small) and 0.75mm (large) punch biopsies (Robbins). IS tendons were exposed and biopsy punched at the tendon-bone interface (depth extended into the cortical bone). The shoulder (left or right) that received a small or large defect was alternated between rats using controlled randomization. The surgery site was closed using sutures (5-0 Vicryl), and rats were given bupivacaine hydrochloride (0.05mg/kg) as analgesia. Rats were euthanized at 3-weeks post-surgery and shoulders were dissected to expose the IS attachment. Images were taken under a stereoscope using a digital camera. Samples were fixed in 4% paraformaldehyde for 24-48hours then scanned in air using micro-computed tomography (microCT; 1276 Skyscan; Bruker). MicroCT images were reconstructed and aligned (DataViewer, Bruker) and the following morphometry was measured using CTan software: defect width, height, area, and bone volume (BV), tissue volume (TV), BV/TV ratio, and bone mineral density (BMD) for both humeral head and injury regions. After microCT, samples were decalcified in EDTA and processed for paraffin histology. Samples were sectioned at 6µm thickness and stained using Hematoxylin & Eosin (H&E) to qualitatively assess fibrosis and cellularity. Sections were stained with DAPI and imaged at 3 individual locations within the attachment ($0.024mm^2$/image) to quantify cell number and aspect ratio using a custom MATLAB code. Technical replicates were averaged, and paired t-tests were used to compare paired small and large defects for all microCT outcomes, collagen alignment, cell number, and aspect ratio (Prism, v7, GraphPad). For ex vivo mechanics, long-Evans rats (N = 14, all female retired breeders, 3-7 months old) were used. Humeri-infraspinatus (IS) tendon complexes were bilaterally dissected and defects were made in the IS attachment using 0.3 mm (small) or 0.75 mm (large) diameter biopsy punches (Robbins). A 0.1 N tare load was applied, and gauge length was recorded before uniaxial tensile tests began (Instron 5943). Extension, ultimate load, and tendon CSA were measured to calculate maximum stress, strain at maximum stress, stiffness, Young's modulus, and area under the curve (AUC) at maximum stress using a custom MATLAB script. The AUC of the last five pre-conditioning cycles of the load-extension (energy loss) curves were assessed per sample using a one-way, repeated measure ANOVA. If no significant variance was present within samples, the AUC of the last five pre-conditioning curves were averaged per sample to measure energy loss. Paired t-tests were used to compare mechanical outcomes between small and large defect groups and one-way ANOVAs with Dunnett's correction for multiple comparisons was used to compare mechanical outcomes of defect groups to intact attachments from [6] using Prism (version 7, GraphPad).

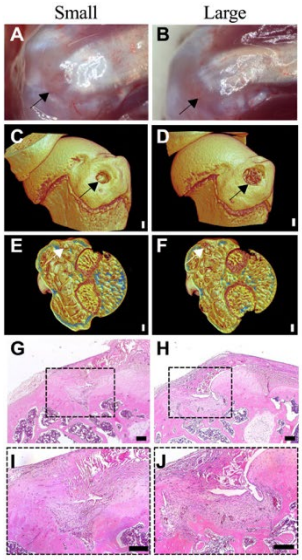

Figure 1. Qualitatively, large partial-width defects remove more tendon attachment and cortical bone, resulting in a less organized tendon and increased cellularity after 3 weeks of healing. Gross images of (A) small and (D) large defects following 3 weeks of healing. Three-dimensional microCT reconstructions of the humeral head in the (C,D) frontal and (E,F) transverse plane through defect. Histological sections stained with H&E of (G&I) small and (H&J) large defects in the transverse plane. Arrowheads = defect. Scale bars in G-J = 100µm.

RESULTS: Even with large defects, no defects propagated into full-width tears. Increased neovascularization was observed for large defects compared to small defects (Fig1 A-D). Large defects had decreased BMD, TV, and BV in the injury region compared to small defects (Fig1 C-F, Fig2 D-E). Qualitatively, a decrease in attachment/tendon organization was observed in large compared to small defects (Fig1 G-J). Cell number was higher in large defects (Fig2F). For ex vivo mechanics modeling acute injury, CSA of the remaining intact attachment was smaller in the large compared to the small defect group (Fig2A). Ultimate load was 25% reduced in large compared to small defects (Fig2B). No other properties had significant differences between the small and large defect groups. Yet, energy loss was greater in large compared to small defects in 70% of paired tests (Fig2C). Ultimate load, stiffness, and AUC were lower in both defect groups compared to intact attachments, corroborating findings of [6] (Fig2B).

DISCUSSION: Larger defects led to increased fibrosis and neovascularization compared to smaller defects. A substantial difference in mechanical outcomes between the two defect sizes was not found, which may suggest that a critical defect to the rat rotator cuff attachment is smaller than 0.3 mm (~1/3 of the attachment width) and/or larger than 0.75 mm (~3/4 of the attachment width). Further studies should compare longer healing time points (e.g., 8 weeks) and the biomechanical consequences of defect size in the healing attachment. Although tear propagation was not found after 3 weeks, a longer time point and/or modulated muscle loading (e.g., treadmill running) may lead to propagation. This recently established model of partial-width full-thickness tears can aid in the research of novel therapies to heal critically sized tendon tears.

SIGNIFICANCE/CLINICAL RELEVANCE: Rotator cuff tears can propagate into full-width tears and require surgical intervention. Determining the width of tears that propagates into a full-width tear in a small animal model is important for developing novel treatments that improve healing of partial tears and to prevent tear propagation in the clinic.

REFERENCES: [1] Miller, et al. J Biomech, 2018. [2] Hersch, et al. Am J Sports Med, 2000. [3] Bell, et al. J Orthop Res, 2014. [4] Killian, et al. AJSM, 2015. [5] Lemmon, et al. Conn Tiss Res, 2018. [6] Locke, et al. J BioMech Eng, 2018.

ACKNOWLEDGEMENTS: This research was conducted under the Delaware NASA Space Grant (# NNX15AI19H).

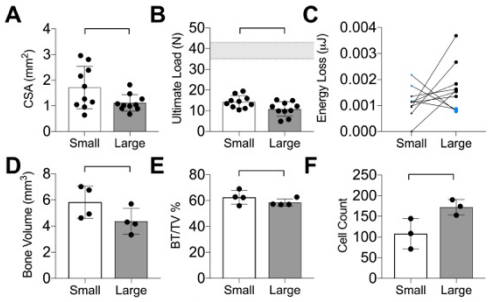

Figure 2. In acute injury large defects, ultimate load and CAS were lower and energy loss trended higher for large defects. Following 3 weeks of healing, large defects had decreased bone quality and quantity with increased cellularity compared to small defects. (A) CSA and (B) ultimate load were lower for large defects. (C) Energy loss, shown as pairs, trended higher for large defects. (D) Bone volume in the injury region, (E) bone volume over total volume of the injury region was smaller for large defects compared to small defects. (F) The number of cells was higher at the injured attachment in large defects compared to small defects. Bars: significant differences ($p<0.05$). Data shown as mean ± standard deviation.

Identification of Gli1 as a progenitor cell marker for meniscus injury repair

Yulong Wei[1], Hao Sun[1], Lutian Yao[1], Leilei Zhong[1], Wei Yu[1], Su Chin Heo[1], Lin Han[2], Fanxin Long[3], Robert L Mauck[1], Jaimo Ahn[1], Ling Qin[1]
[1]Department of Orthopaedic Surgery, School of Medicine, University of Pennsylvania; [2]Drexel University School of Biomedical Engineering; [3]Translational Research Program in Pediatric Orthopaedics, The Children's Hospital of Philadelphia, Philadelphia, Pennsylvania, USA

Disclosures: Yulong Wei (N), Hao Sun (N), Lutian Yao (N), Leilei Zhong (N), Wei Yu (N), Su Chin Heo (N), Lin Han (N), Fanxing Long (N), Robert L Mauck (N), Jaimo Ahn (N) Ling Qin (N)

Introduction: Meniscal tears are one of the most common injuries of the knee. They are likely to be an important early event in the initiation and later propagation of osteoarthritis (OA) and have been accepted as an important risk factor for OA clinically. As a treatment, meniscal resection has been demonstrated to accelerate degenerative disease and the most commonly performed surgery of partial meniscectomy is not restorative and only delays degeneration. Surgical repair remains a viable treatment for only a small portion of individuals. Various approaches, including stem cell transplantation, have been proposed to repair injured meniscus. However, meniscus-specific progenitors are still largely unknown. Gli1 was recently recognized as a marker for bone marrow and periosteal mesenchymal progenitor (1, 2). In this study, we constructed *Gli1-CreER Tomato (Gli1ER/Td)* mice and analyzed the progenitor properties of Gli1-labeled meniscus cells in development, homeostasis, and injury repair.

Methods: *Animals-* *Gli1-CreER* mice were crossed with *Rosa-tdTomato* mice to obtain *Gli1ER/Td*. Mice at various ages received Tamoxifen (Tam) injections (50 mg/kg x 2 days in pups and 75 mg/kg x 5 days in adults). *Surgery-* Male mice at 3 mo of age received Tam followed by surgical transection of the medial meniscus in right knees and sham operation in left knees a week later. During the surgery, the joint capsule was opened and the anterior horn of the medial meniscus was cut into two parts. For cell treatment, 5000 FACS sorted meniscus cells (Td^+ or Td^- cells) were injected into the knee joint space right after meniscus surgery. For activator treatment, 2 µl Purmorphamine (1 mM) were injected into the knee joint space right after surgery. All procedures were approved by the Institutional Animal Care and Use Committee (IACUC) at the University of Pennsylvania. *Cell culture-* Primary meniscus cells were enzymatic digested from the meniscus of 4-wk-old *Gli1ER/Td* mice. FACS sorted Td^+ and Td^- cells were used for CFU, migration, proliferation, differentiation, and qRT-PCR assays. *Histology-* Knee joints were fixed in 4% PFA, decalcified in 10% EDTA, and processed for cryosections or paraffin sections. *Human meniscus samples-* They were prepared from de-identified specimens obtained at the total arthroplasty of the knee joints. Paraffin sections were stained by Safranin O/Fast green to evaluate degenerative stages and neighboring sections were used for Gli1 staining. *Statistics-* Data are expressed as means±SEM and analyzed by paired, two-tailed Student's t-test.

Results: In *Gli1ER/Td* mice, Td did not label meniscus cells in newborn pups (Tam at P5-6). In 2-wk-old mice (Tam at P9-14), Td initially labeled the entire anterior meniscus and gradually concentrated at the superficial cells by 8 wk of age. Td started to label the posterior meniscus in 4-wk-old mice and also later focused on superficial cells only. In adult animals, Td^+ cells only occurred in the superficial layer of meniscus right after Tam injections and long term tracing did not detect their expansion (Fig. 1). In culture, Td^+ cells generated much more CFU-Fs (2.55-fold) and grew much faster than Td^- cells (Fig. 2A). Using an activator (Purmorphamine) and an inhibitor (GANT-61) of hedgehog (Hh) pathway, we found that primary meniscus cells proliferate and migrate in an Hh-dependent manner (Fig. 2B, C). Td^+ meniscus cells also had the abilities to differentiate into osteoblasts and adipocytes (Fig. 2D). During meniscal differentiation, Td^+ cells expressed 2.9-fold more *Col1a1* and 61.2% less *Col2a1* than Td^- cells. After meniscus injury, Td^+ cells quickly emerged at the injury ends and proliferated (Fig. 3). Without treatment, two ends remained separated 3 mo later. However, injection of Td^+ cells, but not Td^- cells, from *GliER/Td* meniscus into the joint capsule of *WT* mice right after injury resulted in the reconnection of two ends within a month (Fig. 4). Injection of Purmorphamine also exhibited a strong repair effect. After meniscus injury, OA generally developed in the cartilage 2 mo later. Strikingly, injection of Td^+ cell or Hh activator right after surgery significantly delayed OA initiation (Fig. 5). Analyzing human meniscus samples from OA patients confirmed an increase of Gli^+ cells in meniscus during degeneration (Fig. 6).

Discussion: By using a lineage tracing line, cell culture, and a meniscus injury model, we demonstrated that Gli1 is a mesenchymal progenitor marker in mouse meniscus. Gli1-labeled cells contribute to meniscus development and injury response. Activation of Gli1/hedgehog signaling in adult meniscus leads to accelerated meniscus healing process in response to surgically induced meniscus degeneration, indicating a protective role of hedgehog signaling on meniscus against degeneration. Analyzing Gli1 expression profile in human meniscus samples with different meniscus degenerative stages strongly implicates the clinical relevance of our study.

Significance: Our studies uncover the critical role of Gli1 in adult knee meniscus and provide proof-of-principle evidence for targeting this novel pathway as meniscus injury therapy for preventing OA development.

References: 1) Shi Y et al. Nat Commun. 2017;8(1):2043; 2) Wang L et al. J Bone Miner Res. 2019;34(3):520-532.

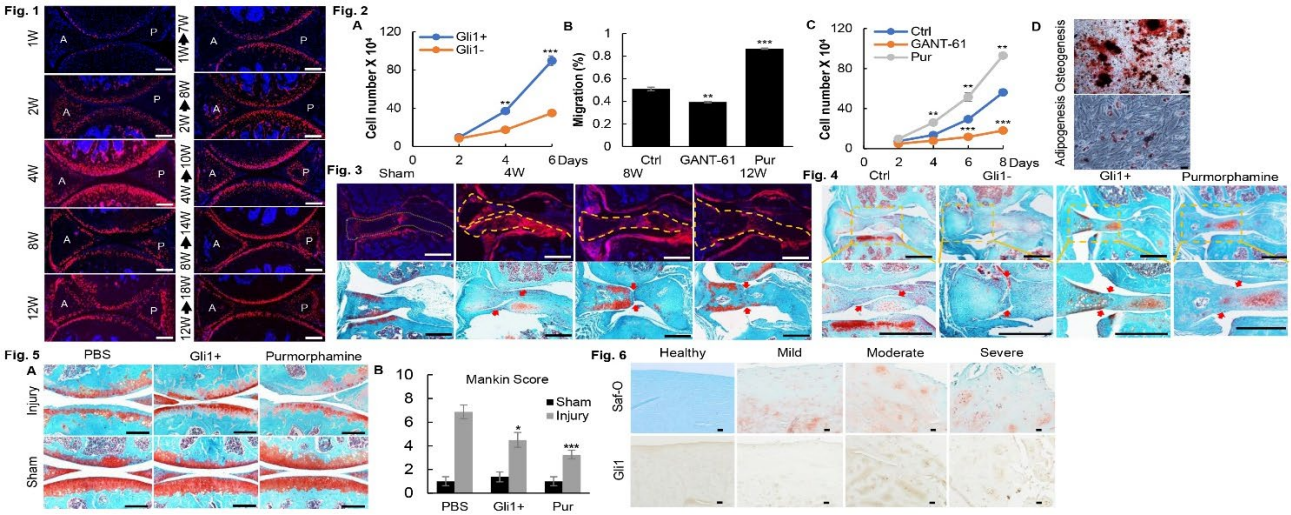

Figure 1. The distribution of $Gli1^+$ cells and their progenies in mouse meniscus during development and homeostasis. *Gli1ER/Td* mice received Tam injections at various ages and their joints were harvested right after injections (left panel) or 6 weeks later (right panel) for sagittal cryosections. A and P represent the anterior and posterior side of meniscus, respectively. n=5/age. **Figure 2. $Gli1^+$ cells exhibit mesenchymal progenitor properties in vitro.** (A) The growth curve of sorted $Gli1^+$ and $Gli1^-$ meniscus cells. (B, C) The growth curve (B) and migration ability (C) of primary meniscus cells treated with GANT-61 (1 µM) or Purmorphamine (0.1 µM). **P<0.01, ***P<0.001 vs Control. (D) Osteogenic (Alizarin Red staining) and adipogenic (Oil Red O staining) differentiation of sorted $Gli1^+$ primary meniscus cells. n=3/group. **Figure 3. Mouse meniscus does not heal at 3 mo post injury.** *Gli1ER/Td* mice received Tam injections at 12 wk of age followed by meniscus injury. Joints harvested at various times were sectioned at a coronal plane for fluorescent image of Td signal (top panel) and Safranin O/Fast Green staining (bottom panel). n=8/group. Red arrows point to injury sites. **Figure 4. Activating Hh signaling promotes meniscus repair.** At 4 wk post injury, mouse knees received Gli1-labeled meniscus cells or Purmorphamine injections right after surgery showed reconnection of two meniscus ends. Red arrows point to prior meniscus injury sites. n=8/group. Bottom panels are magnified images of top panels. **Figure 5. Meniscus repair delays OA initiation.** (A) Safranin O staining of mouse knee joints (sagittal sections) at 8 wk postsurgery. Mice received PBS, $Gli1^+$ cell or Purmorphamine treatment right after surgery. (B) The OA severity was measured by Mankin score. n=10/group. *P<0.05, ***P<0.001 vs PBS injury. **Figure 6. Human meniscus samples from OA patients show a positive correlation between meniscus degeneration severity and Gli1 expression.** n=5/group. Scale bar in all images, 200 µm.

Regulation of phalangeal joint development by *ACVR1* in fibrodysplasia ossificans progressive

O. Will Towler[1,4,5], Sun Peck[6], Frederick S. Kaplan[1,2,4], & Eileen M. Shore[1,3,4,5]

Departments of Orthopaedic Surgery[1], Medicine[2], Genetics[3]; the Center for Research in FOP and Related Disorders[4]; Cell and Molecular Biology Graduate Group[5]; Perelman School of Medicine at the University of Pennsylvania, Philadelphia, PA; Department of Medicine, Division of Clinical Pharmacology, Vanderbilt University Medical Center, Nashville, TN, USA[6]

Fibrodysplasia ossificans progressiva (FOP; MIM #135100) is a genetic disease of heterotopic ossification accompanied by short, laterally deviated great toes. FOP is caused by an activating mutation in the BMP receptor ACVR1/ALK2. To investigate the skeletal developmental phenotype of FOP, we used a conditional knock-in mouse model (MGI:5763014) with the FOP ACVR1 R206H mutation to examine digit and joint formation *in vivo*. Mice expressing the FOP mutation globally or in limb mesenchymal cells *(Prrx1+)* exhibited stunted hindlimb first digits similarly to FOP patients, but also revealed generalized delayed digit development with fused phalanges. Histological analyses revealed disorganized, interphalangeal chondrocytes in mutant mice. Three-dimensional whole-mount pSmad1/5 immunohistochemistry and imaging of embryonic mouse limbs revealed unrestricted BMP signaling throughout the developing digit rays of mutant animals, supporting that BMP pathway activity from the mutant receptor was insufficiently inhibited in the joint space. Together, these data suggest that improper spatiotemporal activation of chondrogenic pathway signaling in the joint space is precipitated by dysregulated BMP pathway signaling through the mutant ACVR1 receptor during development and contributes to skeletal abnormalities in FOP.

Dynamics of Modeling- and Remodeling-Based Bone Formation in response to intermittent parathyroid hormone (PTH) in Male, Female, and Ovariectomized (OVX) Rats

Wenzheng Wang, Wei-Ju Tseng, Hongbo Zhao, Nathaniel Dyment, X. Sherry Liu
[1]McKay Orthopaedic Research Laboratory, Department of Orthopaedic Surgery, University of Pennsylvania, Philadelphia, PA;
Wenzheng.Wang@pennmedicine.upenn.edu

Activation of modeling-based bone formation (MBF), *i.e.*, bone formation without prior activation of bone resorption, has been identified as an important mechanism by which anabolic agents, such as teriparatide (PTH1-34), rapidly elicit new bone formation. To study the dynamics of MBF and remodeling-based bone formation (RBF), we injected calcein (green, G), alizarin complexone (red, R), and tetracycline (yellow, Y) fluorochrome labels to rats in a G-R-Y-G sequence at days -2, 5, 12, 19 (initiation of PTH on day 0), followed by euthanasia at day 21. Based on multi-color fluorochrome labels and cement lines on cryo-sections (Fig A-D), BF sites were identified as MBF (smooth cement line) or RBF (scalloped cement line) in the rat tibial trabecular bone and further stratified by activation time (within wk1, 2, and 3, Fig G). We hypothesized that MBF and RBF respond differently to PTH and between male and female rats.

Mineralizing surface (MS/BS) between MBF and RBF did not differ in vehicle (VEH)-treated 7-mo-old female (n=6), male (n=6), or OVX rats (n=3, OVX at age 4mo, Fig E). 3-wk PTH treatment (equivalent to ~18 mo treatment in human) led to 7.7, 3.3 and 4.6 fold greater MBF-induced MS/BS compared to VEH group in female, male, and OVX rats (n=5-6/group), respectively (Fig E). In contrast, PTH resulted in greater RBF-induced MS/BS only in females (3.6 and 2.9 fold greater vs. VEH for intact and OVX rats, respectively), but not in males (Fig E). No difference in mineral apposition rate (MAR) between MBF and RBF was found in either VEH or PTH groups (Fig F).

39, 51, and 10% of all RBF sites activated by PTH occurred during wk1, 2, and 3, respectively. In contrast, 85% of all MBF sites in response to PTH were activated within wk1, resulting in MS/BS and bone formation rate (BFR/BS) 5.5 and 5.9 fold greater than those of RBF during wk1 in intact females (Fig H&I). During wk2, MBF and RBF induced similar levels of MS/BS and BFR/BS. Despite minimal activation of new bone formation during wk3, the MAR of both MBF and RBF were greater than those of wk1 and 2 (Fig J). Similar dynamics of MBF and RBF in response to PTH were found in male and OVX rats (data not shown).

In summary, MBF and RBF have similar contributions to trabecular bone homeostasis in adult rats. PTH induces new bone formation by programming rapid activation of new MBF, followed by continuous activation of RBF. Compared to female rats, males are less responsive to PTH in activating RBF.

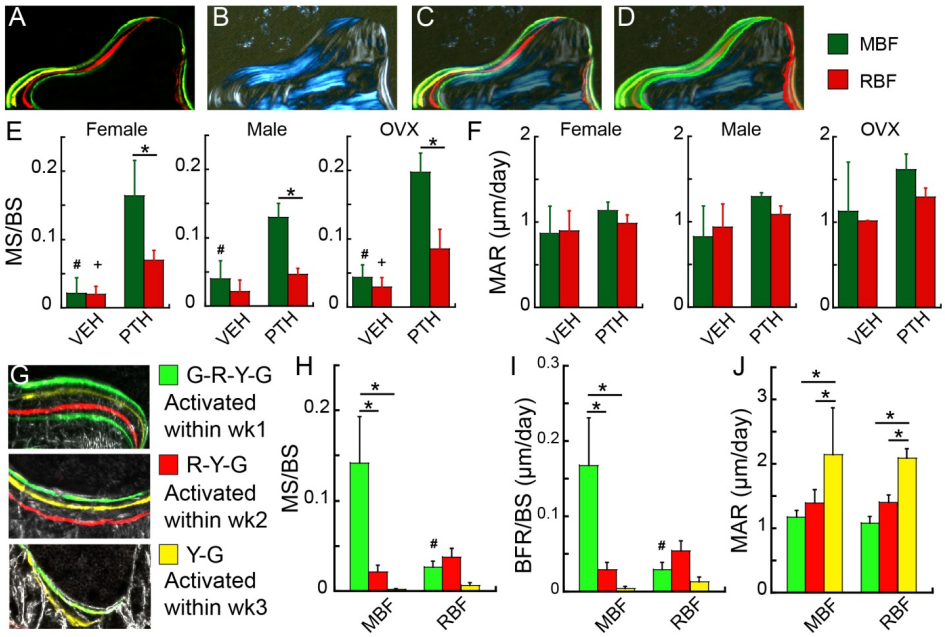

Representative MBF and RBF sites under (A) fluorescent imaging; (B) polarized imaging for cement line; (C) A-B merged; and (D) MBF highlighted in green and RBF in red. (E) MS/BS and (F) MAR of MBF and RBF in response to 3-wk treatments of VEH and PTH, respectively. $p<0.05$: * MBF≠RBF; # MBF: VEH≠PTH; + RBF: VEH≠PTH. (G) Bone formation sites stratified by activation time based on fluorochrome labels. (H) MS/BS; (I) BFR/BS; and (J) MAR of MBF and RBF stratified by activation time in intact female rats treated with PTH. $p<0.05$: * between different activation time; # wk1: MBF≠RBF.

The Regulatory Role of EGFR Signaling in Adult Cartilage Homeostasis and Osteoarthritis

Yulong Wei[1], Xiaoyuan Ma[1], Hao Sun[1], Biao Han[2], Lin Han[2], Frank Beier[3], Motomi Enomoto-Iwamoto[4], and Ling Qin[1]

[1]Department of Orthopaedic Surgery, School of Medicine, University of Pennsylvania, Philadelphia, Pennsylvania, USA; [2]School of Biomedical Engineering, Science and Health Systems, Drexel University, Philadelphia, Pennsylvania, USA; [3]Department of Physiology and Pharmacology, Western University, London, ON, Canada; [4] Department of Orthopaedics, School of Medicine, University of Maryland, Baltimore, Maryland, USA

The uppermost superficial zone of articular cartilage is the first line of defense against the initiation of osteoarthritis (OA). We previously demonstrated that EGFR, a tyrosine kinase receptor, plays an essential role in maintaining superficial chondrocytes during articular cartilage development. Immunostaining of human samples showed that the top layer of cartilage has abundant amounts of EGFR, activated EGFR (p-EGFR), and ligands (TGFa and HB-EGF), but a low amount of Mig6, a cytosolic inhibitor of EGFR. When OA initiated, p-EGFR drastically decreased in the superficial zone, accompanied with decreases of ligand amounts and an increase of Mig6 amount. At late OA stage, EGFR activity resurged in most cell clusters in the middle/deep zones. The same expression patterns were also observed in mouse knee OA cartilage. To investigate the role of EGFR signaling in adult cartilage, we generated cartilage-specific EGFR deficient mice (Aggrecan-Cre Egfrflox/Wa5, iCKO) and WT (Egfrflox/+) and Wa5 (EgfrWa5/+, an EGFR dominant negative allele) siblings. Male mice received Tam injections followed by sham/DMM surgery at 3 months of age. One month later, sham iCKO knees displayed less p-EGFR and Ki-67 staining and more TUNEL staining in the superficial chondrocytes, and 3 months later, reduced cartilage thickness (12% vs Wa5, 29% vs WT, n=6/group, $p<0.01$) and diminished superficial chondrocytes (69% vs Wa5, 83% vs WT, n=6/group, $p<0.01$), suggesting that EGFR signaling is critical for adult cartilage homeostasis. Nanoindentation on femoral cartilage surface revealed that DMM causes a similar decrease of Eind in WT and Wa5 cartilage but an increase of Eind in iCKO 1 month post surgery (n=6/group, $p<0.001$), suggesting that iCKO has more advanced OA progression. At 2 months, iCKO joints showed severer erosion of articular cartilage than controls. At 3 months, iCKO joints lost most articular cartilage (Mankin Scores: WT 7.57, Wa5 10, iCKO 13.5, n=9/group, $p<0.001$), displayed subchondral bone plate thickening and cartilage damage at the lateral site, which did not exist in controls, and showed heigher joint pain scores than controls. Importantly, susceptibility to OA was more clearly evident in female mice (Mankin scores: WT 4, Wa5 7.67, iCKO 12.43, n=7/group, $p<0.001$) at 2 months post DMM compared to male mice. Taken together, our data demonstrated that chondrogenic EGFR signaling is essential for adult cartilage homeostasis and for preventing OA initiation.

Gli1 labels a subpopulation of FAP cells that respond to muscle injury

Lutian Yao[1](Lutian.yao@pennmedicine.upenn.edu), Elisia D. Tichy[1], Leilei Zhong[1], Luqiang Wang[1], Foteini Mourkioti[1,2,3], Ling Qin[1]
[1]Department of Orthopaedic Surgery, [2]Department of Cell and Developmental Biology, [3]Penn Institute for Regenerative Medicine, Musculoskeletal Program, Perelman School of Medicine, University of Pennsylvania, Philadelphia, PA 19104, USA

Disclosures: None

INTRODUCTION: Skeletal muscle has a remarkable capacity for regeneration after injury. Recently, a new type of muscle-resident progenitor cell, referred to as fibro-adipogenic progenitors (FAPs), was identified to be critical in supporting the process of injured muscle regeneration[1]. To date, FAPs remains a poorly defined, heterogeneous population without any specific genetic markers. Gli1 was recently recognized as a marker for bone marrow and periosteal mesenchymal progenitor[2, 3]. In this study, we used *Gli1-CreER* to label FAPs and characterized their changes in healthy, aged, and diseased muscle.
METHODS: *Animals-* All animal work performed in this report was approved by the Institutional Animal Care and Use Committee (IACUC) at the University of Pennsylvania. *Gli1-CreER Rosa-tdTomato* (*Gli1ER/Td*) mice were generated by breeding *Rosa-tdTomato* mice with *Gli1-CreER*. *Gli1ER/Td/mdx* mice were generated by breeding *Gli1ER/Td* mice with *mdx*^{4cv} mice[4]. To induce *CreER* activity, mice received tamoxifen (Tam) injections (75 mg/kg/day) at 2 months of age for 5 days. Acute muscle injury was induced by injection of 10 µl Notexin (10 µg/mL) into Tibialis Anterior (TA) muscle. *Histology-* TA muscle samples were fixed in 4% PFA for 1 day, and then immersed into 30% sucrose at 4°C overnight. They were processed for cryosections followed by H&E, WGA, Biodipy, Sca1, PDGFRα, or αSMA antibodies staining. *FAP cell isolation-* Hindlimb muscles (quadriceps, gastrocnemius, and tibialis anterior) were dissected and enzymatically dissociated with 0.1% collagenase and 4.8 units/mL dispase in DMEM using the gentleMACs system. The cell slurry was pulled through a 21-gauge needle until all remaining muscle tissue was broken apart, after which the cell solution was filtered through a 40 µm cell strainer. After red blood cell lysis, cells were stained with lineage cell markers (CD45, CD31, CD11b), Sca1, α7-integrin (Itga7) and CD34 antibodies for flow analysis. *Statistics-* Data are expressed as means±SEM and analyzed by unpaired, two-tailed Student's t-test.
RESULTS: In the TA muscle of *Gli1ER/Td* mice, Td$^+$ cells were exclusively located in the interstitial area of myofibers after Tam induction (Fig. 1A). The majority of them were co-stained with FAP markers, PDGFRα and Sca1 (Fig. 1B). Quantification revealed that Gli$^+$ cells constitute a small portion of PDGFRα$^+$Sca1$^+$ FAPs (Fig. 1C). In flow analysis, FAPs are defined by Lin$^-$Sca1$^+$CD34$^+$Itga7$^-$. In line with the staining data, Td$^+$ cells were mostly FAPs (97.4% Lin-, 78.5% Sca1$^+$, 78.2% CD34$^+$/Itga7$^-$, Fig. 1D) and they labeled 3.2±0.1% and 7.6±0.5% of digested muscle cells at P66 and P72, respectively (Tam at P61-65). Meanwhile, 10.9±0.7% and of 17.3±0.3% FAPs at P66 and P72, respectively, were Td$^+$ cells (Fig. 1E). In 1-year-old mice, the percentage of FAP cells in digested muscle cells decreased to 7.94±0.6% and *Gli1-CreER* labeled cells (95.15±4.45 cells/mm^2) reduced drastically compared to adult mice (147.09±14.98 cells/mm^2, n=3/age, p<0.05). Though initially presented at a low level in freshly digested muscle cells, Td$^+$ cells constituted 40% of confluent cells after culturing (Fig. 2A). Sorted Td$^+$ cells exhibited fibroblastic and adipogenic differentiation abilities, but not osteogenic differentiation ability (Fig. 2B). To investigate their in vivo function, *Gli1ER/Td* mice received Notexin intramuscularly at P72 (Tam at P61-65) to create acute muscle injury. Td$^+$ cells peaked at day 3 post injury, gradually decreased at day 6, and almost receded to normal levels by day 9 (Fig. 3A, B). To further validate the role of Gli1-labeled cells in chronic injury, we crossed *Gli1ER/Td* mice with dystrophic *mdx*^{4cv} mice. After Tam at P61-65, Td$^+$ cells were significantly increased in the interstitial area of myofibers of *Gli1ER/Td/mdx* muscle compared to *Gli1ER/Td* control muscle (P72, control: 198.81±22.66 cells/mm^2, mdx: 360.33±53.70 cells/mm^2, n=6/group, P<0.05, Fig. 3C).
DISCUSSION: In our study, we demonstrated that *Gli1-CreER* labels a subpopulation of FAP cells that undergo age-dependent reduction. Interestingly, they show the same response kinetics of FAPs after acute and chronic muscle injury, suggesting that Gli1-labeled subpopulation of FAP cells play a predominant role in the regeneration process of injured skeletal muscles. Since Gli1 is an effector of Hedgehog (Hh) signaling, our data also implied a possible role of Hh signaling in regulating FAP action.
SIGNIFICANCE: We identified *Gli1-CreER* as a suitable model to genetically target a subpopulation of FAPs that respond to muscle injury. Understanding the cellular and molecular mechanism of FAPs is crucial for designing new treatments to promote muscle regeneration under aging and diseased conditions.
References: 1. Wosczyna, M. N. & Rando, T. A. Dev cell. 2018;46, 135-143. 2. Shi, Y. et al. Nat commun, 2017;8, 2043. 3. Wang, L. et al. J Bone Miner Res. 2019; 34, 520-532. 4. Tichy, E. D. & Mourkioti, F. Muscle nerve. 2017; 56, 522-524.

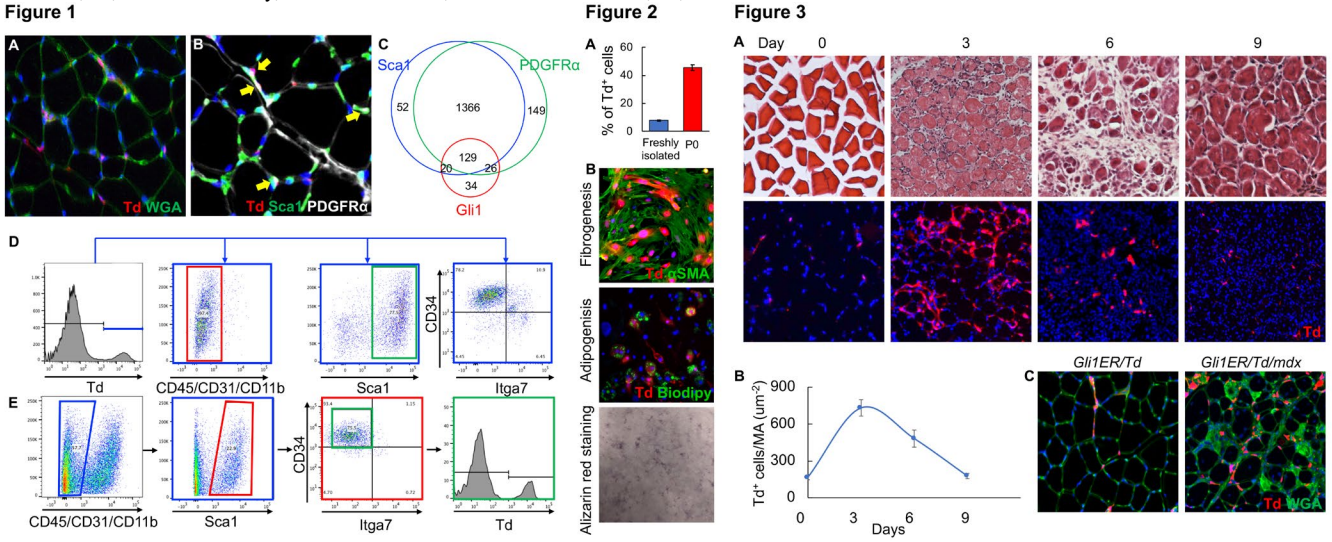

Figure 1. Td in the muscle of *Gli1ER/Td* mice labels a subpopulation of FAPs. (A) Td$^+$ cells located in the interstitial area of TA muscle in *Gli1ER/Td* mice. (B) Td$^+$ cells co-express FAP staining markers, Sca1 and PDGFRα (yellow arrows). (C) Venn diagram of Sca1$^+$, PDGFRα$^+$, and Td$^+$ cells in TA muscles. (D) Examination of FAP flow markers on Td$^+$ cells. (E) A portion of FAPs identified by flow are Td$^+$. **Figure 2. Td$^+$ cells in the muscle of *Gli1ER/Td* mice are FAPs in vitro.** (A) The percentage of Td$^+$ cells in freshly digested muscle cells and in cultured P0 cells. (B) Sorted Td$^+$ cells can differentiate into fibroblasts (αSMA$^+$) and adipocytes (biodipy$^+$) but not osteoblasts (Alizarin red staining). **Figure 3. Td$^+$ cells in the muscle of *Gli1ER/Td* mice rapidly response to muscle injury.** (A) HE staining (top panel) and immunofluorescence of Td$^+$ cells (bottom panel) in TA muscles at day 0, 3, 6 and 9 post Notexin-induced muscle injury. (B) The time course of Td$^+$ cells after injury. MA: muscle area. (C) Immunofluorescence of Td$^+$ cells in TA muscles of control and dystrophic *mdx*^{4cv} mice.

Reduced inflammation in injured tail intervertebral disc of TIPE and TIPE2-deficient mice

Yejia Zhang, MD, PhD; Zuozhen Tian, MS; Honghong Sun, PhD; Hongtao Zhang, PhD; Youhai H. Chen, MD, PhD.

Email address and telephone number of contact: yejia.zhang@uphs.upenn.edu; Phone: 215-868-9951 (cell)

Introduction. TNF-α-induced protein-8 (TNFAIP8, known as TIPE) family members are known to regulate inflammation, at least in part, by regulating leukocyte polarization and migration.(1, 2) Furthermore, TIPE family molecules may up- or down- regulate cell apoptosis, depending on the context. We hypothesize that genetic inactivation of TIPE/TIPE2 results in reduced inflammation in the injured mouse tail IVD. Down-regulation of TIPE activity could represent a therapeutic tool to reduce IVD inflammation and back pain.

Methods. In order to identify targets to reduce IVD inflammation, we have acquired and are currently maintaining colonies of mutant mice lacking two members of the family ($TIPE^{-/-}$, $TIPE2^{-/-}$). Macrophage infiltration and inflammatory cytokine or chemokine gene expression in injured mouse tail IVD tissues in TIPE and TIPE2-deficient mice were compared with those in wild type (WT) controls.

We have recently developed a mouse tail injury model. In this model, the coccygeal (C) 3/4 and C5/6 IVDs in the mouse tail were injured with a 26G needle, and C4/5 and C6/7 served as intact controls. We have acquired and are now maintaining mouse colonies lacking TIPE and TIPE2 (the knockout mice were generated by Dr. Youhai Chen's group). In addition, Dr. Chen's group maintains mice lacking both TIPE and TIPE2 (TIPE and TIPE2 double knockout (dko)). $TIPE^{-/-}$, $TIPE2^{-/-}$, TIPE and TIPE2 dko or WT mice on the B6 background were first subjected totail IVD injury, and sacrificed 24 hours or 1 week after the injury. C3/4 and C4/5 injury/intact control pairs were isolated for gene expression studies by real-time PCR, and C5/6 and C6/7 pairs were isolated en-bloc for morphological studies including immunostaining for macrophage marker (F4/80 antibody, Invitrogen).

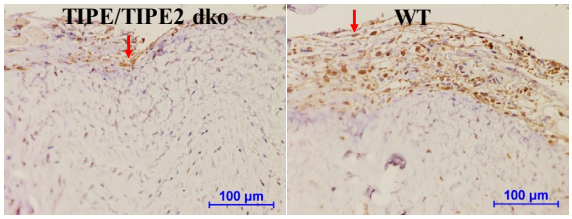

Figure 1. TIPE/TIPE2 double knock out (dko) mouse shows reduced macrophage recruitment compared with wild type (WT) mouse. Red arrow: direction of intervertebral disc injury.

Results. Our preliminary studies have shown that macrophage recruitment to the injured IVD is diminished in the TIPE/TIPE2 dko mice, while macrophages infiltrate the entire AF in the WT mice (n=5 or 3, respectively; Figure 1). We have further shown that IL-6 gene expression in the injured $TIPE^{-/-}$ IVDs is lower than in WT controls (n=6, p=0.0154). IL-6 expression in $TIPE2^{-/-}$ mouse IVD was not statistically significant from that in WT mice (n=6, p=0.4557). Cxcl1 gene expression showed a trend towards reduction in the $TIPE^{-/-}$ IVDs compared with WT controls (n=6, p=0.0847).

Discussion. We have demonstrated reduced IVD macrophage infiltration in TIPE/TIPE2 dko mice post injury. We have further shown a trend of reduced IL-6 gene expression in injured mouse tail IVD tissues in TIPE mice compared with WT controls. Our preliminary data now indicate that TIPE molecules may be key regulators in IVD inflammation, and represent new therapeutic targets for treating the disease.

Significance. The annual costs of spinal conditions related to intervertebral disc (IVD) degeneration exceed $190 billion dollars in the US. Despite the prevalence and soaring cost, there is no specific treatment that restores the physiological function of the diseased IVD. In this study, we aimed to examine the roles and mechanisms of TIPE family members in regulating IVD inflammation, and to develop novel treatment strategies.

References

1. Fayngerts SA, Wang Z, Zamani A, Sun H, Boggs AE, Porturas TP, et al. Direction of leukocyte polarization and migration by the phosphoinositide-transfer protein TIPE2. Nat Immunol. 2017 Dec;18(12):1353-60. PMCID: PMC5690821.

2. Sun H, Gong S, Carmody RJ, Hilliard A, Li L, Sun J, et al. TIPE2, a negative regulator of innate and adaptive immunity that maintains immune homeostasis. Cell. 2008 May 2;133(3):415-26. PMCID: PMC2398615.

Inflammatory Cytokine and Catabolic Enzyme Expression in a Goat Model of Intervertebral Disc Degeneration

Chenghao Zhang[1,2], Thomas P. Schaer[1], Sarah E. Gullbrand[1,2], Zhirui Jiang[1,2], Yian Khai Lau[1,2], Dawn M. Elliott[3], George R. Dodge[1,2], Robert L. Mauck[1,2], Neil R. Malhotra[1] and Lachlan J. Smith[1,2]
[1]University of Pennsylvania, Philadelphia, PA; [2]Corporal Michael J. Crescenz Philadelphia VA Medical Center, Philadelphia, PA; [3]University of Delaware, Newark, DE
chenghao.zhang@pennmedicine.upenn.edu

Disclosures: Chenghao Zhang (N), Thomas P. Schaer (N), Sarah E. Gullbrand (9-ORS Spine Section), Zhirui Jiang (N), Yian Kai Lau (N), Dawn M. Elliott (N), George R. Dodge (N), Robert L. Mauck (9-JOR Spine), Neil R. Malhotra (N) and Lachlan J. Smith (5-Ultragenyx; 9-ORS Spine Section).

INTRODUCTION: Intervertebral disc degeneration is implicated as a leading cause of low back pain. Persistent, localized inflammation within the disc nucleus pulposus (NP) and annulus fibrosus (AF) is considered to be a key mediator of disc degeneration, and is associated with downstream catabolic enzyme activity and extracellular matrix destruction. Disc inflammation is characterized by expression of cytokines including IL-1β, IL-6 and TNF-α, amongst others, with expression levels positively correlating with severity of degeneration [1]. There is currently a lack of validated preclinical animal models of disc degeneration that recapitulate clinically-relevant, persistent local disc inflammation. We recently described a goat model of disc degeneration in which increasing doses of chondroitinase ABC (ChABC) were used to reproducibly induce a spectrum of structural, biomechanical and histological degenerative changes [2]. The objective of this study was to evaluate and extend the clinical-relevance of this model by establishing whether these degenerative changes are associated with tissue-level expression of inflammatory cytokines and downstream catabolic enzymes.

METHODS: With IACUC approval, 9 adult male goats underwent surgery to induce degeneration of the lumbar intervertebral discs. Using an open, lateral, retroperitoneal transpsoatic approach, L1-2, L2-3 and L3-4 lumbar discs were randomized to receive either subtotal mechanical nucleotomy (n=4) or injection of 200μL of 0.1U, 1U or 5U ChABC via a 22G spinal needle (n=4 per dose). The L4-L5 disc (n=4) received a sham saline injection, and the T13-L1 and L5-L6 discs served as intact controls. Animals were euthanized 12 weeks after surgery, and lumbar spines harvested. Discs were imaged using a 3T MRI scanner, and NP T2 and T1ρ relaxation times were determined [2]. Discs (with bony endplates intact) were then isolated, fixed in formalin, decalcified, and processed for paraffin histology. Mid-sagittal sections were double stained with either Alcian blue (glycosaminoglycans) and picrosirius red (collagen), or hematoxylin and eosin. Severity of degeneration was established via semi-quantitative histological grading [2]. Immunohistochemistry was performed to investigate expression of inflammatory cytokines (IL-1β, IL-6, TNF-α) and catabolic enzymes (MMP-1, MMP-13 and ADAMTS4) in the NP and AF. Sections were counterstained with hematoxylin and imaged using bright field microscopy. Expression levels were quantified by determining the percentage of positive vs. total cells in the NP and AF. Differences in expression between groups were established using Kruskal-Wallis tests with post-hoc Dunn's tests ($p<0.05$). Spearman rank correlations between degenerative condition (histology and MRI scores) and expression levels of cytokines and enzymes were determined.

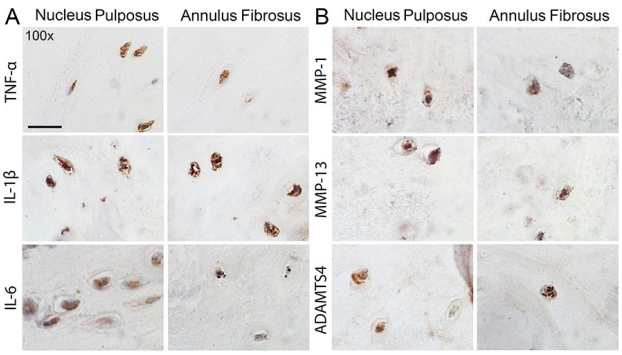

Figure 1. Immunostaining of **A.** Cytokines and **B.** Enzymes in the NP and AF of degenerate (1U ChABC-treated) goat discs. Scale=20μm.

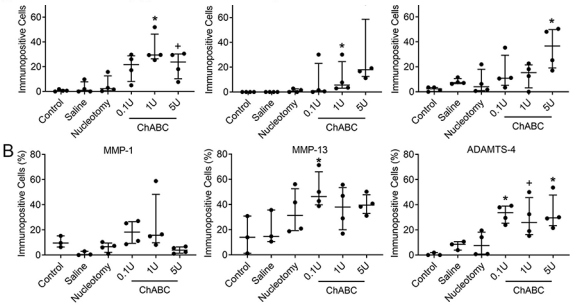

Figure 2. Effects of different surgical interventions on expression levels of **A.** Cytokines and **B.** Enzymes in the NP. N=4; *p<0.05 and +p<0.1 vs Control.

RESULTS: Positive cytokine and enzyme staining was found to various degrees in the NP and AF of most discs (examples, Fig 1). Multiple comparisons tests revealed significant effects of intervention type on expression levels of inflammatory cytokines and catabolic enzymes in both the NP (Fig 2) and AF (not shown). For cytokines, TNF-α expression was significantly elevated in 1U ChABC discs compared to controls, while IL-1β and IL-6 expression were significantly elevated in both the NP and AF of 5U ChABC discs. For enzymes, MMP-13 was significantly elevated in the NPs of 0.1U ChABC discs, while ADAMTS-4 was significantly elevated in the NP and AF of both 0.1 and 5U ChABC discs compared to controls. In general, both cytokine and enzyme expression levels were positively correlated with histological grade, and negatively correlated with MRI T2 (Fig 3) and T1ρ times.

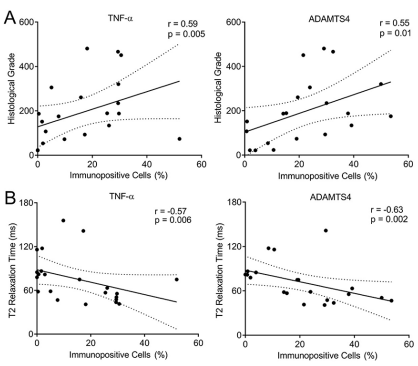

Figure 3. Correlations between NP cytokine and enzyme expression levels and **A.** Overall histological grade; and **B.** NP MRI T2 times.

DISCUSSION: Localized inflammation is a defining feature of human disc degeneration and is a key mediator of tissue breakdown and painful innervation. Anti-inflammatory therapies such as catabolic cytokine inhibitors [3,4] have the potential to slow the degenerative cascade and provide a microenvironment more conducive to stem cell-based disc regeneration; however, the absence of a preclinical animal model that effectively recapitulates inflammation represents an impediment to effective translation of such therapies. In this study, we provide evidence that an established goat model of disc degeneration is characterized by elevated expression of clinically-relevant inflammatory cytokines and downstream catabolic enzymes. This model exhibits significantly elevated expression in moderately to severely degenerate discs treated with ChABC, suggesting that these discs may provide the most suitable models for evaluating anti-inflammatory therapies. We also show that non-invasive, quantitative MRI is a reliable predictor of the inflammatory state of the disc. We are currently applying this model towards our goal of evaluating anti-inflammatory and cell-based therapies for disc regeneration.

SIGNIFICANCE: Anti-inflammatory and cell-based therapies represent promising treatment strategies for painful disc degeneration. The animal model described here provides a platform for preclinical evaluation of such therapies and progressing them towards clinical use.

REFERENCES: [1] Risbud+ Nat Rev Rheumatol 2014; [2] Gullbrand+ Osteoarthritis Cartilage 2017; [3] Gorth+ Arthritis Res Ther 2012; [4] Sainoh+ Pain Med 2016.

ACKNOWLDEGMENTS: This work was supported by the Department of Veteran's Affairs and the Penn Center for Musculoskeletal Disorders.

Identification of a novel adipose lineage cell population that regulates bone marrow environment

Leilei Zhong[1] (leileiz@pennmedicine.upenn.edu), Lutian Yao[1], Robert J. Tower[1], Yulong Wei[1], Luqiang Wang[1], Wei Yu[1], Yejia Zhang[1], Yanqing Gong[2], Fanxin Long[1], Patrick Seale[3], Chider Chen[4], Jaimo Ahn[1], and Ling Qin[1]

[1]Department of Orthopaedic Surgery, [2]Division of Transnational Medicine and Human Genetics, [3]Cell and Developmental Biology, Perelman School of Medicine, [4]Department of Oral and Maxillofacial Surgery/Pharmacology, University of Pennsylvania, Philadelphia, PA 19104, USA.

Disclosures: None

Introduction: Bone marrow adipocytes are conventionally viewed as large cells containing unilocular lipid droplets. Originally considered as space fillers, they are now thought to be a negative regulator of osteogenesis because both adipocytes and osteoblasts are derived from bone marrow mesenchymal stem cells (MSCs). We recently applied single cell RNA-sequencing (scRNA-seq) on sorted bone marrow mesenchymal lineage cells from 1-mo-old mice that has very few marrow adipocytes. Unexpectedly, we identified a large mesenchymal subpopulation that expresses many mature adipocyte markers (*Pparg, Cebpa, Adipoq, Apoe*, and *Lpl*) but not liqid droplet-associated genes (*Perilipin* and *Fabp4*). Here, we constructed mature adipocyte-specific *Adipoq-Cre(ER) Rosa-tdTomato (Adipoq(ER)/Td)* mice to validate this novel cell population and study their actions in bone.

Methods: *Animals-* All animal work performed was approved by the Institutional Animal Care and Use Committee (IACUC) at the University of Pennsylvania. *Col2/Td*, *Adipoq/Td, AdipoqER/Td* mice were obtained by crossing *Rosa-tdTomato* mice with *Col2-Cre*, *Adipoq-Cre, Adipoq-CreER* mice, respectively. *Adipoq/Td/DTR* mice were generated by breeding *Adipoq/Td* mice with *Rosa-DTR* mice. *AdipoqER/Td* mice received Tamoxifen (Tam) injections (75 mg/kg/day) at P6 and P7 and euthanized at 1 mo of age. *Adipoq/Td/DTR* mice received vehicle or diphtheria toxin (DT, 50 μg/kg) every other day for 2 wk. For focal radiation, mouse right femur received a clinically relevant radiation dose of 5 Gy using small animal radiation research platform (SARRP). *Immunofluorescence-* Bones were processed for 50 μm-thick whole mount cryosections and stained with indicated antibodies. *Transplantation-* Freshly FACS-sorted Td^+ cells ($5x10^4$/transplant) were mixed with Gelfoam and placed under the kidney capsule of 2-mo-old *C57Bl/6* mice. 4 wk later, mice received calcein injection (15 mg/kg) 1 day before harvesting grafts. *Statistics-* All analyses were conducted using t-tests.

Results: Td labeled all $Perilipin^+$ adipocytes, many $CD45^-$ stromal cells, and pericytes, but not osteoblasts, osteocytes, and chondrocytes in 1-mo-old *Adipoq/Td* mice (Fig.1A). The majority of Td^+ cells (99.8%) did not harbor lipid droplets and none of them incorporated EdU (Fig.1B,C). Td^+ cells constituted ~18% of $CD45^-Ter119^-$ bone marrow cells. After isolation, they attached to the culture dish but did not form CFU-F colonies (Fig. 1D). While Td^+ cells from *Col2/Td* mice (in which Td labels mesenchymal progenitors) formed bony structure after transplantation, freshly sorted Td^+ cells from *Adipoq/Td* mice did not (Fig.1E), indicating that they are not mesenchymal progenitors. Upon adipogenic differentiation, Td^- mesenchymal progenitors from *Adipoq/Td* mice first became Td^+ cells with no lipid droplets and then evolved into Td^+ cells with lipid (Fig. 1F). Similar cell culture results were also obtained with *AdipoqER/Td* mice. Fate mapping in postnatal *AdipoqER/Td* mice confirmed that $Perilipin^+$ lipid-laden adipocytes are derived from non-lipid-laden Td^+ adipocytes (Fig. 1G). In the bone marrow of young *Adipoq/Td* mice, all pericytes identified by PDGFRβ or Laminin staining in a peri-capillary location were Td^+ (Fig. 2A). Strikingly, using whole mount sectioning and confocal scanning, we found that bone marrow Td^+ stromal cells and pericytes form a 3D network made of cell processes to communicate amongst themselves and other components of bone, including vessel walls (Fig 2B). Ablating those cells in 1-mo-old *Adipoq/Td/DTR* mice after 2 wk of DT injections disrupted bone marrow vasculature and caused drastic *de novo* bone formation in the diaphyseal bone marrow (Fig. 3), suggesting that those cells function in maintaining vessel integrity and inhibiting osteogenesis. Focal radiation on long bones rapidly expanded the non-lipid-laden Td^+ cells at d3, accompanied with vessel dilation and a loss of Td^+ pericytes (Fig. 4). By d7, both vessel structure and Td^+ pericyte density returned to relatively normal levels. These data implied a role of Td^+ adipocytes in the repair and stabilization of marrow vessels after radiation injury.

Discussion: Our study demonstrate that bone marrow contains a large number of non-proliferative, mature adipocytes with no significant lipid stores. Those cells represent a stable transitional cell type situated after mesenchymal progenitors and before classic lipid-laden adipocytes along the adipogenic differentiate route. They are morphologically and functionally distinct from traditional adipocytes. Existing as stromal cells or pericytes, they possess numerous cell processes to form a vast 3D network structure in bone marrow. Our scRNA-seq data suggest that they express many secretory factors, including angiogenic factors. Most likely through secreting these factors into marrow environment, they play pivotal roles in maintaining marrow vasculature, suppressing osteogenic differentiation of mesenchymal progenitors, and participating into vessel repair after radiation injury. Therefore, we name them marrow environment regulating adipose cells (MERAs).

Significance: We discovered a novel type of adipose lineage cell population that regulates bone marrow environment.

Fig. 1

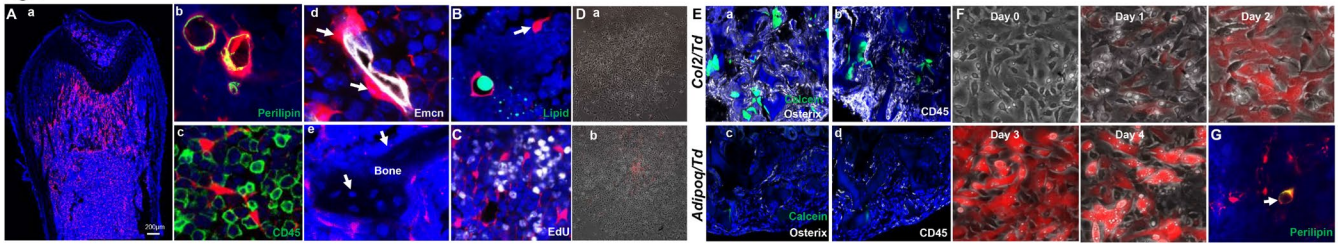

Fig. 2 Fig. 3 Fig. 4

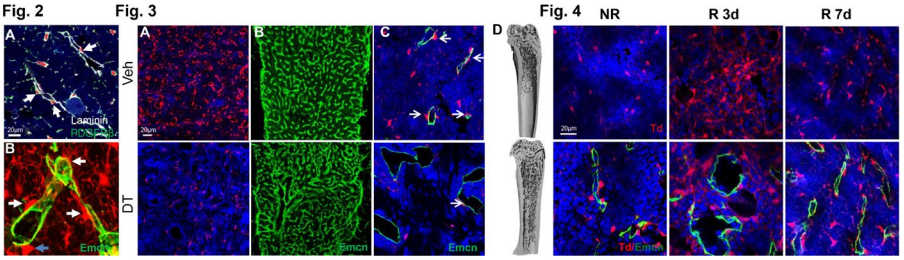

Figure 1. Mouse bone marrow contains abundant non-lipid-laden adipocytes. (A) In a 1-mo-old *Adipoq/Td* femur (a), Td labels $Perilipin^+$ adipocytes (b), $CD45^-$ stromal cells (c), pericytes (d), but not osteoblasts and osteocytes (e). (B) BODIPY lipid staining shows a Td^+ stromal cell (arrow) with no lipid. (C) Td^+ cells do not incorporate EdU. (D) all CFU-F colonies are made of Td^- cells (a) while some Td^+ cells do attach to the dish (b). (E) Td^+ cells from *Col2/Td* mice, but not *Adipoq-Td* mice, form bone-like structure. (F) In vitro adipogenic differentiation assay of Td^- mesenchymal progenitors from *Adipoq/Td* mice. The same area was imaged daily. (G) Bone marrow $Perilipin^+$ adipocytes are derived from non-lipid-laden Td^+ adipocytes in 1-mo-old *AdipoqER/Td* mice (Tam injections at P6, 7 when no $Perilipin^+$ cells can be detected in the bone marrow). **Figure 2. Non-lipid-laden Td^+ cells are stromal cells and pericytes forming a 3D network inside the bone marrow.** (A) All PDGFRβ$^+$ and $Laminin^+$ cells with a pericyte morphology are Td^+ (arrows). (B) Td^+ stromal and pericytes are morphologically similar with many cell processes. **Figure 3. Ablation of adipocytes reveals their roles in maintaining vasculature and bone.** (A) Bone marrow Td^+ cells in *Adipoq/Td/DTR* mice were ablated by DT. (B) DT altered bone marrow vessel structure. (C) High magnified image showed that vessels were dilated coinciding with a depletion of Td^+ pericytes. (D) 3D μCT images show drastic *de novo* bone formation in femoral midshaft after DT injections. **Figure 4. Adipocytes are required for the recovery of bone marrow vasculature after radiation injury.** Fluorescent images of total Td^+ cells (top) and pericytic Td^+ cells (bottom) in the bone marrow of 1-mo-old *Adipoq/Td* femurs before (NR) and after (R) focal radiation (3 and 7 days).

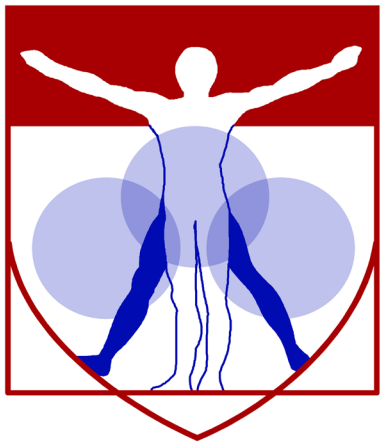

PENN

CENTER for

MUSCULOSKELETAL

DISORDERS

MicroCT Abstracts

A machine learning approach to identify the primary features of *in vivo* disc degeneration

Beth G. Ashinsky[1,2,3], Chao Wang[2], Sai A. Mandalapu[1,3], Edward D. Bonnevie[1,3], Stephen Pickup[1], Lin Han[2], Robert L. Mauck[1,3], Harvey E. Smith[1,3], Sarah E. Gullbrand[1,3]

[1]University of Pennsylvania, Philadelphia, PA; [2]Drexel University, Philadelphia, PA; [3]Corporal Michael J. Crescenz VA Medical Center, Philadelphia, PA

Disclosures: Beth G. Ashinsky (N) Beth.ashinsky@gmail.com, Chao Wang (N), Sai A. Mandalapu (N), Edward Bonnevie (N), Stephen Pickup (N), Lin Han (N), Robert L. Mauck (JOR Spine), Harvey E. Smith (N), Sarah E. Gullbrand (N)

INTRODUCTION: Intervertebral disc (IVD) degeneration is a causative factor in back pain. Despite the immense clinical burden of back pain, the etiology and pathogenesis of disc degeneration remain poorly understood [1]. Genetic factors, disc cell catabolism, aberrant mechanical loading, and reduced nutritional transport into the avascular disc have all been suggested as contributors to end stage disease [3]. Further, IVD degeneration is a multifactorial process that can be described using a spectrum of cellular, compositional, structural and functional changes to the nucleus pulposus (NP), annulus fibrosus (AF), and boney and cartilage endplates (EP) [2]. These attributes are rarely studied in concert, and therefore, their relative contributions to degeneration remain unknown. The purpose of this study was to use an animal model to quantify the structure-function properties of the degenerating spinal motion segment, and use a machine learning model to identify which of these quantitative measurements would be the most informative features of disease status.

METHODS: Following IACUC approval, 29 male New Zealand white rabbits underwent a surgical procedure to puncture 4 lumbar spine levels per animal [4,5]. The adjacent, non-punctured levels were utilized as healthy controls. Animals were euthanized 2, 4, 8, and 12 weeks post puncture and motion segments were harvested for analysis. At each time point, motion segments underwent T2 MRI to quantify disc composition [4], and post-contrast enhanced T1 mapping to assess disc nutrition [2]. Following MRI, motion segments were subjected to tension-compression and creep mechanical testing [4]. Motion segments (n=4-6 per group) underwent μCT scanning to quantify bone volume (BV) fraction and trabecular (Tb.) morphometry parameters in the vertebral EP. Following μCT, atomic force microscopy (AFM)-nanoindentation (n=3-5 per group) was performed on fresh, 20μm thick cryosections at the inner AF, outer AF, AF-EP and NP-EP interfaces, using microspherical tips ($R \approx 12.5$ μm), to calculate the effective indentation modulus, E_{ind} [6]. Motion segments were dissected into AF and NP components to assess biochemical composition via the hydroxyproline (collagen) and dimethylmethylene Blue (glycosoaminoglycan, GAG) assays [4]. A subset of animals (n=1-3 per time point), were reserved to quantify perfusion fraction of the EP via μCT scanning following perfusion of the spinal vasculature with microFil. Additional motion segments (n=3-5 per group) were processed for paraffin histology, sectioned to 10μm thickness, and stained with alcian blue/picrosirius red (GAG/collagen), hematoxylin and eosin (H&E, cellular morphology), or Mallory-Heidenhain trichrome (vascularity). The erythrocyte staining of the Mallory-Heidenhain stained sections was thresholded in ImageJ, and used to calculate vessel area and number for each sample. Slides stained with alcian blue/picrosirius red and H&E were used for histology grading (total 0-500) of AF organization (0-100), AF-NP border acuity (0-100), NP matrix (0-100) and cellularity (0-100), and EP structure (0-100), by two blinded, independent observers [7]. The above assays yielded total of 23 quantitative input parameters that are listed in **Fig. 1A**. These parameters were used as inputs (predictors) into a neural network model (**Fig. 1B**), using the multilayer perceptron (MLP) algorithm, for classification of total histology score (SPSS Modeler). Training of the MLP was performed on iterations of 75% of the dataset using backpropagation, and testing was performed on the remaining 25% of the samples. The algorithm was optimized by minimizing the cross-entropy loss function, and the resulting error values were propagated through each layer of the network, such that each neuron was assigned an error value (bias term) that reflects its contribution to the output.

RESULTS: Progressive degeneration of the disc occurred with time post-puncture, and was accompanied by substantial remodeling of the vertebral bone, vasculature, and cartilage endplate [4]. Mean (+/- standard deviation) of total histology scores for the control, 2, 4, 8 and 12 week groups were 16.8 (17.3), 155.8 (68.5). 210.7 (202.6), 308.2 (31.2), and 258.6 (77.0), respectively (**Fig.1C**). Using 6 hidden layer neurons, the neural network model (**Fig. 1B**) predicted the target variable (histology score) with 95% accuracy. The model identified %T1 reduction in the NP (indicating small molecule diffusion into the NP), outer AF and EP-AF indentation modulus, NP collagen content, and NZ ROM, as parameters with the highest weighted contributions (**Fig 1A-B**).

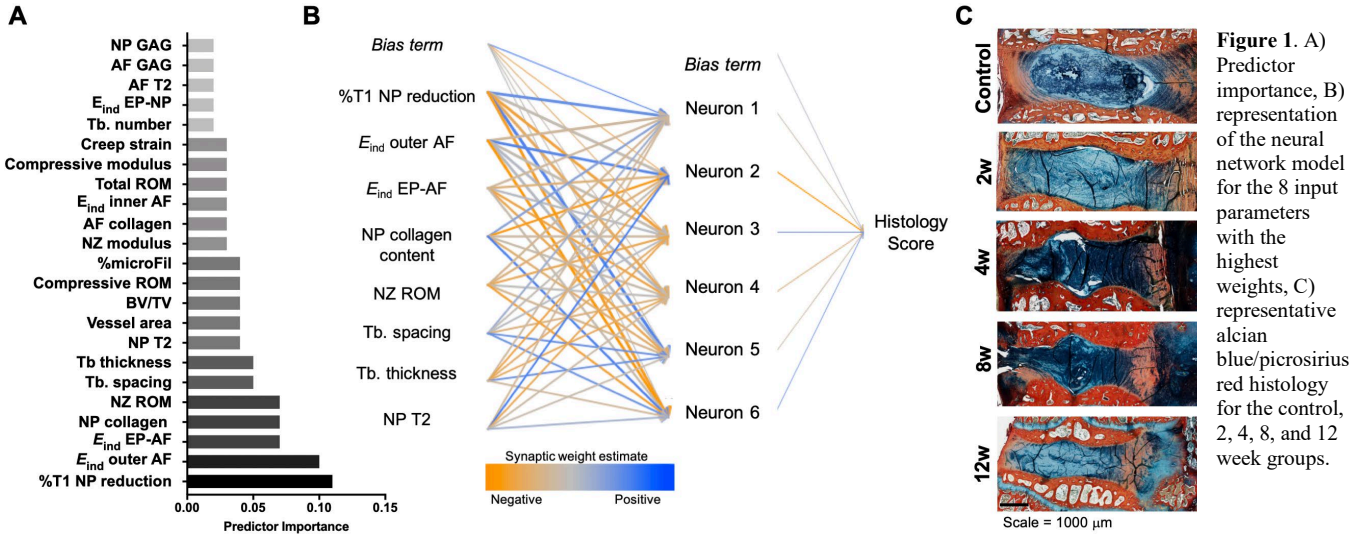

Figure 1. A) Predictor importance, B) representation of the neural network model for the 8 input parameters with the highest weights, C) representative alcian blue/picrosirius red histology for the control, 2, 4, 8, and 12 week groups.

DISCUSSION: Machine learning is a tool that has been previously utilized to assess various diseases, including the pathological state of articular cartilage in knee and hip osteoarthritis [8-9]. In this study, we utilized a neural network model, and found that small molecule diffusion into NP, as measured by contrast enhanced MRI, was most informative feature to predict degeneration grade. Disc nutritional status has long been postulated to be a primary contributor to degeneration [2,3], however, this is the first experimental evidence in an *in vivo* animal model of degeneration to verify this concept. We also identified the micromechanical parameters of the AF and EP as the second most important predictors of degeneration, highlighting the relevance of EP structure and function in disease. These findings have important implications in not only understanding degeneration, but also in developing strategies for disc regeneration, as therapies that do not address deficiencies in disc nutrition or micromechanical alterations to the disc may ultimately be unsuccessful.

SIGNIFICANCE: This work furthers our understanding the primary factors contributing to disc degeneration, and identifies key quantitative experimental outcomes that should be utilized when evaluating both degeneration and regeneration.

REFERENCES: [1] Mokdad et al., *JAMA*, 319:1444, 2018. [2] Gullbrand et al., *Spine*, 40:1158, 2015. [3] Ohshima, Urban, *Spine*, 17: 1992. [4] Ashinsky, Gullbrand et al., *Osteoarthritis Cartilage*, *in press* 2019. [5] Masuda, et al. *Spine*, 30, 2004. [6] Han et al. *Biophysical J*, 100:1846, 2011. [7] Gullbrand et al., *Osteoarthritis Cartilage* 1:146, 2017. [8] Ashinsky et al., *Osteoarthritis Cartilage* 10:1704, 2015. [9] Ashinsky et al. *J Orthop Res* 10:2243, 2017.

ACKNOWLEDGEMENTS: This work was supported by the NIH, the Dept. of Veterans' Affairs, and the Penn Center for Musculoskeletal Disorders.

3D Full-Field Biomechanical Testing of a Glenoid Before and After Implant Placement

Yuxiao Zhou[a], Chujie Gong[b], Gregory S. Lewis[c], April D. Armstrong[c], Jing Du[a*]

[a]Department of Mechanical Engineering, Pennsylvania State University, University Park, PA
[b]Department of Biomedical Engineering, Pennsylvania State University, University Park, PA
[c]Department of Orthopaedics and Rehabilitation, Penn State College of Medicine and M.S. Hershey Medical Center, Hershey, PA

Abstract

Loosening of the glenoid component is the most common cause of failure of total shoulder arthroplasty. While the underlying mechanisms are not fully understood, mechanical factors are widely reported to play a key role in glenoid component loosening. In this study, mechanical testing coupled with micro X-ray computed tomography (micro-CT) is performed to apply various physiologically realistic loads on a native and implanted glenoid. Digital volume correlation of micro-CT images is used to compute the 3D full-field deformation and strain inside the glenoid. The measured strain distributions are in good agreement with the analytical solutions of beam bending models, especially for anteriorly and posteriorly eccentric loadings. The effective moduli of the overall native and implanted glenoid were similar. However, under the same eccentric loading conditions, implanted glenoid exhibited a wider range of strain, because the placement of glenoid component increases the bending moment inside the glenoid. This proof-of-concept study provides a feasible and powerful method for the study of 3D full-field biomechanics in native and implanted glenoids.

Keywords: glenoid, strain, micro-CT

* Correspondence to: Professor Jing Du
316B Leonhard Building
Penn State University
University Park, PA16802
Phone: (814) 863-1043
Email: jingdu@psu.edu

Reproduction and Lactation Lead to Long-Term Changes in Supraspinatus Tendon and Humeral Trabecular Bone Properties in a Rat Model

Ashley K. Fung, Yihan Li, Thomas P. Leahy, Snehal S. Shetye, X. Sherry Liu, Louis J. Soslowsky
McKay Orthopaedic Research Laboratory, University of Pennsylvania, Philadelphia, PA
afung@seas.upenn.edu

Disclosures: Ashley K. Fung (N), Yihan Li (N), Thomas P. Leahy (N), Snehal S. Shetye (N), X. Sherry Liu (N), Louis J. Soslowsky (N)

INTRODUCTION: Physiological changes due to pregnancy increase the risk of developing musculoskeletal complications such as shoulder, lower back, and knee pain [1]. Altered levels of estrogen and relaxin during pregnancy increase knee joint and ligament laxity, compromising joint function, and these changes persist years after pregnancy [2]. Further, tibial and lumbar vertebral trabecular bone structure in reproductive female rats has been shown to be inferior compared to virgins but not different when compared to male, suggesting that reproduction and lactation induce bone loss that is not fully recovered post-weaning [3]. However, the long-term effects of reproduction on tendons and bones of the shoulder have not yet been studied. Therefore, the objective of this study was to evaluate the supraspinatus tendon mechanical response and humeral trabecular bone properties of male, virgin female, and reproductive female rats. We hypothesized that reproduction and lactation would induce long-term changes leading to inferior supraspinatus tendon properties and humeral trabecular bone microstructure in reproductive females as compared to virgin females.

METHODS: 20 Sprague-Dawley rats (IACUC approved) across three groups were used in this study: male (n=9), virgin female (n=6) and reproductive female (n=5). At age 6 months, reproductive female rats underwent two reproductive cycles, each consisting of a 3-week pregnancy, 3 weeks of lactation, and 6 weeks of post-weaning recovery. Rats were sacrificed at 12-14 months of age, and shoulders were harvested for supraspinatus tendon mechanical testing and trabecular bone analysis. Mechanics: Supraspinatus tendons were fine dissected and marked with stain lines for optical strain tracking. Cross-sectional area was measured using a custom laser device, and humeri were secured in polymethyl methacrylate. Right supraspinatus tendons underwent quasi-static tensile testing, consisting of pre-conditioning, stress relaxation at a 5% strain hold for 600s, a dynamic frequency sweep at 5% strain (0.1-10Hz), and ramp to failure at rate of 0.3%/s. Left supraspinatus tendons underwent fatigue testing, consisting of pre-conditioning and fatigue loading until failure at 2Hz between loads corresponding to 7% and 40% maximum stress, as determined from quasi-static testing. Fatigue parameters, including peak cyclic strain, secant modulus, tangent modulus, hysteresis, and laxity, were recorded at two breakpoints marking the ends of the primary (BP1) and secondary (BP2) phases of a triphasic fatigue life curve. Trabecular bone analysis: Left proximal humeri were scanned using μCT (10.5μm, μCT35, Scanco Medical). A 100-slice volume of interest proximal to the humeral growth plate was identified for trabecular bone microstructure analysis. Statistics: Comparisons across groups were made using one-way ANOVAs with Bonferroni post-hoc corrections. Significance was set at $p \leq 0.05$ and trends at $p \leq 0.1$.

RESULTS: Male tendons exhibited significantly higher stiffness compared to virgin and reproductive female tendons (Fig 1A). However, reproductive females had significantly lower modulus compared to virgin females but no difference compared to males (Fig 1B). Males had significantly lower dynamic modulus for all frequencies compared to both female groups (Fig 1C) but no difference in percent relaxation or tan(δ) (not shown). For fatigue properties at BP1, virgin females had significantly higher tangent and secant modulus compared to males and trended towards increasing compared to reproductive females (Fig 2A). However, there were no differences in secant or tangent modulus at BP2. No differences in hysteresis were observed at BP1, but reproductive females had significantly increased hysteresis compared to males at BP2 (Fig 2B). Cycles to failure and peak cyclic strain at BP1 was significantly higher in males compared to both female groups, and there were no differences in laxity at either breakpoint (not shown). Additionally, trabecular bone analysis revealed reduced bone volume fraction (BV/TV) and trabecular number (Tb.N) in reproductive females compared to virgin females but no difference compared to males (Fig 3A,B). Trabecular separation (Tb.Sp) in reproductive females was significantly increased compared to virgin females but trended towards a decrease when compared to males (Fig 3C). While trabecular thickness (Tb.Th) was significantly higher in males, there was no difference between female groups (not shown).

DISCUSSION: This study identified substantial differences in supraspinatus tendon and proximal humerus trabecular bone properties based on sex and reproductive history. Proximal humerus bone microstructure was superior in virgin females, consistent with previous findings in the tibia and vertebra. Previous research has linked ovariectomy to decreased failure stress of rotator cuff tendons and a less pronounced tidemark at the enthesis [4,5], and a similar mechanism may govern irrecoverable reproductive bone loss. Fatigue results also indicate that virgin and reproductive females experience a greater reduction in moduli and capacity to store energy, respectively, and together, these results suggest that females, regardless of reproductive history, may be more susceptible to early tendon degeneration. During pregnancy, hormonal fluctuations induce increased pelvic ligament laxity in preparation for parturition. Though the mechanisms are still unclear, several clinical studies have found sustained biomechanical changes in these ligaments despite a return to pre-pregnancy hormone levels [6,7]. Therefore, supraspinatus tendons following reproduction may be synergistically influenced by a direct effect of hormone changes and an indirect effect of bone loss near the insertion site. Shoulder pain after pregnancy has been associated with frequent breastfeeding that places added stress on the upper extremities. However, these findings suggest that biological changes during reproduction may inherently increase the risk for rotator cuff injury. Future studies will explore transient changes during pregnancy and investigate the mechanisms underlying long-term changes in tendon and bone properties following reproduction.

SIGNIFICANCE: This study identifies long-term changes in supraspinatus tendon and humeral trabecular bone properties that result following pregnancy and lactation, highlighting the importance of considering reproductive history in the diagnosis and treatment of shoulder injuries.

REFERENCES: [1] Koyasu et al, 2015, *Clin Exp Obstet Gynecol.* [2] Chu et al, 2018, *PM&R.* [3] de Bakker et al, 2018, *J Biomech.* [4] Cadet et al, 2010, *J Orthop Res.* [5] Chen et al, 2015, *PLoS One.* [6] Segal et al, 2013, *Am J Phys Med Rehabil.* [7] Damen et al, 2002, *Spine*.

ACKNOWLEDGEMENTS: This study was supported by NIH/NIAMS R03 AR065145, R01 AR071718, and the Penn Center for Musculoskeletal Disorders (P30 AR069619).

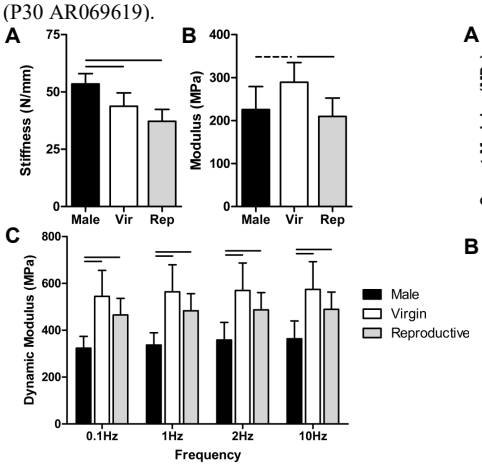

Figure 1: (A) Males had higher stiffness, while virgin females had increased (B) linear modulus and (C) dynamic modulus. Solid lines denote significance at $p \leq 0.05$ and dashed lines denote trends at $p \leq 0.1$

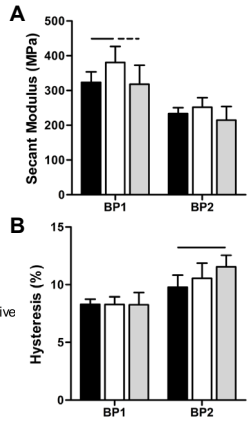

Figure 2: (A) Secant modulus was higher in the virgin group at BP1 and (B) reproductive females had increased hysteresis compared to males at BP2.

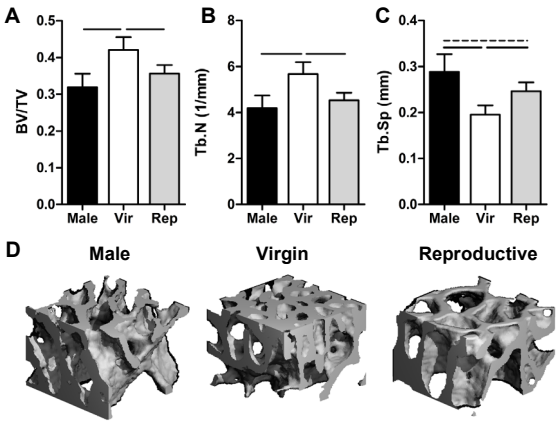

Figure 3: Virgin rats exhibited (A) higher bone volume fraction, (B) higher trabecular number, and (C) lower trabecular spacing compared to male and reproductive rats. Solid lines denote significance at $p \leq 0.05$ and dashed lines denote trends at $p \leq 0.1$. (D) Representative 3D humeral trabecular bone images

Interaction of cartilage and subchondral bone in H3K79 methyltransferase DOT1L loss mouse model

Stephanie Y Jo[1*], Miriam S Domowicz [2], Judith G Henry[2], Nancy B Schwartz[2]
1. University of Pennsylvania
2. University of Chicago

Osteoarthritis and osteoporosis are widely prevalent and have far-reaching public health implications. There is increasing evidence that epigenetics, in particular histone 3 lysine 79 methyltransferase DOT1L, plays an important role in the cartilage and bone biology. In this study, we evaluate the role of *Dot1l* in cartilage, growth plate, and subchondral bone utilizing conditional knockout mouse models.

We generated chondrocyte-specific constitutive and inducible conditional *Dot1l* knockout mouse lines using *Col2a1-Cre* and *Acan-CreER* systems. Techniques including whole-mount alcian blue stain, *in situ* hybridization, micro CT, immunohistochemistry, and quantitative PCR were used for analyzing the mouse model.

Prenatal deletion of *Dot1l* in mouse chondrocytes led to perinatal mortality, accelerated ossification, and dysregulation of *Col10a1* expression. Postnatal deletion of *Dot1l* in mouse chondrocytes resulted in subchondral trabecular weakening, decreased extracellular matrix production, and disruption of the growth plate.

In conclusion, *Dot1l* is important in the maintenance of growth plate, extracellular matrix production, and subchondral bone.

Osteoprogenitor YAP and TAZ Combinatorially Promote Endochondral Fracture Repair

Christopher D. Kegelman[a], Hope B. Pearson[b], James H. Dawahare[b], and Joel D. Boerckel[a,b]
[a]University of Pennsylvania, Philadelphia, PA, USA; [b]University of Notre Dame, Notre Dame, IN, USA

Introduction: Callus-mediated fracture repair occurs through cartilage callus formation, endochondral ossification, and remodeling. This process is coordinated by progressive lineage specification of progenitor cells, but the underlying molecular mechanisms remain incompletely understood. Previously, we found that constitutive ablation of Yes-associated protein (YAP) and Transcriptional co-activator with PDZ-binding motif (TAZ) osteoprogenitor cells and their progeny cause neonatal lethality as a result of bone fragility[1]. Here, we developed femoral fracture models in both constitutive and inducible YAP/TAZ knockout mice to elucidate the combinatorial roles of osteoprogenitor YAP and/or TAZ in endochondral bone fracture repair.

Materials and Methods: We generated two mouse models: 1) constitutive allele dose-dependent YAP/TAZ deletion and 2) adult-induced double homozygous YAP/TAZ deletion by Cre-recombination using the Osterix1 promoter. All animal experiments were approved by the IACUC. Unilateral femoral fractures were created at 20 and 16 weeks old in the constitutive and inducible models, respectively. Fractured limbs were analyzed with microCT at 2- and 6-weeks and 1- and 2-weeks post fracture in the constitutive and inducible models, respectively. Mechanical testing was performed by torsion to failure. Protein and gene expression were evaluated by immunohistochemistry and PCR. Two groups were compared with student's t-tests. Four groups were compared with a one-way ANOVA with post-hoc comparisons performed by a Bonferroni's multiple comparisons test.

Results and Discussion: Constitutive YAP/TAZ deletion reduced callus bone volume fraction at both 2- and 6-weeks post fracture in an allele-dosage dependent manner, concomitant with significantly decreased mechanical properties at both 2- and 6-weeks post fracture (Fig.1A-B). Constitutive homozygous double knockout mice died neonatally[1], so inducible double knockouts (cDKO^{i}) were generated. cDKO^{i} mice had significantly lower callus bone volume at both 1- and 2-weeks post fracture (Fig.1C-D). However, cDKO^{i} mice only had reduced callus total volume at 1-week, but not 2-weeks post fracture, suggesting delayed ossification with prolonged cartilaginous callus content. Accordingly, cDKO^{i} mice had increased glycosaminoglycan content per callus area and decreased Osterix expression in the callus at 2-weeks post fracture (Fig.1E-F). Lastly, cDKO^{i} calluses exhibited an increased trend in collagen-10 transcript expression with significantly reduced osteocalcin transcript expression (Fig.1G).

Conclusions: Together, these data indicate that YAP and TAZ promote endochondral fracture ossification, consistent with our prior observations in skeletal developmental[1]. YAP/TAZ may promote the entry into cartilage hypertrophy as well as transition to ossification to drive endochondral repair. A mechanistic understanding of how these proteins regulate endochondral healing could guide future therapeutic strategies for bone fragility and repair.

Acknowledgements: This work was supported by NIH grants T32 AR007132 and P30 AR069619 as well as the PCMD MicroCT Core.

References: 1) Kegelman+ *FASEB J* 2018, 32 (5), 2706-2721.

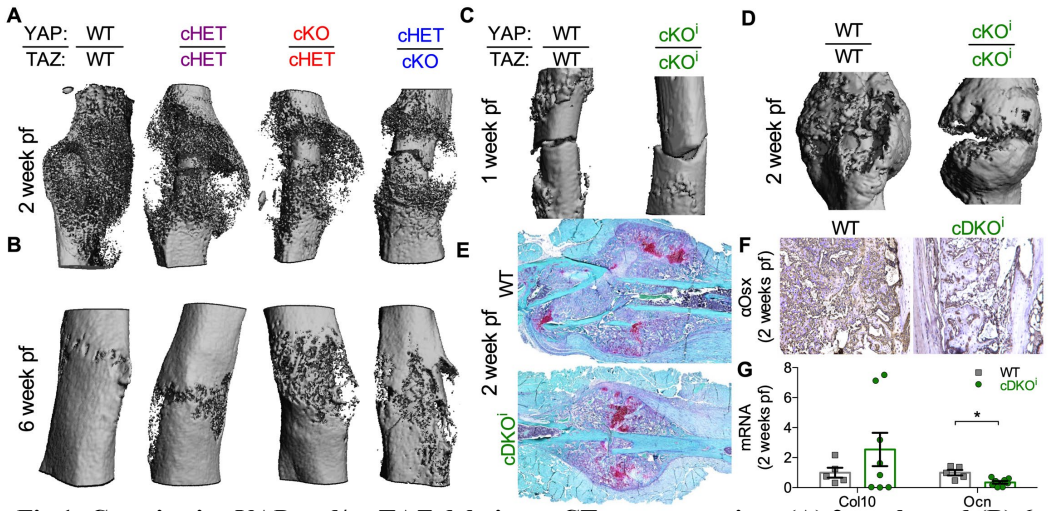

Fig.1: Constitutive YAP and/or TAZ deletion: µCT reconstructions (A) 2-weeks and (B) 6-weeks post fracture (pf). Inducible YAP/TAZ deletion: (E) µCT 3D-reconstructions 1-week post fracture and (F) 2-weeks post fracture. (G) Fracture callus 2 weeks post fracture stained with Safranin-O and (H) Osterix IHC with accompanying (I) mRNA expression of collagen10 (Col10) and osteocalcin (Ocn).

Estrogen Deficiency and Intermittent Parathyroid Hormone Treatment Affect Regional Achilles Tendon Vessel Microarchitecture

Thomas P. Leahy[1], Benjamin R. Freedman[1,2,3], Wei-Ju Tseng[1], Snehal S. Shetye[1], X. Sherry Liu[1], Louis J. Soslowsky[2]
[1]McKay Orthopaedic Research Laboratory, University of Pennsylvania, PA; [2]John A. Paulson School of Engineering and Applied Sciences, Harvard University, Cambridge, MA; [3]Wyss Institute for Biologically Inspired Engineering, Cambridge, MA. tpleahy@seas.upenn.edu.

Disclosures: Thomas P. Leahy (N), Benjamin R. Freedman (N), Wei-Ju Tseng (N), Snehal S. Shetye (N), X. Sherry Liu (N), Louis J. Soslowsky (N)

INTRODUCTION: The Achilles tendon is frequently injured and vascularity has been implicated as a predictor of Achilles tendon injury and healing potential.[1] Estrogen deficiency and intermittent parathyroid hormone (iPTH) treatment have been shown to differentially affect tendon healing response.[2–7] In rat models of tendon injury, estrogen-deficiency results in decreased Achilles tendon mechanical properties,[3] while iPTH treatment increases fibrocartilage formation near the tendon insertion during the healing response.[2,6] Despite the significant effects that estrogen deficiency and iPTH treatment have shown on the tendon healing response in animal models, there has been little research investigating their effect on vascularity of the Achilles tendon. Therefore, the objective of this study was to evaluate how estrogen deficiency and iPTH treatment modulate vessel microarchitecture in a rat Achilles tendon. We hypothesized that estrogen deficiency, simulated by bilateral ovariectomy surgery (OVX), would cause a decrease in Achilles tendon vessel microarchitecture throughout the length of the tendon, while iPTH treatment would result in increased tendon vessel microarchitecture, particularly near the insertion.

METHODS: Study Design: At 3 months of age, female Sprague-Dawley rats (n=14) were divided into three groups (IACUC approved): VEH (n=4), iPTH (n=3), and OVX (n=7). The OVX rats received OVX surgeries at 3 months of age to simulate estrogen deficiency for 4 weeks. At 3.5 months of age, VEH and iPTH rats received subcutaneous injections of saline solution and iPTH (PTH 1-34, 60µg/kg/day, Bachem, Bubendorf, Switzerland), respectively for 5 days a week for 2 weeks. Vascular casting: At 4 months of age, a vascular casting procedure was performed by infusion of Microfil mixture (MV122, Flow Tech Inc., Carver, MA) in the rat vascular network as described.[8–10] Briefly, 50 mL heparin sodium solution, followed by 100 mL 0.9% normal saline and 50 mL 4% PFA into the abdominal aorta at 4.4 mL/min via a perfusion pump (Bio-Rad, Hercules, CA) while the animals were under anesthesia. A syringe was used to inject 5 mL Microfil® mixture with 3% catalyst at 0.3 mL/min and the animals were stored at 4°C for 24 hours to allow complete polymerization. Afterwards, both the left and right Achilles tendons were harvested and µCT-scanned at 3.5µm voxel size (µCT 35, Scanco Medical AG, Brüttisellen, Switzerland) at a 1.6 mm region of the tendon insertion proximal to the calcaneus and another 1.6 mm long region near the midsubstance of the tendon, 3.6 mm proximal from the end of the insertion region (Fig. 1). A custom MATLAB (Mathworks, Natick, MA) script was used to apply a local thresholding technique to segment casted blood vessels from surrounding soft tissue.[11] Finally, the vascular microarchitecture parameters vessel volume (VV), vessel number (Ves.N), vessel thickness (Ves.Th), vessel separation (Ves.Sp), and connectivity density (Conn.D) were evaluated. Analysis: Separate two-way ANOVAs for tendon region and treatment were performed comparing VEH and iPTH, and VEH and OVX. If the ANOVAs determined a significant effect ($p<0.05$), Student's t-tests were performed to compare region and/or treatment between specific groups. Significant interaction terms were also evaluated.

RESULTS: When comparing VEH-OVX, treatment was a significant factor in VV, Conn.D, Ves.N, and Ves.Th, while region was a significant factor in Ves.Th. There was a significant interaction term for Conn.D. Further, the midsubstance region of the OVX tendons had significantly lower VV, Ves.N, Ves.Th, and Conn.D, with a trend toward greater Ves.Sp relative to the VEH group (Fig. 2). In addition, Ves.Th was significantly greater in the midsubstance relative to the insertion in the VEH tendons. When comparing parameters for VEH-iPTH, there were significant effects of region on Ves.Th. However, there were no significant differences between the VEH and iPTH groups (Fig. 3).

DISCUSSION: We investigated the effects of estrogen deficiency and iPTH treatment on vascular microarchitecture in the rat Achilles tendon. As hypothesized, OVX resulted in reduced vascular microarchitecture of the Achilles tendon, with the most profound effects in the tendon midsubstance. While OVX has limited effects on rat Achilles tendon homeostatic function,[4] it has significant detrimental effects on Achilles tendon healing response, resulting in decreased mechanical properties, including reduced max stress and secant modulus during fatigue loading, as well as decreased joint range of motion, cell proliferation, and GAG content.[3,5] As vascularity has been implicated as a predictor of healing potential,[1] the reduced Achilles tendon vessel microarchitecture observed in this study provides a potential explanation for the reduced healing potential seen in estrogen-deficient Achilles tendons. Contrary to our hypothesis, iPTH treatment did not have a drastic effect on vessel microarchitecture. In previous studies in bone, iPTH treatment did not result in osteoangiogenesis but rather relocated the vascular structure closer to the sites of new bone formation, thereby providing a favorable microenvironment for growth.[12] It may be possible that a similar effect happens in tendon, though it is also possible that the increased fibrocartilage formation in the tendon insertion observed previously is specific to the healing response.[2,6] Further studies should evaluate the effects of estrogen deficiency and iPTH treatment on vascular microarchitecture in an Achilles rupture model.

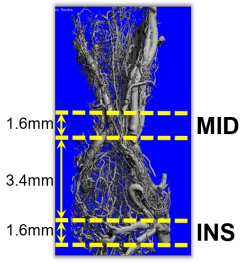

Figure 1. Achilles tendon vascularity, denoting insertion and midsubstance regions.

SIGNIFICANCE: This study highlights estrogen deficiency and iPTH treatment effects on vascular microarchitecture in the rat Achilles tendon. The decrease in tendon vascular microarchitecture in the estrogen-deficient rats could be a possible explanation for the reduced healing potential with estrogen deficiency.

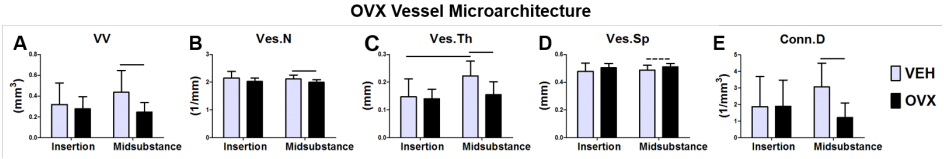

Figure 2. OVX vessel microarchitecture comparisons to the VEH group for VV (A), Ves.N (B), Ves.Th (C), Ves.Sp (D), and Conn.D (E). OVX shows detrimental effects on Achilles tendon vascular microarchitecture, particularly in the midsubstance region.

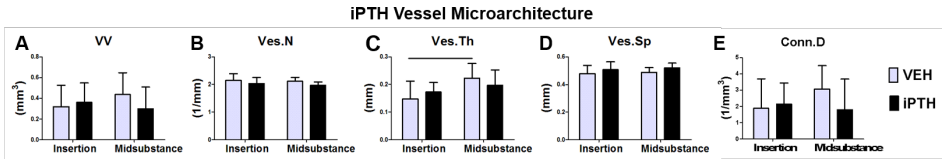

Figure 3. iPTH vessel microarchitecture comparisons to the VEH group for VV (A), Ves.N (B), Ves.Th (C), Ves.Sp (D), and Conn.D (E). iPTH treatment shows no differences compared to the VEH group except for eliminating the difference in Ves.Th between the insertion and midsubstance.

REFERENCES: [1] Theobald P et al., Injury, 2005. [2] Hettrich CM et al., J Orthop Res, 2012. [3] Fryhofer GW et al., J Appl Phsiol, 2016. [4] Pardes AM et al., Ann Biomed Eng, 2016. [5] Circi E et al., Int Orthop, 2009. [6] Duchman KR et al., J Shoulder Elbow Surg, 2016. [7] Lee DJ et al., J Orthop Res, 2015. [8] Wang Y et al., J Clin Invest, 2007. [9] Razavi H et al., Microvasc Res, 2012. [10] Duvall CL et al., Am J Physiol Heart Circ Physiol, 2004. [11] Waarsing JH et al., J Bone Miner Res, 2004. [12] Prisby R et al., J Bone Miner Res, 2011.

ACKNOWLEDGEMENTS: This study was supported by the Penn Center for Musculoskeletal Disorders (NIH/NIAMS P30 AR069619).

Comparisons between Teriparatide and Abaloparatide on Their Anabolic Effects and Responses to Treatment Discontinuation in Ovariectomized (OVX) Rats

Wei-Ju Tseng, Hongbo Zhao, Wenzheng Wang, X. Sherry Liu

[1]McKay Orthopaedic Research Laboratory, Department of Orthopaedic Surgery,
University of Pennsylvania, Philadelphia, PA;

Abaloparatide (ABL), a parathyroid hormone (PTH)-related protein analog, is a new anabolic treatment approved by FDA for postmenopausal osteoporosis. Similar to Teriparatide (TPTD, PTH1-34), ABL increases bone mineral density (BMD) by enhancing bone formation. However, treatment efficacy of ABL on bone microarchitecture and how it is in comparison with TPTD are unclear. Moreover, our previous study demonstrated diminished treatment benefit of TPTD upon discontinuation in estrogen-deficient bone. Therefore, the objective of this study was to compare the responses in bone microarchitecture between TPTD and ABL treatment as well as discontinuation in an OVX rat model.

25 4mo-old SD rats underwent OVX surgery and developed osteopenia for 4 wks (51% and 11% reduction in BV/TV and Tb.Th, respectively) before assigned to 3 groups: VEH (n=9, 12-wk saline), TPTD-VEH (n=9, 3-wk TPTD 40 µg/kg/day followed by 9-wk saline), ABL-VEH (n=6, 3-wk ABL 40 µg/kg/day followed by 9-wk saline). *In vivo* µCT (FigA) indicated that bone loss continued in VEH for 12 wks. In contrast, 3-wk TPTD treatment led to xx% increase in trabecular thickness (Tb.Th). Moreover, 3-wk ABL treatment led to xx% and xx% increases in bone volume fraction (BV/TV) and Tb.Th, respectively (Fig B-C), with trabecular number (Tb.N) unaltered (data not shown). Intriguingly, 1 wk after switching to VEH from TPTD or ABL (wk4), BV/TV and Tb.Th continued to show trends of improvement, indicating an anabolic window upon early withdrawal. Treatment benefit of ABL in BV/TV was still observed at wk 5 (xx% greater than wk 0) while there was no longer difference in BV/TV between wk5 and wk 0 in the TPTD group. Interestingly, at wk 12, Tb.Th in VEH, TPTD, and ABL groups were still xx and xx% greater than wk 0, respectively. At the end of the anabolic window (wk 4), ABL showed greater treatment efficacy in Tb.Th than TPTD (FigE). However, at wk 12 (9 wks after withdrawal), there was no difference in any bone microarchitecture of TPTD or ABL groups from VEH group.

In summary, both TPTD and ABL efficiently increase bone volume by thickening the remaining trabeculae and both treatments require follow-up of anti-catabolic therapy upon discontinuation to maintain their treatment benefit. Our study discovered a continuous anabolic window upon early withdrawal from both TPTD and ABL, which offers a new mechanism in support of the cyclic administration regime of TPTD or ABL to maximize the treatment efficacy.

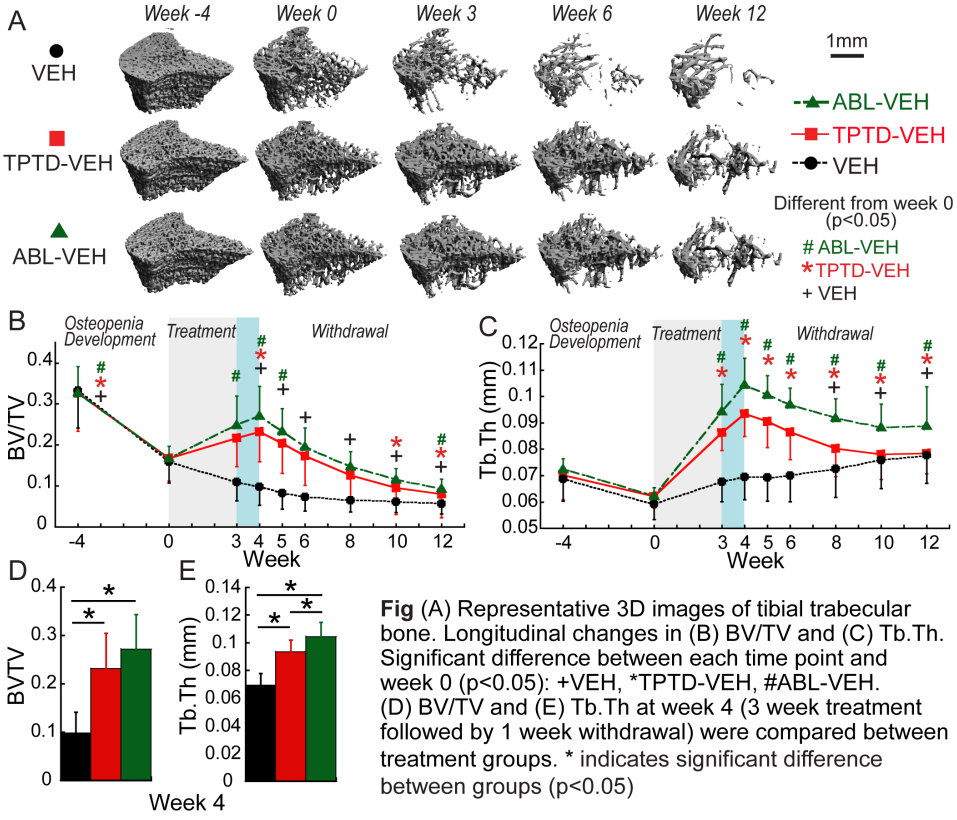

Fig (A) Representative 3D images of tibial trabecular bone. Longitudinal changes in (B) BV/TV and (C) Tb.Th. Significant difference between each time point and week 0 (p<0.05): +VEH, *TPTD-VEH, #ABL-VEH. (D) BV/TV and (E) Tb.Th at week 4 (3 week treatment followed by 1 week withdrawal) were compared between treatment groups. * indicates significant difference between groups (p<0.05)

A Combined Hydrogel and Mesenchymal Stem Cell Therapy Improves Disc Height and Condition in a Goat Model of Disc Degeneration

Chenghao Zhang[1,2], Sarah E. Gullbrand[1,2], Thomas P. Schaer[1], Dawn M. Elliott[3], George R. Dodge[1,2], Robert L. Mauck[1,2], Neil R. Malhotra[1] and Lachlan J. Smith[1,2]
[1]University of Pennsylvania, Philadelphia, PA; [2]Corporal Michael J. Crescenz Philadelphia VA Medical Center, Philadelphia, PA; [3]University of Delaware, Newark, DE
chenghao.zhang@pennmedicine.upenn.edu

Disclosures: Chenghao Zhang (N), Sarah E. Gullbrand (9-ORS Spine Section), Thomas P. Schaer (N), Dawn M. Elliott (N), George R. Dodge (N), Robert L. Mauck (9-JOR Spine), Neil R. Malhotra (N) and Lachlan J. Smith (5-Ultragenyx; 9-ORS Spine Section).

INTRODUCTION: Intervertebral disc degeneration is a cascade of cellular, structural and biomechanical changes that is strongly implicated as a cause of low back pain [1]. The earliest degenerative changes typically occur in the central nucleus pulposus (NP), where progressive loss of proteoglycans and associated hydration compromise tissue mechanical function. Previously, we developed a triple interpenetrating network hydrogel composed of dextran, chitosan and teleostean that is suitable both as an NP implant material and a vehicle for therapeutic mesenchymal stem cell (MSC) delivery [2]. We also established the translational merit of this hydrogel in a goat model of disc degeneration [3,4]. The objective of this study was to progress this therapy further towards clinical application by evaluating the short term regenerative potential of combined hydrogel and MSC injections in a clinically-relevant goat model of moderate-severity disc degeneration.

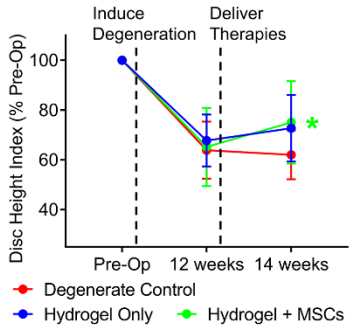

Figure 1. Combined hydrogel+MSC injections result in significant disc height improvement 2

METHODS: *Animals and Surgical Procedures:* With IACUC approval, 10 adult male goats underwent a surgical procedure to induce degeneration in 4 lumbar intervertebral discs (L1-L5) via injection of 1U Chondroitinase ABC (ChABC) using an open retroperitoneal approach [3]. Adjacent T12-L1 and L5-6 discs served as healthy controls. After 12 weeks, a second surgery was conducted to deliver therapies to degenerate discs. Treatments (randomly allocated across disc levels and animals) included: 1.) Degenerate controls (no treatment, n=5 discs); 2.) Hydrogel only (n=9 discs); and 3.) Hydrogel + MSC (n=10 discs). MSCs were labeled with GFP to enable postmortem localization and suspended in the hydrogel at 10 million cells/mL. Zirconia nanoparticles were incorporated into the hydrogel for a subset of treated discs to enable 3D evaluation of hydrogel distribution. Injections were performed using a 22G spinal needle. Animals were euthanized 2 weeks later for short term evaluation of therapeutic efficacy and hydrogel distribution. *Disc Height:* Disc height index (DHI) was measured from longitudinal, lateral lumbar spine radiographs taken before initiation of degeneration, and before and 2 weeks after delivery of therapies. *Hydrogel Distribution:* Vertebrae-disc-vertebrae segments were formalin-fixed and imaged using microcomputed tomography (microCT) to assess zirconia-labeled hydrogel distribution. *Histological Grading and MSC Localization:* Spine segments were decalcified and processed for paraffin histology. Mid-sagittal sections were double-stained with Alcian blue (glycosaminoglycans) and picrosirius red (collagen), or hematoxylin and eosin (cellularity), and disc condition was assessed using semi-quantitative grading [4]. GFP immunostaining was used to localize delivered MSCs. *Statistical Analysis:* Significant changes in DHI with interventions were established using a Wilcoxon matched-pairs signed ranks tests, while differences in histological grade were established using a Kruskal-Wallis test with post-hoc Dunn's tests ($p<0.05$).

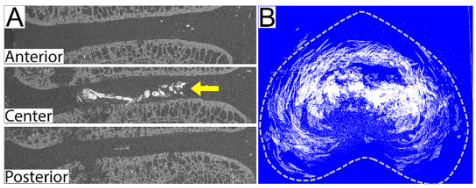

Figure 2. MicroCT imaging of hydrogel 2 weeks after delivery to the disc. **A.** Coronal slices of a single treated disc; and **B.** Composite axial view of all treated discs showing that the majority of hydrogel is centrally located in the disc NP.

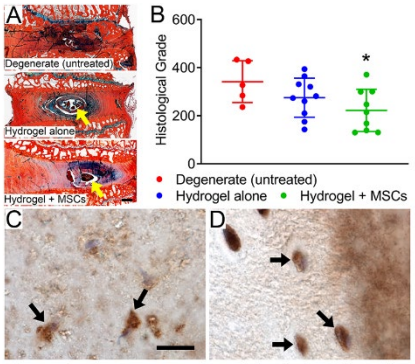

Figure 3. **A.** Representative mid-sagittal Alcian blue /picrosirius red-stained sections of treated and untreated discs (arrows=hydrogel; bar=2mm). **B.** Histological grade (*$p<0.05$ vs untreated). **C.** GFP-positive MSCs (arrows) in the hydrogel and **D.** Surrounding NP tissue. Scale=20μm.

RESULTS: *Disc Height:* 12 weeks after inducing degeneration, DHI was ~66% of pre-operative levels (Fig 1). For discs treated with hydrogel alone, DHI improved by 5.0% 2 weeks after treatment (not significant), while for discs treated with hydrogel+MSCs, DHI improved by 7.6% ($p<0.05$). For untreated controls, DHI declined by 2% from 12 to 14 weeks. *Hydrogel Distribution:* Postmortem MicroCT imaging demonstrated that the majority of hydrogel was localized to the central NP 2 weeks after delivery (Fig 2). *Histological Grading and MSC Localization:* Both groups of treated discs exhibited improved overall histological grade compared to untreated discs (Figs 3A and B), however this improvement only reached significance for hydrogel + MSC-treated discs. Finally, for discs treated with hydrogel + MSCs, GFP-positive MSCs were identified both in the hydrogel itself (Fig 3C) as well as in the surrounding NP tissue (Fig 3D).

DISCUSSION: In this study we demonstrated the short term efficacy of combined hydrogel and MSC injections for treating moderate severity disc degeneration in a clinically-relevant large animal model. Interestingly, while we anticipated acute regenerative effects (i.e. DHI improvement) with hydrogel injection, our results suggest that including MSCs has a additional therapeutic benefit even at this early time point. We found that MSCs were localized not only in the hydrogel delivery vehicle, but also appeared to have migrated into adjacent disc tissue. These MSCs may exert anabolic effects both through suppression of local inflammation and direct reconstitution of native tissue [5]. Using this clinically-relevant large animal model we will further explore the mechanisms of these beneficial effects and establish the long term *in vivo* efficacy of hydrogel and MSC injections for disc regeneration.

SIGNIFICANCE: There is a critical need for new therapies for patients with symptomatic, moderate-severity disc degeneration. A therapy that combines a hydrogel for structural and mechanical stabilization with MSCs for long term tissue regeneration may address this need.

REFERENCES: [1] Vlaeyen+ Nat Rev Dis Primers 2018; [2] Smith+ Tissue Eng Part A 2014; [3] Gullbrand+ Acta Biomater 2017; [4] Gullbrand+ Osteoarthritis Cartilage 2017; [5] Smith+ JOR Spine 2018.

ACKNOWLDEGMENTS: Funding from the Department of Veteran's Affairs and the Penn Center for Musculoskeletal Disorders.

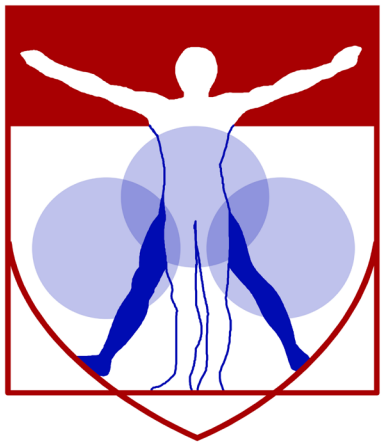

PENN

CENTER for

MUSCULOSKELETAL

DISORDERS

Miscellaneous Abstracts

Glucose Sensitivity in Engineered Adipose Tissue Model of Type 2 Diabetes

Authors: Alexandra Abruzzo, Evangelia Bellas, Ph.D.
Department of Bioengineering, Temple University, Philadelphia, PA

Introduction: Over 30 million U.S. adults have Type 2 Diabetes (T2D) (Diabetes.org). T2D is directly linked to how adipose tissue (AT), primarily made up of adipocytes, metabolizes glucose in the body. Adipocytes that are chronically overexposed to glucose become insulin resistant (IR). Insulin, although actively bound to its receptor, no longer activates adipocytes to uptake the excess glucose. To investigate the effects of IR in adipocytes, we have developed an engineered AT model of T2D. To validate this model, adipocytes were exposed to high glucose concentrations to promote characteristics that have been associated with IR. Also, mechanical changes, using analysis of the mechanosensitive gene ACTa, were examined to note differences in the remodeling of the microenvironment. This model provides a more physiologically relevant way to investigate metabolic diseases, such as T2D, and potentially to show how obesity could influence other disorders like musculoskeletal disorders.

Materials and Methods: Adipocytes, derived from human adult mesenchymal stem cells, were encapsulated in a 3D collagen type I matrix to mimic the physiological environment of human AT and allowing the cells to remodel their microenvironment. We compared high glucose, HG, (4.5g/L) to the control, normal glucose, NG, (1g/L), then sacrificed for end-point analyses at 48h. qPCR was performed for TNFα (inflammatory marker implicated in IR, downstream of the receptor), IRS1 (mediated by the activation of TNFα and inhibits insulin signaling), GLUT4 (glucose transporter stimulated upon insulin binding), and ACTa (varies in response to changes in the ECM). Adipocyte function was evaluated by glycerol secretion to indicate fatty acid metabolism (lipolysis) and by glucose uptake and localization, by 2-NBDG, a fluorescent glucose analog. Statistical analysis was performed by ANOVA and students' t-test with an alpha value of 0.05, in JMP Pro 14.

Results and Discussion: When cells were exposed to HG, there was diffuse glucose localization of 2-NBDG signal (**Fig.1a**) as compared to the NG control, where they contained smaller, consolidated glucose signal regions (**Fig.1b**). In HG, cells had a lower sensitivity to glucose, so fewer glucose molecules were taken up by the cell. Instead, there was a greater overall 2-NBDG signal intensity as a result of the excess glucose (**Fig.1c**). Upon qPCR analysis, ACTa was downregulated in HG, showing that the diseased cells remodeled their environment differently (**Fig.1d**). ACTa expression is statistically significant, with a p-value of 0.0276. TNFα and GLUT4 were downregulated in HG, while IRS1 was upregulated (**Fig.1e-g**). HG cells were becoming IR, as IRS1 was increased and GLUT4 was decreased simultaneously. The lipolysis assays show that in HG, lipolysis is decreased (**Fig. 1h**) as a result of fewer glucose molecules being taken up by the cell and converted to glycerol. Lipolysis results were statistically significant, with a p-value of 0.0343.

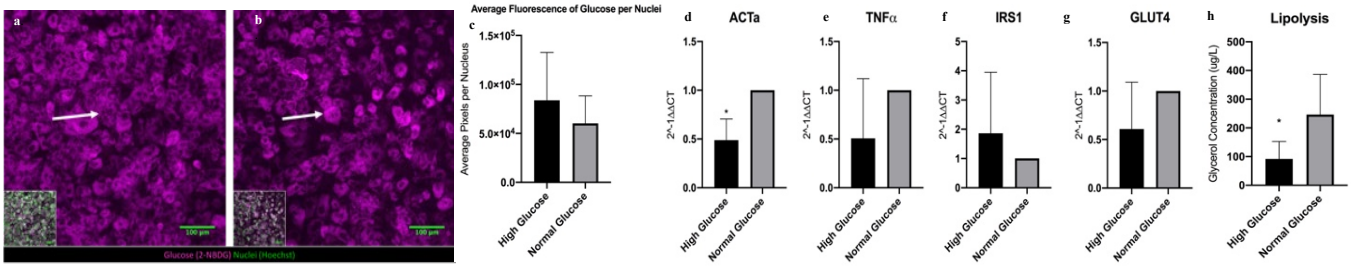

Figure 1. The HG group shows glucose localized at and adjacent to the cell nuclei (a). In the NG condition, the nuclei and glucose molecules are not co-localized (b). 2-NBDG intensity was quantified in ImageJ, n=6 (c). ACTa is downregulated in HG (d). TNFα is downregulated in HG (e). IRS1 is upregulated in HG (f). GLUT4 is downregulated in HG (g). Lipolysis is decreased in HG conditions (h). All n = 4-6.

Conclusions: HG cells do not take up as much glucose, as seen by less glucose localization to the nucleus, and the HG cells secrete less glycerol. Increased IRS1 accompanies IR, and decreased GLUT4 indicates that fewer glucose molecules are being transported into the intracellular space. Downregulation of TNFα reveals that it is no longer serving as a mediator for the IRS1 cell response. ACTa demonstrates biophysical changes in the diseased model, which may provide a new insight for potential therapies. Thus far, the model demonstrates the early stages of IR.

Acknowledgements: We acknowledge funding support from Dr. Bellas' startup funds (Temple University) and the NIH NIDDK Diabetic Complications Consortium DK07616 and DK115255 grants (to EB).

FOP-Acvr1 Signals by Multiple Modalities in the Developing Zebrafish

Allen, Robyn S., Eileen M. Shore, and Mary C. Mullins

Fibrodysplasia ossificans progressiva (FOP) is a rare human genetic disorder characterized by altered skeletal development and extraskeletal ossification. Most cases of FOP are caused by a single nucleotide substitution in the type I BMP/TGFβ cell surface receptor, ACVR1 (R206H), which over-activates signaling through phospho-Smad1/5. To investigate the still uncertain mechanism by which FOP-ACVR1 enhances pSmad1/5 activation, we used zebrafish embryonic dorsoventral (DV) patterning as an assay for BMP pathway activity. The zebrafish DV axis is established by a gradient of BMP-pSmad1/5 signaling. Perturbations to this gradient directly correlate with a series of distinct, dose-dependent signaling phenotypes in the developing zebrafish embryo. In this system, expression of human ACVR1-R206H causes increased pSmad1/5 signaling and ventralization of zebrafish embryos. Recent studies suggest that FOP-ACVR1 may have altered ligand responsiveness compared to WT-ACVR1. We determined that ACVR1-R206H does not require its ligand binding domain to over-activate BMP pathway signaling. It is, however, hyper-responsive in the presence of BMP ligand, supporting that the receptor has both ligand-independent and dependent hyperactivity. Because WT-ACVR1 normally binds ligand in a receptor heterotetramer, we examined the receptor partner requirements of ACVR1-R206H. We found that BMPR1, a type I BMP receptor normally required for DV patterning in the zebrafish, is not required for ligand independent or dependent pSmad1/5 over-activation by ACVR1-R206H. ACVR1-R206H still requires presumptive activation by a type II BMP receptor, but it has a decreased requirement for activation compared to WT-ACVR1 in the presence of ligand. These data demonstrate that FOP-ACVR1 is not constrained by the same receptor and ligand partner requirements as WT-ACVR1. These and further studies of FOP-ACVR1 will provide unique insight into how the BMP signaling pathway functions.

Funding Sources: NIH R01 GM56326, Cali Grant

Critical roles of SoxC transcription factors in cranial bone formation

Angelozzi M, Bhattaram P, Karvande A, Mata F, Gonzalez M, Pellegrino R, Lefebvre V

Division of Orthopaedics Surgery, Children's Hospital of Philadelphia, Pennsylvania, USA

The development of the skull is a complex process that must be tightly regulated spatially and temporally to form and assemble the cranial vault bones and the intervening sutures. It involves progenitor cells derived from both mesoderm and neural crest and initially located in the supraorbital ridge of the embryo. While some of these cells coalesce and start forming bone rudiments, others proliferate and migrate to the top of the head allowing apical and lateral expansion of bone primordia. Thus, cell proliferation, migration and differentiation represent essential processes in the cranial vault formation. Perturbations in any of these processes cause defects in skull formation, often associated with neurological abnormalities, and lead to severe repercussions in the health of the patients. For this reason, it is fundamental to understand which molecular pathways control these processes. In order to address this point, we performed single-cell RNA-sequencing (scRNA-seq) analysis of calvaria at different developmental stages. Among the cell clusters belonging to the osteogenic lineage, 4 corresponded to progenitor cells characterized by specific transcriptome signatures, possibly reflecting different functional roles of these cells. Two members of the SoxC transcription factors, *Sox4* and *Sox11*, were highly expressed in these populations. To determine the involvement of these genes in calvarium development, we specifically inactivated these genes with a *Prx1Cr*e transgene (*SoxC*$^{fl/fl}$*Prx1Cre* mice). Mutant mice were born with an underdeveloped calvarium, characterized by the lack of the intraparietal bone and by the presence of frontal and parietal bones that were thin and nonmineralized at the apex. Progenitor cell populations were under-represented in mutant calvarium and showed significant downregulation of genes involved in cell proliferation and cytoskeleton organization. Together, our findings support the use of the scRNA-seq technology to identify gene networks involved in skull formation and possibly altered in diseases. Our identification of key roles for SoxC genes in this process provides insights into the mechanisms whereby Sox4 and Sox11 heterozygous mutations cause craniofacial dysmorphism in humans.

Fibroblasts Mitigate Extracellular Remodeling in Obese Adipose Tissue

Golnaz Anvari, M.S., Evangelia Bellas, Ph.D.
Department of Bioengineering, College of Engineering, Temple University, Philadelphia, PA

Introduction: Obesity is a global epidemic and a risk factor for many major diseases such as type II diabetes, cardiovascular disease, stroke, cancer and plays a role in development and progression of musculoskeletal disorders such as osteoarthritis, back pain and osteoporosis. The mechanisms underlying these effects is not clear therefore it is important to study how changes in the obese adipose tissue can ultimately affect the progression of these musculoskeletal disorders. In simplest terms, obesity is defined as excess white adipose tissue (WAT). In addition to adipocytes, the main cellular component of WAT, the microenvironment consists of support cells and extracellular matrix (ECM) components. The ECM plays a vital role in the structure and function of all tissues including WAT. The highly dynamic microenvironment of WAT is remodeled during development, healthy expansion but also during obesity. However, the hypertrophic expansion during obesity leads to hypoxia, fibrosis and inflammation. *Therefore, it is critical to study the healthy WAT microenvironment and how this microenvironment is altered during obesity.* Fibroblasts play a supporting role in adipose tissue but their contribution to fibrosis and disease progression is unknown. The aim of the present study is to evaluate the role of fibroblasts in early stage of obesity and during fibrosis.

Materials and Methods: Human mesenchymal stem cells (hMSCs) are expanded in 2D until confluent followed by addition of adipogenic induction media for 7 days. Human primary dermal fibroblasts are expanded in 2D. Adipocytes and fibroblasts were co-cultured in 50:1 ratio within 2mg/ml 3D collagen type I gels, with seeding density of 8 million/ml. After 24 hours in normoxia, the constructs were either maintained in normoxia, to mimic the healthy condition, or exposed to 1mM Dimethyloxalylglycine (DMOG), to induce hypoxia, mimicking the early stage of obesity. After 7 days, constructs were sacrificed for endpoint assays. Gene expression for adipocyte related and ECM remodeling genes were assessed through q-PCR. To study adipocyte morphology, lipid droplets were visualized by using Bodipy and nuclei by Hoechst. Fibroblasts were visualized by phalloidin staining. Furthermore, the organization of collagen fibers were imaged by second harmonic generation (SHG) microscopy.

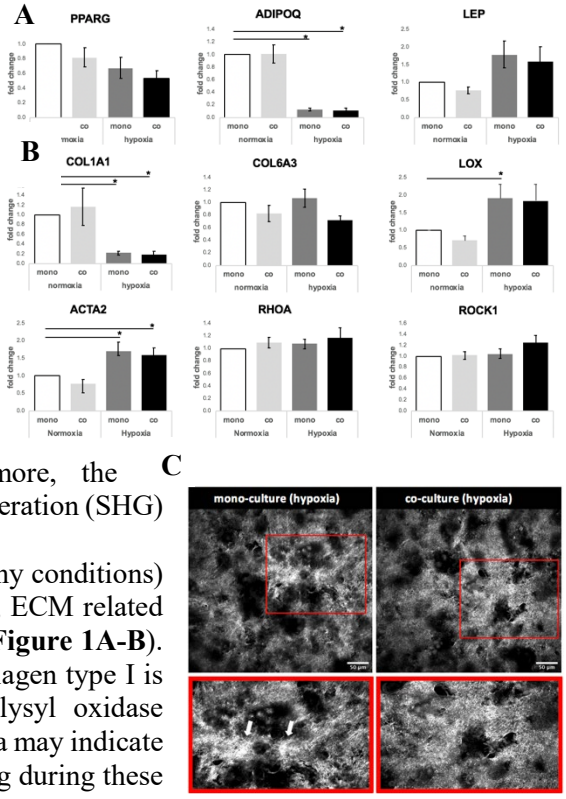

Figure 1. **A) Gene expression for adipocyte related genes. Peroxisome Proliferator Activated Receptor Gamma (PPARG) and adipokines: adiponectin (ADIPOQ), Leptin (LEP). (n=6, SEM, *p<0.05 co-culture ratio-50:1). B) Gene expression for ECM related genes. Synthesis genes: collagen type I alpha 1 (COLA1), collagen type 6 alpha 3 (COL6A3); remodeling genes: lysyl oxidase (LOX), ras homolog family member A (RhoA), Rho kinase 1 (ROCK1), actin alpha 2 (ACTA2). (n=6, SEM, *p<0.05 co-culture ratio-50:1). C) The structure of collagen in hypoxic 3D constructs after 7 days. Collagen fibers are visualized in gray by SHG. Arrows point to regions of collagen fiber clustering. Scale bar- 50 microns.**

Results and Discussion: Our data indicate that normoxia (i.e. healthy conditions) and co-culture with fibroblasts has no effect on adipocyte function, ECM related proteins and remodeling gene expression in our co-culture model (**Figure 1A-B**). However, in hypoxia (early stage of obesity), we observed that collagen type I is downregulated while smooth muscle cell actin (ACTA2) and lysyl oxidase are upregulated. Lysyl oxidase upregulation in mono-culture/hypoxia may indicate that fibroblasts can mitigate the negative impact of ECM remodeling during these early stages of obesity (**Figure 1B**). Furthermore, we can observe more collagen clusters in mono-culture/hypoxia (**Figure 1C**).

Conclusions: Our current results indicate that fibroblasts can improve adipocyte function in early stages of obesity. Our future work will include examining the role of RhoA and its downstream signaling pathway, ROCK1, MLC and alpha- SMA in adipose tissue hypoxia and ECM remodeling.

Effects of Aging on the Molecular Profile of Cultured Tendon Cells

Carrie E. Barnum, Julianne Huegel, Louis J. Soslowsky, Andrew F. Kuntz
McKay Orthopaedic Research Laboratory, University of Pennsylvania, Philadelphia, PA

DISCLOSURES: Barnum C (N), Huegel J (N), Soslowsky LJ (N), Kuntz AF (N)

INTRODUCTION: Rotator cuff tears affect millions of individuals each year, with a higher incidence in the elderly. Although surgical repair can improve function and reduce pain, rotator cuff repair failure is common [1]. To improve surgical outcomes, biologic augmentation via delivery of cells or growth factors has been investigated [2-4]. Recently, autologous biceps cells delivered via nanofibrous scaffold to the repair site during supraspinatus repair were shown to improve healing in juvenile and aged rats, but did not affect healing in adult rats [5]. However, the molecular mechanisms behind these differential effects are not well understood. Therefore, the objective of this study was to determine the differences in the RNA signature of primary tendon-derived cells cultured from the long head of the biceps of juvenile, adult, and aged animals. Our hypotheses were: 1) tendon-derived cells from juvenile animals would exhibit a molecular profile more characteristic of stem cells than tendon-derived cells from adult or aged animals, and 2) tendon-derived cells from aged rats would have increased expression of genes associated with tendon homeostasis and differentiation compared to cells derived from juvenile or adult rats.

METHODS: 27 Fisher (F344) rats were used (IACUC approved) across three age groups: juvenile (4 weeks), adult (8 months), and aged (16 months) (n=9/age group). Animals were sacrificed and the intra-articular biceps tendons were collected. *Cell Culture*: Biceps tendon cells were harvested from the tissue via morselization and cell migration. Cells were expanded in culture using basal media and split at confluence. Subcultured (P1) cells were allowed to reach 75-85% confluence (average 12 days in culture) at which time they were lysed and homogenized in TRIzol. *RNA Isolation*: RNA was isolated using the TRIspin method and processed via RNA Clean & Concentrator 5 columns (Zymo Research). *Rat Transcriptome Array and Bioinformatics Analysis*: cDNA made with 250ng of RNA using the Affymetrix WT PLUS Kit and was run on a Clariom™ D Rat Transcriptome Array 1.0 (Applied Biosystems, n=5/age group). Bioinformatics processing was performed using Transcriptome Analysis Console Software and DAVID analysis (cut-offs set at |FC|>2 and $p<0.05$ for all pair-wise age comparisons). *qRT-PCR*: Reverse transcription was performed using a High Capacity cDNA Reverse Transcription Kit (Applied Biosystems). To validate microarray results, qPCR was run in quadruplicate using TaqMan Assays on a QuantStudio 12K Flex Real-Time PCR system (ThermoFisher, n=8/age group). Data was analyzed using the ΔΔCt method, and expression levels were compared between age groups with one-way ANOVAs and post-hoc Tukey tests. *Cell Staining*: At 50% confluence, P1 cells were fixed, permeabilized, and stained with Alexa Fluor 488 Phalloidin and DAPI. Slides were imaged with a Leica TCS SP8 Multiphoton Confocal.

RESULTS: Principle component analysis demonstrated that cell expression profiles grouped into distinct regions by age (Fig. 1). The majority of gene expression clustered into six distinct patterns when comparing between ages (data not shown). The majority of differential gene expression exists between juvenile and aged cells (640 genes significantly decreased, 531 increased), while the fewest differences exist between adult and aged cells (54 genes significantly decreased, 101 genes increased). Comparison of juvenile cells to adult cells identified 216 significantly increased genes and 203 significantly decreased genes. No qualitative differences were observed in cell morphology between age groups (data not shown). Gene ontology identified differences in genes related to: 1) cell adhesion, wound healing, and chondrocyte differentiation between juvenile and adult cells, 2) cell division and cell adhesion between juvenile and aged cells, and 3) wound healing and vasculogenesis between adult and aged cells. qPCR confirmed that genes associated with stemness are downregulated with age, including *Postn*, *Fgf10*, *Osr1*, and *Gpmnb* (Fig. 2). Additionally, genes related to inflammation are differentially expressed with age, including increased *Cd28* and *Cd200* expression and decreased *Il6* and *Il6st* expression (Fig. 3).

DISCUSSION: Results demonstrate distinct molecular profiles for juvenile, adult, and aged biceps tendon-derived cells. Juvenile cells showed increased expression of genes associated with mesenchymal stem cells, such as *Postn and Fgf10*, supporting our first hypothesis. Furthermore, although stem cell associated markers are present in both juvenile and adult cells, they are significantly decreased in aged cells, suggesting that a greater population of aged tendon cells may have terminally differentiated. However, contrary to our second hypothesis, there were no consistent increases in the expression of tendon markers in aged cells, suggesting that there may be significant population heterogeneity. Interestingly, aged cells demonstrate a decreased pro-inflammatory signature, including decreased expression of pro-inflammatory cytokine *Il6* and its signaling receptor *Il6st,* as well as an increased anti-inflammatory milieu, including increases in both *Cd28* and *Cd200* expression compared to juvenile cells. Previous work demonstrated that Il6-null mice (simulating an aged phenotype) have increased native tendon mechanical properties [6], but show a similar healing response as WT mice [7], suggesting a role for this cytokine in how delivered cells integrate into and contribute to new tendon formation. This study specifically explored RNA level changes in biceps tendons in culture, and we have not yet shown that these findings relate to changes at the protein level. However, these age-specific expression signatures can begin to uncover the mechanisms behind functional differences previously shown between age groups after cell delivery [5]. Future research will investigate protein level changes as well as how these changes relate to functional differences in tendon healing with age. It will be important to discern how both population heterogeneity and inflammation affect the contribution of scaffold-delivered biceps cells for rotator cuff repair.

SIGNIFICANCE/CLINICAL RELEVANCE: We previously demonstrated age-specific differences in supraspinatus healing after autologous biceps cell delivery [5]; the current study demonstrates that these cell populations display distinct molecular differences. These differences should be considered when addressing musculoskeletal regenerative medicine, particularly in the context of augmented tendon repair. Furthermore, modulating the molecular profile of adult or aged cells may further improve tendon repair.

REFERENCES: [1] Galatz LM et al. J Bone Joint Surg Am, 2004. [2] Hernigou P et al. Int Orthop, 2014. [3] Chen JM et al. Tissue Eng, 2007. [4] Longo UG et al. Br Med Bull, 2010. [5] Huegel J et al. J Orthop Res. 2017. [6] Lin TW et al. J Biomech. 2005. [7] Lin TW et al. J Biomech. 2006.

ACKNOWLEDGEMENTS: This study was supported by the American Shoulder and Elbow Surgeons Research Grant. We would like to thank Dr. Snehal Shetye for his help with the cluster analysis.

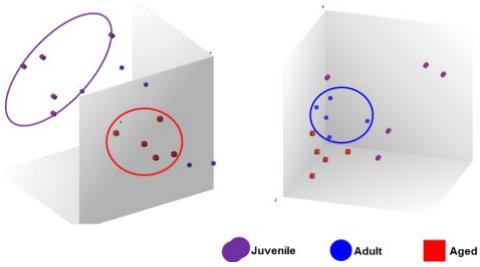

Figure 1.Two Principle Component Analysis plots from Rat Transcriptome Analysis. Juvenile cells shown as purple cylinders, adult cells are shown as blue spheres, and aged cells are represented as red cubes. Age groups are circled to demonstrate distinct clusters.

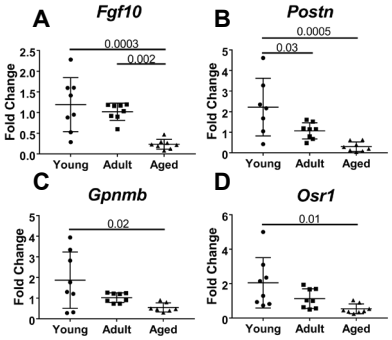

Figure 2. Decreased expression of stem related mRNAs measured via qPCR. (A) *Fgf10* (B) *Postn* (C) *Gpnmb* and (D) *Osr1* expression decreased with aging. Significance is denoted with solid lines (n=8/group).

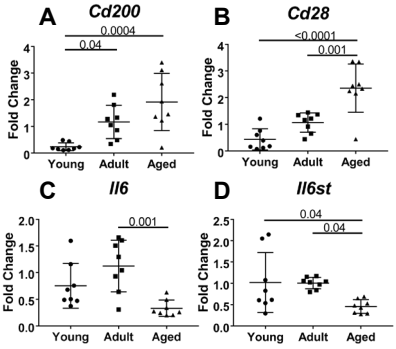

Figure 3. qPCR confirms changes in inflammatory response with age. (A) *Cd200* and (B) *Cd28* increased with age, while (C) *Il6* decreased in aged cells only and (D) *Il6st* decreased with aging. Significance is denoted with solid lines (n=8/group).

Investigating the Effects of Collagen Density on Adipocyte Behavior

Anthony J. Berger[1], Evangelia Bellas[1]
[1]Department of Bioengineering, Temple University, Philadelphia, PA

Introduction: While initially viewed as a simple means of storing excess energy, we now know that adipose tissue (AT) has many roles in human biology, including critical functions in regulating metabolic homeostasis. Obesity can lead to dysregulation of these functions, resulting in diseased states such as insulin resistance, hypertension, and dyslipidemia. These metabolic complications elicited by obesity also increase the risk for some of the most prominent musculoskeletal diseases, including osteoporosis, tendinopathy, and osteoarthritis. Pathological obesity often coincides with extracellular matrix (ECM) remodeling, leading to drastic changes in the biochemical and physical properties of the microenvironment. However, little research has been conducted with *in vitro* models to determine how these alterations affect adipocyte function. Currently, natural and synthetic scaffolds can be physically tuned via chemical modifications; however, current approaches either cannot recapitulate physiologically relevant ranges of stiffness and/or fiber densities (natural materials) or are unable to generate the inherently bioactive fibrous structure of *in vivo* tissues (synthetic materials). To address these limitations, we have utilized an interpenetrating network (IPN) of gelatin-methacrylate (gelMA) and collagen I, which allows for tuning of scaffold stiffness and fiber density, to better understand the relationship between ECM and adipocyte behavior.

Materials and Methods: Gelatin type A was dissolved in PBS and mixed with 0.25-2.5% v/v methacrylic anhydride to yield GelMA stocks with different crosslinking potential. Lyophilized gelMA was resuspended at 20% w/v in ddH_2O and diluted to 3% in acetic acid containing rat tail collagen I (0-4.5 mg/mL). The photoinitiator lithium phenyl-2,4,6-trimethylbenzoylphosphinate (LAP) was added and the solution was neutralized and mixed thoroughly. Collagen was polymerized at 37°C for 1 hr, at which point the gelMA was photocrosslinked via UV exposure. Collagen organization was visualized via second harmonic generation and elastic moduli were quantified by rheometry. Adipocytes were derived by induction of human mesenchymal stem cells in adipogenic media in 2D culture for 5 days prior to embedding. To embed cells, adipocytes were detached and a single-cell suspension was mixed into the precursor solution directly after neutralization. Cell-laden gels were cultured for 7 days, at which point cell morphology and lipid accumulation was examined via phalloidin and Bodipy staining, respectively.

Results and Discussion: GelMA was copolymerized with varying amounts of collagen I (0-3 mg/mL) to yield scaffolds with a wide range of collagen fiber densities; however, total protein content and scaffold stiffness were kept constant, the latter of which was held to <1 kPa to mimic normal AT. The collagen formed a network of randomly-oriented fibers that increased in density as collagen concentration was increased. Adipocytes embedded into gelMA/coll gels retained their phenotypical round morphology for the duration of experiments while simultaneously showing lipid accumulation within the cell body (**Figure 1**), indicating the scaffold was able to support adipogenic behavior and function. Cell size decreased as collagen increased and adipocyte-related gene expression was found to decrease in gels with the highest collagen content (3 mg/mL).

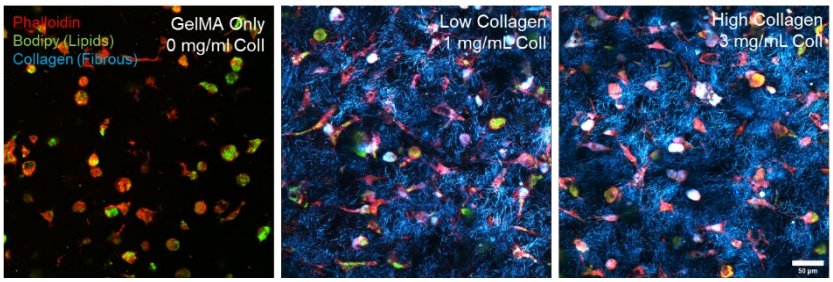

Figure 1: GelMA/Coll hydrogels support adipocyte function. *A.) Adipocytes embedded in gelMA blended with 0 (left), 1 (middle) or 3 (right) mg/mL collagen show rounded morphology and lipid droplets after 7 days in culture. Scale bar = 50 µm.*

Conclusions: Prior studies have shown ECM remodeling in AT, such as fibrosis, coincides with AT-related disease progressions. However, previous studies have either been unable to distinguish between the many physical aspects of the extracellular microenvironment, such as stiffness and fibrosity, or are unable to recapitulate physiologically relevant properties of AT. The model system presented here has the ability to produce a large range of ECM fiber densities while maintaining a constant, soft scaffold stiffness to mimic normal tissue. This approach may ultimately provide insight into how alterations to the microenvironment during the progression of obesity can affect adipocyte dysfunction, opening the door for potential therapeutics, thus preventing the onset of musculoskeletal problems by eliminating obesity as a driving factor.

Neural Networks to Identify Aberrant Mechanosensing in Fibrous Environments

Edward D. Bonnevie[1,2], Beth G. Ashinsky[1, 2, 3], Bassil Dekky[1], Susan Volk[1], Harvey E. Smith[1,2], Robert L. Mauck[1,2]
[1]University of Pennsylvania, Philadelphia, PA, [2]CMC VA Medical Center, Philadelphia, PA, [3]Drexel University, Philadelphia, PA
edbon@pennmedicine.upenn.edu

INTRODUCTION: Following injury and during degeneration, fibrous tissues of the musculoskeletal system undergo fibrotic remodeling that significantly limits their function. Often, these functional changes occur with a loss of prestress, such as in the annulus fibrosus of the disc following a herniation injury or in a tendon following rupture of the attachment. Following this loss of prestress, an overactive mechanosensing state emerges within endogenous cells, characterized by high YAP/TAZ signaling and increase expression of α-smooth muscle actin (αSMA).[1,2] However, the connection between the fiber environment, cell spreading, and mechanobiology are not fully understood. Here, we utilize engineered fiber environments to determine how cells interrogate their microenvironment to regulate mechanosensing. Using neural network modeling, we show that fiber organization dictates cell and nuclear shape, size, orientation, mechanosensing, and phenotype. We further extended this approach to predict the mechanobiologic state of cells and identify when this state is decoupled from cell spreading, in cases of aberrant mechanobiology.

METHODS: Electrospun scaffolds were fabricated using poly(ε-caprolactone) as previously described[3]. Both aligned and non-aligned scaffolds were stretched to 0%, 3%, 6%, or 9% strain prior to cell seeding. Bovine annulus fibrosus cells (bAFC), bovine mesenchymal stromal cells (bMSC), and human cancer cell lines (MCF-7 and MDA-MB-231) were used in this study. Neural networks for clustering (trained by batch self-organizing map, **Fig 1**), predicting mechanobiologic state (2-layer feed-forward, Bayesian regularization, **Fig 2abc**), and classifying cancer cell type (2-layer feed-forward, scaled conjugant gradient backpropagation, **Fig 2d**) were generated in MATLAB using the neural network toolbox. In each case, 14 cell and nuclear metrics describing shape, size, and orientation were used for validation and testing of the networks. Statistical evaluation included Pearson correlation and one-way ANOVA to make comparisons between groups.

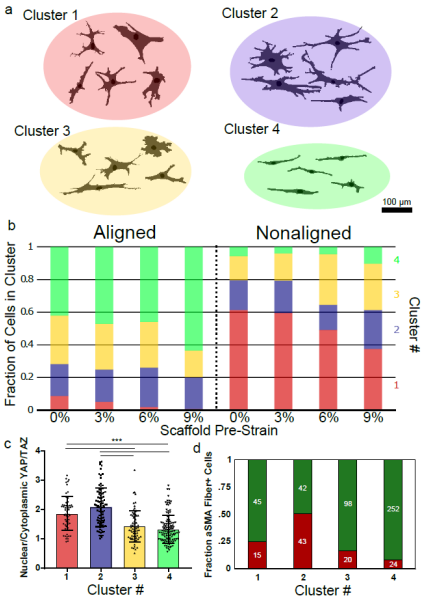

Figure 1 (a) Morphologic clusters identified in fiber environments by machine learning (n = 1044 cells). (b) Role of fiber organization and prestress on cell morphology. (c) Clusters represent different mechanobiologic states (YAP/TAZ signaling, n = 338 cells). (d) Clusters also identify downstream αSMA+ phenotype (n = 539 cells) *** p < 0.001

RESULTS: Prestrain of fibrous scaffolds leads to fiber reorganization and increased alignment as a function of strain for both aligned and nonaligned scaffolds. Cells spreading in these fiber microenvironments is heterogeneous, however, and so we employed a neural network approach to identify clusters based on cell and nuclear size, shape, and orientation (**Fig 1a**). Notably, as fiber environments became more aligned, there was a decrease in large, off-axis cells (cluster 1, $R^2 = 0.93$ in nonaligned) and an increase in aligned, high aspect ratio cells (cluster 4, $R^2 = 0.74$ in aligned, **Fig 1b**). As cell shape and size are often indicators of mechanobiology-driven phenotypic changes[4], we assessed mechano-signaling in these identified clusters. This analysis showed that clusters represent different YAP/TAZ signaling states (**Fig 1c**). In line with these changes, cells in clusters that were high in YAP/TAZ signaling also adopted a pro-fibrotic phenotype indicated by the presence of α-smooth muscle actin (**Fig 1d**). Given this connection between cell morphology and mechanosensing, we next developed a model to predict YAP/TAZ state (**Fig 2ab**). We found good agreement (r = 0.72) between the predicted and measured signaling states in single cells within our independent testing sets, and that this morphology-mechanosensing relationship could be applied to other mesenchymal cell types (bovine MSCs, **Fig 2c**). We also found that this predictive morphology-mechanosensing connection could be broken by altering the contractile state of cells using the rho-ROCK mediators fasudil or lysophosphatidic acid (LPA) (**Fig 2c**). This indicates that such neural networks may be capable of identifying aberrant mechanosensing within cell subpopulations within these in fiber environments. To test this hypothesis, we employed a model of aberrant mechanobiology using non-invasive (MCF7) and invasive cancer cells (MDA-MB-231). Using just morphology or YAP/TAZ signaling alone, the false-negative rates were 13.7% and 6.9%, respectively, when asked to identify the invasive phenotype. However, when the neural network classifier incorporated information on both morphology and YAP/TAZ signaling, false-negative rates dropped to 2.0% (**Fig 2d**), supporting that the network analysis could identify aberrant mechanosensing.

DISCUSSION: Understanding how cells interrogate their environment in cases of injury, degeneration, and disease is essential for improving therapy. Here, we developed a tool (1) to understand how cells interrogate fiber environments to dictate morphology, (2) to define how morphology dictates mechanobiologic state, and (3) to identify when mechanosensing goes awry, in cases such as cancer.

SIGNIFICANCE/CLINICAL RELEVANCE: Integrating multi-factorial data on cellular morphology and signaling into a neural network framework revealed new insight and tools to identify aberrant mechanosensing at the single cell level in fibrous microenvironments.

REFERENCES: [1] Gardner+ *JOR* 2012, [2] Bonnevie+ *Trans ORS* 2019, [3] Li+ *J Biomech* 2007, [4] McBeath+ *Dev Cell* 2004

ACKNOWLEDGEMENTS: F32 AR072478, R01 AR056624, R01 AR075418, IK2 RX001476, CMMI-1548571, R21 CA216552

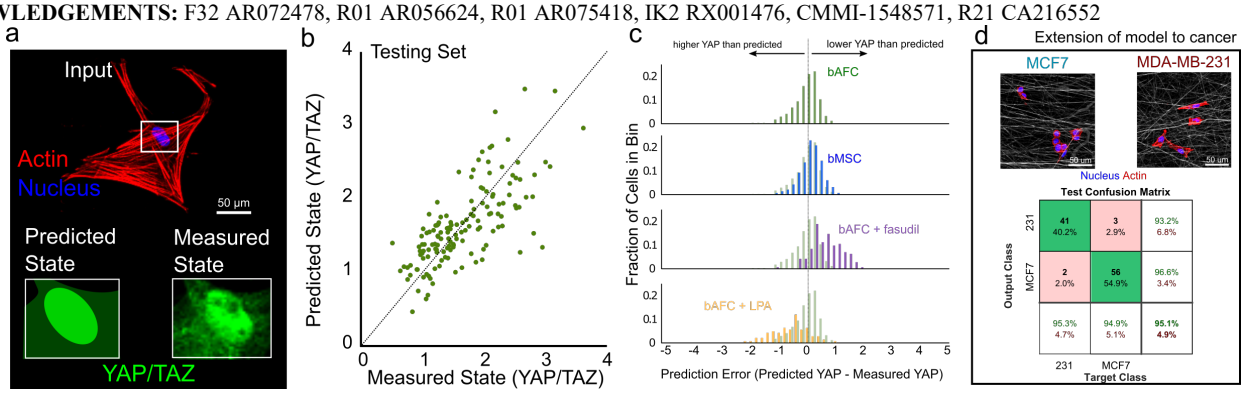

Fig 2: (a,b) A neural network was developed to predict YAP/TAZ levels based on cell and nuclear morphology using bAFCs (n = 338 cells). (c) This relationship held for bMSCs (n = 278 cells), but altering contractility disrupted the morphology-mechanosensing relationship; fasudil: n = 142 cells, LPA: n = 89 cells). (d) Using this network as a classifier, the model was also able to identify aberrant mechanosensing in invasive cancer cells (n = 292 cells).

The Effect of Macrophage Cross Talk on Adipose Tissue Inflammation

Eleanor Caston, Evangelia Bellas, Ph.D.
Department of Bioengineering, College of Engineering, Temple University, Philadelphia, PA

Introduction: Obesity is an epidemic that can lead to stroke, type 2 diabetes, cardiovascular disease and certain types of cancer and affects over 93.3 million US adults (CDC.gov). Adipose tissue (AT) macrophages play a role in AT inflammation and in the development of insulin resistance, both of which are associated with obesity. We hypothesize that AT inflammation occurs with increased cross talk between macrophages and adipocytes, the main cell type in AT, that leads to the release of inflammatory factors.

Materials and Methods: Adipocytes, derived from human mesenchymal stem cells, and THP-1 macrophages were indirectly co-cultured using a transwell setup (**Fig. 1A)**. For 3D culture, adipocytes were encapsulated in a 2 mg/mL collagen type I gel to mimic their physiological state. The cross talk was observed in a 1:0, 1:1, and 0:1 ratio of adipocytes to macrophages at a density of 8 million/mL collagen. After 48 hours of co-culture in adipomaintenance media, adipocytes and macrophages were harvested separately and sacrificed for end-point analysis, including qPCR and confocal microscopy for cell organization (lipid droplets (BODIPY), cell nuclei (Hoechst 33342)). Spent media was banked for biochemical assays. Statistical analysis was performed using ANOVA and students' t-test (alpha value of 0.05).

Results and Discussion: QPCR was performed for genes relevant to adipocytes: adiponectin (ADIPOQ), leptin (LEP), peroxisome proliferator activated receptor gamma (PPARG) and inflammation: monocyte chemoattractant protein-1 (MCP-1), matrix metallopeptidase 9 (MMP-9), and tumor necrosis factor alpha (TNFa). The adipocyte gene, leptin, was upregulated in adipocytes when co-cultured (not shown). MCP-1, a monocyte recruitment gene, was upregulated in the 3D 1:1 adipocyte compartment, which demonstrates the cross talk signaling of adipocytes to macrophages (**Fig. 1B**). In the 3D 1:1 adipocyte compartment and the 3D 1:1 macrophage compartment, MMP9, which encodes for collagen type IV and V degradation, was also upregulated, indicating that matrix remodeling may be a factor in their cross talk (**Fig. 1C**). TNFa was upregulated in all 3D groups compared to the adipocyte only control; however, expression was approximately 15-fold greater in the macrophage compartments (**Fig. 1D**). The significant upregulation of TNFa in the 1:1 adipocyte compartment points to an inflammatory response when the cell types were allowed to communicate through soluble factors alone.

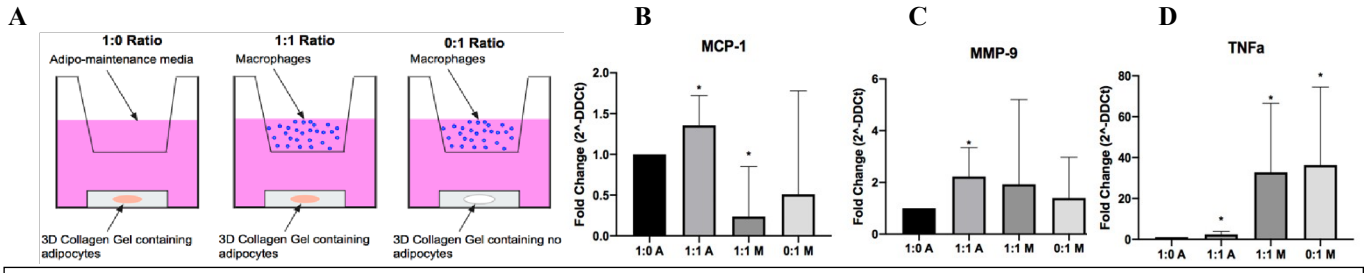

Figure 1. A: Experimental setup using transwell inserts. Ratio is adipocytes:macrophages. B-D: Adipocyte and macrophage gene expression normalized to 1:0 adipocytes after 48h in 3D culture. Statistical significance for p-values less than an alpha of 0.05 are depicted with an asterisk (*).

Conclusions: The 3D co-culture model demonstrated that adipocytes and macrophages communicate through soluble factors. The significant upregulation of pro-inflammatory genes, such as TNFa, MCP-1 and MMP-9, demonstrates that there is a relationship between macrophage activity, inflammation and remodeling in adipocytes, which can contribute to a diseased state. Future studies will look at collagen IV and V remodeling, as well as macrophage polarization. A deeper understanding of the cross talk between macrophages and adipocytes that leads to AT inflammation will allow for new potential therapeutic targets for obesity and type 2 diabetes.

Acknowledgements: Dr. Bellas' startup funds and the NIH NIDDK Diabetic Complications Consortium DK07616 and DK115255 grants (to EB).

References: 1. Permana P.A et al. Biochem Biophys Res Commun. 2005;341:507-514.

Repairing the degenerated annulus fibrosus using 3D printed poly(vinyl alcohol) tissue engineering scaffolds

Kayla Heider[1], Casey Garrell[1], Nicole Rosselli[1], TR Christiani [1]

[1] Chemical Engineering, Rowan University, Glassboro, NJ 08028

Introduction: Intervertebral disc degeneration (IVD) is frequently associated with lower back pain (LBP) and characterized by morphological changes in the tissue [1]. Discectomy, a commonly performed procedure, involves removing injurious tissue to alleviate symptoms of LBP, however this surgery does not aim to restore the usual physiological function of the disc. Therefore, an unmet need exists for the development of a technology to repair and replace damaged AF tissue following discectomy. Tissue engineering is one potential alternative strategy to replacing damaged disc tissue. In previous work, scaffolds composed of polylactic acid (PLA) were 3D printed and evaluated for their potential as AF tissue engineering scaffolds [2]. Hereon, we describe the use of 3D printed natural poly(vinyl alcohol) scaffolds for AF repair. The soluble behaviour of PVA in an aqueous environment can be exploited for potential degradative applications.

Methods: Scaffolds composed of natural PVA were created using 3D printing (Ultimaker 3 Extended). Scaffolds with a total volume of 125 mm^3 and a single pore size of 20 mm^3, 45 mm^3, and 80 mm^3 were selected for evaluation. Porosity (n = 5) was calculated using Equation 1, where ρ_{porous} and ρ_{solid} are the densities of the porous and solid PVA scaffolds, respectively.

$$P(\%) = 100 \cdot \left[1 - \frac{\rho_{porous}}{\rho_{solid}}\right] \qquad \text{(Eqn. 1)}$$

Changes in scaffold mass over time in phosphate buffered saline at 37 °C were measured as a function of porosity (n = 5). Solid blocks of PVA and PLA served as controls.

Results: The porosity of scaffolds containing a 20 mm^3, 45 mm^3, and 80 mm^3 pore were 14.9 ± 0.4 %, 36.5 ± 0.9, and 68.4 ± 0.94 %, respectively (Figure 1). Measured values of porosity matched their theoretical calculated values. In general, increased scaffold porosity resulted in significant increases in initial swelling and subsequent mass loss from the scaffold (Figure 2). As anticipated, PLA scaffolds exhibited minimal change in mass over time. The scaffold with the largest pore exhibited significant increase in mass compared to all other scaffold types and controls ($p < 0.05$).

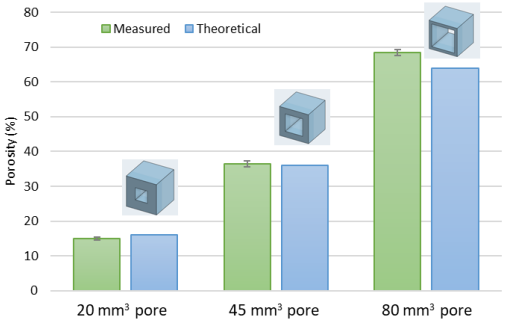

Figure 1. Measured porosity for 3D printed scaffolds matched their calculated theoretical values.

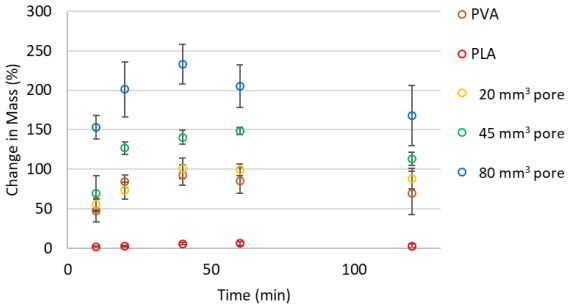

Figure 2. Change in mass over time of the porous PVA scaffolds and the control samples. Swelling and subsequent dissolution of PVA is a function of porosity.

Discussion & Conclusions: Scaffold dissolution and porosity are important properties to consider when repairing the degenerated AF. It can be concluded that as the surface area to volume ratio of the uncrosslinked PVA scaffold increases, so will its swelling and dissolution. Future work will include studying mechanical strength and viability of seeded caudal bovine AF cells as a function of scaffold architecture, porosity, and crosslinking.

References:

[1] J.P.G. Urban and S. Roberts, "Degeneration of the intervertebral disc," *Arthritis Research & Therapy*, 5 (3): 120 – 130, 2003.

[2] T.R. Christiani, E. Baroncini, J. Stanzione, and A.J. Vernengo, "In vitro evaluation of 3D printed polycaprolactone with angle-ply architecture for annulus fibrosus tissue engineering," *Regenerative Biomaterials*, 6 (3): 175 – 184, 2019.

Impact of differentiation, substrate stiffness, and contractility on nesprin expression and localization

Ryan Daniels[1], and Robert Mauck[1], PhD
[1]McKay Orthopaedic Research Laboratory, University of Pennsylvania, Philadelphia, PA

Introduction: Mechanotransduction is the process by which cells convert biophysical cues to biochemical cues[1]. The cytoskeleton transfers forces from the ECM to the nucleus via the Linker of Nucleoskeleton and Cytoskeleton (LINC) complex[1]. A primary component of the LINC complex are nesprins, which bind cytoskeletal elements and are required for cytoskeletal-nuclear mechanotransduction[1]. Nesprins 1 and 2 can bind both actin (directly) and microtubules (indirectly)[2]. Nesprins exhibit a wide range of alternative splicing, with some localizing to the nucleus or endoplasmic reticulum[3]. In mice, only the full-length (Giant) isoforms of nesprins participate in cytoskeletal-nuclear mechanotransduction[3]. While much is known on the role of the LINC complex in mechanotransduction less is known about how the LINC complex is initially set up during development and cellular differentiation, and how these factors are regulated by their microenvironment. To this end, mouse embryonic stem cells (mESCs) were used to model development in vitro and to determine which nesprins are expressed and how the LINC complex changes with differentiation. Nesprin regulation in response to biophysical stimuli were investigated in NIH3T3 cells. We hypothesized that mechanotransductive nesprins increase with differentiation and biophysical signals regulate nesprin expression and localization.

Materials and Methods: To study the effects of differentiation on nesprin expression, mESCs were differentiated towards a chondrogenic lineage. Nesprin expression was measured by quantitative polymerase chain reaction (qPCR) towards each isoform of nesprin 1 and 2. Immunofluorescence (IF) was used to evaluate nesprin localization, nesprin-cytoskeletal engagement, and qualitative expression based on intensity. To understand how substrate stiffness influence nesprin expression and localization, 3T3 cells were seeded on fibronectin-coated polyacrylamide (PA) gels of increasing stiffness (5, 15, and 55kPa) and were stained by IF for f-actin, microtubules, and Nesprin1/2. To determine how contractility regulated nesprin expression and nesprin-cytoskeletal engagement, NIH3T3 cells were seeded onto fibronectin-coated glass and the ROCK inhibitor (Y-27632) was used to inhibit contractility and a Rho agonist (CNO3) was used to promote contractility. One-way ANOVA was used to evaluate statistical significance in Figure 1.

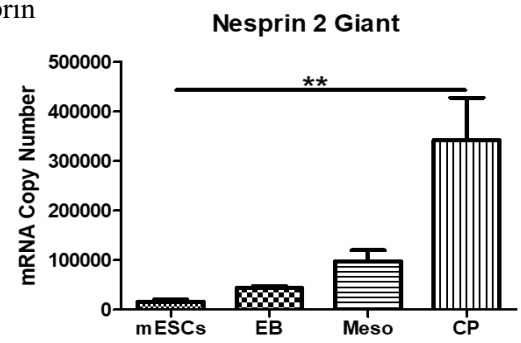

Figure 1 Nesprin 2 Giant increases with differentiation. mRNA copy number of Nesprin 2 Giant was determined using genomic DNA as a standard. EB are embryoid body cells, Meso is mesoderm primitive streak cells, and CP are chondroprogenitor cells. Box and whisker plots are shown with (N=3 replicates) and ** indicates $p<0.01$.

Results: Nesprin 2 Giant increased with each step of differentiation towards the chondrogenic lineage, as measured by qPCR (Figure 1). By IF, nuclear nesprin 2 intensity and actin-nesprin 2 colocalization increased with differentiation through the chondroprogenitor induction step. At this stage, microtubule-nesprin 2 colocalization became predominate. In 3T3 cells, decreasing substrate stiffness from glass to 5kPa, resulted in an increase in nuclear nesprin 1 staining intensity, as measure by IF. Decreasing substrate stiffness also showed an increase in cytoplasmic staining, presumably due to increased expression of the shorter isoforms of nesprin 2. 3T3 cells seeded on Fn-coated glass showed primarily actin-nesprin 2 colocalization. However, with inhibition of contractility using Y-27632, actin-nesprin2 colocalization was abolished and microtubule-nesprin colocalization increased. With increasing contractility with CNO3, both actin- and microtubule-nesprin 2 colocalization increased. Interestingly, contractility had no effect on nesprin 2 expression measured by IF intensity.

Conclusions: Taken together, mechanotransductive nesprins and cytoskeletal engagement of these nesprins appear to increase with differentiation and could be an initiator of differentiation from a pluripotent state. Substrate stiffness also appears to be a regulator of nesprin expression and localization, and contractility impacts which cytoskeletal element engages with nesprins. It could be that decreasing substrate stiffness increases nesprin expression to help anchor the cells to a softer environment and contractility regulates which cytoskeletal element participates in this cytoskeletal-nuclear mechanotransduction. Further work will be done to evaluate the functional consequences of increasing Nesprin 2 giant expression is mESCs and molecular mechanisms of nesprin regulation and localization.

Acknowledgements: NIH (RO1 AR071399, RO1 EB008722), Center for Engineering Mechanobiology (CMMI-1548571)

References: 1. Driscoll, T. P. Cytoskeletal to Nuclear Strain Transfer Regulates YAP Signaling in Mesenchymal Stem Cells. *Biophys. J.* (2015). 2.Wilson, M. H. Nesprins anchor kinesin-1 motors to the nucleus to drive nuclear distribution in muscle cells. *J. Cell Sci.* (2015). 3.Chang, W.Accessorizing and anchoring the LINC complex for multifunctionality. *Journal of Cell Biology* (2015).

Gambogic amide augments skeletal adaptation to mechanical loading through actions on both sensory nerves and osteoblasts

Gabriella Fioravanti, Phuong Q. Hua, Ryan E. Tomlinson
Thomas Jefferson University, Philadelphia, PA

The surfaces of mature bone are densely innervated by sensory nerves expressing TrkA, the high-affinity receptor for nerve growth factor (NGF). In previous work, we demonstrated that administration of exogenous NGF significantly increased load-induced bone formation, albeit with the induction of substantial mechanical and thermal hyperalgesia in adult mice. In this project, we evaluated the use of gambogic amide (GA), a recently identified robust small molecule agonist for TrkA, for augmenting skeletal adaptation to mechanical forces. First, the right forelimb of adult C57BL/6J mice was subjected to non-damaging axial compression (3 N, 100 cycles, 2 Hz rest-inserted) for three consecutive days. Administration of GA (0.4 mg/kg) one hour prior to the first bout of loading resulted in a significant increase in relative periosteal bone formation rate (+63%) as compared to vehicle (DMSO). Importantly, GA was not associated with the hyperalgesia observed following exogenous administration of NGF. In a separate experiment, the central third of the ulna was harvested after a single bout of non-damaging axial forelimb compression to isolate mRNA. qRT-PCR revealed a significant upregulation of *Wnt1* (+1.5 fold vs. non-loaded), *Wnt7b* (+1.8 fold), and *NGF* (+1.8 fold) in bones from GA-treated mice at 24 hours as compared to vehicle. To determine if these effects were exclusively mediated by NGF-TrkA signaling in sensory nerves, we cultured MC3T3-E1 cells for 7 or 14 days in osteogenic differentiation media containing NGF (50 ng/mL), GA (5, 50, or 500 nM), or vehicle (DMSO). After 7 days of culture, we observed a dose-dependent increase in the osteoblastic differentiation markers *Runx2*, *Bglap2*, and *Sp7* in response to GA; NGF treatment was not different than vehicle. However, 500 nM of GA essentially eliminated calcium deposition by alizarin red staining after 14 days of culture. Similarly, only the cells treated with 500 nM of GA had significantly impaired cell proliferation as quantified by 72 hour colorimetric MTS assay. Thus, these results indicate that an appropriate dose of GA may enhance osteoblast differentiation in addition to its function as a TrkA agonist, unlike NGF. In conclusion, these results support our overall hypothesis that GA may be useful for augmenting skeletal adaptation to mechanical forces without inducing the hyperalgesia observed following administration of NGF through actions on both sensory nerves and osteoblasts.

Implications of Deep Evolutionary History of Locomotion for Muscular Dystrophy Transgene Design

Christopher D. Greer, Andrew F. Mead, Yafeng Song, Hansell H. Stedman

Genes discovered by positional cloning generally encode low abundance proteins of uncertain function. The incidence of associated diseases strongly correlates with the size of the genes and/or encoded proteins, complicating gene therapy for some of the most common genetic diseases. For instance, in the case of Duchenne muscular dystrophy, with a global incidence of approximately 1/4000 males, the protein dystrophin is almost three times the size of the largest protein deliverable by AAV (the only current vector system capable of widespread targeting of muscle). We used comparative phylogenomics to gain insight into heretofore unrecognized structural constraints on dystrophin and identified patterns that might contribute to an improved understating of protein function. We reconstructed the deep evolutionary histories of dystrophin and titin to address a seemingly simplistic question with critical implications for DMD gene therapy: which came first, dystrophin or the sarcomere? In large animals, rapid locomotion is invariably powered by sarcomeric myosin, whereas the fastest moving unicellular eukaryotes and earliest branching animal lineages use ciliary dynein as the dominant locomotive power source. Selective pressures driving the evolutionary transition from dynein to myosin must reflect geometric constraints imposed by the organelles in which these motors achieve maximal power density, with sarcomeres but not cilia amenable to three-dimensional scaling. The molecular basis of this pivotal transition is poorly understood. We show that the emergence of sarcomeres correlates with the appearance of an ancestral titin ortholog, whereas dystrophin and its associated complex of membrane-bound glycoproteins arose piecemeal prior to the divergence of earlier branching lineages. We identify invertebrate species that retain the inferred ancestral titin supergene structure, providing a unified view of gene rearrangements that previously obscured gene orthology and the common origin of sarcomeres in animals with radial and bilateral symmetry. Surprisingly, gene structures provide compelling evidence that the extraordinary size of dystrophin's rod domain reflects the historical legacy of a parologous class of microtubule-binding proteins in which selection for increasing length occurred before the dawn of sarcomeres. These findings have critical implications for the mechanobiology of dystrophin and the design of miniaturized, AAV-deliverable proteins for therapeutic use in Duchenne and Becker muscular dystrophy.

Adipocyte-Directed Matrix Remodeling for Vascular Network Assembly in Engineered Adipose Tissue

Jennifer Hammel[1], Evangelia Bellas, PhD[1]
[1] *Department of Bioengineering, Temple University, Philadelphia PA*

Introduction: Adipose tissue regulates whole body metabolism. In order to meet these metabolic demands, this tissue is highly vascularized. During obesity, adipocytes experience hypertrophy, growing in size faster than angiogenesis can occur. This lack of vasculature results in a lack of nutrient and oxygen exchange, causing hypoxia and necrosis, leading to fibrosis and insulin resistance. In 2016, 39.8% of adults in the United States were obese and at risk for comorbidities such as Type II Diabetes, cardiovascular disease, and musculoskeletal disorders, and these rates are increasing (CDC.gov). In a previous study, we found that direct contact between adipocytes and endothelial cells led to a delay in adipocyte maturation, and that the ideal ratio for co-culture was 1:1. In this study, indirect and direct co-cultures of adipocytes and endothelial cells were performed in order to better understand how direct contact and soluble factors mediate vascular networking in engineered adipose tissue.

Materials and Methods: Human mesenchymal stem cell derived adipocytes were co-cultured with human umbilical vein endothelial cells (HUVECs) at a 1:1 ratio in 2 mg/mL Type I collagen gels, with each cell type having a density of 4 million cells/mL. Indirect co-cultures were performed using Transwells. To inhibit MMP activity, Marimastat was added to the co-cultures for the duration of the experiment. Genes involved in angiogenesis, adipocyte function, ECM deposition, integrin binding, and matrix remodeling are evaluated via qPCR. Confocal microscopy is used to visualize lipid droplets (Bodipy), vascular networks (CD31), Fibronectin and Collagen IV.

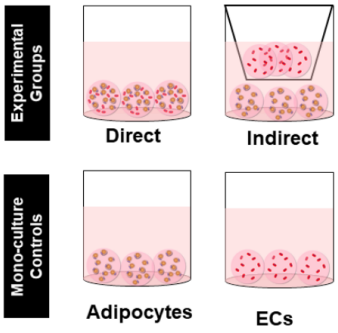

Figure 1. Experimental Set-Up.

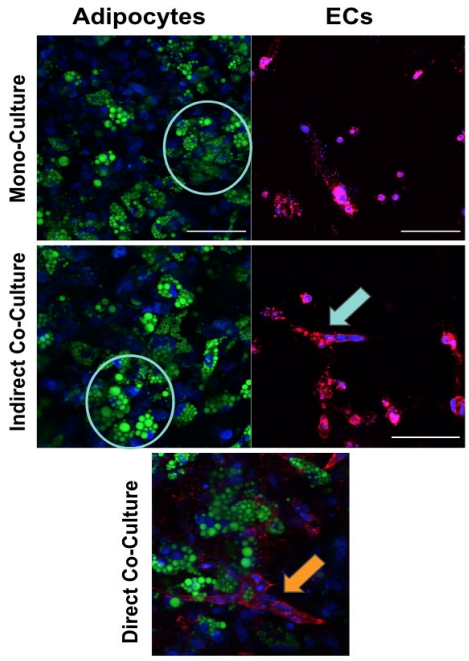

Figure 2. Confocal images of co-culture groups, with nuclei (blue), lipid droplets (green), and endothelial cells (red). Scale

Results and Discussion: Confocal microscopy demonstrated vascular network assembly to the highest degree in the direct co-culture groups (orange arrow), with little-to-no organization in endothelial cells alone (teal arrow). The direct co-culture group also demonstrated the highest fibronectin deposition, shown via confocal microscopy. On the gene expression level, fibronectin is upregulated in the indirect adipocytes compared to adipocytes-alone and direct co-culture groups. ITGB3 was upregulated in direct co-culture compared to the indirect adipocytes. MMP9 is upregulated in direct co-culture compared to indirect adipocytes and adipocytes-alone. Preliminary lipid droplet analysis suggests that the delay in maturation of adipocytes is mediated by direct contact with a vascular network. Next steps include the analysis of co-cultures with MMP inhibition and Collagen IV deposition analysis.

Acknowledgements: This study was supported by the MARC-U*Star Program, NIH T34 GM 087239 (JH), the NIDDK Diabetic Complications Consortium (www.diacomp.org), grants DK076169 and DK115255 (EB).

Aging and Degeneration Alter Chromatin Organization and Mechano-Responsivity in Human Tenocytes

Su Chin Heo[1], Shreyasi Thakur[1], Boao Xia[1], Rowena Mcbeath[2], Melike Lakadamyali[1], Robert Mauck[1]
[1]University of Pennsylvania, Philadelphia, PA; [2]Thomas Jefferson University Hospital, Philadelphia, PA

Disclosures: Su-Jin Heo (N), Shreyasi Thakur (N), Boao Xia (N), Rowena Mcbeath (N), Melike Lakadamyali (N), Robert Mauck (*JOR Spine*)

INTRODUCTION: Aged-related fibrous connective tissue degeneration (e.g. tendinosis) is a significant and costly clinical problem. Development, aging, and degeneration alter the mechanical environment of fibrous tissues, changing the biophysical inputs to resident cells and impacting their phenotype [**1**]. For instance, our group and other groups have shown that, with degeneration of fibrous tissues (e.g. meniscus and tendon), organized fibrous tissue structure begins to fail and micro-domains of non-fibrous material emerge, characterized by cells that locally change in phenotype and begin producing aberrant proteoglycan-rich ECM [**1, 2**]. While it has been well understood that chromatin organization plays an important role in gene expression and differentiation to impact cell phenotype [**3**], these studies not been applied to the context of tissue aging and degeneration, and how biophysical cues regulate these processes is not known. Here, using a super-resolution nanoscopy [i.e. stochastic optical reconstruction microscopy (STORM)], we assessed how tissue aging and/or degeneration altered chromatin organization at the nano-scale in tenocytes isolated from human donors that were young, aged, or diagnosed with tendinosis (a common tendon pathology, associated with repetitive use and mechanical overload [**2**]), and how this changed in response to biophysical perturbation.

METHODS: Human tenocytes were isolated from young [Young (y), 42 years, male], degenerative [Tendinosis (t), 35 years, male], or aged [Aged (a), 81 years, female] finger flexor tendons according to established protocols [**2**]. To observe Histone-H2B organization, cells were plated on chambered-cover glasses (500 cells/mm^2) followed by 2 days of culture in basal growth media. Fixed cells were immunostained for histone-H2B (H2B, Proteintech), and then incubated with secondary antibodies custom-labeled with activator-reporter dye pairs (Alexa Fluor 405-Alexa Fluor 647, Invitrogen) for STORM imaging (Nanoimager, ONI) [**4**]. STORM images were analyzed and rendered using Nanoimager software (ONI). For quantitative analysis, Voronoi tessellation of the H2B localizations was implemented in MATLAB to segment super-resolution images [**4**]. To investigate the effect of substrate stiffness, young (y) healthy tendon cells were cultured on cover glass (Glass), 5 kPa (soft), or 55 kPa (stiff) methacrylated hyaluronic acid hydrogels (MeHA) [**Fig. 2 (A), 5**], followed by 2 days of culture, and were then imaged by STORM. Additionally, to investigate the effect of fluid-induced shear stress (FSS), a custom-PDMS microfluidic chamber was used [**6**] to impose FSS to tenocytes seeded on cover glass (500 cells/mm^2) at 5 dyne/cm^2 for 30 min. After the cessation of flow, cells were imaged as above.

RESULTS: Super-resolution images of Hisone-H2B and Voronoi tessellation analysis showed that, on glass, H2B localizations clustered to form distinct and spatially separated nanodmains in young healthy tenocyte nuclei [Young (y)]. Conversely, degenerated [Tendinosis (t)], or aged [Aged (y)] tenocyte nuclei contained smaller domains (**Fig. 1A-B**). Interestingly, H2B nanodomains were localized at nuclear periphery in the degenerative [Tendinosis (t)] tenocyte nuclei (**Fig.1 A**). This led us to the next question how exogenous biophysical cues might effect chromatin organization in these cells. When young healthy tenocytes (y) were cultured on soft substrates, nanodomain size decreased to levels comparable to that seen in degenerative (tendinosis) or aged tenocytes and, strikingly, these H2B nanodomains relocated to the nuclear periphery on the 5 kPa substrates (soft) (**Fig. 2A-D**). When FSS was applied to cells from all three conditions, we noted an increase in the number of localizations per histone cluster and the cluster area in both young and aged tenocytes (**Fig. 3B-C**), with levels in FSS-stimulated aged tenocytes reaching that of young healthy tenocytes. However, tendinopathic cells did not respond to FSS, remaining at baseline (**Fig. 3B-C**).

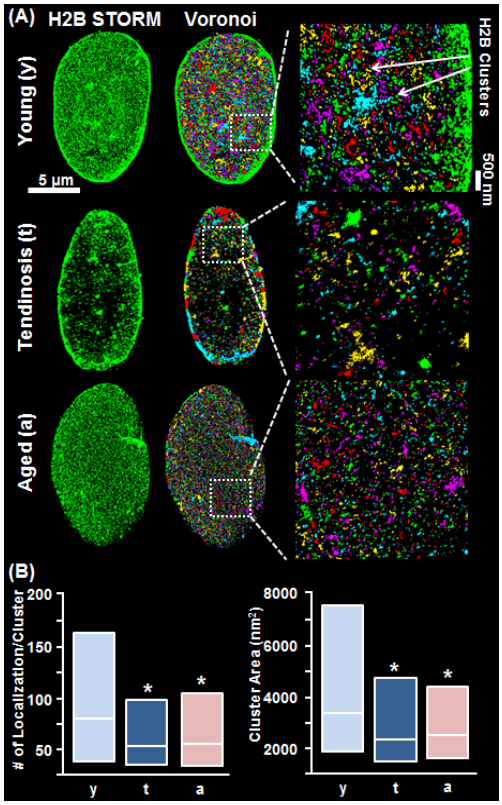

Fig. 1: (A) Histone H2B STORM images and Voronoi cluster analysis of H2B localizations in young (y), tendinosis (t) or aged (a) human tendon cell nuclei. (B) Quantification of the number of H2B localizations per cluster and the cluster area [n ≥ 10,275 clusters from 5 cells, *p<0.01vs. Young (y)]; the box and line correspond to the interdecile range (IDR, 10th~90th percentile) and median respectively.

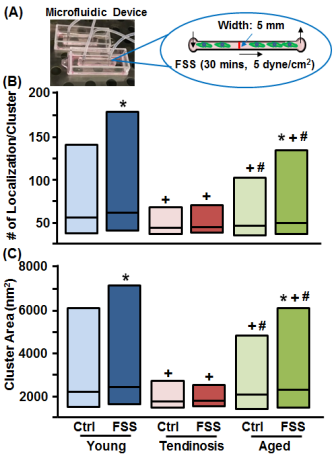

Fig. 3: (A) Schematic showing FSS study set up. (B, C) Quantification of the number of H2B localizations per cluster and the cluster area [n ≥ 13,225 clusters from 5 cells, *p<0.01 vs. Ctrl, +p<0.05 vs. Young, #p<0.05 vs. Tendinosis]; the box and line correspond to the interdecile range (IDR, 10th~90th percentile) and median respectively.

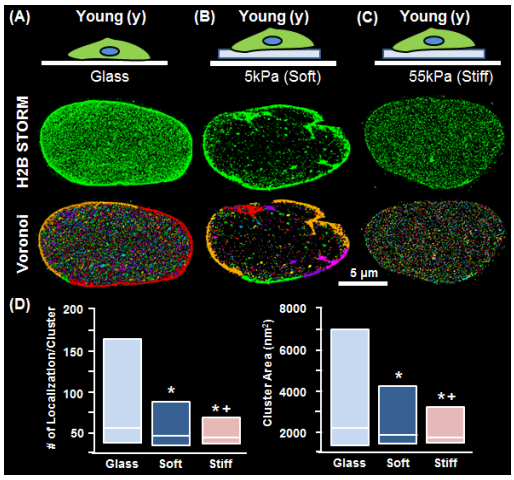

Fig. 2: (A) Histone H2B STORM images and Voronoi cluster analysis of localizations in young (y) tendon nuclei seeded on glass (A), 5kPa (Soft, B), or 55kPa (Stiff, C) substrates. (D) Quantification of the number of H2B localizations per cluster and the cluster area [n ≥ 12,334 clusters from 5 cells, *p<0.01vs. Glass, +p<0.05 vs. Soft]; the box and line correspond to the interdecile range (IDR, 10th~90th percentile) and median respectively.

DISCUSSION: In this study, we show that aging and degeneration alter chromatin organization and mechano-responsivity in tenocytes. Interestingly, aging decreased the number and area of localizations, while disease increased the concentration of these nanodomains to the periphery. This region of the genome is understood to be generally heterochromatic (condensed) and inactive. Interestingly, when healthy young cells were plated onto soft substrates, this bias in nanodomain localization to the periphery increased, suggesting perhaps that tendon micro-damage and softening drives aberrant cell behavior. When these tendinopathic cells were exposed to FSS, they remained unresponsive, suggesting that the prolonged alterations in nano-scale chromatin organization may be associated with a loss of mechanical sensitivity. Ongoing studies are focused on elucidating how this nano-scale organization impacts expression and phenotype in tendon aging and disease.

SIGNIFICANCE: Here, we evaluate spatial chromatin reorganization at the nano-scale in tenocytes with aging or degeneration. These studies d may inform new therapeutic strategies for treating connective tissue pathologies.

REFERENCES: [1] Han+, Nat Mater 2016; [2] McBeath+, Aging Cell 2019; [3] Heo+, eLife 2016; [4] Ricci+, Cell 2015; [5] Cosgrove+, Nat Mater 2016; [6] Heo+, ORS 2019. **ACKNOWLEDGEMENTS:** This work was supported by the NIH (R01 AR056624) and the NSF (CMMI-1548571).

Chondrocytes rely on SOX9 in both growth plate and adult articular cartilage to fulfill pancartilaginous rather than osteogenic activities

Ranjan Kc[1*], Abdul Haseeb[1*], Charles de Charleroy and Véronique Lefebvre[1]

[1]Translational Research Program in Pediatric Orthopaedics, Division of Orthopaedic Surgery, The Children's Hospital of Philadelphia, Philadelphia, PA 19104

*These authors equally contributed to this work

Growth plate and articular cartilage are essential skeletal structures in development and throughout life, respectively. Growth plate chondrocytes derive ontogenically from osteochondroprogenitor cells, and articular chondrocytes from joint progenitor cells. The two cell subtypes share a pan-cartilaginous differentiation program, but differ in other phenotypic aspects and ultimate fates. Growth plate chondrocytes progress fast through early, proliferative and maturation stages, and either die or convert into osteoblasts as their tissue is replaced by endochondral bone. After actively turning over during development, growth plates close (disappear) at puberty in humans and greatly slow down their activities in adult mice. Articular chondrocytes, in contrast, are arrested at a non-proliferative, early differentiation stage and their permanent tissue undergoes limited turnover. Premature growth plate closure in childhood and osteoarthritic degeneration of articular cartilage in adulthood are prevalent, severe diseases in humans, but their underlying mechanisms remain incompletely understood. To help fill this knowledge gap, we asked whether the SOX9 transcription factor, well known for its master roles in developmental chondrogenesis through activation of pan-cartilaginous genes, is also involved in growth plate and articular cartilage maintenance in juvenile and adult mice. We found that conditional inactivation of *Sox9* in chondrocytes in these mice quickly resulted in growth plate closure, while articular cartilage appeared to lose its specific proteoglycans but to remain otherwise intact. Growth plate closure was contributed by chondrocyte proliferation arrest and by accelerated tissue invasion by the endochondral ossification front. Moreover, both growth plate closure and articular cartilage changes could be explained by drastic downregulation of most pan-cartilaginous genes, including those for essential extracellular matrix components and signaling pathway modulators. While *Sox9* deletion severely impaired the expression of growth plate-specific genes, it only partially impaired the expression of articular cartilage-specific genes, and it also resulted in the activation or upregulation of major osteoblast-specific masters and markers in both growth plate and articular chondrocytes. Our findings thus reveal that both growth plate and articular chondrocytes rely on SOX9 throughout life to fulfill pancartilaginous rather than osteogenic activities and thereby maintain a healthy skeleton. By increasing understanding of physiological mechanisms, these findings will certainly help explain various cartilage pathologies and devise strategies for the prevention and treatment of these diseases.

Crosstalk Between Glycolysis and Mitochondrial Metabolism in Osteoblasts

Wen-Chih Lee and Fanxin Long

Translational Research Program in Pediatric Orthopaedics, Department of Surgery, Division of Orthopaedic Surgery, Children's Hospital of Philadelphia

Mounting evidence from diabetes indicates a link between whole-body glucose metabolism and bone health. To elucidate the metabolic features of osteoblast-lineage cells, we have studied cellular metabolism in primary murine calvarial preosteoblasts before and after further differentiation *in vitro*. RNA-seq confirmed marked upregulation of the marker genes for mature osteoblasts following seven days of differentiation. Energy substrate analyses showed that both preosteoblasts and mature osteoblasts mainly relied on glucose, but not glutamine or fatty acids, for ATP production, but that mature osteoblasts consumed more glucose per cell than preosteoblasts. Importantly, both preosteoblasts and osteoblasts extracted energy form glucose mainly by metabolizing it to lactate, even in the presence of abundant oxygen (21%), as inhibition of OXPHOS with the ATP synthase inhibitor oligomycin only minimally affected the intracellular ATP levels. Real-time measurements of lactate production (ECAR) and oxygen consumption rate (OCR) with Seahorse technology detected a marked increase in ECAR coupled with a notable suppression of OCR in mature osteoblasts compared to preosteoblasts. Metabolic tracing with U-^{13}C glucose showed that in mature osteoblasts, glucose-derived pyruvate was mostly converted to malate through malic enzyme without significant contribution to citrate or succinate via the canonical TCA cycle. This finding indicates that mature osteoblasts likely activate the malate-aspartate shuttle to regenerate cytosolic NAD+ that is necessary to sustain the more active glycolysis. Interestingly, RNA-seq experiments showed that the genes encoding mitochondrial electron transport chain (ETC) components were upregulated in mature osteoblasts compared to preosteoblasts even through OCR was reduced. Increased ETC activity may be necessary for regenerating NAD+ in the mitochondria to sustain the malate-aspartate shuttle. In summary, both preosteoblasts and mature osteoblasts metabolize glucose t0 lactate as the predominant mode of energy production, but the glycolytic flux is further elevated in mature osteoblasts. The high demand for cytosolic NAD+ recycling from NADH in mature osteoblasts likely requires the upregulated malate-aspartate shuttle that operates across the mitochondrial inner membrane. Further elucidation of the cytoplasmic-mitochondrial metabolic crosstalk in osteoblasts may open new avenues for developing bone-enhancing therapies.

Metabolic Labeling to Probe Temporal Changes in the Pericellular Matrix at the Cell-Hydrogel Interface

Claudia Loebel, Mi Kwon, Tianbi Duan, Robert L. Mauck, Jason A. Burdick
Department of Bioengineering, University of Pennsylvania, 210 South 33rd Street, Philadelphia PA 19104, PA

Introduction: Cell-laden hydrogels are engineered with various biochemical cues to recreate aspects of the native microenvironment and define cellular function such as differentiation and extracellular matrix (ECM) deposition[1]. However, this ECM that is deposited rapidly within the pericellular space likely affects how cells sense these engineered hydrogel cues, a process that is not well understood. Thus, we employed metabolic labeling strategies to visualize proteins and proteoglycans secreted by cells within hydrogels[2] and investigated their ability to physically separate the cell membrane from the hydrogel, including as a function of hydrogel crosslink density.

Materials and Methods: Hydrogels were synthesized through norbornene-modified hyaluronic acid (NorHA) crosslinked with dithiothreitol (DTT) via a light-mediated thiol-ene reaction[3] to form hydrogels with an elastic modulus of either 5 or 20 kPa based on DTT concentration and used to encapsulate bovine chondrocytes at 5 million cells/mL. Constructs were cultured in methionine-free chondrogenic media (DMEM+TGFβ3, ITS) and secreted proteins or proteoglycans were labeled with fluorophore conjugated DBCO of incorporated azidohomoalanine (AHA) or N-azidoacetylmannosamine-tetraacylated (Ac4ManNAz, Fig. 1A). Fluorescent polystyrene beads (nominal diameter ~0.02 um) were co-embedded with cells at ~3 x 10^{10} beads/mL to visualize the hydrogel.

Results and Discussion: Staining of secreted ECM proteins (AHA) showed formation of a pericellular matrix around chondrocytes as early as one day after encapsulation (Fig. 1B). This matrix accumulated as indicated by increased ECM protein thickness over 7 days (Fig. 1C), which depended on the initial hydrogel mechanics with lower thicknesses observed for stiffer hydrogels (not shown). Beads were encapsulated in hydrogels and were stable over time, allowing their use to approximate the hydrogel position in fluorescent images. Imaging indicated a close proximity of the hydrogel/beads to the cell after encapsulation (Fig. 1D); however, emerging ECM proteins physically displaced the hydrogel over time (e.g., day 7) (Fig. 1E). Ac4ManNAz labeled proteoglycans colocalized with secreted ECM proteins (AHA), but were also present beyond the ECM protein-hydrogel interface without further displacing the hydrogel (Fig. 1E). This is likely due to the smaller sizes of proteoglycans when compared to ECM proteins.

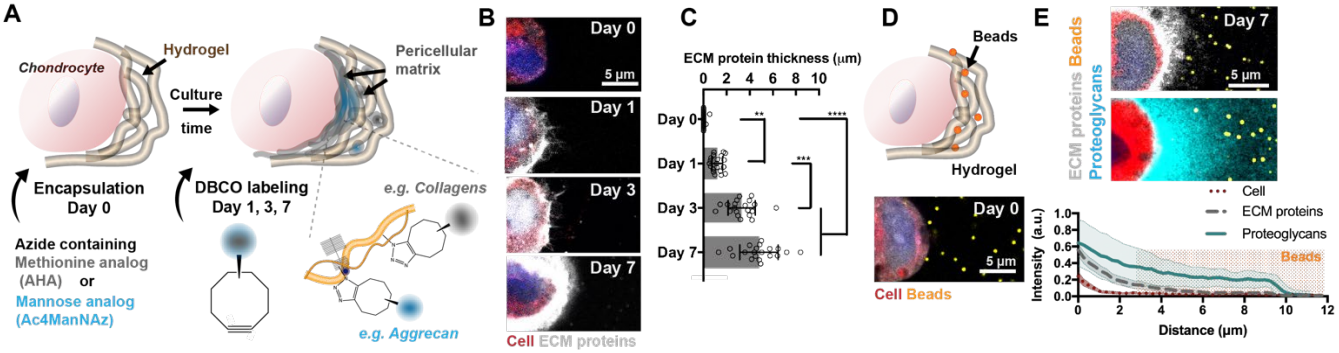

Figure 1 A Schematic illustrating chondrocyte encapsulation and pericellular matrix labeling via introduction of AHA or Ac4ManNAz and labeling with fluorophore-conjugated DBCO. **B** Images and **C** quantification of ECM protein (AHA) labeling in 5 kPa hydrogels over time (n = 20 cells per group, mean ± SD, *p≤0.05, ***p≤ 0.001, ****p≤ 0.0001). **D** Schematic and image of cells embedded with fluorescently labeled beads to visualize the cell-hydrogel interface. **E** Images and profile analysis of ECM protein (AHA) and proteoglycans (Ac4ManNAz) including beads (n = 20 cells per group, mean ± 95% confidence interval).

Conclusions: Metabolic labeling with AHA and Ac4ManNAz enabled the visualization of both secreted proteins and proteoglycans to understand their spatial localization and temporal presentation at the cell hydrogel interface. Our results indicate that ECM proteins physically displace the hydrogel from the cell membrane early during cell culture, while proteoglycans appear to distribute further into the hydrogel. These findings suggest that the secreted ECM increasingly masks the presentation of engineered biochemical cues, with timing dependent on hydrogel crosslink density. This understanding may have direct implications on the design of hydrogels in tissue engineering. Ongoing work is to understand changes in the local mechanics due to deposition of this pericellular matrix.

References: [1]Guvendiren M. et al Curr Opin Biotech 2013;841-846, [2]Loebel C. et al Nat Mater 2019, 18, 883-891, [3]Gramlich WM. et al Biomaterials 2013;34, 9803−11

Sustained interleukin-10 transgene expression following intra-articular AAV5-IL-10 administration in horses

Kyla Ortved, DVM, PhD,
Jacques Jenny Endowed Term Chair in Orthopedic Surgery, University of Pennsylvania School of Veterinary Medicine

Background

Joint trauma leads to post-traumatic inflammation with upregulation of inflammatory cytokines and degradative enzymes. If severe enough, this response can lead to irreversible post-traumatic osteoarthritis (PTOA). A therapeutic that mitigates inflammation in the posttraumatic joint would be of great benefit. Interleukin-10 (IL-10) has potent anti-inflammatory effects and has protective effects in inflamed equine chondrocytes. (1) A gene therapy approach using a vector to overexpress IL-10 in the joint represents a feasible method of delivering sustained, high doses of IL-10 in the posttraumatic joint. Adeno-associated virus (AAV) is non-pathogenic viral vector that represents an ideal gene therapy vector for intraarticular therapy.

Objective/Hypothesis

The objectives were to investigate the intraarticular response to vector injection including inflammation and transgene production, and to investigate systemic distribution of transgene and vector. We hypothesized that AAV5-IL-10 injection would result in sustained IL-10 expression without inducing intrasynovial inflammation and that injection that would not affect systemic IL-10.

Methods

The middle carpal joint of horses free of carpal OA were injected with AAV5-IL-10 (n=6) or saline (n=6). Synovial fluid (SF) was collected on days 0, 1, 2, 4, 7, 14, 28, 56, and 84. Nucleated cell content (NCC), total protein (TP) and inflammatory cytokines (IL-10, IL-6, IL-17a, IL-1β, TNFα, and IFN-γ) were quantified. Serum IL-10 was also quantified. Total SF and serum vector genomes were quantified using qPCR. A mixed effects model was used to analyze continuous data. Statistically significant differences between groups were determined using a Wilcoxon rank sum test. $P < 0.05$ was considered to be significant.

Results

Injection with saline and AAV5-IL-10 led to transient increases in NCC and TP **(Fig 1)**. Inflammatory cytokines were not significantly different between groups, except IL-17a (increased on day 2 in AAV5-IL-10 joints), and IL-1β and IL-6 (decreased on day 84 in AAV5-IL-10 joints) **(Fig 2)**. IL-10 was significantly increased in AAV5-IL-10 SF at all time points **(Fig 3).** Serum IL-10 was not different between groups **(Fig 3)**. Vector genomes were not detectable in SF, serum or synovial fluid in saline injected horses. Vector genomes were detectable in SF, serum and synovial membrane of all AAV5-IL-10 horses **(Fig 4, 5)**.

Discussion

AAV5-IL-10 injection led to sustained increase in SF IL-10. One major concern with IL-10 overexpression is systemic perturbations, however, no changes in serum IL-10 were noted. Additionally, intraarticular AAV5-IL-10 did not lead to a clinically significant inflammatory response and may actually decrease inflammatory cytokine production over time as IL-1β and IL-6 were lower on day 84. Interleukin-10 is a potent, anti-inflammatory cytokine with potential to modulate articular inflammation, thereby protecting articular cartilage from degradation and PTOA. This study demonstrates the feasibility of intraarticular AAV5-IL-10 and future studies are planned to evaluate IL-10 gene therapy in joints with experimentally-induced PTOA.

References

1. Ortved KF, Begum L, Stefanovski D, Nixon AJ. AAV-mediated Overexpression of IL-10 mitigates the inflammatory cascade in stimulated equine chondrocyte pellets. Curr Gene Ther 2018;18(3):171–9.
2. Finnegan A, Kaplan CD, Cao Y, Eibel H, Glant TT, Zhang J. Collagen-induced arthritis is exacerbated in IL-10-deficient mice. Arthritis Res Ther. 2003;5(1):R18-24.
3. Watson Levings RS, Broome TA, Smith AD, Rice BL, Gibbs EP, Myara DA, et al. Gene therapy for osteoarthritis: Pharmacokinetics of intra-articular self-complementary AAV interleukin-1 receptor antagonist delivery in an equine model. Hum Gene Ther Clin Dev 2018;29(2):90–100.

Engineering the Microenvironment of the Damaged Cartilage Interface to Direct MSC Localization and Response

Jay M. Patel[1,2], Claudia Loebel[1,2], Brian C. Wise[1], Kamiel S. Saleh[1,2], James L. Carey[1], Jason A. Burdick[1], Robert L. Mauck[1,2]
[1]University of Pennsylvania, Philadelphia, PA, [2]Corporal Michael J Crescenz VA Medical Center, Philadelphia, PA.
jaymilanpatel@gmail.com

Disclosures: JM Patel (3B, NovoPedics), JL Carey (3C, Vericel), RL Mauck (8, JOR Spine)

Introduction: Articular cartilage consists of a dense extracellular matrix (especially in the superficial zone) that allows the tissue to undergo fluid pressurization during compressive loading. Cartilage injuries compromise this function, introducing free boundaries that result in the loss of proteoglycans and other matrix elements [1], and often progress in size and severity. A biomaterial at this interface may functionally restore the properties of the defect boundary [2], however synthetic materials may wear or delaminate with time. Here, we developed a novel material to direct the formation of a living fibrous "biosealant" at the damaged interface (via targeted progenitor cell recruitment and differentiation), to restore cartilage biomechanical function. Specifically, we used a modified hyaluronic acid to reprogram the defect interface to 1) enhance the attachment of mesenchymal stem cells (MSCs), 2) to induce these cells to undergo fibrogenesis via mechanical cues, and 3) to promote deposition of fibrous matrix to seal the defect.

Methods: Biomaterial Microenvironment: Methacrylated hyaluronic acid (~40% mod) was conjugated with FITC peptides for visualization and fibronectin-mimicking peptides (RGD) to promote cell adhesion. The material was oxidized to introduce aldehydes (~30% substitution), which form covalent linkages with exposed amines in damaged tissue [3]. Bovine cartilage plugs were retrieved and sectioned (6mm diameter x 100µm thick). These discs were maintained as naïve samples (FD; mimicking a focal defect) or were digested in collagenase (0.01% for 30 minutes) to mimic degenerated cartilage (DD). Biomaterial solution (4% w/v, 10µL) was applied and UV-crosslinked for 0, 5, or 15 minutes, followed by PBS washes to remove non-adhered biomaterial. Focal Adhesion Analysis: Tissue-biomaterial composites were seeded with juvenile bovine MSCs (P1-P2, 500 cells per disc) for 24 hours. Cells were stained for paxillin to quantify the focal adhesion complexes (cellular adhesion; **Fig 1B**). Adhesion area per cell was quantified using the UNC Focal Adhesion Server. MSC Fibrogenesis and Barrier Formation: Cartilage discs (both FD and DD) were subjected to biomaterial application and cross-linking. One half of the discs were seeded with 500 cells and cultured for 7 days, followed by staining for α-smooth muscle actin (α-SMA). The percentage of "fibrogenic" cells was determined by counting cells with co-localization of F-actin and α-SMA. The remaining discs were seeded with 5,000 cells and cultured for 7 days in media containing L-azidohomoalanine (an analog to L-methionine that is incorporated into nascent matrix; **Fig 3A**), enabling staining and visualization of newly synthesized matrix proteins [4].

Results: Confocal microscopy showed that the biomaterial infiltrated throughout the 100µm section prior to cross-linking, forming an integrated biomaterial microenvironment with the existing cartilage matrix (not shown). Biomaterial application and cross-linking enhanced MSC adhesion (**Fig 1A**) to the tissue-biomaterial interface, increasing focal adhesion area per cell (**Fig 1C**). MSCs cultured for 7d on both FD and DD cartilage discs had greater α-SMA and F-actin co-localization (**Fig 2A**), resulting in a greater percentage of cells that were "fibrogenic" (**Fig 2B**). Finally, while discs with no biomaterial showed little matrix deposition, application of biomaterial prior to cell seeding promoted new matrix formation (**Fig 3B**). In fact, in the FD+15 condition, a dense fibrillar matrix was observed on top of the biomaterial microenvironment (**Fig 3C**), covering up to 50% of the defect after 7 days (**Fig 3D**).

Discussion: This study details the development of a modified biomaterial that: 1) enhances MSC adhesion to cartilage defects, 2) guides these cells towards a fibrogenic phenotype, and 3) promotes the deposition of matrix at the interface. Future studies will investigate the ability of this barrier to seal defects and preserve cartilage integrity in vivo in a large animal model.

Significance/Clinical Relevance: Biomaterial modification of the cartilage defect interface may enhance the localization of intra-articular MSC injections and direct these cells towards biosealant formation for cartilage repair.

References: [1] Basalo+ J Biomech Eng, 2004. [2] Greiner+ J Biomech, 2015. [3] Wang+ Nat Mater, 2007. [4] McLeod+ Sci Rep, 2016.

Acknowledgements: This work was supported by the NIH, VA, AOSSM, and the NSF/CEMB.

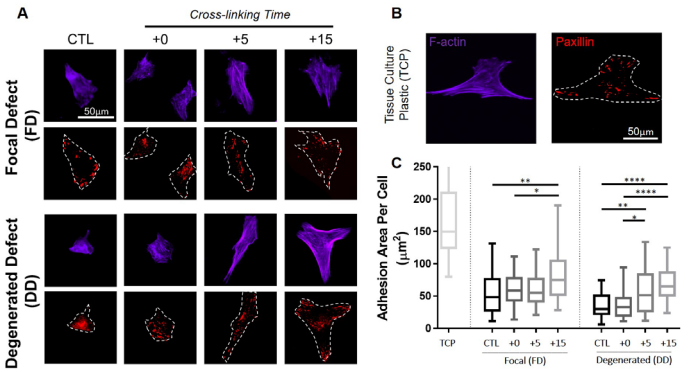

↑ **Fig 1.** [A] F-actin and paxillin staining of MSCs on cartilage without biomaterial (CTL) and with biomaterial with 0, 5, or 15 minutes of cross-linking. t=24hr. Scale = 50µm. [B] Control cell on tissue culture plastic (TCP). [C] Adhesion area per cell. *, **, **** represent $p < 0.05, 0.01, 0.0001$, respectively.

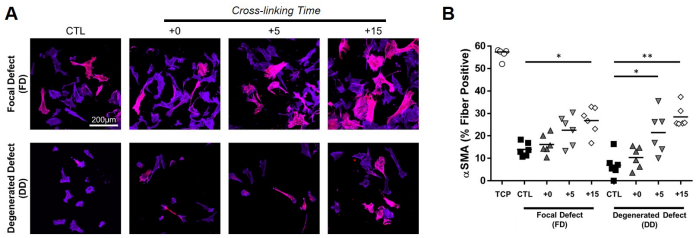

↑ **Fig 2.** [A] Co-localization (pink) of F-actin and α-SMA indicating "fibrogenic" cells. Scale = 200µm. [B] Percentage of cells positive for co-localization of α-SMA and F-actin fibers. *, ** represent $p < 0.05, 0.01$, respectively.

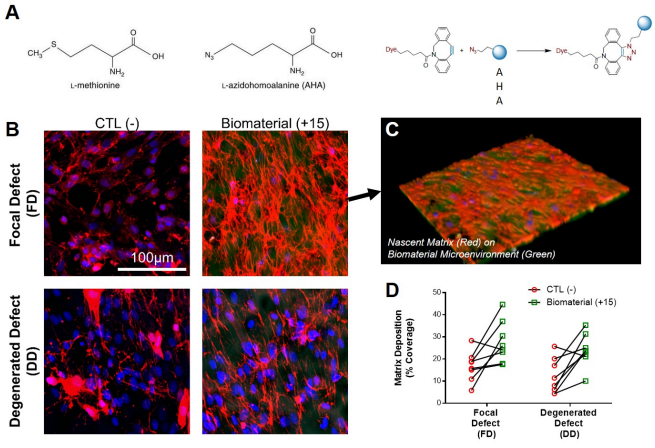

↑ **Fig 3.** [A] AHA is an L-methionine analog that can be stained to visualize nascent matrix production. [B] Matrix deposition on FD and DD samples without (CTL) and with biomaterial (+15). [C] FD+15 shows dense matrix formation on top of biomaterial. [D] Area covered by new matrix. *, ** represent $p < 0.05, 0.01$, respectively.

Directed Microfiber Alignment within Hydrogel Inks during Extrusion Bioprinting

Margaret E. Prendergast, Matthew D. Davidson, Jason A. Burdick
Department of Bioengineering, University of Pennsylvania, Philadelphia, P*A*

INTRODUCTION: The mimicking of native extracellular matrix (ECM) cues such as fiber composition and orientation impacts cell behavior, including spreading and anisotropy [1]. While traditional extrusion bioprinting is a promising technology in tissue repair, current printed filament structures exhibit resolutions (≈0.2 mm) much larger than the fibrous structures of the ECM [2]. Here, we embedded short fibers within bioinks and printed filaments to fabricate constructs with tunable structures at multiple length-scales [3]. Additionally, control over fiber orientation introduces alignment to cells, a feature that is important particularly in the engineering of anisotropic connective tissues.

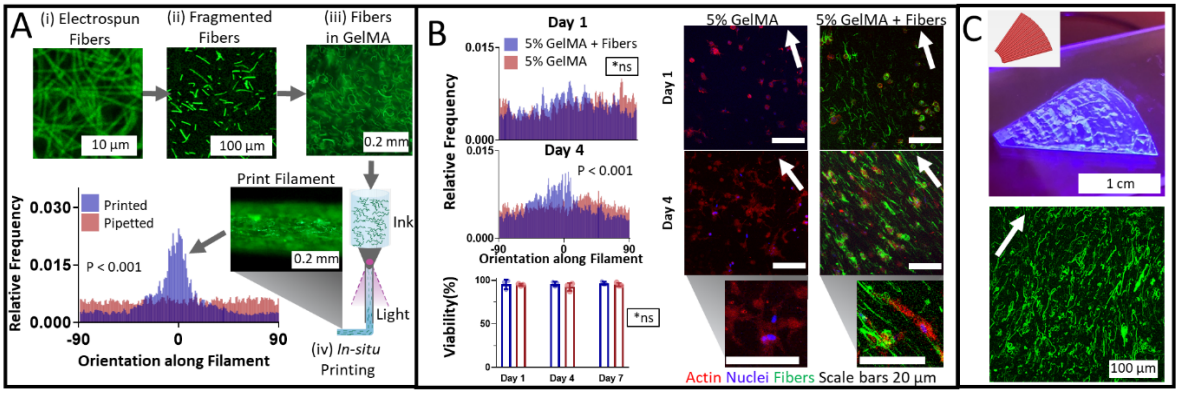

EXPERIMENTAL METHODS: Norbornene-functionalized hyaluronic acid (NorHA) was used to generate fluorescent electrospun fibers, which were then fragmented into short fibers by repeatedly passing through a needle, and then mixed with gelatin methacrylate (GelMA) for bioprinting (Fig. 1Ai-iii). Structures were printed across a range of parameters (e.g., capillary diameter, print pressure/temperature, light intensity) through an *in-situ* crosslinking process to control fiber orientation, where inks were exposed to visible light (405 nm) during extrusion via a transparent capillary (Fig. 1Aiv). Meniscal fibrochondrocytes (MFCs) were mixed with fiber-laden inks and printed, with cell viability analyzed via Live/Dead imaging and fiber and cell orientation quantified via ImageJ and FiberFit software. Comparisons between angle orientations were assessed via a Watson's Two-Sample Test of Homogeneity (R circular package) and viability results were analyzed with two-way ANOVA (GraphPad Prism, $p<0.05$ significant).

RESULTS AND DISCUSSION: Electrospun fibers were successfully fragmented into short fibers that could be added to bioinks. Microfiber alignment within printed filaments (0.2 ± 0.1 mm diameter, $n=6$) was modulated by tuning various print parameters (e.g., greater pressures increased fiber alignment), with optimization resulting in high fiber alignment when compared to the same formulation simply pipetted (Fig. 1A, $p<0.001$). MFC-laden filaments maintained viability above 90% over 7 days, with no significant differences in viability within GelMA constructs with or without fibers (Fig. 1B). Printed and aligned microfibers induced MFC alignment over time, likely acting as directional cues as the MFCs degraded the GelMA filaments, with significant differences in cell orientation observed in constructs with or without fibers by 4 days of culture (Fig. 1B, $p<0.001$, arrows denotes direction of filament). Bulk constructs with circumferential and radial oriented filaments were successfully fabricated (Fig. 1C), with fiber orientation along filaments maintained, illustrating multi-scale fibrous structures (Fig. 1C, arrow denotes direction of filament).

CONCLUSIONS: The *in-situ* printing process allowed for control of construct features on multiple length scales, including microfiber alignment that induced cell alignment with culture time. This is a significant advanced in the design of extrusion bioinks, as there are currently few examples where the ink guides directionality of the cell behavior. Potential scalability of this method is demonstrated through successful fabrication of bulk constructs with radial and circumferential oriented filaments, which we are exploring for the engineering of fibrous connective tissues (e.g., meniscus).

REFERENCES: 1. Ruijter, M et al. Adv Health Mater 2019, 8:1800418; 2. Wade, RJ et al. Adv Mater 2015, 27:1356-1362; 3. Ouyang, L et al, Adv Mater 2017, 29:1604983.

Vitamin D deficiency is associated with reduced mobility after hip fracture surgery: a prospective study.

Hao L[1], Carson JL[2], Schlussel Y[1], Noveck H[2], Shapses SA [1-2]
[1] Department of Nutritional Sciences, and the Institute Food Health Nutrition, Rutgers University; [2] Department of Medicine, Rutgers-Robert Wood Johnson Medical School, New Brunswick, NJ

Background: Hip fractures are associated with a high rate of morbidity and mortality, and successful ambulation after surgery is an important outcome in this patient population.
Objective: This study aims to determine whether 25-hydroxyvitamin D (25(OH)D) level or the Geriatric Nutritional Risk Index (GNRI) is associated with mortality or ability to walk in a patient cohort after hip fracture surgery.
Design: Patients undergoing hip fracture repair from a multi-site study in North America were included. Mortality and mobility were assessed at 30 and 60 days after surgery. Serum albumin, 25(OH)D and intact parathyroid hormone (iPTH) were measured. Patients were characterized with 25(OH)D <12ng/mL, 12 to <20, 20 to <30 or ≥ 30. GNRI was categorized into major/moderate nutritional risk (<92), low risk (92 to <98) or in good nutritional status (≥ 98).
Results: Of the 290 patients (82 ± 7 years, body mass index 25 ± 5 kg/m^2), 73% were females. Compared to patients with <12 ng/mL, those with higher 25(OH)D levels had greater ability to walk at 30 days (p=0.031): 12 to <20 ng/ml (adjusted odds ratio=2.61; 95%confidence interval= 1.13-5.99); 20 to <30 ng/mL (3.48; 1.53-7.95); ≥ 30 ng/ml (2.84; 1.12-7.20). In addition, there was also greater mobility at 60 days (p=0.028) in patients with higher 25(OH)D compared to the reference group (<12 ng/mL). Poor nutritional status (GNRI < 92) showed an overall trend to reduce mobility (unadjusted p=0.044 and adjusted p=0.058) at 30, but not at 60 days. There was no association of vitamin D or GNRI with mortality at either time point.
Conclusions: Vitamin D deficiency (<12 ng/mL) is associated with reduced ambulation after hip fracture surgery whereas GNRI also contributes to immobility but is a less reliable predictor. Mechanisms that can explain why vitamin D deficiency affects mobility should be addressed in future studies.

Microphysiological Modeling of Adipose Tissue for High Throughput Applications

Michael Struss B.S.[1], Evangelia Bellas Ph.D.[1]
[1]Department of Bioengineering, College of Engineering, Temple University, Philadelphia, PA

Introduction: Adipose tissue is a highly vascularized endocrine organ, dependent on its vasculature to maintain whole body metabolic homeostasis. Inadequate vascularization, in cases such as obesity, leads to tissue hypoxia ultimately resulting in metabolic dysfunction. Metabolic dysfunction is a risk factor for many co-morbidities, including various musculoskeletal disorders. Traditionally, adipose tissue has been studied in-vitro using 2D or 3D cultures, but these methods fail to model the spatiotemporal organization of adipocytes and endothelial cells carrying out this endocrine signaling. Microphysiological models are newly developed platforms aimed at recapitulating the complexity of biological systems in-vitro, but are often too large in size, limiting their integration into traditional culture ware. Here, we introduce a novel, miniaturized microphysiological adipose tissue model (μAT) compatible with standard culture ware and thus amenable to high-throughput platforms.

Materials and Methods: The μAT consists a central hydrogel reservoir, containing adipocytes encapsulated within a collagen type I hydrogel, a microchannel guide serving as a precursor of the endothelialized vessel fabrication, and two media reservoirs allowing for media perfusion through the vessel, across the device (*Figure 1A*). The vessel lumen is formed via subtractive molding (*Figure 1C)* and seeded with human umbilical vein endothelial cells (HUVECs, *Figure 1D*). The μAT devices are cultured in 24 wells plates on a Biorocker to induce physiological flow through the endothelialized vessel, mimicking the tissue environment seen in vivo.

Results: The spatial organization of cells within the μAT model was validated using confocal imaging. The homogeneous distribution of adipocytes within the hydrogel was verified using Bodipy (lipid droplet stain) and Hoechst (nuclei stain) while the endothelialized vessel was visualized with CD31 immunofluorescence (*Figure 1B)*.

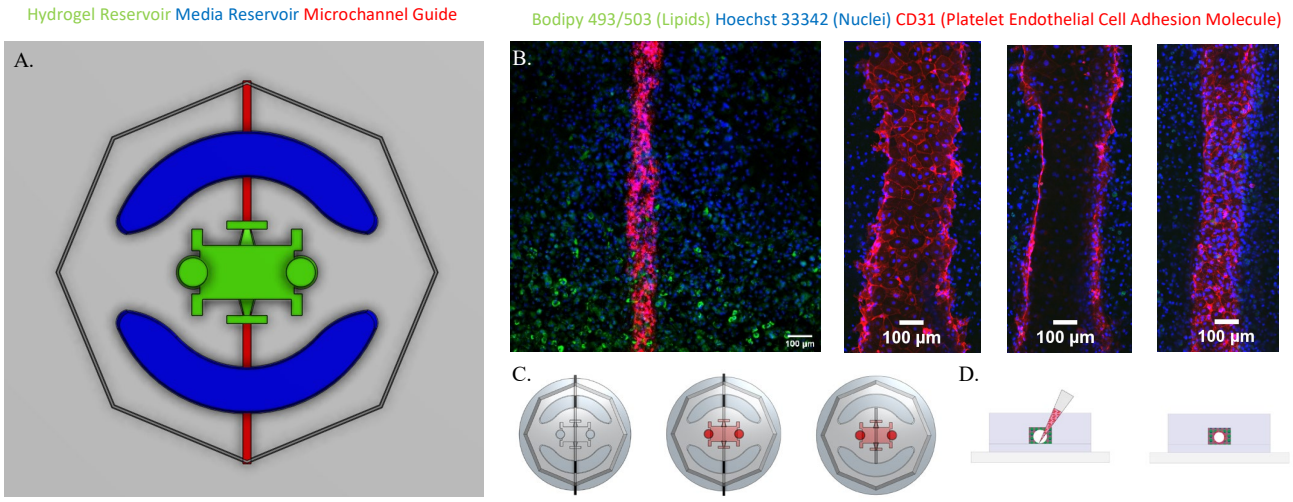

Figure 1. A. The μAT is designed with two media reservoirs (blue), one hydrogel reservoir (green), and one microchannel guide (red). **B.** Confocal images representing the μAT including the top, middle, and bottom view of the endothelialized vessel. μAT is stained with Hoechst (blue, nuclei), Bodipy (green, lipids), and for CD31 (red, endothelial cells). **C.** The microchannel is fabricated via subtractive molding. **D.** The microchannel is seeded with HUVECs prior to being cultured on a biorocker.

Future Work: In order to verify the μAT function, we will perform the following functional assays: endothelial vessel barrier function via fluorescently labeled dextran perfusion assay, glucose uptake and lipolysis for adipocyte metabolism. Lastly, stimulated lipolysis using forskolin, an adenylyl cyclase, will be performed in order to model cases of increased metabolic demand from other tissues in the body, seen in cases such as fasting or exercise.

Telomere Length Regulation of Muscle Stem Cells in Chronic Injuries

Elisia D. Tichy, Nuoying Ma, David Sidibe, Delia Chen, Jacob Kocan, and Foteini Mourkioti

Department of Orthopaedic Surgery, McKay Laboratories, University of Pennsylvania College of Medicine, Philadelphia, PA 19104

Duchenne muscular dystrophy (DMD) is a muscle disease characterized by multiple rounds of skeletal muscle injury and repair. Skeletal muscle regeneration relies on the proper functioning of muscle stem cells (MuSCs), which upon injury, become activated, proliferate, differentiate, and fuse to form a repaired muscle fiber. Previous studies by the lab have shown that telomeres play a pivotal role in the severity and progression of dystrophy in mouse models, particularly in MuSCs. Recently, we have shown that telomeres are also shortened in DMD-diseased MuSCs from young patients, compared with those from healthy donors. To identify dysregulated signaling pathways in DMD that may contribute to telomere length changes, we screened dystrophic murine MuSCs, and we found that the NF-κB signaling pathway was aberrantly upregulated in the dystrophic MuSCs, as compared with controls. Using an inducible, MuSC-specific mouse model, where NF-κB signaling is upregulated in the absence of stimuli, we queried the effects of enforced NF-κB signaling in MuSCs during in both normal and chronic muscle injury conditions. We found no ill effects resulting from NF-κB activation in either MuSCs or skeletal muscle tissue, when muscles were not injured. However, upon chronic injury, we observed rapid telomere shortening of NF-κB MuSCs compared to controls, where more repetitive injuries resulted in more significant telomere shortening. This finding correlated well with increasingly poor muscle histology. We next asked whether increased activation of NF-κB signaling in mice experiencing dystrophy enhanced the phenotype of the disease. We observed a much more severe pathology, increased muscle damage, reduced muscle strength, and telomere shortening in dystrophic mice and MuSCs, when NF-κB signaling was further enhanced. To identify the mechanism by which NF-κB promotes telomere attrition in chronic injury conditions, we investigated several different aspects. We found that NF-κB MuSCs do not exhibit increased proliferation, but they do show a downregulation of Ku80 RNA. Ku80 can reside at the telomere, but its function at this location is still being elucidated. However, Ku80 is also involved in DNA damage repair by nonhomologous end joining. To assess whether more DNA damage is present at the telomere, MuSCs from injured NF-κB mice were stained with a DNA damage marker, a MuSC marker, and a telomere probe. We found increased DNA damage at the telomere, which is known mechanism for induction of telomere shortening. We observed the same phenomenon in MuSCs derived from DMD patients, as compared to healthy human MuSCs. Finally, we asked whether the NF-κB-dependent reduction of telomere length correlated with stem cell exhaustion, similar to what is observed in the DMD disease process. Using two-photon microscopy and GFP-labeled MuSCs, we observed a significant reduction in MuSC numbers in chronically injured NF-κB mice, compared to control mice. These findings are the first to identify a role for NF-κB signaling in telomere length loss and stem cell exhaustion in chronic muscle injuries, and may lead to alternative avenues for the treatment of patients with DMD.

3D Printing of Heterogeneous Jammed Microgel Bioinks for Cartilage Defect Repair

Katrina M. Wisdom, Jonathan H. Galarraga, Margaret E. Prendergast, and Jason A. Burdick
Department of Bioengineering, University of Pennsylvania, Philadelphia, PA 19104, USA

Introduction: Spheroids have gained increasing attention as 3D building blocks for tissue engineering applications (1). While scaffold-free cartilage tissue engineering approaches can offer dynamic self-assembly and ultimately superior mechanical properties, they are limited in size due to mass-transport concerns. Scaffold approaches offer physical integrity, protection from shear during injection, and directed diffusion pathways, but can hinder tissue formation, constrain cells, and dilute cell-cell contacts. To leverage the benefits of scaffold- and scaffold-free approaches, as well as offer excellent injectability and printability for 3D bioprinting applications, we propose a combined approach, where spheroids are mixed with microgels that act as a scaffold during the formation of cartilage tissue.

Materials and Methods: Primary juvenile bovine mesenchymal stromal cell (MSC) spheroids of different sizes (1k, 5k, 15k, and 100k cells initially seeded) were individually cultured and chondrogenically induced in round-bottom, 96-well plates over a 4-week period. Spheroids were analyzed for DNA content using a PicoGreen assay, as well as sulfated glycosaminoglycan (sGAG) content using a Dimethylmethylene Blue (DMMB) assay and Alcian blue staining. MSC spheroid formation was also investigated using AggreWell™ 400 and 800 microwells. Hyaluronic acid (HA) was modified with norbornene groups (NorHA, 33% of HA repeat units modified) and dissolved (3 wt%) in phosphate buffered saline (PBS) with photoinitiator (lithium phenyl-2,4,6-trimethylbenzoylphosphinate), and dithiol crosslinker, with or without 70 kDa FITC dextran. Visible or UV light was used to crosslink microgels formed via microfluidic emulsion by reacting 40% of the available norbornene groups with dithiol crosslinker (2). Microgels were then packed by vacuum-driven filtration (0.22 μm-pore filter paper, Millipore). Combinations of microgels, or of microgels and spheroids, were then mixed and extruded. These heterogeneous bioinks were either photocrosslinked (annealed) by reacting the remaining norbornene functional groups with dithiol crosslinker, or extruded without annealing to monitor shape retention properties.

Results and Discussion: Smaller spheroids exhibited the greatest growth, and increases in DNA content were observed in all spheroids except for large (100k-cell) spheroids. Smaller spheroids trended with more efficient sGAG output efficiency (sGAG per cell initially seeded). Compared to the traditional 96-well method, production of these small spheroids could be scaled-up by seeding cells on microwells (1k: AggreWell™ 400, ~ 150 μm diameter; 5k: AggreWell™ 800, ~ 200 μm diameter). Microgels fabricated with microfluidics/photo-crosslinking exhibited diameters of ~200 μm. Microgels were mixed, jammed, and used as an ink to 3D print a dual-layer, femoral condyle-shaped, annealed construct. This construct remained intact when submerged in PBS. Similarly, when MSC spheroids and microgels were combined at a volume ratio of 75:25 (microgels:spheroids), they sufficiently annealed and remained intact upon immediate submersion in PBS. These microgel-spheroid constructs, chondrogenically induced over a period of 4-weeks, facilitated high cell viability and stained strongly and uniformly for sGAG, suggesting that cellular proliferation and matrix secretion/accumulation occurred between and around microgels. Finally, 3D printing with a combination of microgels and spheroids was possible and extruded filaments as a whole exhibited good shape-retention without post-crosslinking; individually, spheroids exhibited plastic deformation and flow, yet maintained a high, local density of cell-cell contacts.

Conclusion: Microgels can be combined with cell spheroids to form 3D printable bioinks for cartilage repair applications. To maximize cartilage-relevant matrix production from MSCs over a 4-week period, cells should be processed into small spheroids. Volume ratios of ~75% NorHa microgels and ~25% MSC spheroids, when these components are each approximately the same size, can enable sufficient microgel scaffold annealing and promote extensive sGAG production and retention. Future studies will investigate sGAG, Collagen I, and Collagen II content in constructs with different formulations.

References: (1) Makris et al, Nat Rev Rheum, 2015; **(2)** Highley et al, Adv Sci, 2018

Signaling Pathways in the Regulation of Tenogenic Gene Expression in Equine Bone Marrow Mesenchymal Stem Cells

Feikun Yang, Aiwu Zhang, Dean W. Richardson

Department of Clinic Studies at New Bolton Center, University of Pennsylvania, 382 West Street Road, Kennett Square, PA 19348

Abstract:

Traumatic tendon injuries are common in both humans and horses. Bone marrow derived mesenchymal stem cells (BMSCs) have shown great promise as part of cell-based "regenerative medicine" approaches to therapy. Despite their widespread use, however, all of the underlying mechanisms remain debatable. In this study, we investigated the potential signaling pathways involved in the tenogenesis of equine BMSCs. Western blotting results showed significantly lower level of the tenocyte marker tenomodulin (TNMD) in BMSCs cultivated in the medium supplemented with basic fibroblast growth factor (bFGF). This effect can be prevented by the addition of fibroblast growth factor receptor (FGFR) specific inhibitor PD173074, suggesting that bFGF may have anti-tenogenic effects on equine BMSCs. Moreover, the expression of TNMD was boosted when BMSCs were exposed to FGF/ERK inhibitor PD184352. Interestingly, the expression of TNMD was not affected by either mTOR signaling inhibitor rapamycin or Wnt/β-Catenin signaling inhibitor IWR, but significantly downregulated by Wnt/β-Catenin signaling activator BIO. Results from quantitative real-time PCR further revealed that the expression of other tenogenic related extracellular matrix (ECM) genes, including *BGN*, *Col1A2*, *Col14*, *DCN*, *ELN*, *FMOD,* and *TNC*, was upregulated or trended upwards by treatment with either PD184352, or rapamycin, or IWR, and downregulated by BIO treatment. Taken together, our data suggest that blockage of bFGF signaling pathway may facilitate the tenogenic differentiation of BMSCs.

RGS12 is a novel critical NF-κB activator in rheumatoid arthritis

Gongsheng Yuan[1], Shuting Yang[1], Andrew Ng[2], Merry Jo Oursler[3], Shuying Yang[1,4*]

[1]Department of Anatomy and Cell Biology, University of Pennsylvania, School of Dental Medicine, Philadelphia, PA
[2]Department of Oral Biology, School of Dental Medicine, University of Buffalo, State University of New York, Buffalo, NY
[3]Department of Medicine, Endocrine Research Unit, Mayo Clinic, Rochester, MN
[4]The Penn Center for Musculoskeletal Disorders, University of Pennsylvania, School of Medicine, Philadelphia, PA
[*]Corresponding author: Dr. Shuying Yang, Department of Anatomy and Cell Biology, University of Pennsylvania, School of Dental Medicine, Philadelphia, PA. shuyingy@upenn.edu

Background: Rheumatoid arthritis (RA) is a chronic autoinflammatory disease that affects 1-2% of the world's population and is characterized by widespread joint inflammation. Regulator of G Protein Signaling 12 (RGS12) is an essential regulator of bone remodeling, cardiac hypertrophy and tumorigenesis and is also expressed in macrophages. However, the functional relevance of RGS12 in inflammation is entirely unknown.

Methods and materials: The global expression of genes (>1500) were first profiled in synovial fluid macrophages from RA patients (RA-SF macrophages) by analyzing NCBI's Gene Expression Omnibus (GEO) database (GSE49604). Global Rgs12 knockout (GKO) mice and monocyte-targeted Rgs12 conditional knockout (CKO) mice were respectively generated by crossing $Rgs12^{fl/fl}$ mice with CMV-Cre or LysM-Cre transgenic mice (CMV; $Rgs12^{fl/fl}$ or LysM; $Rgs12^{fl/fl}$). RA mouse models were created by type II collagen-induced arthritis (CIA) and evaluated by clinical scoring, histology, X-ray and inflammatory factor analysis. Intra-articular injection with nanoparticles containing Rgs12-silencing vectors (psi-nU6.1-shRgs12) were performed in mild RA mice. Alternatively, bone marrow macrophages (BMMs) from control mice ($Rgs12^{fl/fl}$) and Rgs12 CKO mice were induced with LPS at different doses and time points. Molecular events and inflammatory markers were examined by qPCR, western blot, ELISA, immunofluorescence and histochemical staining. Transcriptional regulatory activity of NF-κB was determined by luciferase and ChIP assays in macrophages (RAW264.7 cells and BMMs).

Results: Transcriptomic analysis of revealed that Rgs12 critically regulates diverse pathologic processes in RA synovial macrophages. Rgs12 is highly expressed in macrophages, and significantly up-regulated in RA patients. Rgs12 GKO and CKO mice are resistant to CIA, which exhibits a dramatic decrease in clinical score (57%; 59%, $P < 0.001$), paw thickness (78%; 74%, $P < 0.01$), incidence rate (32%; 34%, $P < 0.01$), bone erosion, pannus, synovitis, and inflammatory factors. Mechanistically, TNFα- and lipopolysaccharide-treatment in monocytes promote Rgs12 expression in NF-κB pathways. Rgs12 through its PTB domain directly binds to NF-κB and activates its phosphorylation and nuclear translocation. Moreover, NFκB transcriptionally activates Rgs12 expression in a dose dependent manner. Cyclooxygenase-2, which catalyses the synthesis of pro-inflammatory prostaglandins, in particular prostaglandin E 2, binds with NF-κB and Rgs12 to promote NF-κB/Rgs12 nuclear translocation. Furthermore, injection of nanoparticles containing psi-nU6.1-shRgs12 in RA mice can inhibit NF-κB activation, neutralize proinflammatory cytokines, suppress synovial inflammation, and provide strong chondroprotection against joint damage, therefore demonstrating the essential role of the Rgs12/NF-κB axis in arthritis progression *in vivo*.

Conclusion: Our findings demonstrate that Rgs12 is a proinflammatory factor and plays a critical role in the pathogenesis of inflammatory arthritis in mice through controlling Rgs12/NFκB axis. Our findings provide novel genetic evidence and the new potential therapeutic interventions for various Rgs12-mediated inflammatory diseases, including RA.

Functional Decline in Mice Overexpressing Human Interleukin (IL)-8 with Age

Yejia Zhang, MD, PhD., Zuozhen Tian, MS, Julie M. Brent, DVM, MPH, Frances Shofer, PhD, Alec Z. Sandroni, Carla R. Scanzello, MD, PhD, Lan Zhao, PhD, Di Chen, MD, PhD, Flavia Vitale, PhD.

Email address and telephone number of contact: yejia.zhang@uphs.upenn.edu; Phone: 215-868-9951 (cell)

Introduction: We and others have shown that inflammatory mediators found in annulus fibrosus (AF) tissues from patients with discogenic back pain may play a key role in back pain.(1-3) Among the chemokines identified, IL-8 is the most inducible in vitro.[2] Patients with back pain often have joint pain, commonly affecting knees, hips, and facet joints of the spine. Some patients with chronic back and joint pain develop pain behavior, including verbal (e.g. verbal descriptions of the intensity, location, and quality of pain; vocalizations of distress; moaning, or complaining) or nonverbal (e.g. withdrawing from activities, taking pain medication, or pain-related body postures or facial expressions). These pain behaviors can disrupt work and normal social activities. To model IVD degeneration and related pain behavior *in vivo*, we have generated a conditional IL-8 transgenic mouse model.

Methods. Transgenic mouse generation: pCALL2 plasmid was used to construct human Interleukin (hIL)-8 transgene. pCALL2-hIL-8 mice were then bred with GDF5-Cre mice (generously provided by David Kinsley, Stanford University) to conditionally express the transgene in cartilage and intervertebral disc tissues. Transgene expression was confirmed with PCR and hIL-8 ELISA. Mouse behavior was tested with Laboras (laboratory animal behavior observation, registration and analysis system, Metris®), a fully automatic and non-invasive system, to record 18 spontaneous behaviors, including locomotion, ambulation speed and distance, grooming, eating and drinking.

Results. At 8 week of age, mice in all groups (hIL-8^+ or control, male and female) traveled the longest distances over the 16-hour observation period (Figure, Left panel). With increasing age, male hIL-8^+ mice traveled progressively less distance, decreasing from 10.6 m/hr at 12 weeks of age to 5.6 m/hr at 28 weeks of age (n=6; $p<0.05$; Figure, right panel). The decline in distance traveled is not statistically significant in female hIL-8^+ mice or in control mice of either sex. Male hIL-8^+ mice spent significantly less time in locomotion than female hIL-8^+ or control mice of either sex (n=6/group; $p<0.01$), while there was no significant slowing of travel speed in any of the groups. Interestingly, female hIL-8^+ mice spent more time than male hIL-8^+ mice climbing, and the same result was found when comparing female and male control mice (n=6/group; $p<0.01$).

Male hIL-8^+ mice spent less time eating as age increased, with the decrease starting at 16 weeks of age (n=6, $p<0.01$), but spent more time in eating than their control littermates (209.0 and 132.8 seconds/hr; n=6/group, $p<0.01$). Male hIL-8^+ mice spent less time drinking than their littermate controls (n=6/group, $p<0.01$), while there was no significant difference in time spent drinking between female hIL-8^+ mice and their littermate controls (n=6/group, $p>0.05$). Interestingly, control mice of both sexes spent more time drinking at 28 weeks than at 8 weeks of age (n=6, $p<0.01$), but drinking time did not increase with age in hIL-8^+ mice of either sex (n=6, $p>0.05$).

Discussion. We have generated a mouse line to overexpress hIL-8. We have evidence that male hIL-8^+ mice traveled shorter distance as age increased from 16 weeks onward, mainly because they spent less time in locomotion. The time spent drinking did not increase in male hIL-8^+ mice, or in their female counterparts and control litternates. The mechanisms for behavior changes in mice with chronic inflammation remain to be determined.

Significance. Chronic back pain and related pain behavior is common, and cost billions of dollars each year in direct medical cost and loss of productivity. We aimed to generate a mouse inflammation model to examine the impacts of chronic inflammation on mouse function.

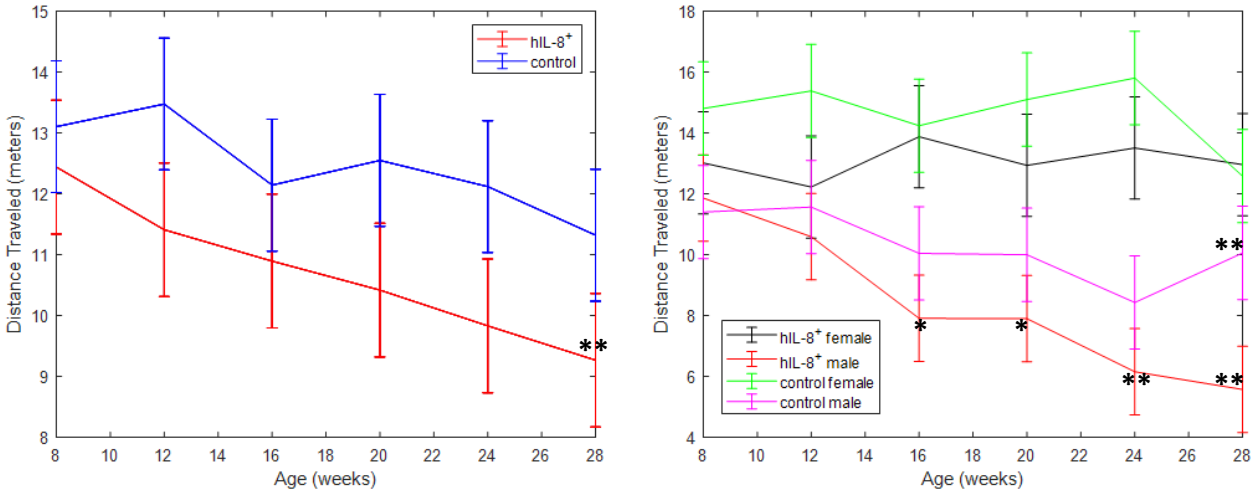

Figure. Distance traveled overnight (16 hours) in IL-8^+ mice (IL-8Tg/GDF5Cre) and their control littermates (GDF5Cre). Bar: 95% confidence interval; **p≤0.01; **p≤0.05.